University of Modena and Reggio Emilia

PhD School in Physics and Nanosciences

PhD Dissertation

Strong coupling between light and molecules:
a Quantum Chemistry approach

Author:
Jacopo Fregoni

Supervisor:
Prof. Stefano Corni

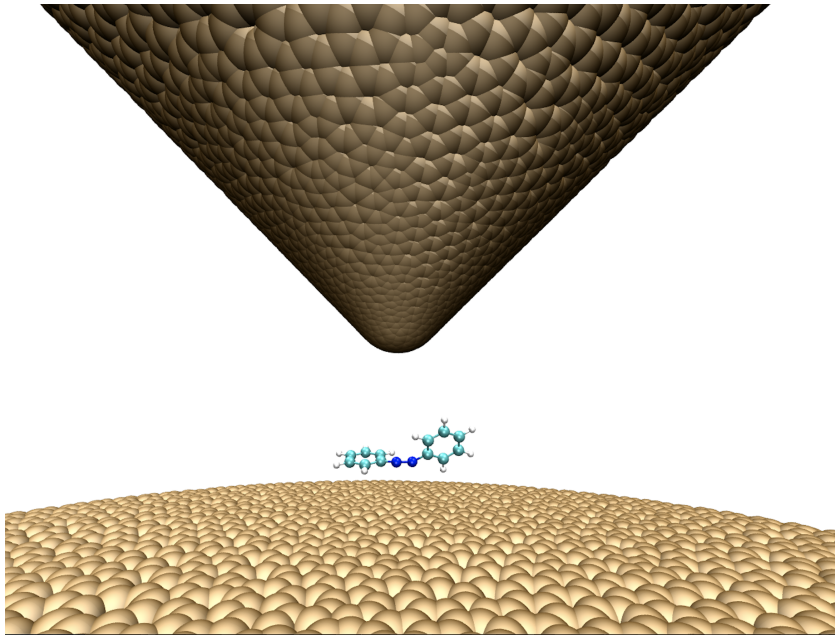

XXXII cycle - A.Y. 2019-2020

Abstract

When light and organic molecules interact in confined nanometric volumes, their exchange of energy becomes coherent over a few tens of femtoseconds. As the rate of such exchange becomes quicker than the decay of the system, the so-called strong coupling regime is achieved. In strong coupling, the degrees of freedom of light and molecule mix, offering a brand-new way to modify chemical processes. A straightforward description of molecules in strong coupling is promptly obtained by describing the eigenstates state of the system as hybrids between light and matter: the polaritons. The experiments driving this field exploited polaritons to modify the rate of photochemical processes and observed polaritons down to the single molecule level at room temperature. In parallel, the theoretical models developed a simple interpretative framework to polaritons, pioneering a new, rich polaritonic chemistry. However, the complexity of real-life polaritonic systems can quickly become cumbersome to describe theoretically, resulting detrimental for the predictive power of such models. In this thesis, the typical quantum chemistry concepts are revised for the polaritonic case. The same concepts are then exploited to extend a QM/MM surface hopping method to polaritons. In the end, the developed method is successfully applied to the study of a complete polaritonic photochemical reaction, allowing to predict a remarkable enhancement of the quantum yields and explain its mechanism.

Quando luce e molecole organiche interagiscono confinati in un volume nanometrico, scambiano energia coerentemente su scale di tempi dellordine di decine di femtosecondi. Se la velocit di scambio di energia risulta maggiore delle velocit di decadimento del sistema, si raggiunge il regime di accoppiamento forte. In questa condizione, i gradi di libert di luce e molecole si mescolano ed il sistema caratterizzato da una reattivit chimica modificata. Un modo conveniente di descrivere luce e molecole in accoppiamento forte quello di trattare gli autostati del sistemi come ibridi fra luce e materia: i polaritoni. I primi esperimenti in questo ambito hanno utilizzato i polaritoni per modificare sensibilmente le velocit di processi fotochimici. Inoltre, i polaritoni sono stati osservati a temperatura ambiente con una risoluzione fino alla singola molecola. Parallelamente, i modelli teorici sviluppati forniscono uno schema concettuale semplice per descrivere una nuova e ricca chimica polaritonica. Tuttavia, descrivere teoricamente e simulare sistemi polaritonici realistici si rivelato arduo per le dimensioni e la complessit del sistema. In questa tesi, viene presentato un metodo in grado di simulare sistemi polaritonici simulando esperimenti realistici. Il metodo si basa su un approccio Quantum Chemistry ed estende i tipici oggetti presenti in chimica quantistica al caso polaritonico. Gli stessi concetti trovano successivamente impiego nellestensione ai polaritoni di un metodo semiclassico QM/MM basato sulla tecnica Surface Hopping e nella simulazione unintera reazione fotochimica in condizioni di accoppiamento forte. Il metodo sviluppato permette di caratterizzare il meccanismo di reazione e di prevedere la possibilit di aumentare o sopprimere selettivamente le rese quantiche di reazione.

Contents

Introduction

The milestone of changing chemistry with light dates back to the very beginning of the 19$^{\text{th}}$ century, when in 1801 J. Cruickshank observed the violent reaction between hydrogen and chlorine under UV-irradiation to form chloridric acid.[1] That was the first photochemical experiment recognized and described. Ever since, the knowledge to modify physicochemical phenomena through absorption of light has been recollected in what, nowadays, is modern photochemistry. Even if hypothesized that light could induce new chemistry, the lacking of molecular structure theory and scarce knowledge of light at the beginning of the 19$^{\text{th}}$ century made the comprehension of the underlying phenomena impossible to grasp. For the scientific knowledge of light, the second half 19$^{\text{th}}$ century has provided the foundation of classical electrodynamics. Yet, one more century was needed to formulate a theory of photophysical and photochemical phenomena beyond the empirical perspective. A more advanced molecular structure theory was required and the answer heavily relies on quantum mechanics.

With the advent of the quantum theory in 20$^{\text{th}}$ century, the quantized nature of both light and matter was unraveled. Such achievement drove to a reformulation of the knowledge collected on the classical electrodynamics, taking into account the quantized nature of light through the formal introduction of photons. Interlaced with the developing theory of light, the modern molecular structure theory sprouted based on quantum mechanics. The development of the quantized theory of light and matter allowed to delve further in their interaction as well, finally leading to discover the rich phenomenology underlying the archetypical photochemical experiments of the previous century. Stark and Einstein firstly defined the absorption of a single photon as a trigger for a single physical or chemical event with the photochemical equivalence law. Few years later, the term Quantum Electrodynamics was coined by Dirac. It is the 1927 and it is just the beginning of how light can be used to manipulate matter.[2]

Fast forward to the second half of the century, it is the turning point in controlling the light

properties: the first laser is built.[3] Ever since, the interaction between light and matter is widely exploited in the development of technologies which quickly become irreplaceable in medicine, industries, imaging, sensors and communication (*e.g.* the Internet infrastructure deeply supporting the realization of the present work). In scientific research, lasers are an everyday tool for both driving a system and probing its response. The relevance of controlled light in driving a photochemical event comes by itself.

In the last decades, the routine introduction of nanoparticles as efficient tools to modulate light brought along a new era for the control of light-matter interaction at the nanoscale. Here, the light properties can be remarkably modulated via the different materials, shapes and setups of nanoparticles. The modulation exploits collective excitations of charges occurring propagating on the nanoparticle surfaces: the plasmons. As plasmonic oscillations are triggered by an external driving, a molecule close to an excited nanoparticle experiences an electromagnetic environment modified by the nanoparticle. Even more practically, suitable nanoparticles setups can act as efficient electromagnetic field enhancers, antennas, quenchers and even cavities.[4] The interaction of molecules and electromagnetic field modulated by nanoparticles is already central in advanced probing techniques as plasmon-enhanced fluorescence spectroscopy,[5] surface-enhanced Raman scattering[6,7] (SERS) and tip-enhanced Raman scattering[8,9] (TERS).

Yet, with the possibilities to manipulate light properties offered by the nanoplasmonic devices down to the sub-molecular scale, a fundamental question opens: how far can the nanoscale control of light be pushed to control photochemistry? This question is the main motivation of the present work. To answer, it is necessary to take into account the quantized nature of light at the nanoscale and a refined description of the molecular structure.

The quantum interaction between a metal nanoparticle and a neighbouring molecule is the

interaction occurring between the surface plasmons of the nanoparticle and molecular transitions. When the molecule and the plasmonic field are confined in a nanometric volume, the excited plasmonic modes resonate with either the vibrational or the electronic transitions of the molecule. The high intensity of the plasmonic field due to the nanometric confinement allows the nanoparticle to exchange energy coherently with the molecule or a portion of it, provided that the molecular transition exhibits a strong transition dipole moment. If such coherent exchange of energy between molecule and nanoparticle occurs, and if it occurs on time scales quicker than the decay channels of the system, the system enters the strong coupling regime. Namely, to achieve this condition, the plasmonic mode and the molecular exciton need to live long enough not to damp the coherent energy exchange energy. Upon entering the strong coupling regime, the states of the system are best described as hybrids between light and matter: the polaritons.

The capability of strong coupling to affect chemistry has been assessed in the last few years by coupling many molecules with metal nanoparticles,[10,11] the experimental devising of a setup to achieve single molecule strong coupling at room temperature[12,13] is encouraging the idea that also single-molecule chemistry can be tailored by shaping quantum light. More practically, we are interested to assess the capabilities of strong coupling to guide photochemical events towards a desired outcome. In these regards, this work contributes to determining whether strong coupling has a real capability to be exploited in sub-nanometric control devices, *e.g.* molecular photoswitches. As the experimental verification to probe photochemistry in strong coupling at the single molecule level has not been yet realised, we rely on computational simulations to explore the strong-coupling photochemistry phenomenology at a high level of realism. The work develops and applies a strong-coupling quantum chemical method to investigate the mechanism and the outcome of photochemical reactions in this regime.

The goal of theoretically describing the dynamical modification of the properties of nanocav-

ities and molecules in strong coupling is a formidable task. The strong light-molecule Hamiltonian ($\hat{H}_{SC}$) in its general shape consists of three contributions:

$$\hat{H}_{SC} = \hat{H}_{mol} + \hat{H}_{cav} + \hat{H}_{int}. \tag{1}$$

Here, $\hat{H}_{mol}$ is the molecular Hamiltonian described at a certain level of theory, $\hat{H}_{cav}$ is the quantized electromagnetic field Hamiltonian and $\hat{H}_{int}$ is the light-matter interaction. The global level of description is affected by the quality of the description of each subcomponent of the system. A poor choice in the description of the molecule, of the quantized electromagnetic modes or of the interaction could lead to an oversimplified description of the dynamics, irremediably flawing the predicting and interpretative capability of the models.

The ideal model should be able to propagate a manifold of quantum modes for the cavity together with the quantum treatment of the molecule, eventually including the external driving field and the non-radiative events in both the molecule and the nanoparticle.[16–19] As any of these aspects is individually subject to approximations to make the system treatable, the degree of description of the global system suffers severe limitations. A realistic (yet far from complete) description of the system is lacking in most -if not all- the works treating strong coupling between emitters and nanocavities, with drastic approximations disregarding either the complexity of the plasmonic structure or the complexity of the molecules. The minimal models to treat light-molecule strong coupling are borrowed by from traditional approaches in quantum optics (Figure 1a and 1b). Hence, they consist in taking a 2-level (Figure 1c and 1d) quantum emitter as $\hat{H}_{mol}$ and couple it via a dipolar transition to a single photon mode, *i.e.* the Jaynes-Cummings model[20] either including counter rotating terms[21] (Rabi model) or many 2-level emitters[22,23] (Dicke and Tavis-Cummings models):

$$\hat{H} = \sum_{n}^{N_{emit}} \omega_n \hat{\sigma}_n^{\dagger}\hat{\sigma}_n + \omega_{cav}\hat{b}^{\dagger}\hat{b} + \sum_{n}^{N_{emit}} \left[g_n \left(\hat{\sigma}_n^{\dagger} + \hat{\sigma}_n \right) \left(\hat{b}^{\dagger} + \hat{b} \right) \right]. \tag{2}$$

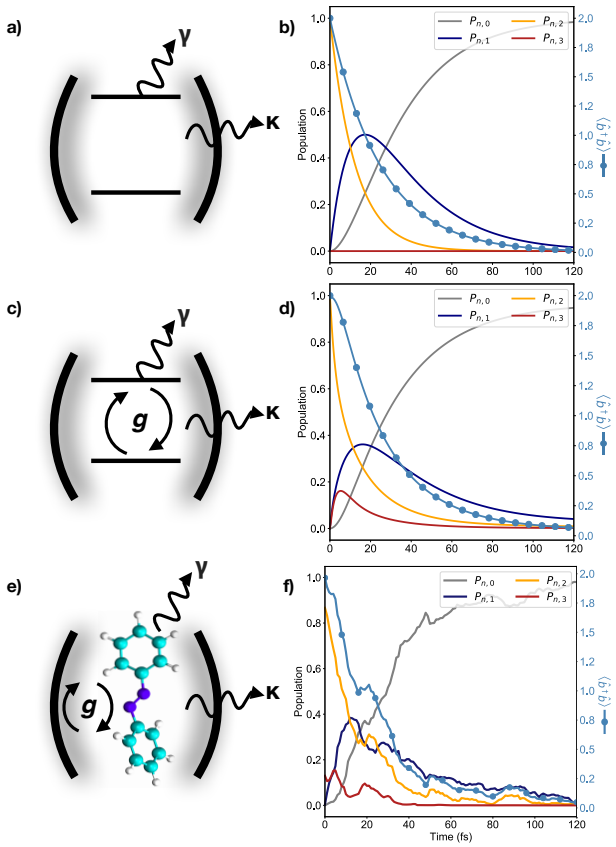

Figure 1: **Population dynamics of a quantum emitter in a cavity starting with photon occupation number** $p = 2$— **a)-b)** Spontaneous emission in presence of two decay channels κ and γ, namely the cavity loss and non-radiative decay for the emitter. The dynamics of $p = 2$ in weak coupling is governed by the dissipative behaviour. **c)-d)** Quantum-Rabi model describing the strong coupling regime. Several features in the population dynamics arise, such as a non-purely dissipative behaviour for $p = 2$, together with a transient population of the $p = 3$ subspace in the first few femtoseconds.**e)-f)** Quantum-Rabi model for a 5-level molecule including non-adiabatic events and nuclear dynamics via Surface-Hopping.[14,15] Together with a transiently increasing total photon number (circled markers), a richer oscillating dynamics is shown (see Chapters 2 and 3) as a result of the interplay between strong coupling and non-radiative events. The realistic treatment for the molecule also provides on-the-fly information on the molecular structure allowing to track down the progress of a polaritonic chemical reaction.

The Tavis-Cummings Hamiltonian couples a certain number N_{emit} of 2-level quantum emitters to a single mode of the cavity. Here ω_n and ω_{cav} are the transition frequencies of the n-th emitter and the cavity, while g_n is the coupling strength between the n-th emitter and the quantized light. While this Hamiltonian is successful in describing large ensembles of emitters characterized by neighboring transition frequencies and similar coupling strengths,

it does not provide any insight on the nuclear structure of the emitters and on the plasmonic dynamics for the field part.

On the other hand, surface plasmons full quantum calculations are instead limited due to the dimensions of the nanoparticle, forcing to resort to more traditional continuum model methods to solve Maxwell's equations,[24–26] where the limitation becomes the huge number of modes or the assumptions on the dielectric constant. On top of those complexities, the interaction itself embodies debated approximations, such as considering the coupling at dipolar level within the Coulomb gauge and long-wavelength approximation,[27–30] with very few works moving beyond the dipolar approach.[31,32]

Indeed, simplified models offer a perspective towards a whole new strong coupling chemical reactivity[17,33–35] providing the ground to root the so-called polaritonic chemistry.[17,36,37] Such new reactivity includes enhanced energy transfer,[38–40] quenching and enhancement[14,15,41] of photochemical events, remote control of chemical reactions.[42] Unsurprisingly, neglecting molecular complexity may flatten the rich polariton-assisted chemical reactivity (Figure 1e and 1f),[43,44] eventually missing alternative pathways leading to modified relaxation dynamics[45,46] or enhanced photoisomerization quantum yields.[15]

In line with what happens to molecular reactivity, also light properties are modified via light-matter strong coupling. One can think to strong light-molecule coupling as an alternative device to shape and enhance the properties of confined light. It has already been observed that the dynamics of cavities is strictly dependent on the emitters coupled to them. So far, organic polaritons have been exploited to design several room-temperature devices[47] as picocavities,[48,49] organic polariton transistor,[50] ultra-low threshold lasers,[51] hybrid organic-inorganic polariton LED.[52]

The outstanding possibilities to exploit light-molecule interaction to control either molecular properties and reactivity or emitted light property call for several theoretical challenges. While the potential of nanocavities to guide the realization of molecular devices and novel polaritonic chemistry is by now well established, each developed model present weaknesses. The greatest challenges are indeed due to the dimensions and complexity of the system. In turn, the system components (light, molecule, environment, light-matter interaction) are individually complex enough to be supported by separated communities. Taming light-matter interaction is at the base of moving beyond mechanical technologies, still the phenomenology and possibilities are countless and challenging. Theoretical efforts are then required to merge the knowledge of detached communities into computationally feasible techniques, with the aim of conducting the fundamental investigation together with aiding the devising of light-matter devices and develop new photochemistry.

Goal of the work and contribution

This thesis is aimed at developing and applying an original quantum chemical computational methodology to assess the role of chemical complexity in a realistic polaritonic photochemical reactions. Such chemical complexity arises from different sources: photochemical and environmental.

The photochemical complexity lies in the inability to simulate a photochemical reaction by taking into account the completeness of the degrees of freedom of even small systems.[53] The computational techniques to simulate photochemistry rely on non-adiabatic dynamics methodologies. This class of techniques interfaces a proper method to compute the electronic properties with a propagation scheme for the nuclei in several flavours.[54] The non-adiabatic dynamics methods can be (very) roughly divided in two branches:[55]

- semiclassical: the nuclei are classical individual trajectories moving on the electronic potential energy surfaces (PESs) computed at quantum level. The transition between

states to simulate non-radiative reaction pathways (like internal conversions, passage through conical intersection) is described through hops of the trajectories between the PESs.

- full quantum: the nuclear wavefunction is explicitly computed. Several approximation schemes have been developed to cut the outstanding computational cost of a full quantum propagation,[56,57] ranging from grid-based methods[58,59] on selected degrees of freedom to adaptive spawning methods.[60]

Although semiclassical methods are generally approximated, they allow to explicitly simulate the degrees of freedom of large systems at a semi-quantitative level.[61–64] In the recent years, their formulation has been widely improved to take into account quantum effects involving the nuclei in an effective way.[65–69] It is an excellent class of methods to investigate unexplored processes and grants a very intuitive representation of the photochemical events.

On the contrary, the wide majority of the efforts in the full quantum methods is based on cutting the outstanding computational cost.[70–72] Due to the impossibility to simulate large systems at a full quantum level, this class of methods relies on an *a priori* choice of the degrees of freedom to investigate. The aim is to achieve quantitative results when nuclear quantum effects are strongly involved and semiclassical methods are expected to fail.[73–75]

An additional point of the photochemical complexity is the level of computation of the electronic potential energy surfaces themselves. Several photochemical reactive pathways, particularly when involving organic molecules and biological systems, are characterized by the passage of the nuclear wavepacket through a conical intersection[76–78] or involve doubly excited states and charge transfer states.[79–81] To properly describe such electronic features, the electronic structure approach must be able to tackle the variation of the states composition.[82] Consequently, the computationally expensive multiconfigurational wavefunction methods[83–87] are one of the most recommended approaches to these simulations. Yet, par-

ticularly severe limitations on the electronic states calculation cost arise for trajectory-based methods which rely on an on-the-fly dynamics. A common solution to overcome such limitations is to use semiempirical Hamiltonians,[88–91] which retain all the flexibility of the multiconfigurational wavefunctions at a lower computational cost, provided a previous parameterization is performed for the class of molecules in exam.

Aiming at including the molecular complexity, the description of the molecule adopts a semiempirical formulation of the electronic Hamiltonian.[89] The nuclear propagation scheme chosen is a semiclassical on-the-fly Surface Hopping scheme[92–95] (Direct Trajectory Surface Hopping, DTSH), allowing to treat the completeness of the degrees of freedom of the test cases presented. *In this thesis, I adapt the quantum chemistry formalism of a multiconfigurational wavefunction to the polaritonic case, building the polaritonic analogous of every feature necessary to simulate a photochemical reaction. This adaptation involves building a multiconfigurational wavefunction based on polaritonic states, defining the diabatic/adiabatic representations in the polaritonic case. To compute the forces acting on the classical nuclei, I derive analytically the gradients of the polaritonic contribution to the energy with respect to the cartesian nuclear coordinates. The derivation and implementation have been carried out in collaboration with G. Granucci and M. Persico (University of Pisa), which originally developed the DTSH algorithm for the electronic case. The implementation has been carried out in a developer version of MOPAC2002.*[96]

Accounting for the environmental complexity in photochemistry typically means to include the solvent effects and the chemical surrounding of the photochemical reaction center.[87,97] The two main approaches to include the environmental complexity are to either include it implicitly or explicitly. The polarizable continuum model[98] (PCM) with its more advanced formulations[99,100] provides a plethora of recipes to include implicitly the environmental effects. Such technique allows to investigate effects induced by either the solvent or a nanoparticle

on the molecule, provided that the solvent or the nanoparticle can be described as a continuous dielectric. This formulation is particularly suitable to investigate solvatochromic[101–104] effects for the solvent interacting with the molecule and the modified optical properties of nanoparticles interacting with molecules.[25,26,105–109] In addition, the PCM-based approaches also allow to include the effect of the external driving field in terms of a polarization contribution to the medium.[100,110] As the interactions between molecule and environment involve a very heterogeneous chemical environment (like in proteins) an explicit approach to the environment is required.[111–114] The several formulations of the interface between Quantum Mechanics and Molecular Mechanics (QM/MM) satisfy such requirement, with the molecule treated at QM level is embedded in a chemical environment of classical MM molecules.

The additional environmental complexity in the polaritonic case comes from the effect of the environment on the polaritonic dynamics. The action of the environment in such case is not restrained to the relaxation and dephasing channels induced by the environment on the molecule. Namely, the multimode field for nanoparticles of different shapes shall be included, together with the cavity losses associated to it. *For the chemical surrounding, the method developed for the photochemical simulation exploits the pre-existing electrostatic embedding QM/MM interface of the QM code with the TINKER package[115] to integrate the MM part. The effort done on reformulating the polaritonic problem in a quantum chemical way allows to directly interface the QM code with the MM part without modifications. For the confined electromagnetic field, I firstly implemented a parametric single mode electromagnetic field. In the last part, I present and discuss the method to explicitly include the quantum coupling between a setup of realistic nanoparticles of arbitrary shape with realistic molecules. The implementation I realized is currently limited to the static calculations, for which validation results are shown. An explicative case of the importance to describe the geometrical features of both nanoparticles and molecules is presented. This last section opens up several further developments, ranging from the application of the same interaction scheme to polaritonic*

non-adiabatic dynamics, the investigation of Surface Enhanced Raman Scattering effects and the investigation of the strong coupling regime phenomenology to the sub-molecular level. This thesis is organized in 4 chapters.

Chapter 1 is based on the article: J. Fregoni, S. Corni, M. Persico, G. Giovanni, Photochemistry in the strong coupling regime: a trajectory surface hopping scheme, currently *accepted* on J. Comput. Chem. There, I will introduce the method and the formalism developed for polaritonic photochemical reactions. The starting point of the development is to adapt the quantum chemical formalism of non-adiabatic dynamics to the case of a polaritonic wavefunction. Here, I discuss the approximations on which this approach relies and build a conceptual representation for polaritonic system. Such representation is based on the polaritonic analogous of diabatic and adiabatic states. Chapter 1 continues with the derivation of analytical forces acting on the nuclei when the states of the molecule are polaritons, derived in the framework of multiconfigurational wavefunctions. Here, the derivation aims at computing the polaritonic forces acting on the nuclei to perform a semiclassical on-the-fly dynamics,*i.e.* the adaptation of the DTSH algorithm to polaritonic states. At last, the algorithm to include the cavity losses in the dynamics is presented. The method has been developed and refined during the whole PhD activity, so the presented version is more complete and refined with respect to the variants applied in Chapters 2 and 3.

Chapter 2 is based on J. Fregoni, G. Granucci, E. Coccia, M. Persico, S. Corni, Manipulating azobenzene photochemistry through strong light-molecule coupling. *Nat. Commun.* **9**(1), 1-9, 2018. The Chapter offers a first example of simulation of a well characterized polaritonic photoisomerization reaction in the strong coupling regime. This chapter is aimed at introducing all the relevant tools and quantities to interpret the outcome of the calculations such as the Rabi splittings in molecules, polaritonic conical intersections, quantum yields of the reaction and tools to visualize the motion of the classical nuclear trajectories

on polaritonic potential energy surfaces. With the aid of such tools developed during the PhD activity, I characterize the mechanism leading to a suppression of the trans-cis photoisomerization reaction in azobenzene. Such chemical mechanism modified by polaritons gives rise to strong coherent oscillations of the wavepacket between polaritonic states, that may be amenable to experimental verification.

Chapter 3 is based on J. Fregoni, G. Granucci, M. Persico, S. Corni, Strong coupling with light enhances the photoisomerization quantum yield of azobenzene. *Chem* **6**(1), 250-256, 2020. The Chapter presents an investigation where conditions are determined to display enhanced photoisomerization quantum yields of azobenzene as a result o the strong coupling. There, I simulate the azobenzene photoisomerization reaction with the molecule encapsulated in a nanocavity. The environment is described via the QM/MM interface of the polaritonic DTSH algorithm, with one single photon which can be multiply occupied. The setup is inspired to the one proposed by Baumberg and collaborators for single-molecule strong coupling. Chapter 3 extends the polaritonic description to include the whole photochemical complexity of the system in a simulation, like mimicking a realistic excitation of the molecule to a manifold of polaritonic states, discussing the importance of including all the molecular degrees of freedom or investigating the photostationary equilibrium in the case of a reversible photochemical reaction. The main result of the work is that the trans-cis photoisomerization reaction of azobenzene can be enhanced in suitable strong coupling conditions. I characterize such conditions and extend all the analysis tools previously developed to characterize the involved mechanism leading to such enhancement. Chapter 3 is indeed showing that molecular complexity can strongly impact the outcome of simulations, highlighting the limits of model approaches.

Chapter 4 is based on J. Fregoni, T. Haugland, S. Pipolo, H. Koch, S. Corni, Quantum coupling between classical nanoparticles and quantum molecules, which is currently

in preparation. In this Chapter, I present the methodology and the preliminary results to treat quantum coupling between realistic molecules and realistic nanoparticles. Namely, I present the approach to replace the cavity field parameters exploited in previous chapters with realistic multimode quantized fields, coming from calculations of nanoparticle setups with an arbitrary shape. I present the derivation of how to compute the quantum coupling element between such setups and a molecule. I discuss the importance of moving beyond the single-mode description of the electromagnetic field and beyond the dipole approximation when treating the light-molecule interaction. Numerical results to illustrate the theory are also reported, focusing on azobenzene.

The results are presented in the form of published papers with supporting information as well as unpublished drafts and manuscripts. With respect to the up-to-date state of the art, the approach and application presented here provide the ground to develop a very robust framework to guide and reproduce strong light-molecule coupling experiments at an unprecedented level of realism. The formulation of the method, together with the collection of tools developed to investigate the mechanism, provide insight into the polaritonic properties from a chemically-intuitive point of view and shine new light on the rich phenomenology of polaritonic chemistry.

List of Publications

List of publications related to this thesis:

- J. Fregoni, G. Granucci, E. Coccia, M. Persico, S. Corni, Manipulating azobenzene photochemistry through strong light-molecule coupling. *Nat. Commun.* **9**(1), 1-9, 2018
- J. Fregoni, G. Granucci, M. Persico, S. Corni, Strong coupling with light enhances the photoisomerization quantum yield of azobenzene. *Chem* **6**(1), 250-256, 2020
- J. Fregoni, S. Corni, M. Persico, G. Giovanni, Photochemistry in the strong coupling regime: a trajectory surface hopping scheme. *J. Comput. Chem.*, *accepted*
- E. Coccia, J. Fregoni, S. Pipolo, C. A. Guido, M. Marsili, S. Corni, Hybrid theoretical models for molecular plasmonics nanophotonics. *submitted*
- J. Fregoni, T. Haugland, S. Pipolo, H. Koch, S. Corni, Quantum coupling between classical nanoparticles and quantum molecules, *in preparation*

Other projects:

- M. C. Maschio, J. Fregoni, C. Molteni, S. Corni, Proline isomerization effects in the amyloidogenic protein β2-microglobulin, *to be submitted*
- S. Felicetti, J. Fregoni, T. Schnappinger, S. Reiter, R. de Vivie-Riedle, J. Feist, Photoprotecting uracil nucleotid with inefficient nanocavities, *submitted*

The list of authors for the *in preparation* papers may be subject to changes.

Chapter 1

This Chapter presents the formalism and the main features of the method developed to perform polaritonic photochemistry simulations, in a form of a drafted paper submitted for publication to J. Comput. Chem. The formulation presented in the followings corresponds to the latest developments achieved by the end of the PhD activity.

This Chapter firstly introduces the unsolvable problem of a correlated photon-electron-nuclei system, discussing the suitable approximations to its wavefunction. On the basis of the chosen approximation, I build the uncoupled states and polaritonic states by direct analogy with the diabatic and adiabatic electronic states. Lately, I define the relevant quantities for such states in a Quantum Chemistry formalism, like the polaritonic wavefunction, polaritonic density matrix and the polaritonic contribution to the energy. The cavity mode-molecule interaction is taken as dipolar, as it is tipically assumed when treating organic molecules in the strong coupling regime. The choice of the interaction Hamiltonian is Rabi-like,[14,21,34] hence it goes beyond the rotating-wave approximation. In the present chapter I discuss how such additional terms, together with the strength of the electromagnetic field and its orientation, can strongly alter the shape of polaritonic potential energy surfaces.

The second part of the Chapter is devoted to the adaptation of the Surface Hopping algorithm[92,94] to the polaritonic case. Starting from the quantities presented in the first part, I derive the analytical gradients for the polaritonic contribution to the energy. Although the implementation of such gradients was done for a FOMO-CI wavefunction, the derivation is rather general for multiconfigurational wavefunction methods. Among the features to adapt the DTSH algorithm to the polaritonic case, I exploit the stochastic nature of Surface hopping to include the cavity losses via a Stochastic Schröedinger equation approach.[105,106,116,117] As a test for the method, I discuss the energy conservation for both the absence and presence of cavity losses. For both cases, I characterize the dissipation of the loss of the photon from

the cavity from a kinetic perspective.

The method presented in this chapter is part of my personal contribution to this work. The most of the development and implementation were conducted by me in collaboration with Prof. Giovanni Granucci (University of Pisa). To achieve the present version of the code, the basic features such as the computation of the polaritonic wavefunction, the interface to the Surface Hopping algorithm via computation of analytical gradients for polaritonic states and the cavity losses were implemented by me during the PhD project. I also extended the formalism to multiple occupation numbers of the same mode and implemented it. The method and results are hereby presented as drafted paper, which is currently accepted for publication in Journal of Computational Chemistry. My personal contribution to the work was to devise the extension of the non-adiabatic dynamics method and implement it. In addition, I personally devised and performed the test application and drafted the paper.

Received: 22 April 2020 | Revised: 4 June 2020 | Accepted: 4 June 2020

DOI: 10.1002/jcc.26369

FULL PAPER

Journal of COMPUTATIONAL CHEMISTRY WILEY

Photochemistry in the strong coupling regime: A trajectory surface hopping scheme

Jacopo Fregoni[1] | Stefano Corni[2] | Maurizio Persico[3] | Giovanni Granucci[3]

[1]Dipartimento di Scienze Fisiche Informatiche e Matematiche, University of Modena and Reggio Emilia, Modena, Italy

[2]Dipartimento di Scienze Chimiche, University of Padova, Padova, Italy

[3]Dipartimento di Chimica e Chimica Industriale, University of Pisa, Pisa, Italy

Correspondence
Giovanni Granucci, Dipartimento di Chimica e Chimica Industriale, University of Pisa, I-56124 Pisa, Italy.
Email: granucci@dcci.unipi.it

Funding information
H2020 European Research Council, Grant/Award Number: 681285; Università di Pisa, Grant/Award Numbers: PRA 2017 28, PRA 2018 36

Abstract

The strong coupling regime between confined light and organic molecules turned out to be promising in modifying both the ground state and the excited states properties. Under this peculiar condition, the electronic states of the molecule are mixed with the quantum states of light. The dynamical processes occurring on such hybrid states undergo several modifications accordingly. Hence, the dynamical description of chemical reactivity in polaritonic systems needs to explicitly take into account the photon degrees of freedom and nonadiabatic events. With the aim of describing photochemical polaritonic processes, in the present work, we extend the direct trajectory surface hopping scheme to investigate photochemistry under strong coupling between light and matter.

KEYWORDS

nonadiabatic dynamics, photochemistry, polaritonic chemistry, strong coupling, surface hopping

1 | INTRODUCTION

The coherent interaction between light and matter in confined systems offers an alternative pathway to tailor optical and chemical properties of molecules. While the spectroscopy of atoms and molecules in resonant cavities is well established, the possibility to manipulate the molecular reactivity through quantum coupling with light has only recently been addressed. By devising microcavities[1,2] and nanocavities,[3,4] the experimental efforts[5,6] to bring molecules in the strong coupling regime down to the single molecule level have driven an increasing theoretical interest.[7–10] Yet, the modeling of such complex systems experiences limitations both theoretical and computational.

Understanding which approximations can hold for a correlated nuclear–photonic–electronic system is indeed challenging.[11,12] Even more, an important option is whether to couple the photonic degrees of freedom to the nuclear ones or to the electronic ones.[8,13,14] Within the first approach, the photonic degrees of freedom are treated so as the nuclear ones, allowing to study the effect of the electron–nuclei–photon coupling on adiabatic potential energy surfaces. Such approach provides insightful tools of analysis for phenomena like Raman Scattering,[15,16] modified molecular properties,[14,17] and ground state reactivity.[18–20] Instead, the second approach, in which electronic and photonic states are mixed, is suitable to describe the modified photochemical properties[8,21] and reactivity,[22–24] provided that nonadiabatic couplings are taken into account.

A full quantum approach has been developed by Rubio's group in the DFT framework. The method is based on rewriting the DFT formulation in terms of a current density functional which allows to include the photonic degrees of freedom[10,25] (QEDFT). Later on, the same group reformulated the Born–Oppenheimer approximation to partially decouple the nuclear–photonic–electronic problem with the so-called Cavity Born–Oppenheimer approximation.[13,14] Such works opened a way to a full ab-initio investigation of strongly coupled light–matter systems,[10,17,26] with successful applications in strong-coupling modified properties of single and many molecules.

Aiming to investigate polaritonic photochemical reactions, the complexity of the system can quickly become cumbersome. The correct computation of excited states is mandatory, together with the treatment of the photonic degree of freedom.[27–29] Further complexity to the problem is added by interfacing a propagation scheme for

the nuclei[30] and by accounting for environmental effects. In addition, the common problems encountered in photochemical simulations[31] are directly transposed to the study of polaritonic photochemical reactions.

A pioneering conceptual display of novel photochemical events in the strong coupling regime is offered by the works of Mukamel and collaborators[7,32,33] and Feist and collaborators[8,22,23] on model molecules. Such works collect a plethora of insights for a novel chemical reactivity ranging from single-molecule strong coupling to collective strong coupling effects. We have also recently shown how moving beyond model treatments to investigate polaritonic chemistry can also reveal noteworthy effects like enhanced photoisomerization quantum yields.[34]

To simulate mixed light–molecule systems, a toolbox of strong-coupling techniques for photochemistry has been developed in the last three years.[24,35,36] Among them, we mention the multiscale MD approach devised by Groenhof and collaborators, which allows to investigate the collective polariton behavior in biological environments through a QM/MM approach.[35,37,38] For events occurring in small ensembles of realistic molecules in cavities on a shorter timescale, the extension of the MCTDH technique to polaritonic systems[36,39] is also remarkable. In recent works,[24,34] we showed how the Surface Hopping scheme in a semiempirical framework can be used to describe the photochemistry of molecules in a strong coupling environment with a high level of realism. A similar Surface Hopping scheme has been used by Tretiak et al.,[40] which studied the stilbene photoisomerization under strong coupling, employing a single reference quantum chemical approach for the electronic states. Comparatively, in our scheme, we also include cavity losses, and our semiempirical multireference FOMO-CI scheme allows for a qualitatively correct description of potential energy surfaces and couplings, which is also quantitatively accurate since we reparametrize the semiempirical Hamiltonian.

In the present contribution, we show in detail the theoretical approximations and the implementation techniques of our approach to polaritonic chemistry. To this aim, we show first how polaritonic states are built on top of the semiempirical FOMO-CI[41–44] technique for the computation of electronic states. Then, we derive the analytical gradients for the strong coupling contribution to the CI energy via the Z-vector[45,46] algorithm. We also discuss the interface with the on-the-fly Direct Trajectory Surface Hopping (DTSH), with emphasis on the method we have adopted to include the effect of cavity losses on the dynamics.

We want to stress that the hereby presented gradients and Surface Hopping interface have a general applicability to multiconfigurational wavefunction methods. The choice of a semiempirical approach to solve the electronic problem resides in the good compromise between efficiency and accuracy.[31] We also mention that such approach has been successfully applied to deal with the molecular complexity of polaritons when all the degrees of freedom are taken into account,[24] and also in the presence of an environment[34] inspired to a realistic setup.[5] We also stress that, while our method carries the potential to treat a few chromophores, the study of a large ensemble of molecular systems is beyond the aim of the present work.

2 | METHODOLOGY

2.1 | Polaritonic wavefunction in a semiclassical framework

To build polaritonic states, we consider a generalized correlated photon–electron–nuclear system:

$$\widehat{H}_{tot} = \widehat{T}_e + \widehat{T}_n + \widehat{T}_{ph} + \widehat{W}_{e,e} + \widehat{W}_{e,n} + \widehat{W}_{n,n} + \widehat{W}_{e,ph} + \widehat{W}_{ph,n} + \widehat{W}_{ph,n,e} \quad (1)$$

where the electronic degrees of freedom are described by the *e* subscript (***r*** coordinates), the nuclear ones by the *n* subscript (***R*** coordinates), and the photon one by the *ph* subscript (***q*** coordinates). The total wavefunction of the correlated electron–photon–nuclei system is $\Psi(\boldsymbol{r}, \boldsymbol{R}, \boldsymbol{q})$. Two approaches to approximate the eigenstates and the time-evolution of strongly coupled systems have been applied so far: the first is to embed the photon degrees of freedom into the nuclear wavefunction[14] while the second is to embed the photon into the electronic wavefunction.[8]

Such two different approaches provide different insight on two classes of processes. In fact, the molecular properties and the dynamics in the Cavity Born–Oppenheimer approximation[13,17] are optimally described by incorporating the photon in the nuclear wavefunction ($\Psi_{n+ph,\ e}$). Instead, the processes involving nuclear dynamics on polaritonic states, that is, photochemical processes, are accurately described by considering hybrid electron–photon states (polaritons, $\Psi_{n,\ e+ph}$).[7,24,32,34,47] The Born–Huang factorizations of the wavefunction in these cases respectively correspond to:

$$\Psi_{n+ph,e}(\boldsymbol{r},\boldsymbol{q},\boldsymbol{R},t) = \sum_k \chi_k(\boldsymbol{R},\boldsymbol{q},t)\,\phi_k^{el}(\boldsymbol{r};\boldsymbol{q},\boldsymbol{R}), \quad (2)$$

$$\Psi_{n,e+ph}(\boldsymbol{r},\boldsymbol{q},\boldsymbol{R},t) = \sum_k \chi_k(\boldsymbol{R},t)\,\phi_k^{e+ph}(\boldsymbol{r},\boldsymbol{q};\boldsymbol{R}). \quad (3)$$

Equation (2) represents the case where the photon degrees of freedom are considered slow. Hence, they are treated alike to the nuclear degrees of freedom in the Cavity Born–Oppenheimer framework.[13,17] Based on this assumption, the purely electronic wavefunction and the related electronic potential energy surfaces show a parametric dependence on both the nuclear and photonic coordinates. This framework explicitly requires to compute the quantum nuclear wavefunction to include the photon effects, hence it is not properly interfaced with semiclassical methods developed treating the whole nuclear dynamics as classical.

In the factorization presented in Equation (3), the photonic degrees of freedom are considered fast and possibly resonant with optical transitions. Within this framework, the parametric dependence of the mixed electronic-photonic wavefunction with respect to the nuclear degrees of freedom allows to describe the time evolution of a polaritonic wavefunction with semiclassical trajectory-based methods. In that case, the nuclei are moving according to a classical trajectory $\boldsymbol{R}(t)$, and the polaritonic nonadiabatic couplings can be included as for

the purely electronic case. In the semiclassical case, we define by analogy with Equation (3) the polaritonic wavefunction:

$$|\Psi_{pol}(\boldsymbol{r},\boldsymbol{q},\boldsymbol{R}(t),t)\rangle = \sum_A \mathcal{C}_A(t)\,|A(\boldsymbol{r},\boldsymbol{q};\boldsymbol{R})\rangle, \tag{4}$$

where $|A\rangle$ are the semiclassical analogous of the polaritonic states ϕ_k^{ph+e} of Equation (3). We choose $|A\rangle$ to label such states to directly refer to their adiabatic behavior, as they are the eigenstates of the polaritonic Hamiltonian:

$$\widehat{H}_{pol}\,|A\rangle = E_A\,|A\rangle, \tag{5}$$

with

$$\widehat{H}_{pol} = \widehat{H}_{el} + \widehat{H}_{ph} + \widehat{H}_{int}. \tag{6}$$

Here, $\widehat{H}_{el}$ is the standard electronic Hamiltonian and $\widehat{H}_{ph}$ is the Hamiltonian of the quantized electromagnetic field (we consider here a single mode for the field),

$$\widehat{H}_{ph} = \hbar\omega_{ph}\left(\widehat{b}^\dagger\widehat{b} + \frac{1}{2}\right) \tag{7}$$

where $\widehat{b}^\dagger$, $\widehat{b}$ are the creation and annihilation operators for the electromagnetic field. In principle, the approach considered in this work could be extended in a straightforward way to consider several cavity modes. However, it is uncommon that many modes can reach a coupling strength large enough to require a strong coupling treatment, not to mention that they may also be well separated in energy. As interaction Hamiltonian H_{int}, we take the dipolar light–matter interaction in the Coulomb gauge and long wavelength approximation:

$$\widehat{H}_{int} = \mathscr{E}_{1ph}\boldsymbol{\lambda}\cdot\widehat{\boldsymbol{\mu}}_{tr}\left(\widehat{b}^\dagger + \widehat{b}\right). \tag{8}$$

In the light–matter interaction, we refer to $\mathscr{E}_{1ph}$ as the 1-photon field strength, with the electromagnetic field polarization $\boldsymbol{\lambda}$. $\widehat{\boldsymbol{\mu}}_{tr}$ is the electronic transition dipole moment between the electronic states. Notice that $\widehat{H}_{pol}$ is parametrically dependent on the nuclear coordinates through $\widehat{H}_{el}$ and $\widehat{H}_{int}$. As we have numerically verified in previous works,[24,34] for the case of strong coupling with optical frequencies, it is enough to restrain to the transition dipole operator. In the next section we focus term-by-term on the two individual subcomponents of the polaritonic Hamiltonian, namely $\widehat{H}_{el}$ and $\widehat{H}_{ph}$.

2.2 | FOMO-CI wavefunction and uncoupled states

The method for the computation of electronic states, that is, the eigenstates of $\widehat{H}_{el}$, is based on floating occupation of molecular orbitals (FOMO).[42,43] This variant relies on the optimization of a single determinant wavefunction with fractional variational occupation of the molecular orbitals through a self-consistent field calculation (SCF). The single-determinant SCF calculation is formally closed-shell. Here, the energy of the i-th orbital (φ_i) is the Fock eigenvalue ε_i corresponding to that orbital, while the occupation number O_i of φ_i is obtained integrating a function $f_i(\varepsilon)$ normally distributed along the energy axis around ε_i:

$$\widehat{F}\varphi_i = \varepsilon_i\varphi_i, \tag{9}$$

$$O_i = \int_{-\infty}^{\varepsilon_F} f_i(\varepsilon)d\varepsilon = \int_{-\infty}^{\varepsilon_F} \frac{\sqrt{2}}{\sqrt{\pi}\sigma} e^{-\frac{(\varepsilon-\varepsilon_i)^2}{2\sigma^2}} d\varepsilon. \tag{10}$$

Here, σ is an arbitrary parameter and the Fermi energy ε_F is determined by imposing that the sum of the orbital occupation numbers O_i equals the total number of electrons. The Fock operator $\widehat{F}$ is obtained from the density (orbitals are considered as real functions in the present work)

$$\rho\left(\vec{r}\right) = \sum_i O_i\varphi_i^2\left(\vec{r}\right). \tag{11}$$

Through this procedure, the lower virtual orbitals can be populated without resorting to a MCSCF optimization of the wavefunction, allowing to smoothly adapt the orbitals to the internal coordinate's variations with just a single determinant. The electronic wavefunctions are obtained performing a CI calculation on top of the FOMO-SCF, resulting in a multiconfigurational FOMO-CI. This approach can be taken as a replacement of the more accurate but much more complex CASSCF procedure.

As electronic Hamiltonian $\widehat{H}_{el}$, we consider a semiempirical Hamiltonian, as this allows to treat relatively large chromophores, including all the degrees of freedom in the simulation of polaritonic photochemistry, for timescales up to several picoseconds. In particular, for our test case we used a reparametrized version of the AM1 semiempirical Hamiltonian.[41] Notice that the standard semiempirical parameters are normally determined to reproduce ground state properties, with a SCF wavefunction. Therefore, to deal with excited states, a reparametrization is often mandatory, as what has been done in Reference [41].

As we adopt a CI-type wavefunction, the (approximated) eigenstates $|n\rangle$ of $\widehat{H}_{el}$ and the corresponding eigenenergies U_n are obtained by diagonalizing the electronic Hamiltonian matrix:

$$\widehat{H}_{el}\,|n\rangle = U_n\,|n\rangle, \tag{12}$$

on the basis of a chosen set of N_{CI} Slater's determinants $\{\Phi\}$, so that

$$|n\rangle = \sum_K^{N_{CI}} C_{K,n}\,|\Phi_K\rangle \tag{13}$$

Similarly to the electronic states, the photon states are the eigenstates $|p\rangle$ of $\widehat{H}_{ph}$:

$$\hat{H}_{ph}\,|\,p\rangle = \hbar\omega_{ph}\left(p+\frac{1}{2}\right)|\,p\rangle. \tag{14}$$

The meaning of p is a photon occupation state number, for the single electromagnetic mode of frequency ω_{ph} considered here.

The product states between the electronic and photonic eigenstates $|n,\,p\rangle$ are then the eigenstates of the light–matter non-interacting Hamiltonian $\hat{H}_{el}+\hat{H}_{ph}$. We shall address to them as uncoupled states through all the present work. Such set of uncoupled states $|n,\,p\rangle$ are the polaritonic equivalent of, for example, the spin-diabatic states for the purely electronic case with spin-orbit coupling.[48]

2.3 | Polaritonic states evolution and energies

The time evolution of the wavefunction is performed in terms of the polaritonic adiabatic states $|A\rangle$, which are obtained by diagonalization of the matrix of $\hat{H}_{pol}$ (Equation (6)) on a selected subspace of $N\times(p_{max}+1)$ uncoupled states $\{n,\,p\}$, where $N\le N_{CI}$ is the number (usually small) of electronic states considered, and p_{max} is the maximum value of the photon occupation number. The set of adiabatic states $|A\rangle$ is used to perform the time evolution as the surface hopping approach is representation-dependent, and usually performs better in the adiabatic basis. However, the set of uncoupled states $|n,\,p\rangle$ is still useful, mainly in order to ease the interpretation of the results. Within the described framework, the polaritonic wavefunction evolves according to the "polaritonic TDSE" $i\hbar\dot{\Psi}_{pol}=\hat{H}_{pol}\Psi_{pol}$, which gives

$$\dot{\mathcal{C}}_A(t) = -\sum_B\left(\frac{i}{\hbar}H_{AB}+\left\langle A\middle|\frac{d}{dt}\middle|B\right\rangle\right)\mathcal{C}_B(t) \tag{15}$$

$$= -\sum_B\left(\frac{i}{\hbar}H_{AB}+\boldsymbol{G}_{AB}\cdot\dot{\boldsymbol{R}}(t)\right)\mathcal{C}_B(t), \tag{16}$$

where $H_{AB}=\left\langle A\middle|\hat{H}_{pol}\middle|B\right\rangle$ and $\boldsymbol{G}_{AB}$ is the derivative coupling vector between the polaritonic states $|A\rangle$ and $|B\rangle$, namely

$$\boldsymbol{G}_{AB}=\left\langle A\middle|\hat{\boldsymbol{\nabla}}_R\middle|B\right\rangle. \tag{17}$$

According to Equation (13), a polaritonic state can be written as

$$|A\rangle=\sum_{n=1}^{N}\sum_{p=0}^{p_{max}}D^A_{n,p}|n,p\rangle=\sum_{n,p}D^A_{n,p}\sum_K^{N_{CI}}C_{K,n}|\Phi_K,p\rangle, \tag{18}$$

and its energy is

$$E^A_{pol}=E^A_{el}+E^A_{ph}+E^A_{int}, \tag{19}$$

where the contribution of the uncoupled part can be extracted by exploiting Equations (14) and (18), resulting in:

$$E^A_{el}=\sum_n U_n\sum_p\left|D^A_{n,p}\right|^2 \tag{20}$$

$$E^A_{ph}=\hbar\omega_{ph}\left(\sum_{n,p}p\left|D^A_{n,p}\right|^2+\frac{1}{2}\right). \tag{21}$$

The interaction term E^A_{int} is given by

$$E^A_{int}=\mathscr{E}_{1ph}\sum_{n\neq m}\langle m|\boldsymbol{\lambda}\cdot\hat{\boldsymbol{\mu}}(\boldsymbol{R})|n\rangle D(A\,|\,m,n) \tag{22}$$

where we used the shorthand

$$D(A\,|\,m,n)=\sum_{p=0}^{p_{max}-1}\sqrt{p+1}\left(D^A_{n,p}D^A_{m,p+1}+D^A_{n,p+1}D^A_{m,p}\right). \tag{23}$$

Notice that $D(A\,|\,m,n)=D(A\,|\,n,m)$.

When $m<n$ the process described is the molecule exchanging the photon of frequency ω_{ph} with the cavity. The rate of such exchange is the Rabi splitting (Jaynes-Cummings Hamiltonian).[49,50] In this regime, the emission rate and efficiency is greatly enhanced through the Purcell effect[47,51] and the energy is coherently exchanged between matter and cavity. Such energy contribution is the Rabi splitting. Instead, when $m>n$, the so-called counter rotating terms account for the simultaneous creation/annihilation of two off-resonant excitations within the cavity. Such terms become non-negligible, together with the dipolar self-energy of the molecule, in the ultrastrong coupling regime.[11,12]

From now on, we will use i, j, … to label CI-active molecular orbitals (MO) and a, b for any kind of MO. A more appealing expression, from the computational point of view, of the interaction energy E^A_{int} is obtained by using the spinless electronic density matrix, suitably modified, of the polaritonic state $|A\rangle$ considered. In particular, we have

$$E^A_{int}=\mathscr{E}_{1ph}\sum_{ij}\rho^{int}_{ij}(A)\mu_{ij}, \tag{24}$$

where $\mu_{ij}=\langle i|\boldsymbol{\lambda}\cdot\hat{\boldsymbol{\mu}}|\,j\rangle$ and

$$\rho^{int}_{ij}(A)=\sum_{n\neq m}D(A\,|\,m,n)\Delta^{el}_{ij}(m,n). \tag{25}$$

$\Delta^{el}_{ij}(m,n)$ is the spinless transition density matrix between the electronic states m and n, expanded on the molecular orbital basis. The action of the bosonic creators and annihilators of Equation (8) is embedded into the $D(A\,|\,m,\,n)$ coefficients. Therefore, $\Delta^{el}_{ij}(m,n)$ is purely electronic:

$$\Delta^{el}_{ij}(m,n)=\langle m|\hat{a}^\dagger_i\hat{a}_j|n\rangle=\sum_{I,J}C_{I,m}\langle\Phi_I|\hat{a}^\dagger_i\hat{a}_j|\Phi_J\rangle C_{J,n} \tag{26}$$

Within our method, we are able to compute the Polaritonic Potential Energy Surfaces (PoPESs) up to an arbitrary occupation number of the photonic mode involved in strong coupling.

We shall now briefly discuss the dependence of the PoPESs on the molecular transition dipole moments. Upon diagonalization, a crossing of the uncoupled states PES is converted to a polaritonic avoided crossing. The magnitude of the splitting (Rabi splitting) is proportional to the transition dipole moment between the crossing states, potentially reaching zero for vanishing transition dipole moments (polaritonic conical intersection). The strong dependence of the Rabi splitting on the transition dipole moment also embodies a strong dependence on the nuclear geometry at which the crossing between uncoupled states occurs, as the transition dipole moments variation with nuclear geometry may be large. Note that the orientation of the molecule here plays the same role as the internal coordinates, because it affects the projection of the transition dipole on the field polarization vector.

While the polaritonic conical intersection and avoided crossings have been reported in previous works,[8,24,39,52,53] here we stress that they are an easy-to-predict feature only when limited to two level strong coupling models, that is, Jaynes-Cummings like. Two-level models imply a linear dependence of the Rabi splitting on the coupling constant $\mathscr{E}_{1ph}$. As the number of electronic states is extended by including upper states (Figure 1a), the interaction between the polaritons originating the avoided crossing or conical intersections becomes more involved. This behavior is due to the interaction between the uncoupled states not directly crossing, originated by the counter-rotating terms in the Hamiltonian. The sum of such interactions deeply affects the polaritonic energy landscape by modifying both the splitting and the crossing geometry, as shown in Figure 1a,b for the azobenzene molecule.

We stick to azobenzene as a test case, since the phenomenology of polaritonic photochemistry has been investigated in recent works.[24,34] In the present work, instead, we focus on discussing the change of shape of the polaritonic avoided crossing regions, computed along NNC for different values of $\mathscr{E}_{1ph}$. For mode volumes smaller than 20 nm^3 ($\mathscr{E}_{1ph}$ > 0.003), the polaritonic crossing seam gets displaced to up to 8° along the NNC coordinate while the Rabi splitting is not much affected, as shown in Figure 1. The curves here are computed within a model space of uncoupled states composed by 5 electronic states and photon occupation number ranging from 0 to 3. The polaritonic state energies are computed along the symmetric NNC bending angles with fixed CNNC (180°) and optimizing all the other degrees of freedom for the ground state energy, resulting in a C_2 symmetry. The photon frequency is set at 2.30 eV and the polarization of the field is oriented along the longitudinal axis of the molecule. Here, the high transition dipole moment between the state S_0 and the S_2, S_3, and S_4 states manifold is instrumental in modifying the avoided $|S_0, 1\rangle$,$|S_1, 0\rangle$ crossing landscape by effect of the interaction between the state $|S_0, 1\rangle$ and the $|S_2, 0\rangle$, $|S_3, 0\rangle$, and $|S_4, 0\rangle$ manifold.

We examine the whole range of $\mathscr{E}_{1ph}$ going from 0.002 au (corresponding to a mode volume of ∼40 nm^3) to $\mathscr{E}_{1ph}$ = 0.010 au (∼1.6 nm^3). While a mode volume of 40 nm^3 is in line with typical nanocavities,[5] the extreme limit of ∼1 nm^3 has been accessed experimentally via single-atom hotspots.[54,55] In all the conditions examined in this work, the mode volume is enough to fully embed the molecule (the molecular volume being ∼0.25 nm^3). A few works pioneer the interaction beyond the dipolar approximation for small mode volumes for TERS experiments,[56,57] but not in connection with polaritonic photochemistry. More practically, it is not clear at which volumes and in which conditions the dipolar approximation ceases to be valid in the framework of dynamical processes. Moving beyond the dipolar treatment for polaritonic photochemistry carries the promise to reveal new effects for strong coupling at submolecular level.

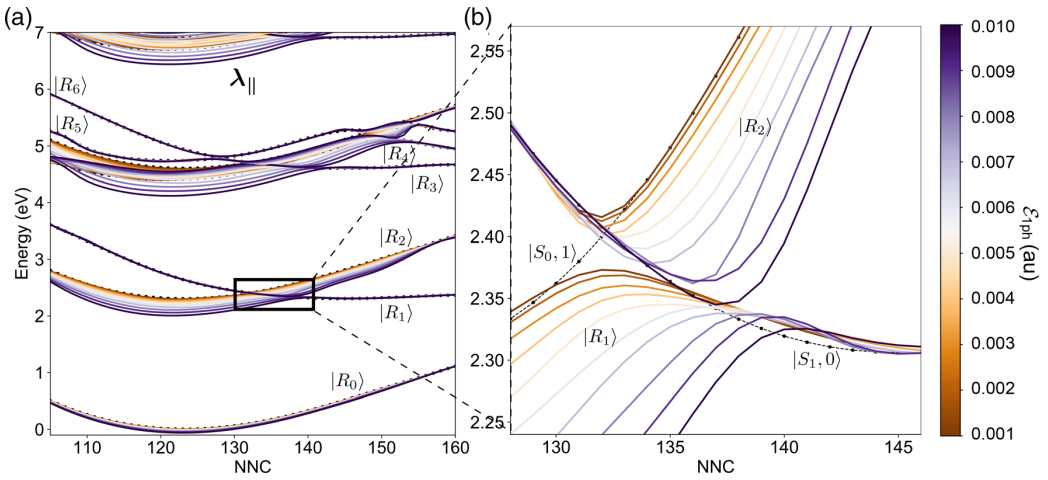

FIGURE 1 Polaritonic crossing seams for weak to ultrastrong values of $\mathscr{E}_{1ph}$. (a) Polaritonic PESs along the NNC coordinate with CNNC fixed at 175°, relaxing all the other degrees of freedom and including multiple states and counter-rotating terms. The field polarization $\lambda_\parallel$ is taken parallel to the longitudinal axis of the molecule. Although values of $\mathscr{E}_{1ph}$ > 0.005 au (<7 nm^3 mode volume) can actually be reached through single-atom hotspots,[54,55] (b) a drastic effect on the PESs shape is observed also for intermediate values of $\mathscr{E}_{1ph}$, ranging from 0.002 au (∼46 nm^3 mode volume) to 0.004 au (∼12 nm^3 mode volume), resulting in the seam shifting up to 3–4° along the NNC coordinate. In both panels, the dotted-dashed lines label purely electronic states (no strong coupling) [Color figure can be viewed at wileyonlinelibrary.com]

However, in the present case, we limit ourselves to the dipolar approximation for the whole range of mode volumes investigated.

The polarization of the field is another important issue to deal with when computing polaritonic states. Indeed, the anisotropy of the transition dipole moment components with respect to the axes of the molecule impacts the outcoming energy landscape as well. For *trans*-azobenzene at nearly planar geometries, the largest component of the transition dipole moments lies in the molecular plane. In particular, at C_{2h} geometries the $\langle S_0|\hat{\boldsymbol{\mu}}|S_1\rangle$ transition dipole vanishes. As a consequence, by changing the polarization of the field from longitudinal ($\lambda_{\parallel}$) to perpendicular ($\lambda_{\perp}$) to the plane of the molecule, the PoPESs change from the ones in Figure 1a to the ones in Figure 2a. In the latter case, the dependence of the splitting on the coupling strength is lost due to a vanishing transition dipole moment when CNNC is 180°.

Although the uncoupled states used in the calculation are the same as in Figure 1, almost all the lines corresponding to different $\mathscr{E}_{1ph}$ are overlapped in Figure 2a. The transition dipole moments perpendicular to the plane of the molecule begin to rapidly grow when twisting the molecule, that is, with a change along the CNNC coordinate. Consequently, the polaritons are split again by a twisting of the CNNC dihedral, resulting in a polaritonic conical intersection (Figure 2b) at CNNC 180° and NNC 132°. All these features provide a clear evidence that the molecular complexity must be dealt with to correctly describe the photochemical dynamics on polaritonic states.

2.4 | Analytical gradients for CI-expanded polaritonic states

After showing the strong coupling contribution to the energy in the previous section (Equation (24)), here we derive the analytical energy gradient with respect to the nuclear coordinates R_α for a generic FOMO-CI expanded polaritonic state. The present approach is based on previous works,[43,58] where the Z-vector method has been applied. In particular, here we adapt to the polaritonic case the "contracted" strategy that was developed in a spin-orbit framework.[44] As in References [44, 58], only the active MOs are allowed to have floating occupation numbers. The gradient of the energy can be partitioned in a response term, containing the derivatives of CI and MO coefficients, and a static term. The static contribution specific to the present case is given by the derivative of the molecular dipole operator matrix elements in terms of atomic orbitals (AO). As for the response terms, notice that the derivatives of the expansion coefficients $D^A_{n,p}$ of the polaritonic adiabatic state $|A\rangle$ give a null contribution to $\frac{\partial E^A_{pol}}{\partial R_\alpha}$, since $\frac{\partial E^A_{pol}}{\partial D^A_{n,p}} = 0$ by construction. As a consequence, since E^A_{ph} does not involve geometry dependent quantities other than the D_A coefficients (in the long wavelength approximation), it does not contribute to the gradient and will not be considered further here. At variance, the derivatives of the electronic CI coefficients $C_{I,\,n}$ have to be considered.

We have then

$$\frac{\partial E^A_{pol}}{\partial R_\alpha} = \frac{\partial E^A_{el}}{\partial R_\alpha} + \frac{\partial E^A_{int}}{\partial R_\alpha}. \tag{27}$$

The gradients for the electronic energies U_n entering $\frac{\partial E^A_{el}}{\partial R_\alpha}$ are known.[43,44,46,58] Hence, here we only show explicitly the evaluation of $\frac{\partial E^A_{int}}{\partial R_\alpha}$. By making use of Equation (24) one gets

$$\frac{\partial E^A_{int}}{\partial R_\alpha} = \mathscr{E}_{1ph}\sum_{ij}\left[\frac{\partial \rho^{int}_{ij}(A)}{\partial R_\alpha}\mu_{ij} + \rho^{int}_{ij}(A)\frac{\partial \mu_{ij}}{\partial R_\alpha}\right]. \tag{28}$$

Let μ_{ij} be the matrix element of the molecular dipole operator $\hat{\mu}_\lambda$ in the MO basis, and **c** the transformation matrix from the AO to the

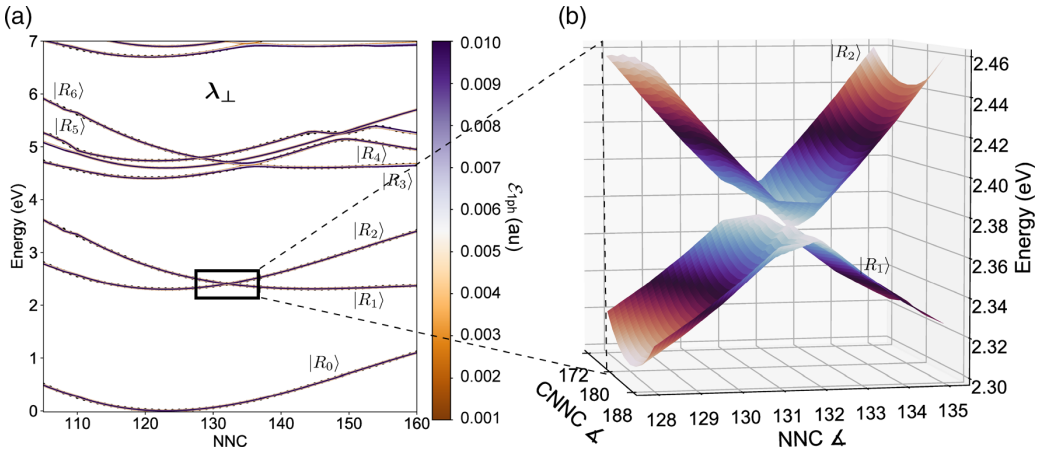

FIGURE 2 Polaritonic conical intersection for weak to ultrastrong values of $\mathscr{E}_{1ph}$, with the field polarization perpendicular to the longitudinal axis of the molecule. (a) Polaritonic states computed along the NNC coordinate in the same conditions as in Figure 1a. The polarization of the field $\lambda_\perp$ is perpendicular to the longitudinal axis of the molecule. Along this direction, the vanishing $S_0 \rightarrow S_1$ transition dipole moment at azobenzene trans-planar geometries (CNNC$\sim$175 − 180°) causes (b) a polaritonic conical intersection to arise, independently of the coupling strength [Color figure can be viewed at wileyonlinelibrary.com]

MO set (**c** is real orthogonal in the semiempirical framework considered here). We have then $\boldsymbol{\mu} = \mathbf{c}^{\dagger}\boldsymbol{\mu}_{AO}\mathbf{c}$, where $\boldsymbol{\mu}_{AO}$ is the matrix of $\hat{\mu}_{\lambda}$ in the AO basis. Therefore, the derivatives of $\boldsymbol{\mu}$ can be expressed as

$$\frac{\partial \boldsymbol{\mu}}{\partial R_{\alpha}} = \boldsymbol{B}^{\alpha}\boldsymbol{\mu} - \boldsymbol{\mu}\boldsymbol{B}^{\alpha} + \mathbf{c}^{\dagger}\frac{\partial \boldsymbol{\mu}_{AO}}{\partial R_{\alpha}}\mathbf{c} \quad \text{with} \quad \boldsymbol{B}^{\alpha} = \frac{\partial \mathbf{c}^{\dagger}}{\partial R_{\alpha}}\mathbf{c}, \tag{29}$$

which can be decomposed into a static part and a response part,[43,44,58]

$$\left.\frac{\partial \boldsymbol{\mu}}{\partial R_{\alpha}}\right|_{static} = \mathbf{c}^{\dagger}\frac{\partial \boldsymbol{\mu}_{AO}}{\partial R_{\alpha}}\mathbf{c}, \tag{30}$$

$$\left.\frac{\partial \boldsymbol{\mu}}{\partial R_{\alpha}}\right|_{resp} = \boldsymbol{B}^{\alpha}\boldsymbol{\mu} - \boldsymbol{\mu}\boldsymbol{B}^{\alpha} \tag{31}$$

The static term (Equation (30)) is easily evaluated as follows. Let $\chi_{\sigma}^{\alpha}\left(\vec{R}\right)$ be an AO belonging to nucleus α centered on $\vec{R}_{\alpha}$, with $\vec{r}_{rel} = \vec{r} - \vec{R}_{\alpha}$. The dipole matrix elements $\mu_{\sigma\tau}$ are then, in the semiempirical framework

$$\vec{\mu}_{\sigma\tau} = -e\left\langle \chi_{\sigma}^{\alpha}\left(\vec{r}_{rel}\right)\middle|\vec{r}\middle|\chi_{\tau}^{\beta}\left(\vec{r}_{rel}\right)\right\rangle = -e\delta_{\alpha\beta}\left(\delta_{\sigma\tau}\vec{R}_{\alpha} + \vec{f}_{\sigma\tau}\right) \tag{32}$$

where $-e$ is the electronic charge and the Kronecker delta $\delta_{\alpha\beta}$ is due to the semiempirical NDDO approximation. Moreover, the term

$$\vec{f}_{\sigma\tau} = \left\langle \chi_{\sigma}^{\alpha}\left(\vec{r}_{rel}\right)\middle|\vec{r}_{rel}\middle|\chi_{\tau}^{\beta}\left(\vec{r}_{rel}\right)\right\rangle \tag{33}$$

is independent on the nuclear coordinates. Therefore, the derivative of $\vec{\mu}_{\sigma\tau}$ with respect to $\vec{R}_{\alpha}$ vanishes unless the two atomic orbitals σ and τ are both centered on the nucleus α, and in that case it simply evaluates to $-e\frac{\partial \vec{R}_{\alpha}}{\partial \vec{R}_{\alpha}}$. In an ab initio context, one would have to compute also the derivative of the dipole matrix elements between atomic orbitals centered on different atoms, which has a more involved expression with respect to the term considered here. However, that would not be expected to have a large impact on the computational cost, which is mainly influenced by the response part of the gradient.

The contribution of the response term of Equation (31) to the derivative of E_{int}^{A} (Equation (28)) can be recast in this way, following Patchkovskii and Thiel[45,46]

$$\mathscr{C}_{1ph}\sum_{ij}\rho_{ij}^{int}(A)\left.\frac{\partial \mu_{ij}}{\partial R_{\alpha}}\right|_{resp} = \sum_{i}\sum_{a}\left(B_{ia}^{\alpha} + \frac{\partial \varepsilon_i}{\partial R_{\alpha}}\delta_{ia}\right)q_{ia}^{int}, \tag{34}$$

where ε_i is the energy of MO i and

$$\begin{aligned} q_{ii}^{int} &= 0 \\ q_{ia}^{int} &= 2\mathscr{C}_{1ph}\sum_{j}\rho_{ij}^{int}(A)\mu_{aj} \quad i \neq a. \end{aligned} \tag{35}$$

As $q_{ii}^{int} = 0$, the term containing the derivative of the orbital energy ε_i gives a null contribution to the sum of Equation (34). Such term has been included to recover the same formalism of previous works.[43,44,58]

We now turn to the derivative of $\rho_{ij}^{int}(A)$, which is a response term (i.e., the CI response contribution to the polaritonic energy), evaluated by taking the derivative of $\Delta_{ij}^{el}(m,n)$. Such derivative is obtained by following the same procedure outlined for the MOs response terms (Equation (31))

$$\frac{\partial \Delta_{ij}^{el}(m,n)}{\partial R_{\alpha}} = \sum_{k}^{N_{CI}}\left(d_{mk}^{\alpha}\Delta_{ij}^{el}(k,n) - \Delta_{ij}^{el}(m,k)d_{kn}^{\alpha}\right) \tag{36}$$

with

$$d_{mn}^{\alpha} = \sum_{J}\frac{\partial C_{Jm}}{\partial R_{\alpha}}C_{Jn} \tag{37}$$

Notice that the sum in Equation (36) is extended to N_{CI} rather than to the number N of states selected: in principle, the evaluation of the CI response contribution requires the full diagonalization of the CI space considered. While this may be too demanding in an ab initio context, normally it does not represent a problem in a semiempirical framework, where N_{CI} is usually small. The antisymmetric matrix d_{nm}^{α}, expressing the response of the CI coefficients, represents the CI contribution to the derivative couplings. We have then

$$\begin{aligned} \left.\frac{\partial E_{int}^{A}}{\partial R_{\alpha}}\right|_{resp}^{CI} &\equiv \mathscr{C}_{1ph}\sum_{ij}\frac{\partial \rho_{ij}^{int}(A)}{\partial R_{\alpha}}\mu_{ij} \\ &= \sum_{i\leq j}\sum_{n\neq m}G_{ij}(A\,|\,m,n)\sum_{k}^{N_{CI}}\left(d_{mk}^{\alpha}\Delta_{ij}^{el}(k,n) + d_{nk}^{\alpha}\Delta_{ij}^{el}(m,k)\right), \end{aligned} \tag{38}$$

where

$$G_{ij}(A\,|\,m,n) = \mathscr{C}_{1ph}D(A\,|\,m,n)\mu_{ij}\left(2-\delta_{ij}\right). \tag{39}$$

According to Reference [44], we evaluate the derivative coupling terms d_{mn}^{α} by exploiting the Hellmann–Feynman theorem

$$d_{mn}^{\alpha} = (U_m - U_n)^{-1}\sum_{IJ}C_{I,m}\frac{\partial\langle\Phi_I|\hat{H}_{el}|\Phi_J\rangle}{\partial R_{\alpha}}C_{J,n} \tag{40}$$

$$= \sum_{ij}\frac{\Delta_{ij}^{el}(m,n)}{U_m - U_n}\frac{\partial \varepsilon_{ij}^{+}}{\partial R_{\alpha}} + \sum_{ijkl}\frac{\Gamma_{ijkl}^{el}(m,n)}{U_m - U_n}\frac{\partial\langle ij|kl\rangle}{\partial R_{\alpha}}. \tag{41}$$

for $m \neq n$, and $d_{nn}^{\alpha} = 0$. Here, $\Gamma_{ijkl}^{el}(m,n) = \left\langle m\middle|\hat{a}_i^{\dagger}\hat{a}_j^{\dagger}\hat{a}_l\hat{a}_k\middle|n\right\rangle$ are the two-electron density matrices and the terms ε_{ij}^{+} are defined in equation (36) of Reference [44].

Inserting Equation (41) into (38), we obtain the following expression for the CI response term induced by the strong coupling interaction:

$$\left.\frac{\partial E_{int}^{A}}{\partial R_{\alpha}}\right|_{resp}^{CI} = \sum_{ij}\frac{\partial \varepsilon_{ij}^{+}}{\partial R_{\alpha}}\Delta_{ij}^{int}(A) + \sum_{ijkl}\frac{\partial\langle ij|kl\rangle}{\partial R_{\alpha}}\Gamma_{ijkl}^{int}(A). \tag{42}$$

where

$$\Delta_{ij}^{int}(A) = \sum_{k}^{N_{CI}} \sum_{\substack{m \\ m \neq k}} \frac{\Delta_{ij}^{el}(m,k)}{U_m - U_k} R(A \mid k,m) \tag{43}$$

$$\Gamma_{ijkl}^{int}(A) = \sum_{k}^{N_{CI}} \sum_{\substack{m \\ m \neq k}} \frac{\Gamma_{ijkl}^{el}(m,k)}{U_m - U_k} R(A \mid k,m) \tag{44}$$

$$R(A \mid k,m) = \sum_{i \leq j} \sum_{\substack{n \\ n \neq m}} 2G_{ij}(A \mid m,n)\Delta_{ij}^{symm}(k,n) \tag{45}$$

$$\Delta_{ij}^{symm}(k,n) = \frac{\Delta_{ij}^{el}(k,n) + \Delta_{ji}^{el}(k,n)}{2} \tag{46}$$

Here, $\Delta_{ij}^{symm}(k,n)$ is the symmetric part of $\Delta_{ij}^{el}(k,n)$. Notice that it is symmetric with respect to both i, j and k, n indices, since $\Delta_{ij}^{el}(k,n) = \Delta_{ji}^{el}(n,k)$.

To obtain the final expression for the gradient of E_{pol}^{A}, we have also to consider the contribution given by the derivative of the naked electronic state energy U_n (see Reference [58])

$$\frac{\partial U_n}{\partial R_\alpha} = \frac{\partial E_0}{\partial R_\alpha} + \sum_{ij} \Delta_{ij}^{el}(n) \frac{\partial \varepsilon_{ij}^{+}}{\partial R_\alpha} + \sum_{ijkl} \Gamma_{ijkl}^{el} \frac{\partial \langle ij|kl\rangle}{\partial R_\alpha}. \tag{47}$$

By putting all the terms together we arrive at

$$\begin{aligned} \frac{\partial E_{pol}^{A}}{\partial R_\alpha} = & \frac{\partial E_0}{\partial R_\alpha} + \sum_{ij} \Delta_{ij}^{pol}(A) \frac{\partial \varepsilon_{ij}^{+}}{\partial R_\alpha} + \sum_{ijkl} \Gamma_{ijkl}^{pol}(A) \frac{\partial \langle ij|kl\rangle}{\partial R_\alpha} \\ & + \sum_{ai} B_{ia}^{\alpha} q_{ia}^{int} + \mathscr{C}_{1ph} \sum_{ij} \rho_{ij}^{int}(A) \sum_{\sigma\tau} c_{\sigma i} \frac{\partial \mu_{\sigma\tau}}{\partial R_\alpha} c_{\tau j} \end{aligned} \tag{48}$$

where we made use of the modified electronic density matrices

$$\Delta_{ij}^{pol}(A) = \sum_{n} \Delta_{ij}^{el}(n) \sum_{p} \left| D_{n,p}^{A} \right|^2 + \Delta_{ij}^{int}(A) \tag{49}$$

$$\Gamma_{ijkl}^{pol}(A) = \sum_{ijkl} \Gamma_{ijkl}^{el}(n) \sum_{p} \left| D_{n,p}^{A} \right|^2 + \Gamma_{ijkl}^{int}(A). \tag{50}$$

The evaluation of the gradient of E_{pol}^{A} can proceed in the way outlined in Reference [58], using the modified density matrices $\Delta_{ij}^{pol}(A)$ and $\Gamma_{ijkl}^{pol}(A)$. In particular, the response term is

$$\left. \frac{\partial E_{pol}^{A}}{\partial R_\alpha} \right|_{resp} = \sum_{i} \sum_{a} \left(B_{ia}^{\alpha} + \frac{\partial \varepsilon_i}{\partial R_\alpha} \right) \left(q_{ia}^{el} + q_{ia}^{int} \right), \tag{51}$$

where q^{el}, defined as done in[58] (see also[44]), is explicitly reported below for reader's convenience

$$q_{ii}^{el} = \Delta_{ii}^{pol}(A) - O_i - \frac{1}{2} \sum_{jkl} \beta_{ki} \langle lj||kk\rangle \left(\Delta_{lj}^{pol}(A) - \delta_{lj} O_l \right) \tag{52}$$

$$q_{ia}^{el} = 4 \sum_{jkl} \Gamma_{ijkl}^{pol}(A) \langle aj|kl\rangle - \sum_{jk} \Delta_{ij}^{pol}(A) O_k \langle kk||aj\rangle - \tag{53}$$

$$\sum_{jk} \Delta_{jk}^{pol}(A) O_i \langle ai||jk\rangle + \sum_{j} O_i O_j \langle ai||jj\rangle \quad (\text{for } i \neq a)$$

$$\beta_{ki} = f_k(\varepsilon_F) \left(\frac{f_i(\varepsilon_F)}{\sum_j f_j(\varepsilon_F)} - \delta_{ik} \right) \tag{54}$$

In the above equations, we used the shorthand $\langle ij||kl\rangle = 2\langle ij|\,kl\rangle - \langle ik|\,jl\rangle$, and f_i is the Gaussian function defined in Equation (10). Finally, for the static part, one has just to add the last term of Equation (48), representing the static dipole derivative (see above).

2.5 | Surface hopping

In the framework of Direct Trajectory Surface Hopping, the formulation of strong coupling given in this work allows to include the decoherence corrections[59] and environmental effects through the QM/MM interface previously devised.[60–62] For the time evolution of the polaritonic wavefunction, we adopt the local diabatization technique,[48,63] with a recently improved evaluation of transition probabilities. Such probabilities are compliant with Tully's Fewest Switches prescription and particularly effective when many states are involved in nonadiabatic events,[64] as commonly happens in single-molecule polaritonic systems (see Figure 1b).

As a test case, we examine the azobenzene strong coupling dynamics with ω_{ph} = 2.7 eV and $\mathscr{C}_{1ph}$ = 0.004 au (∼12 nm^3) in the absence of the cavity losses. The initial conditions are sampled on the ground state via a 20 ps dynamics, thermostated at room temperature (with a Bussi-Parrinello thermostat[65]). In particular, 230 starting structures and velocities are extracted from the sampling dynamics, and the system is initially vertically excited to the $|R_8\rangle$ state, that is mostly $|S_2, 2\rangle$ state. Rather than the simulation of a realistic excitation (the transition $|S_0, 0\rangle \rightarrow |S_2, 2\rangle$ would require a multiphoton pumping), this is a test case to investigate the effect of photon occupation numbers greater than 1 (up to p = 3). In Figure 3a, we show the behavior of the population of the photon states during the dynamics, in the absence of cavity losses. The blue line with circle markers (right y scale) shows the total photon number within the cavity, namely $\left\langle \hat{b}^{+}\hat{b} \right\rangle$.

The full lines (left y scale) show the populations of each photon state, that is, $\sum_n |D_{n,\,p}|^2$, with p = 0, …, 3. While no cavity loss is explicitly included in the dynamics, still the total photon number in the system decreases. Through strong coupling, a photon is continuously exchanged between the molecule and the cavity. However, the electronic component keeps decaying via internal conversion, meaning that when the photon is absorbed, its energy can be redistributed to the nuclear degrees of freedom. While the total number of photons decreases in the ongoing dynamics, the energy of the system is still

conserved (Figure 3b). The initial conditions are chosen such that the resonant region between the $p = 3$ states (namely S_0, 3) and the $p = 2$ states $|S_1, 2\rangle$ is interested, so both the subspaces $|n, 3\rangle$ and $|n, 2\rangle$ are populated. This results into an average photon occupation number greater than $|2\rangle$, namely 2.23.

2.6 | Cavity losses

Aiming to provide a realistic model, we deal with the issue of lossy cavities. The strong coupling regime for single molecules is usually reached by exploiting a nanocavity setup of the system.[5,6,66,67] The typical lifetime of nanocavities is few tens of femtoseconds. However, we have recently shown that the overall photon lifetime of the system is way longer than the individual cavity lifetime,[34] reaching a time scale comparable to several ultrafast photochemical processes. This effect is due to the transient passage of the wavepacket through strongly coupled regions, so that the composition of the polaritonic state keeps interchanging between electronic and photonic. As a consequence of the mixing, the lifetime of states with the photon partially absorbed is extended up to hundreds of fs, depending on the strong coupling conditions. Within our model, we adapt a quantum jump algorithm[68–71] already exploited in the Stochastic Schrödinger Equation (SSE) framework[72] to account for relaxation and dephasing channels. Stochastic methods in the framework of SSE are also commonly exploited as an equivalent alternative to master equations in treating cavity losses.[73–75] We then follow a standard implementation of this approach, similar to others already present in Quantum Optics simulation packages like QuTip.[76]

The quantum jump is a natural choice as it fully exploits the trajectory-based machinery of the surface hopping. Having to deal with semiclassical trajectories, both the polaritonic wavefunction and the "current state" (i.e., the adiabatic state on which PES the nuclei are evolving) must be taken into account whenever a photon loss occurs. We start with the expression of the polaritonic wavefunction in terms of the uncoupled states basis:

$$\Psi_{pol} = \sum_A \mathcal{C}_A \,|\, A\rangle = \sum_{n,p} d_{n,p} \,|\, n,p\rangle. \tag{55}$$

where $d_{n,p} = \sum_A D^A_{n,p} \mathcal{C}_A$. Only states with free photons can decay via cavity losses, namely states with $p \geq 1$. We evaluate the photon loss probability P_{dec} by taking the squared modulus of the uncoupled states coefficients with $p \geq 1$ in the total wavefunction Ψ_{pol}, that is, $d_{n,\, p\geq 1}$:

$$P_{dec} = \sum_{p\geq 1, n} |d_{n,p}|^2 \frac{\Delta t}{\tau}. \tag{56}$$

Here, Δt is the integration time step and τ is the cavity lifetime, namely the inverse of the cavity decay rate κ. We generate a uniform random number within the interval [0, 1]. If the random number falls in $[P_{dec}, 1]$, the photon is retained and the cavity loss does not occur. If not, the photon is lost. Upon photon loss, the photon occupation number is lowered by 1 via application of the projector $\hat{P}$ which includes the photon annihilation operator $\hat{b}$:

$$\hat{P}\Psi_{pol} = \left(\mathbb{I}_{el} \otimes \hat{b}\right)\Psi_{pol} = \sum_n \sum_{p=1}^{p_{max}} d_{n,p-1}\sqrt{p}\,|\, n,p-1\rangle. \tag{57}$$

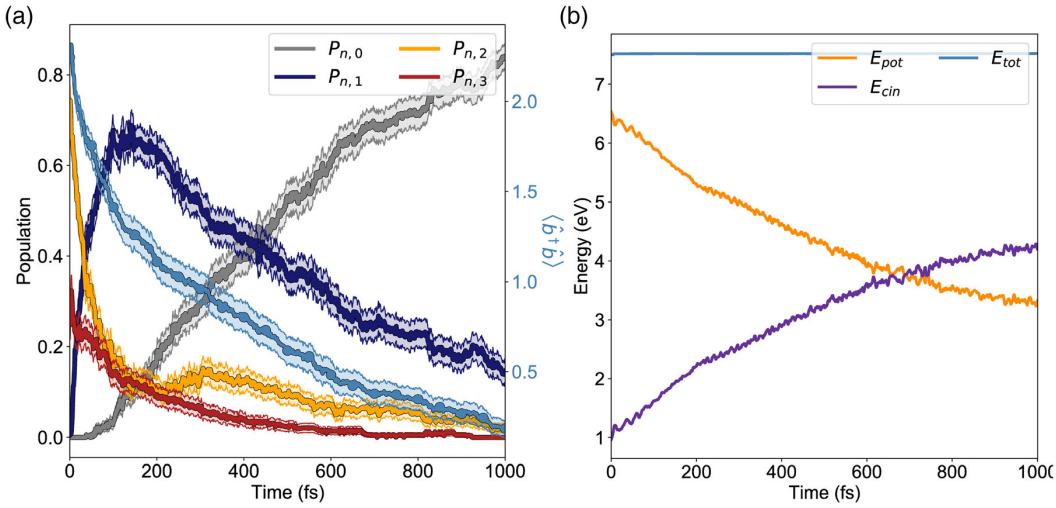

FIGURE 3 Photon statistics and energy conservation. (a) Dynamics of the photons in the cavity during the internal relaxation of the strongly-coupled azobenzene molecule, in absence of cavity losses. The dynamics is started from the $|R_8\rangle$ state and runs for 1 ps, with $\mathscr{E}_{1ph} = 0.004$ au ($\sim$12 nm^3 mode volume), $\omega_{ph} = 2.7$ eV and longitudinal field polarization. The molecule is in gas phase.[24] The curves with full lines show the dynamics of each p subspace, while the light blue line with circle markers (with the scale on the right) represents the total photon number within the cavity. Error bars, represented as lighter bands, are also shown. Even in absence of cavity losses, the average photon number decreases during the dynamics. While the photon is in its absorbed state, the energy stored within the molecule is redistributed via internal conversion to nuclear kinetic energy. The overall process is still conserving the energy, as shown in panel (b) [Color figure can be viewed at wileyonlinelibrary.com]

Here, the projector $\hat{P}$ preserves the electronic coherence within each p subspace, apart of course for $p = 0$ that is annihilated. The photonic annihilation operator $\hat{b}$ is applied to mimic the loss of the photon from the cavity, resulting in a manifold of states with photon number lowered by one. The wavefunction is normalized after application of P.

To reinitialize the dynamics after the photon loss has occurred, we need both the wavefunction to propagate and a polaritonic surface to resume the nuclear trajectory integration, $|F\rangle$. The wavefunction is simply a linear combination of polaritonic states $|A\rangle$:

$$\Psi'_{pol} = \hat{P}\Psi_{pol} = \sum_A C'_A |A\rangle, \tag{58}$$

where the ' symbol denotes the quantities after the jump. As a polaritonic energy surface to resume the nuclear trajectory propagation, we choose the polaritonic surface $|F\rangle$ that has the maximum overlap with the polaritonic wavefunction after the jump:

$$|F\rangle = |A\rangle \,|\, \max\left\{|\langle A|\Psi'_{pol}\rangle|\right\}. \tag{59}$$

If the quantum jump does not occur, the wavefunction is propagated with the non-Hermitian Hamiltonian[68,72,77]:

$$\hat{H}_{eff} = \hat{H}_{pol} - i\hbar\frac{\kappa}{2}\hat{b}^\dagger\hat{b}. \tag{60}$$

For each timestep, this is accomplished by first propagating according to H_{pol}, and then modifying Ψ_{pol} in the following way

$$\Psi_{pol} = \sum_A \sum_{n,p} C_A D^A_{n,p}\left(1 - \frac{\kappa}{2}p\Delta t\right)|n,p\rangle. \tag{61}$$

The polaritonic wavefunction Ψ_{pol} is then renormalized. The propagation between each attempted jump should be performed with the non-Hermitian $\hat{H}_{eff}$ of Equation (60), leading to un-normalized wavefunction. Anyway, in our algorithm, the jump is attempted at each time step and so the wavefunction is always normalized, one way or the other. A consequence of the photon loss is that the total energy of the system is not conserved.

In Figure 4, we replicate the dynamics performed for the lossless case (Figure 3) in presence of a cavity lifetime τ of 65 fs. The same color scheme and notation is applied. While the relaxation dynamics is of course quicker (Figure 4a) due to the presence of an extra relaxation channel (cavity loss), the decay dynamics is better described by a biexponential function, rather than a simple exponential (Figure 4b).

The main reason is that photons can be exchanged back and forth between the cavity and the molecule, via transitions $|n, p\rangle \rightarrow |n+1, p-1\rangle$ and vice versa, slowing down the cavity loss rate. This is especially important when $p = 1$, as there is no way to lose the photon from a state $|n', 0\rangle$ with zero free photons in the cavity. In particular, this happens for the system considered here, which shows transitions back and forth from $|S_1, 0\rangle$ to $|S_0, 1\rangle$. Here, the single photon remaining appears to decay with a lifetime which is 20 fs longer than the nominal decay time of the cavity. Notice that, if the single photon remaining is adsorbed by the molecule due to strong coupling, the lifetime of the system is ascribable to that of the pure electronic states. Conversely, when the photon is free within the cavity, the lifetime of the system becomes that of the nominal cavity lifetime.

The consequence of the cavity losses becomes also evident in the energy conservation plot (Figure 4c), where the initial part of the dynamics is characterized by a quick drop of the total energy due to the photon losses with no kinetic energy compensation. As a last remark, we stress that the current implementation takes advantage of dressing the chemical quantities for the strong coupling effect. Consequently, it directly supports the interface with the TINKER package to

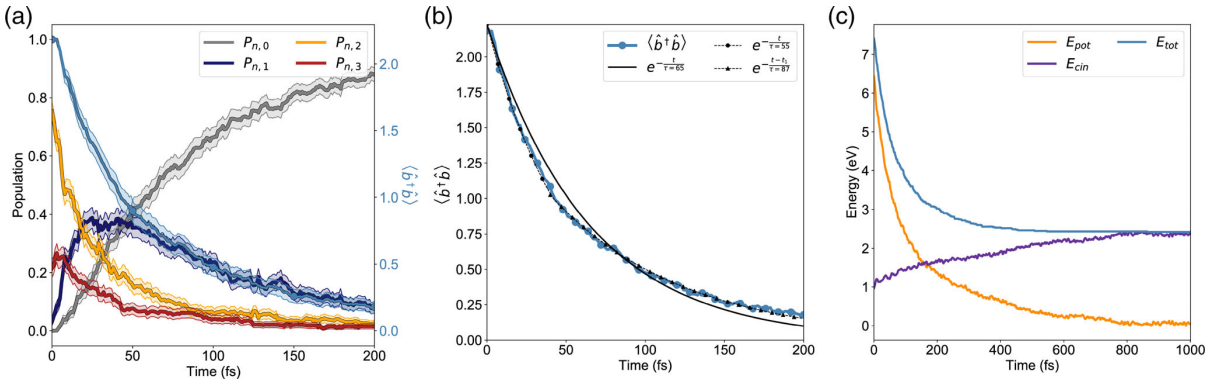

FIGURE 4 Cavity losses in strong coupling. Same conditions of Figure 3, with the same notation and color scheme. A cavity lifetime $\tau = 65$ fs is considered. (a) The overall population dynamics is definitely shorter in this case, with a transient population of the $|n, 1\rangle$ subspace. (b) Photon number in the cavity at each time step. Remarkably, the kinetics is not simply dissipative. While $p \geq 1$, the photon loss occurs at a faster rate than the cavity lifetime (circle markers fit). After only one photon remains, the loss dynamics slows down, as the only photon remaining is partially absorbed by the molecule and cannot be lost. (c) Breakdown of the energy conservation, due to cavity losses [Color figure can be viewed at wileyonlinelibrary.com]

perform QM/MM simulations with electrostatic embedding, as described and applied in References [34, 61, 62].

3 | CONCLUSIONS

In the present work, we describe a scheme we have implemented to perform direct nonadiabatic molecular dynamics simulations for semiclassical molecules in strong coupling, based on classical nuclear trajectories and on multiconfigurational wavefunctions. We build polaritonic states and present the evaluation of analytical gradients for polaritonic CI energies, extending the DTSH machinery to the polaritonic systems. Among the DTSH[42,43,58] exploitable features, we count the decoherence corrections,[59] the QM/MM interface with electrostatic embedding[60,62] and the local diabatization scheme[48,63] for wavefunction propagation. Cavity losses are included in the simulations through quantum jumps, relying on the stochastic nature of Surface Hopping. We choose the test case to highlight the complex features of the potential energy surfaces arising when moving beyond the one-dimensional 2-level molecular models. The results presented for the test dynamics highlight the delicate interplay between radiative and nonradiative emissions, both impacting the relaxation dynamics of strongly coupled systems. Especially, we show that losses are competitive with usual nonadiabatic events and that the outcoming dynamics cannot be described as simply dissipative, the photon actually living longer than the nominal lifetime of the cavity. The content of this work provides both formal and conceptual tools to approach the polaritonic photochemical simulations within a semiclassical ansatz, allowing to simulate complete photochemical reactions with a trivially parallelizable technique.

ACKNOWLEDGMENTS

J. F. and S. C. acknowledge funding from the ERC under the grant ERC-CoG-681285 TAME-Plasmons. G. G. and M. P. acknowledge funding from the University of Pisa, PRA 2017 28 and PRA 2018 36.

ORCID

Jacopo Fregoni https://orcid.org/0000-0002-4356-3060
Stefano Corni https://orcid.org/0000-0001-6707-108X
Maurizio Persico https://orcid.org/0000-0001-6861-9289
Giovanni Granucci https://orcid.org/0000-0002-4753-6318

REFERENCES

[1] D. Wang, H. Kelkar, D. Martin-Cano, T. Utikal, S. Götzinger, V. Sandoghdar, *Phys. Rev. X* **2017**, *7*, 021014.
[2] P. Zhang, I. Protsenko, V. Sandoghdar, X.-W. Chen, *ACS Photon.* **2017**, *4*, 2738.
[3] J. A. Hutchison, T. Schwartz, C. Genet, E. Devaux, T. W. Ebbesen, *Angew. Chem. Int. Ed.* **2012**, *51*, 1592.
[4] J. A. Hutchison, A. Liscio, T. Schwartz, A. Canaguier-Durand, C. Genet, V. Palermo, P. Samorì, T. W. Ebbesen, *Adv. Mater.* **2013**, *25*, 2481.
[5] R. Chikkaraddy, B. de Nijs, F. Benz, S. J. Barrow, O. A. Scherman, E. Rosta, A. Demetriadou, P. Fox, O. Hess, J. J. Baumberg, *Nature* **2016**, *535*, 127.
[6] N. Kongsuwan, A. Demetriadou, R. Chikkaraddy, F. Benz, V. A. Turek, U. F. Keyser, J. J. Baumberg, O. Hess, *ACS Photon.* **2018**, *5*, 186.
[7] M. Kowalewski, K. Bennett, S. Mukamel, *J. Phys. Chem. Lett.* **2016**, *7*, 2050.
[8] J. Feist, J. Galego, F. J. Garcia-Vidal, *ACS Photon.* **2018**, *5*, 205.
[9] F. Herrera, F. C. Spano, *Phys. Rev. Lett.* **2016**, *116*, 238301.
[10] M. Ruggenthaler, N. Tancogne-Dejean, J. Flick, H. Appel, A. Rubio, *Nat. Rev. Chem.* **2018**, *2*, 0118.
[11] D. De Bernardis, T. Jaako, P. Rabl, *Phys. Rev. A* **2018**, *97*, 043820.
[12] D. De Bernardis, P. Pilar, T. Jaako, S. De Liberato, P. Rabl, *Phys. Rev. A* **2018**, *98*, 053819.
[13] J. Flick, H. Appel, M. Ruggenthaler, A. Rubio, *J. Chem. Theor. Comp.* **2017**, *13*, 1616.
[14] J. Flick, M. Ruggenthaler, H. Appel, A. Rubio, *Proc. Natl. Acad. Sci. USA* **2017**, *114*, 3026.
[15] J. del Pino, J. Feist, F. J. Garcia-Vidal, *J. Phys. Chem. C* **2015**, *119*, 29132.
[16] T. Itoh, Y. S. Yamamoto, *J. Chem. Phys.* **2018**, *149*, 244701.
[17] J. Flick, C. Schäfer, M. Ruggenthaler, H. Appel, A. Rubio, *ACS Photon.* **2018**, *5*, 992.
[18] C. Climent, J. Galego, F. J. Garcia-Vidal, J. Feist, *Angew. Chem. Int. Ed.* **2019**, *58*, 8698.
[19] J. Galego, C. Climent, F. J. Garcia-Vidal, J. Feist, *Phys. Rev. X* **2019**, *9*, 021057.
[20] M. Du, R. F. Ribeiro, J. Yuen-Zhou, *Chemistry* **2019**, *5*, 1167.
[21] J. Galego, F. J. Garcia-Vidal, J. Feist, *Phys. Rev. X* **2015**, *5*, 041022.
[22] J. Galego, F. J. Garcia-Vidal, J. Feist, *Phys. Rev. Lett.* **2017**, *119*, 136001.
[23] J. Galego, F. J. Garcia-Vidal, J. Feist, *Nat. Comm.* **2016**, *7*, 13841.
[24] J. Fregoni, G. Granucci, E. Coccia, M. Persico, S. Corni, *Nat. Comm.* **2018**, *9*, 4688.
[25] M. Ruggenthaler, J. Flick, C. Pellegrini, H. Appel, I. V. Tokatly, A. Rubio, *Phys. Rev. A* **2014**, *90*, 012508.
[26] J. Flick, P. Narang, *Phys. Rev. Lett.* **2018**, *121*, 113002.
[27] H. Nakamura, *Nonadiabatic transition: Concepts, basic theory and applications*, World Scientific, Singapore, **2012**.
[28] W. Domcke, D. Yarkony, H. Köppel Eds., *Conical intersections: Electronic structure, dynamics & spectroscopy, advanced series in physical chemistry*, World Scientific, Singapore, **2004**.
[29] M. Olivucci, *Computational photochemistry, vol. 16 of theoretical and computational chemistry*, Elsevier, Amsterdam, **2005**.
[30] G. Granucci, M. Persico, *Photochemistry: A modern theoretical perspective*, Springer, Switzerland, **2018**.
[31] M. Persico, G. Granucci, *Theor. Chem. Acc.* **2014**, *133*, 1526.
[32] K. Bennett, M. Kowalewski, S. Mukamel, *Faraday Discuss.* **2016**, *194*, 259.
[33] M. Kowalewski, K. Bennett, S. Mukamel, *J. Chem. Phys.* **2016**, *144*, 054309.
[34] J. Fregoni, G. Granucci, M. Persico, S. Corni, *Chem* **2020**, *6*, 250.
[35] H. L. Luk, J. Feist, J. J. Toppari, G. Groenhof, *J. Chem. Theory Comput.* **2017**, *13*, 4324.
[36] O. Vendrell, *Chem. Phys.* **2018**, *509*, 55.
[37] G. Groenhof, J. J. Toppari, *J. Phys. Chem. Lett.* **2018**, *9*, 4848.
[38] G. Groenhof, C. Climent, J. Feist, D. Morozov, J. J. Toppari, *J. Phys. Chem. Lett.* **2019**, *10*, 5476.
[39] I. S. Ulusoy, J. A. Gomez, O. Vendrell, *J. Phys. Chem. A* **2019**, *123*, 8832.
[40] Y. Zhang, T. Nelson, S. Tretiak, *J. Chem. Phys.* **2019**, *151*, 154109.
[41] T. Cusati, G. Granucci, E. Martínez-Núñez, F. Martini, M. Persico, S. Vázquez, *J. Phys. Chem. A* **2012**, *116*, 98.
[42] G. Granucci, M. Persico, A. Toniolo, *J. Chem. Phys.* **2001**, *114*, 10608.
[43] G. Granucci, A. Toniolo, *Chem. Phys. Lett.* **2000**, *325*, 79.
[44] G. Granucci, M. Persico, *J. Comput. Chem.* **2011**, *32*, 2690.
[45] S. Patchkovskii, W. Thiel, *Theor. Chim. Acta* **1996**, *93*, 87.
[46] S. Patchkovskii, W. Thiel, *Theor. Chem. Acc.* **1997**, *98*, 1.

[47] R. F. Ribeiro, L. A. Martínez-Martínez, M. Du, J. Campos-Gonzalez-Angulo, J. Yuen-Zhou, *Chem. Sci.* **2018**, *9*, 6325.
[48] G. Granucci, M. Persico, G. Spighi, *J. Chem. Phys.* **2012**, *137*, 22A501.
[49] E. T. Jaynes, F. W. Cummings, *Proc. IEEE* **1963**, *51*, 89.
[50] R. H. Dicke, *Phys. Rev.* **1954**, *93*, 99.
[51] B. Barnes, F. García Vidal, J. Aizpurua, *ACS Photon.* **2018**, *5*, 1.
[52] C. Gonzalez-Ballestero, J. Feist, E. Gonzalo Badía, E. Moreno, F. J. Garcia-Vidal, *Phys. Rev. Lett.* **2016**, *117*, 156402.
[53] O. Vendrell, *Phys. Rev. Lett.* **2018**, *121*, 253001.
[54] F. Benz, M. K. Schmidt, A. Dreismann, R. Chikkaraddy, Y. Zhang, A. Demetriadou, C. Carnegie, H. Ohadi, B. de Nijs, R. Esteban, J. Aizpurua, J. J. Baumberg, *Science* **2016**, *354*, 726.
[55] M. Urbieta, M. Barbry, Y. Zhang, P. Koval, D. Sánchez-Portal, N. Zabala, J. Aizpurua, *ACS Nano* **2018**, *12*, 585.
[56] T. Neuman, R. Esteban, D. Casanova, F. J. Garca-Vidal, J. Aizpurua, *Nano Lett.* **2018**, *18*, 2358.
[57] B. Doppagne, T. Neuman, R. Soria-Martinez, L. E. P. López, H. Bulou, M. Romeo, S. Berciaud, F. Scheurer, J. Aizpurua, G. Schull, *Nat. Nanotechnol.* **2020**, *15*, 207.
[58] C. Ciminelli, G. Granucci, M. Persico, *J. Chem. Phys.* **2005**, *123*, 174317.
[59] G. Granucci, M. Persico, A. Zoccante, *J. Chem. Phys.* **2010**, *133*, 134111.
[60] M. Persico, G. Granucci, S. Inglese, T. Laino, A. Toniolo, *J. Mol. Struct.: THEOCHEM* **2003**, *621*, 119.
[61] A. Toniolo, G. Granucci, T. J. Martínez, *J. Phys. Chem. A* **2003**, *107*, 3822.
[62] A. Toniolo, C. Ciminelli, G. Granucci, T. Laino, M. Persico, *Theor. Chem. Acc.* **2004**, *111*, 270.
[63] F. Plasser, G. Granucci, J. Pittner, M. Barbatti, M. Persico, H. Lischka, *J. Chem. Phys.* **2012**, *137*, 22A514.
[64] N. Aguilera-Porta, I. Corral, J. Munoz-Muriedas, G. Granucci, *Comput. Theor. Chem.* **2019**, *1152*, 20.
[65] G. Bussi, D. Donadio, M. Parrinello, *J. Chem. Phys* **2007**, *126*, 014101.
[66] Y. Zhang, Q.-S. Meng, L. Zhang, Y. Luo, Y.-J. Yu, B. Yang, Y. Zhang, R. Esteban, J. Aizpurua, Y. Luo, J. L. Yang, Z. C. Dong, J. G. Hou, *Nat. Comm.* **2017**, *8*, 15225.
[67] J. T. Hugall, A. Singh, N. F. van Hulst, *ACS Photon.* **2018**, *5*, 43.
[68] K. Mølmer, Y. Castin, J. Dalibard, *J. Opt. Soc. Am. B* **1993**, *10*, 524.
[69] J. Dalibard, Y. Castin, K. Mølmer, *Phys. Rev. Lett.* **1992**, *68*, 580.
[70] R. Dum, P. Zoller, H. Ritsch, *Phys. Rev. A* **1992**, *45*, 4879.
[71] M. B. Plenio, P. L. Knight, *Rev. Mod. Phys.* **1998**, *70*, 101.
[72] E. Coccia, F. Troiani, S. Corni, *J. Chem. Phys.* **2018**, *148*, 204112.
[73] H. Carmichael, *An open systems approach to quantum optics, vol. 16 of lecture notes in physics*, Springer, Berlin, **1993**.
[74] T. B. L. Kist, M. Orszag, T. A. Brun, L. Davidovich, *J. Opt. B: Quant. Semiclassical Opt.* **1999**, *1*, 251.
[75] R. Biele, R. D'Agosta, *J. Phys.: Condens. Matter* **2012**, *24*, 273201.
[76] J. Johansson, P. Nation, F. Nori, *Comput. Phys. Commun.* **2013**, *184*, 1234.
[77] A. White, V. Gorshkov, R. Wang, S. Tretiak, D. Mozyrsky, *J. Chem. Phys.* **2015**, *141*, 184101.

How to cite this article: Fregoni J, Corni S, Persico M, Granucci G. Photochemistry in the strong coupling regime: A trajectory surface hopping scheme. *J Comput Chem*. 2020; 1–12. https://doi.org/10.1002/jcc.26369

Chapter 2

The starting point of this chapter is the renown azobenzene photoisomerization. Grounded on such basis, I make extensive use of the features presented in the previous chapter, aiming at exploring how different light-molecule coupling conditions can impact both the photoisomerization mechanism and quantum yields. All the results are produced for both the weak coupling case and the strong coupling case in absence of environment. Through this means, all the modifications occurring in the mechanism are tied to the effect of the strong coupling regime between light and molecule. All the presented results have been originally produced by me during the PhD activity and are reported in the followings as published article and supporting information. The formalism adopted in the article partially differs from the one adopted in Chapter 1. However, it is thoroughly explained in the main text. With the aim of aiding the interpretation of the modified reaction mechanism, I have realized several visualization tools which have been exploited to realize the figures and the movies in the section: Supplementary Movies. Such movies are consultable as Supplementary Material of the online version of the article or by scanning the QR code in the dedicated section.

nature COMMUNICATIONS

ARTICLE

DOI: 10.1038/s41467-018-06971-y OPEN

Manipulating azobenzene photoisomerization through strong light–molecule coupling

J. Fregoni[1,2], G. Granucci[3], E. Coccia[4], M. Persico[3] & S. Corni[2,4]

The formation of hybrid light–molecule states (polaritons) offers a new strategy to manipulate the photochemistry of molecules. To fully exploit its potential, one needs to build a toolbox of polaritonic phenomenologies that supplement those of standard photochemistry. By means of a state-of-the-art computational photochemistry approach extended to the strong-coupling regime, here we disclose various mechanisms peculiar of polaritonic chemistry: coherent population oscillations between polaritons, quenching by trapping in dead-end polaritonic states and the alteration of the photochemical reaction pathway and quantum yields. We focus on azobenzene photoisomerization, that encompasses the essential features of complex photochemical reactions such as the presence of conical intersections and reaction coordinates involving multiple internal modes. In the strong coupling regime, a polaritonic conical intersection arises and we characterize its role in the photochemical process. Our chemically detailed simulations provide a framework to rationalize how the strong coupling impacts the photochemistry of realistic molecules.

[1] Dipartimento di Scienze Fisiche, Informatiche e Matematiche, University of Modena and Reggio Emilia, I-41125 Modena, Italy. [2] Istituto Nanoscienze, Consiglio Nazionale delle Ricerche CNR-NANO, I-41125 Modena, Italy. [3] Dipartimento di Chimica e Chimica Industriale, University of Pisa, I-56124 Pisa, Italy. [4] Dipartimento di Scienze Chimiche, University of Padova, I-35131 Padova, Italy. Correspondence and requests for materials should be addressed to G.G. (email: giovanni.granucci@unipi.it) or to S.C. (email: stefano.corni@unipd.it)

Control and manipulation of the photochemistry of molecules has traditionally relied on synthetic[1] chemical modifications or changes in the environment surrounding the photoactive molecule[2]. Precise control of the main products, the reaction yields and rates is achievable through addition or removal of functional groups that modify the properties of the ground and excited states. Together with the idea that light–matter interaction in both the weak-field and strong-field limits can be exploited to control molecular processes[3–7], it has been suggested recently that the light–molecule interaction itself can be used to modify the photochemistry of the molecules, with no other direct changes in the molecule or its environment[8–10]. We specifically refer to the regime where the coherent energy exchange rate g (also addressed as a coupling constant) between light and molecules becomes faster than any decay rate of the system itself (strong-coupling limit) (Fig. 1a). In this regime, the states of the system become hybrid between light and matter, the so-called polaritons[11–13].

Such states mix the photonic and the electronic degrees of freedom: when compared to the pure electronic states, the properties of the polaritons show a different dependence on the molecular geometry. This applies, in particular, to the polaritonic potential energy surfaces (PPESs) and any feature related to them, such as avoided crossings and conical intersections. As a consequence, the polaritons may impart a new photochemistry, laying the basis for polaritonic chemistry[8,9,13–16].

To achieve the strong coupling required to exploit such hybrid states, resonant or nanoplasmonic cavities have been devised only in the last years[17,18] and recently the single-molecule level has been reached[11,19] at room temperature. Coherent coupling between a single organic molecule and a microcavity has also been recently achieved[20], opening a way to the investigation of coherence effects in the light–matter interactions on a longer timescale than in the nanocavity case. Such groundbreaking experimental findings have spurred an intense and pioneering theoretical activity[12,14,21–23]. Various interesting phenomena were predicted in prototypical systems (model potential energy surfaces—PESs—along one or two coordinates, representing specific internal coordinates in more complex systems), such as the modification of quantum yields and the creation of polaritonic conical intersections by light–molecule coupling[13,15,21,24,25].

The computational investigation of weak-field photochemistry[5,6,26–29] has undoubtedly shown that even for the simplest and best characterized systems, such as azobenzene, the chemical complexity of the molecule cannot be disregarded. To tackle such complexity, the inclusion of all the molecular degrees of freedom is necessary to describe the main features of photochemical processes: the occurring events where the Born–Oppenheimer approximation breaks down and the correct account of the quantum nature of the nuclear motion. In the past few decades, many efforts in this field resulted in detailed and realistic models[30,31] of photoactive systems.

An equivalent investigation of the photochemical properties and peculiar features of realistic molecules in the strong-coupling regime is still an open challenge[14]. Recently, methodologically remarkable advancements have been made along such direction: Luk et al. investigated the formation of collective polaritonic states for systems of hundreds of realistic dye molecules[22], and Vendrell focused on collective quantum effects for up to five diatomic molecules strongly coupled to a cavity mode[23]. Yet, the characterization of a photochemical reaction in the strong-coupling regime for a molecule of realistic complexity is still lacking. To move further in the characterization of photochemical processes, we focus on azobenzene. Azobenzene and its derivatives are a prototypical benchmark for studying photochemical processes[32,33]. The photo-reversible switch of configuration between *trans* and *cis* (Fig. 1b) in this class of molecules has been studied extensively, due to the wide applicability in the field of photocontrol of biomolecular structures[34], of sensing[35], and photoresponsive materials[36].

To investigate such system, we rely on an on-the-fly surface hopping technique[37] already validated for several applications[31,38,39]. Here we characterize the PPESs by relying on the detailed description of the molecule taking into account the full space of the internal degrees of freedom of azobenzene. We make use of such characterization to discuss the effects of strong coupling on photochemistry, as the birth of coherent oscillations of the populations between the polaritonic states. For coupling strengths comparable to what was already achieved in experiments[11], we show how the mechanism of the *trans–cis* photoisomerization is modified, leading to a decrease in the quantum yield[24,25]. Finally, we investigate the oscillations referred above by including the effect of cavity losses to mimic realistic plasmonic nanocavities. Through our results, we emphasize the significant role of quantum coherence in controlling the molecular processes, including in the picture also the polaritonic coherences beside electronic and vibrational ones[29,40,41].

Results

Azobenzene polaritonic PESs. The azobenzene electronic PESs are represented with respect to the *CNNC* and one of the *NNC*

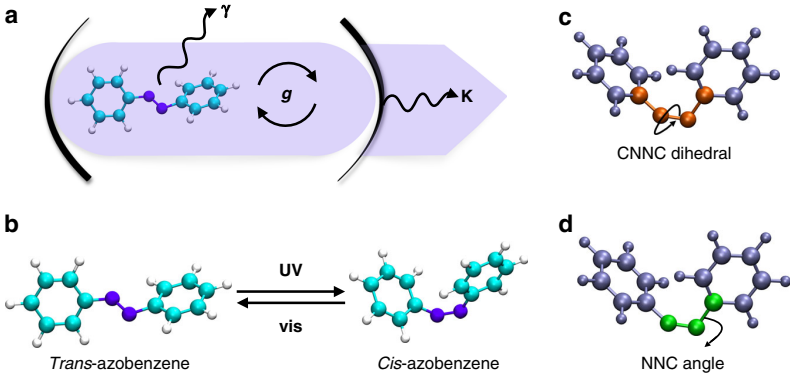

Fig. 1 Scheme of the modeled system. **a** *Trans* azobenzene molecule inside a resonant cavity. The decay rate of the system is γ for the molecule and κ for the cavity. **b** Isomerization of the azobenzene molecule: the switch of configuration can be achieved by irradiation with UV–Vis light. **c**, **d** Photoisomerization coordinates of azobenzene: the reaction occurs through the torsion of the *CNNC* dihedral angle, with a simultaneous relaxation of the *NNC* angle

angular coordinates (Fig. 1c, d) with all the other nuclear degrees of freedom optimized with respect to the first excited state and for each choice of such coordinates. These two angles are directly involved in the photoisomerization mechanism[42]. The *CNNC* dihedral angle (Fig. 1c) represents the torsion around the N=N double bond and it is the main reaction coordinate for the photoisomerization. Together with the torsion, the *NNC* angles are necessary to successfully describe the photoisomerization mechanism[38,42,43]. Electronic wavefunctions and PESs (Fig. 2a) were computed exploiting a semiempirical quantum chemistry approach, developed by Persico and collaborators[38,43]. Such approach has been extensively validated in the past for azobenzene and its derivatives[38,43,44]. Accuracy and low computational cost make this method extremely suitable to simulate the photochemistry of realistic molecules, as it allows the inclusion of all the internal degrees of freedom.

We build (see Methods) the polaritonic states as eigenstates of the total (molecule + light) Hamiltonian on the basis of product states between the electronic eigenstates S_0, S_1, and a photon occupation state number $|0\rangle$, $|1\rangle$, that is $|S_0, 0\rangle$, $|S_1, 0\rangle$, $|S_0, 1\rangle$, and $|S_1, 1\rangle$. The strong-coupling interaction only mixes states differing by one in the photon occupation state number. The mixing between $|S_0, 1\rangle$ and $|S_1, 0\rangle$ is by far the most relevant, as these two states are close in energy. In particular, such mixing gives rise to the lower and upper polaritons ($|-\rangle$ and $|+\rangle$, respectively, see Fig. 2b)[12,21,24,45].

In Fig. 2b, they have been obtained with a coupling constant (see Methods) g of 0.010 au and a photon energy E_{ph} of 1.3 eV. As shown there, a new avoided crossing arises for the polaritonic states as a signature of the coupling. Such avoided crossing is found in the coordinate range where the $|S_1, 0\rangle$ and $|S_0, 1\rangle$ states would cross. The energy splitting contribution along the avoided crossing line between the $|-\rangle$ and $|+\rangle$ states is proportional to the coupling between $|S_0, 1\rangle$ and $|S_1, 0\rangle$ before the diagonalization. Such coupling depends on the expectation value of the component of the transition dipole moment between the pure electronic states, $\boldsymbol{\mu}_{S_0,S_1}(Q)$, taken along the polarization direction of the electric field (see Methods). Therefore, the splitting magnitude depends indirectly on the nuclear coordinates through the transition dipole moment. In turn, since the geometry where the strong-coupling avoided crossing occurs is tuned by E_{ph}, different splitting energies are obtained as a function of E_{ph}. Such dependence has been noted in previous works and included in the models[21,22,24,25], though its role for the photochemistry of realistic molecules has not been explored yet. By showing in Supplementary Figs. 1 and 2 that the effect of such dependence is

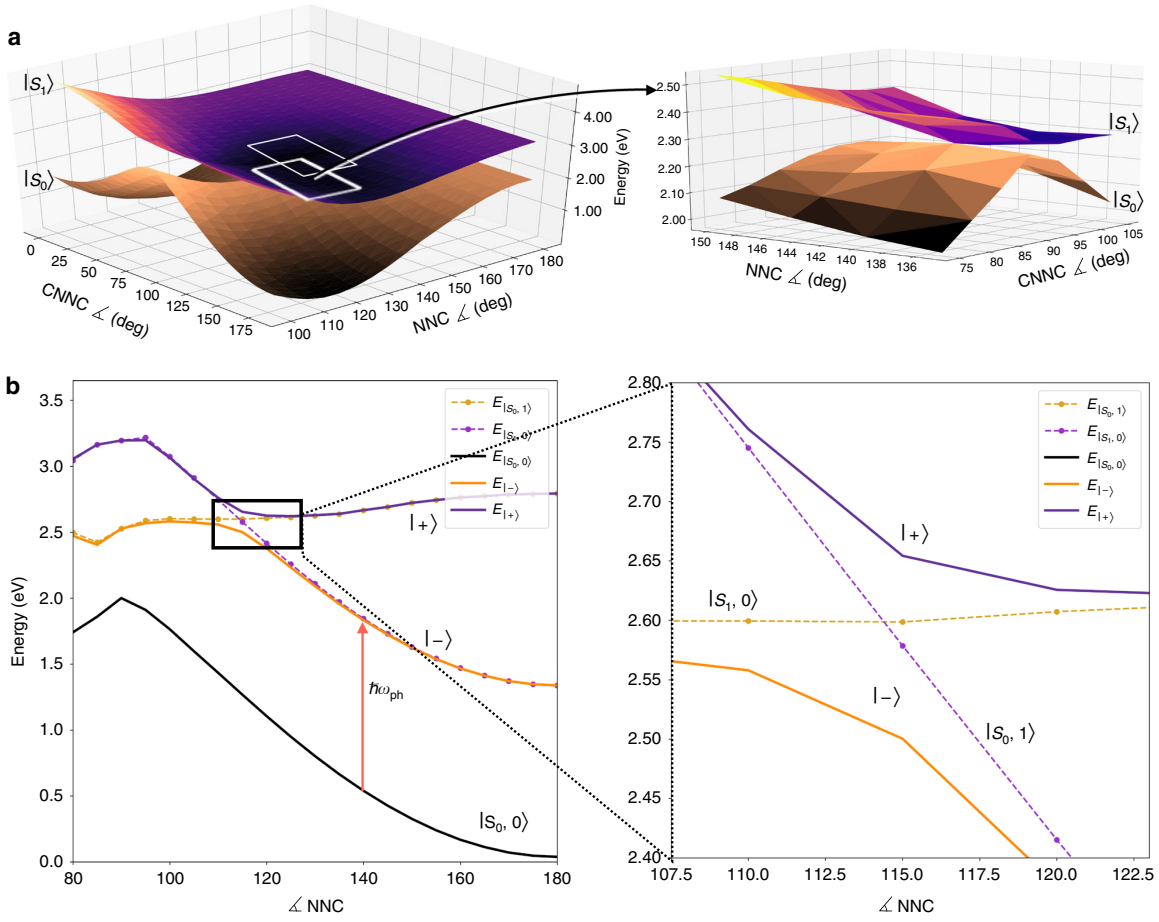

Fig. 2 Electronic and polaritonic states of azobenzene. **a** Pure electronic ground (brown surface) and first excited (purple surface) PESs of azobenzene, plotted with respect to the torsion and inversion coordinates. The S_0 and S_1 PESs are characterized by the presence of a conical intersection. **b** Polaritonic potential energy curves (black, dark orange, and purple full lines) of azobenzene with respect to the *CNNC* coordinate with *NNC* 115°, obtained as linear combinations of uncoupled states (dotted lines, orange and violet) for a photon energy E_{ph} of 1.3 eV and a coupling constant g of 0.010 au. The splitting between the polaritonic states ($|-\rangle$, $|+\rangle$) depends on the transition dipole moment between the electronic states, evaluated at the crossing geometry (*CNNC* 130° and *NNC* 115°)

remarkable, we anticipate that the transition dipole moment at a given crossing geometry (governed by E_{ph}) is a further parameter to take into account to manipulate the PPESs features and, as a consequence, the photochemical reaction. The splitting can range from zero (for dipole forbidden transitions) to very large, depending on the transition dipole magnitude and orientation.

The out-of-plane component of the transition dipole moment between S_0, and S_1 vanishes at planar geometries. Therefore, for a field polarization perpendicular to the plane of the molecule as in the present case, the $|-\rangle$ and $|+\rangle$ states become exactly degenerate at crossing points between $|S_1, 0\rangle$ and $|S_0, 1\rangle$ at planar geometries. In other words, a polaritonic conical intersection (indicated with a red arrow in Figs. 3, 4a and 4d) is originated (see Supplementary Note 1 for more details).

Aiming to highlight how deeply the conical intersection features can influence the photoisomerization yields and mechanism, we chose two limiting cases which shape very differently the PPESs. Within such two cases, the photon energy E_{ph} is set to 1.3 and 2.2 eV, while g is equal to 0.010 au and the field is polarized perpendicularly to the plane of the molecule for both. By doing so, we obtain coupling magnitudes which are comparable to what has recently been observed experimentally for single molecules in the strong-coupling regime[11,19]. In the next section, we analyze the differences between strong coupling-induced avoided crossings under different conditions and discuss the consequences of the photoisomerization process of azobenzene.

Photochemistry in the strong-coupling regime. The simulation of a photochemical process is carried out by non-adiabatic molecular dynamics methods: this manifold of techniques[37,46–48] consists in mimicking the nuclear wavepacket motion on the excited electronic PESs and aims to correctly retrieve the quantum yields of a reaction when the Born–Oppenheimer approximation breaks down. Such breaking can occur either for electronic states degeneracy, quasi degeneracy[49,50] or, in the strong-coupling regime we are considering, for polaritonic state avoided crossings[12,25,51]. In these critical regions, reproducing the correct splitting of the wavepacket through crossing seams is the key to correctly retrieve the molecular mechanism[30,44,49,50,52].

To this purpose, an effective[46,47] strategy is to rely on the semiclassical surface hopping method pioneered by Tully[53]. Such framework provides an accurate description of de-excitation mechanisms in molecules. A recent improvement to such an approach includes decoherence effects[54], which have been proven successful to describe multiple passages of the wavepacket through the crossing seams. The accurate description of multiple passages is essential to our system: the presence of the conical intersection and the strong-coupling avoided crossing entails multiple wavepacket branchings in rapid succession. Therefore, we have devised a propagation scheme for the nuclear trajectories on the PPESs, in the framework of an on-the-fly trajectory surface hopping technique[37] (see Methods for more details).

As mentioned above, we compare two cases with different photon energies ($E_{ph} = 1.3$ eV and 2.2 eV), g equal to 0.010 au and the field polarized along the z-axis perpendicular to the plane of the molecule for both. The initial conditions (nuclear coordinates and momenta) for the swarm of trajectories mimicking the nuclear wavepacket are sampled from a room-temperature Boltzmann distribution, obtained from a single trajectory propagated for 10 ps on the ground state with a Bussi–Parrinello thermostat[55]. A vertical excitation is performed to the upper polariton for each trajectory (Fig. 3a). The PPESs and some snapshots of the 1.3 eV dynamics are shown in Fig. 3 (for the 2.2 eV case and the movies of the whole dynamics, see Supplementary Movies 1 and 2). In order to compare the effect of different coupling conditions on the photochemical process, the population evolution and the characterization of the polaritons are shown for the two cases in Fig. 4.

In both cases, the vertical excitation brings the sampled trajectories on a slope of the upper PPES. As shown for the 1.3 eV case at 10 fs, the trajectories start propagating, accumulating kinetic energy toward the minimum of the upper polariton (Fig. 3a). At 20 fs, as the ensemble approaches the strong-coupling avoided crossing as well as the related polaritonic conical intersection, the trajectories split and start oscillating between the $|-\rangle$ and $|+\rangle$ polaritonic states (Fig. 3b, c). At 30 fs,

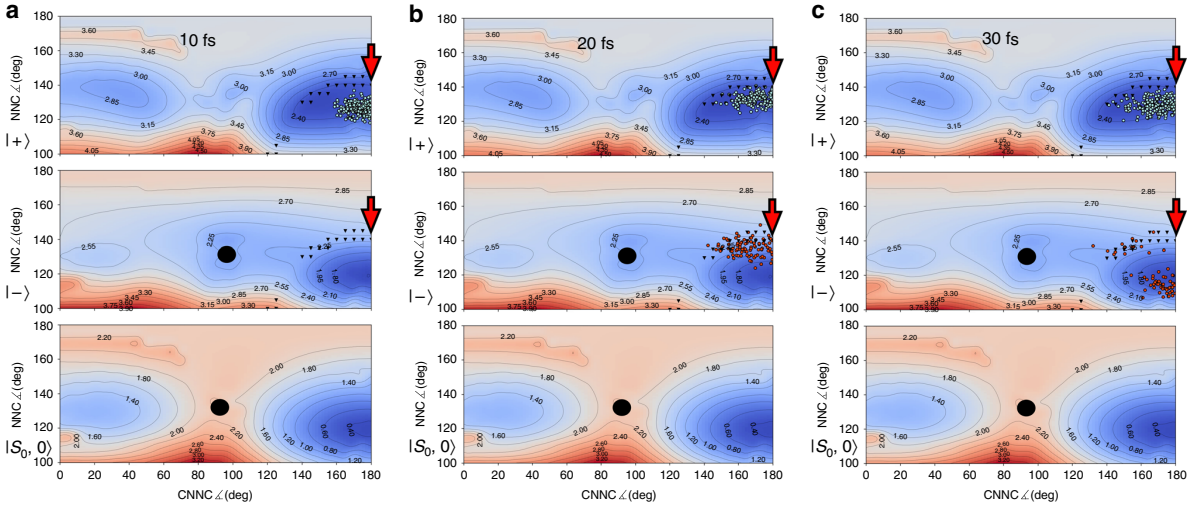

Fig. 3 Snapshots of the photoisomerization on PPESs for E_{ph} 1.3 eV and g 0.010 au. The black triangles identify the strong-coupling avoided crossing line, the red arrow identifies the polaritonic conical intersection while the black circle is the conical intersection between the pure electronic states. Light blue trajectories are referred to the upper polaritons and orange trajectories are referred to the lower polariton. **a** Upon the vertical excitation, the ensemble of trajectories is found in a high slope region of the upper PPES. **b** The trajectories move toward the upper polariton minimum and **c** start oscillating between the upper and lower polaritons, with several trajectories trapped in the lower polariton minimum after the splitting (see Supplementary Movie 1)

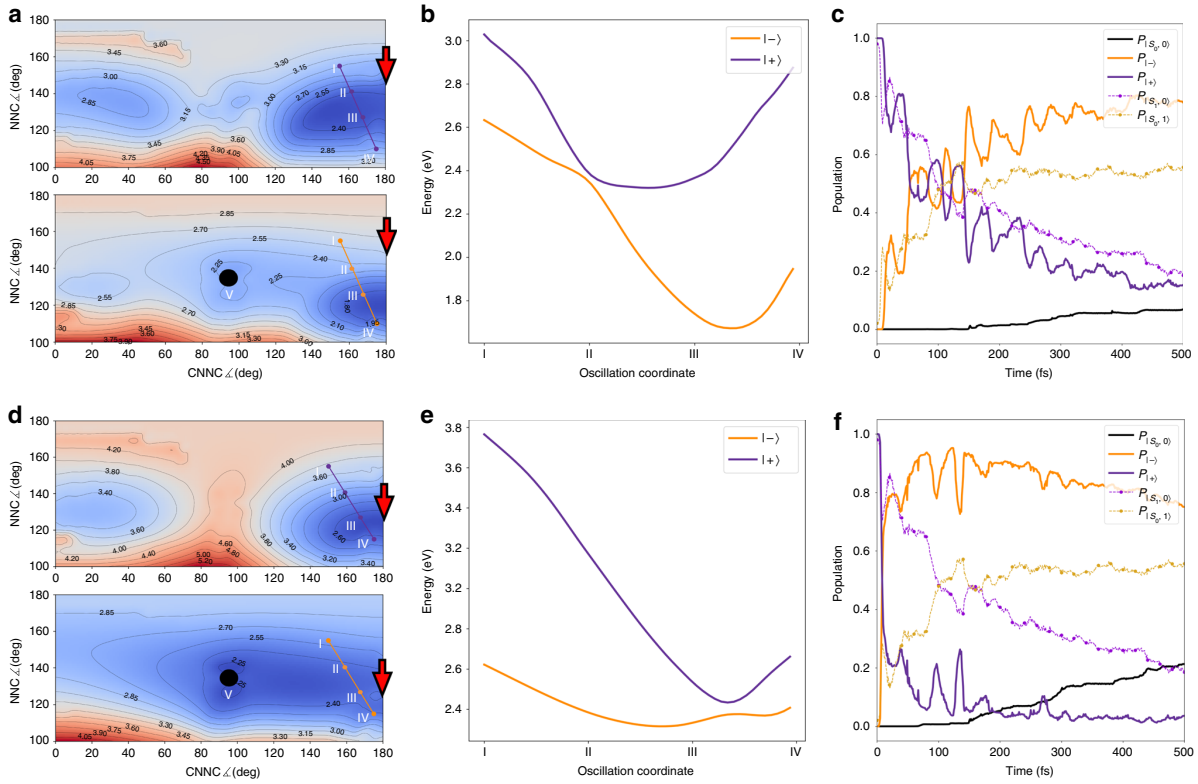

Fig. 4 Non-adiabatic dynamics in the strong coupling regime. **a**, **b**, **d**, **e** Potential energy surfaces and state populations. The upper (respectively, lower) panels refer to photon energy E_{ph} 1.3 eV (respectively, 2.2 eV). In both cases, we set the coupling constant g to 0.010 au and field polarized along z. Contour maps of the $|-\rangle$ and $|+\rangle$ PPESs are shown in **a** and **d**, while the section along the oscillation coordinate (see text) is shown in **b** and **e**. The red arrow identifies the polaritonic conical intersection, points I and IV identify the extrema of oscillations (see text), and point V indicates the electronic conical intersection. **c**, **f** Time evolution of the state populations. Full lines are referred to polaritonic states and dashed lines to the uncoupled states, according to the color scheme defined in Fig. 2

we observe a branching of the trajectories on the lower PPES, with a cluster of trajectories moving toward the lower PPES minimum (Fig. 3c).

Such oscillations were characterized for both the 1.3 and 2.2 eV cases, as shown in the population plot reported in Fig. 4. To this aim, we extracted the oscillation coordinate by averaging the *NNC* and *CNNC* angles for the oscillating trajectories, and we plotted the avoided crossing profiles for both the dynamics (Fig. 4a, b, d, e) along such a coordinate. The extrema of the (*CNNC, NNC*) couple of angles during the oscillations are indicated as I and IV in the figure. In both cases, we observe that the oscillation coordinate is hybrid between *CNNC* and *NNC*, though with a different mixing of the two. We also stress the different shape of the surfaces and of the crossing profiles between the polaritonic states in the two cases, despite the same coupling constant. The splitting extent at the avoided crossing (hence, proportional to the coupling) is a signature of the geometric dependence of the coupling through the transition dipole moment. This dependence carries non-trivial effects on the dynamics and the oscillation feature, as it becomes clear by analyzing the populations of the two cases reported in Fig. 4c, f. The different decay rates of the upper polaritonic state and the oscillation peaks strengths and occurrences in time can be rationalized by exploring further the potential energy curves along the oscillation coordinate.

In the 1.3 eV case (Fig. 4c), the excited trajectories starting in the Franck–Condon region on the upper PPES (close to point IV in Fig. 4a) are dragged toward a strong-interaction region between the two polaritonic states. As a consequence, a diabatic behavior is obtained, with the trajectories oscillating on the $|S_1, 0\rangle$ PES between the points I and IV (Fig. 4b). However, during the oscillations, some trajectories get trapped in the minimum region of the lower polariton, which becomes therefore more and more populated (see Supplementary Fig. 3 for a sketch representation). In this specific case, a motion toward the conical intersection (point V, Fig. 4a) becomes unfavorable due to the oscillation trap triggered by the peculiar shaping of the PESs. This process occurs completely in the *trans* region of the conformational space: as a consequence, an almost complete quenching of the reaction is observed (the quantum yield is reduced to 3.1%). The 2.2 eV case is substantially different: the wavepacket starts its propagation close to the avoided crossing located at the point II of Fig. 4e, and 4f, entailing the quick upper polariton population drop reported in Fig. 4f.

In this case, the upper PES has a minimum coincident with the strong-coupling avoided crossing: while few trajectories oscillate due to the coupling effects, the wavepacket can evolve toward the conical intersection on the lower polariton (point V, Fig. 4d), damping the oscillation trap effect and resulting in a quantum yield of 16.1% (going toward the 33.1% for the isolated molecule). We also observe an effect on the populations driven by the different PPESs shapes in the two cases. For E_{ph} 1.3 eV, the $|-\rangle$ state has a deeper minimum, which is located far from the avoided crossing. As a consequence, the polaritonic and

uncoupled populations tend to coincide quicker than in the 2.2 eV case. Due to the trajectories falling in the $|-\rangle$ PPES minimum (coincident with the $|S_0, 1\rangle$ state in that region), the $|S_0, 1\rangle$ state population grows significantly higher than the $|S_1, 0\rangle$ population. In the 2.2 eV case, the presence of a shallow minimum close to the avoided crossing entails that the trajectories are located in a region where the $|S_0, 1\rangle$ and $|S_1, 0\rangle$ states are very mixed. This behavior is well shown in Fig. 4f by the remarkable difference between the polaritonic and uncoupled states populations. It is clear from Fig.4a, d that the oscillation coordinate involves the polaritonic conical intersection neither for the 1.3 eV nor for the 2.2 eV case. Yet, inspection of the trajectory swarm shows that in both cases, some trajectories do approach the polaritonic conical intersection (and turn to the lower PPES there), with a higher probability for the 2.2 eV case due to the local shape of the PPES.

Comparing the presented results with the weak-coupling case (see Supplementary Movie 3), the pathway followed by the swarm of trajectories is substantially different. The presence of the trapping minimum in the polaritonic case (absent in the isolated molecule) limits the motion along the *CNNC* coordinate. As a consequence, the torsional photoisomerization mechanism turns out to be quenched. In addition, the oscillations along the *NNC* coordinate, inducing the periodic crossing of the polaritonic conical intersection region, not only elicit the oscillations of the polaritonic populations discussed so far: indeed, they provide a channel to intermittently fall in the electronic ground state (actually $|S_1, 0\rangle$), which is fully missing in the weak-coupling regime. The effect of such process on the ground-state population retrieval is discussed in the next section.

Finally, we evaluated the quantum yield as a function of the photon frequency in the strong-coupling regime. The trend, that is presented and discussed in the Supplementary Note 2, is non-trivial. In particular, it encompasses three different regions (a decrease, a plateau, and a recovery, reaching even a modest improvement of the yield with respect to the weak-coupling result), that testify the complexity of the strong-coupling effects on photochemistry.

Effect of cavity losses on the photochemistry. So far, we have presented results that explicitly account for the decay of excited electronic states. Nevertheless, they did not take into account the finite lifetime of the photon in the resonant cavity driven by the unavoidable cavity losses. While a promising coherent energy exchange has been recently shown for a single molecule within a high-quality factor (i.e., low losses) microcavity[20], so far lossy plasmonic nanocavities have been used to achieve strong coupling at the single-molecule level[11,17–19]. The electromagnetic excitation of such systems is typically characterized by a lifetime of few tens of femtoseconds, i.e., on the same timescale of the coherent oscillations described in previous sections (Fig. 4c, f). As a consequence, the lifetime of the electromagnetic excitation cannot be neglected.

In this section, we investigate the consequences of the cavity losses by means of a Monte Carlo approach (see Methods). In particular, we check whether the observed coherent oscillations persist or are dismantled by the loss of photon. We hereby consider photon lifetimes $\tau_c = 1/\kappa$ of 10 fs, 50 fs, 100 fs (Fig. 5a–c, respectively), and 150 fs to investigate their impact on the 1.3 eV dynamics (see Supplementary Note 3 for the 2.2 eV case). The main finding here is that, regardless of the specific value of the cavity lifetime used in our analysis, oscillations of the polaritonic states are retained.

To explain the persistence of such oscillations between polaritons for each investigated lifetime, it is useful to consider how the photon loss probability is determined. Akin to ref. [22], the probability of disappearance of the photon at a given time is proportional to the probability of the system to be in the state $|S_0, 1\rangle$ (the photon loss collapses the state on $|S_0, 0\rangle$). Therefore, during the time intervals in which such a probability is low, the system is protected against photon loss (i.e., the effective decay rate is much slower than τ_c). On the contrary, when the state is predominantly $|S_0, 1\rangle$, such state will decay exponentially with a rate close to κ. This is evident for τ_c 10 fs (Fig. 5): every time the mimicked nuclear wavepacket passes through the polaritonic avoided crossing and $|S_1, 0\rangle$ converts to $|S_0, 1\rangle$, a clear decay with a time constant in the tens of femtoseconds range is visible. The protection against losses offered by disguising the photon in the $|S_1, 0\rangle$ state makes the dynamical features, observed above, robust in the range of hundreds of femtoseconds, despite a photon lifetime of 10 fs only.

Remarkably, the excited states oscillatory behavior translates into an oscillating probability of the molecule of being in the electronic ground state, as shown in Fig. 5d. Oscillations are clearly visible for τ_c 50 fs, and even for a limit value of τ_c 10 fs (rather short even for plasmonic nanocavities) clear periodic plateaus are visible. Current ultrafast optical experiments provide viable time resolution to observe such features, found missing in the weak-coupling regime (No SC) in Fig. 5d. Incidentally, such a panel also illustrates well the different mechanism of the reaction in the strong-coupling regime vs. weak coupling: in the former case, the ground state starts to be populated at the very beginning of the simulation due to the change in polaritonic nature upon traversing the polaritonic avoided crossing (one can interpret this as an enhanced radiative decay); in the latter, no decay takes place until the molecule reaches the electronic conical intersection (that requires around 150 fs).

Although the qualitative features are conserved, the introduction of the cavity losses does affect the results: the trapping into the lowest polaritonic state is now only transient, as it evolves toward the $|S_0, 0\rangle$ state. Moreover, the decay rate to the ground state is overall (moderately) increasing by decreasing τ_c: this behavior is expected as, once $|S_0, 0\rangle$ is reached, going back to $|S_1, 0\rangle$ would require a thermal activated event. Yet, the features of the strong-coupling regime are clearly visible for all the τ_c. The case of E_{ph} 2.2 eV is discussed in the Supplementary Note 3; the notable point there is that for the lowest τ_c, only the polaritonic state that coincides with $|S_1, 0\rangle$ survives. As a consequence, the difference between the population of polaritons and the population of the uncoupled states, shown in Fig. 4f, is also suppressed, indicating the loss of coherence between the electronic and photonic states in this very lossy cavity regime.

Discussion

Building upon well-established methods to simulate photochemistry, we have characterized the PPESs for a realistic molecule. The simulation of the photoisomerization has shown how the reaction pathway and quantum yields can be modified in the strong-coupling regime (see Supplementary Movies 1 and 2). Tunable parameters are the coupling constant, the field mode polarization, and the resonant photon frequency, carrying strong consequences on the polaritonic splitting. In particular, the resonant frequency affects the photochemistry both by the positioning of the polaritonic avoided crossing and via the dependence of the local transition dipole moment on the avoided crossing geometry, offering a powerful (but difficult to set) handle to affect photochemistry. We have highlighted and characterized the peculiar population oscillations arising in strongly coupled azobenzene photoisomerization, promising to be probed by experimental ultrafast spectroscopy (whose role in probing polaritonic photochemistry has been already underlined)[21]. We

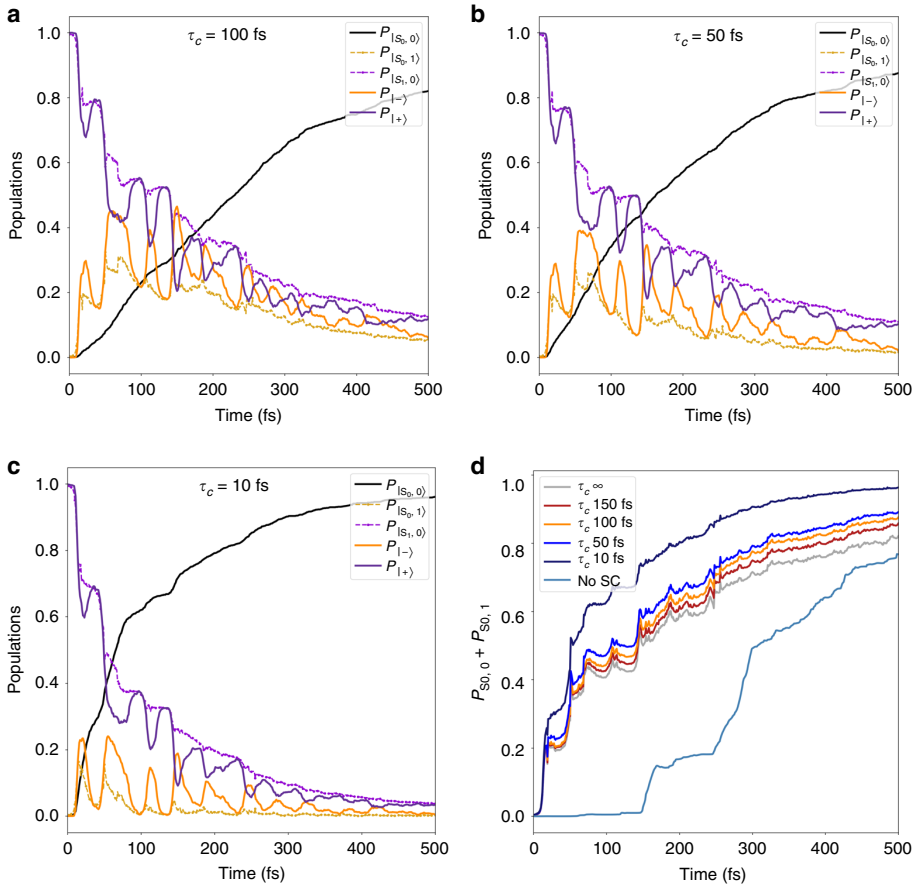

Fig. 5 Effect of the cavity losses on the dynamics. **a**–**c** Full lines are referred to polaritonic states and dashed lines to the uncoupled states, according to the color scheme defined for Fig. 2. Evolution of polaritonic populations for the 1.3 eV dynamics (see Fig. 4a–c) including cavity lifetimes of 100, 50, and 10 fs, respectively. **d** Retrieval of ground-state population for different cavity lifetimes compared to the purely electronic (No SC, light blue) and the cavity lossless cases (gray)

have shown that such features are qualitatively conserved even when fast photon losses in the cavity are accounted for (much faster than the time span of the dynamics), and explained why this is the case. In addition, we have calculated and commented the non-trivial dependence of the quantum yields on different photon energies and coupling constants.

Our results open the way to the rational design of polariton-induced control of the molecular photochemistry as, for instance, high-throughput computational investigations of the optical parameter space (photon energy, coupling strength, and electric field polarization) can be performed to find out how to control photochemistry. Among the unexplored photochemical features, the strong-coupling conditions can potentially be tuned to retrieve quantum yield enhancements instead of quenching, to maximize the photostationary state concentrations of reactant and product, to maximize the coherent oscillation aspects of the reaction mechanisms, and to tune PESs features such as the position of the electron and polaritonic conical intersections, possibly to engineer new photochemical reaction pathways.

Methods

Electronic states . The electronic calculations are performed in a semiempirical framework, with an AM1 Hamiltonian, which was carefully reparameterized for azobenzene in a previous work[43]. In particular, the FOMO-CI[37,43] method has been used for the evaluation of electronic energies, wavefunctions, and couplings.

Polaritonic states. We rely on recent theoretical developments for strongly coupled systems[24,25,51] to build the polaritonic states. The total Hamiltonian for the system is composed by three different contributions[12,21,24]: molecule, electromagnetic field, and coupling,

$$\hat{H}_{\mathrm{sc}} = \hat{H}_{\mathrm{mol}} + \hat{H}_{\mathrm{ph}} + \hat{H}_{\mathrm{int}}. \quad (1)$$

A single quantized mode for the electromagnetic field is considered[56]:

$$\hat{H}_{\mathrm{ph}} = \omega_{\mathrm{ph}}\left(\hat{b}^{\dagger}\hat{b} + \frac{1}{2}\right), \quad (2)$$

where ω_{ph} is the resonant photon frequency and $\hat{b}^{\dagger}$, $\hat{b}$ are the creation and annihilation operators for the bosonic mode, respectively. This term represents the light mode confined in resonant cavities or nanocavities. The uncoupled system, whose Hamiltonian reads $\hat{H}_{\mathrm{mol}} + \hat{H}_{\mathrm{ph}}$, is described by the product states $|S_0, 0\rangle$, $|S_1, 0\rangle$ (molecular electronic states with no photon) and the same electronic states with a photon present, $|S_0, 1\rangle$, $|S_1, 1\rangle$. The positioning of the crossing between the uncoupled states $|S_0, 1\rangle$, $|S_1, 0\rangle$ is governed by the confined mode frequency only. The PPESs are obtained by including light–matter interaction in the Coulomb gauge with a dipolar light–matter Hamiltonian (the dipolar formulation allows to exploit the molecular quantities as computed by quantum chemistry calculations):

$$\hat{H}_{\mathrm{int}}(Q) = g\hat{\mu}_{S_0,S_1}(Q) \cdot \boldsymbol{\lambda}\left(\hat{\boldsymbol{b}}^{\dagger} + \hat{\boldsymbol{b}}\right), \quad (3)$$

where $\hat{\mu}_{S_0,S_1}(Q)$ is the transition dipole moment between the electronic states at

given nuclear coordinates Q, while λ is the field polarization vector. Within our treatment, we include the counter rotating terms usually disregarded in the Jaynes–Cummings model, which account for the Lamb shift of the $|S_0, 0\rangle$, $|S_1, 1\rangle$ states. As the total Hamiltonian is diagonalized, the polaritonic states ($|S_0, 0\rangle$, $|-\rangle$, $|+\rangle$, $|S_1, 1\rangle$ for the present case) are obtained as linear combinations of the uncoupled states. The $|-\rangle$ and $|+\rangle$ states are the minus and plus combination between the $|S_0, 1\rangle$ and $|S_1, 0\rangle$ states, respectively. It is worth noticing that the $|S_0, 0\rangle$ and $|S_1, 1\rangle$ states are coupled as well with the other states, as a result of the diagonalization. In the present case, they are labeled as the uncoupled states since their mixing with other states is negligible for each geometry.

About dipolar formulation. To compute the polaritonic states, we work in the Coulomb gauge with an extended Jaynes–Cummings Hamiltonian (see Supplementary Note 4). A recent discussion about the gauge choice to treat strong-coupled systems has been proposed by Flick et al.[12], where they show that for low photon frequencies and high field intensities, a complete dipolar formulation (or minimal coupling as well) is needed[45]. To this aim, we numerically tested the complete dipolar, minimal coupling and extended Jaynes–Cummings formulations for the computation of polaritonic states. Within the resonant frequencies and field strength investigated in this work, we proved numerically that the additional terms of a complete dipolar formulation can be disregarded (Supplementary Fig. 6). Therefore, we restrain the treatment to an extended Jaynes–Cummings formulation.

Strong-coupling non-adiabatic dynamics. In the trajectory surface hopping framework, the nuclear wavepacket motion on the electronic PESs is mimicked by a swarm of independent classical nuclear trajectories. The electronic wavefunction is propagated on-the-fly, according to the time-dependent Schrodinger equation. The propagation of the wavefunction is carried on the adiabatic basis of the polaritonic states. As a consequence, the non-adiabatic couplings between polaritonic states take into account both the couplings between electrons and nuclei and between photon and electrons. The integration of the TDSE is performed using the local diabatization (LD) scheme[37], and the transition probabilities between polaritonic states are computed according to Tully's fewest switches algorithm[53], as adapted to local diabatization. In this version, the decoherence corrections are included as presented in ref. [54].

The classical nuclear trajectories are evolved according to Newton's equation of motion. The force acting on each atom is given by the gradient of the adiabatic polaritonic state energy. The gradients for the pure electronic states are evaluated as reported in ref. [57]. In order to evaluate the gradients arising from the light–molecule interaction contribution to the energy, we rely on the scheme proposed for spin orbit coupled systems, presented in ref. [58] (see Supplementary Methods for the flowchart).

Cavity losses. The cavity losses are included through a Monte Carlo scheme applied, a posteriori, on the swarm of trajectories evaluated without losses. The disappearance of the photon from the cavity is included as a stochastic event whose realization is evaluated at each time step. Each of the 300 original trajectories are replicated five times, and the resulting set of 1500 trajectories is rerun. The probability of photon loss $p_{cav}(t)$ at a given time (t) is evaluated as:

$$p_{cav} = \frac{1}{\tau_c}\Delta t\left|C^{\Gamma}_{S_0,1}(t)\right|^2 = \frac{1}{\tau_c}\Delta t P^{\Gamma}_{S_0,1}, \quad (4)$$

where Γ is the current polaritonic state for the current trajectory, τ_c is the photon lifetime in the cavity, and Δt is the timestep of the dynamics. The population $P^{\Gamma}_{S_0,1}$ of the $|S_0, 1\rangle$ uncoupled state in the current polaritonic state Γ is defined as the square modulus of $C^{\Gamma}_{S_0,1}$, which is one of the expansion coefficients of the current state Γ on the uncoupled basis. In each step, this probability is evaluated and a uniform random number in the interval [0, 1] is generated. If such a number is lower than the decay probability, the total wavefunction for the trajectory is collapsed on the $|S_0, 0\rangle$ state, and the trajectory is stopped. Compared to the direct inclusion of the photon decay in the dynamics, this procedure is neglecting the (very unlikely) event that once in the $|S_0, 1\rangle$ state, the system fluctuates back into the higher energy $|S_1, 0\rangle$ state (or rather the corresponding polaritonic state).

Code availability. The calculations were based on a locally modified version of MOPAC2002, which is available from G.G. and M.P. upon reasonable request.

Data availability

The data that support the findings of this study are available from the open Zenodo repository https://doi.org/10.5281/zenodo.1423796. Additional data are available from the corresponding authors upon reasonable request.

Received: 22 April 2018 Accepted: 4 October 2018
Published online: 08 November 2018

References

1. Allen, G. H., White, R. P., Rillema, D. P. & Meyer, T. J. Synthetic control of excited-state properties. Tris-chelate complexes containing the ligands 2,2′-bipyrazine, 2,2′-bipyridine, and 2,2′- bipyrimidine. *J. Am. Chem. Soc.* **106**, 2613–2620 (1984).
2. Ogunsipe, A., Chen, J.-Y. & Nyokong, T. Highly efficient co-sensitization of nanocrystalline TiO2 electrodes with plural organic dyes. *New J. Chem.* **28**, 822–827 (2014).
3. Pepino, A. J., Segarra-Mart, J., Nenov, A., Improta, R. & Garavelli, M. Resolving ultrafast photoinduced deactivations in water-solvated pyrimidine nucleosides. *J. Phys. Chem. Lett.* **8**, 1777–1783 (2017).
4. Demoulin, B., Altavilla, S. F., Rivalta, I. & Garavelli, M. Fine tuning of retinal photoinduced decay in solution. *J. Phys. Chem. Lett.* **8**, 4407–4412 (2017).
5. Garavelli, M. Computational organic photochemistry: strategy, achievements and perspectives. *Theor. Chem. Acc.* **116**, 87–105 (2006).
6. Olivucci, M. *Computational Photochemistry* Vol. **16**, 191 (Elsevier, 2005, Oxford, United Kingdom).
7. Shapiro, M. & Brumer, P. *Principles of the Quantum Control of Molecular Processes*, Vol. **250** (Wiley, 2003, Singapore).
8. Schwartz, T., Hutchison, J. A., Genet, C. & Ebbesen, T. W. Reversible switching of ultrastrong light-molecule coupling. *Phys. Rev. Lett.* **106**, 196405 (2011).
9. Hutchison, J. A., Schwartz, T., Genet, C., Devaux, E. & Ebbesen, T. W. Modifying chemical landscapes by coupling to vacuum fields. *Angew. Chem. Int. Ed.* **51**, 1592–1596 (2012).
10. Fontcuberta, A. & Stellacci, F. Light-matter interactions: ultrastrong routes to new chemistry. *Nat. Mater.* **11**, 272 (2012).
11. Chikkaraddy, R. et al. Single-molecule strong coupling at room temperature in plasmonic nanocavities. *Nature* **535**, 127–130 (2016).
12. Flick, J., Ruggenthaler, M., Appel, H. & Rubio, A. Atoms and molecules in cavities, from weak to strong coupling in quantum-electrodynamics (QED) chemistry. *Proc. Natl Acad. Sci. USA* **114**, 3026–3034 (2017).
13. Galego, J., Garcia-Vidal, F. J. & Feist, J. Cavity-induced modifications of molecular structure in the strong-coupling regime. *Phys. Rev. X* **5**, 041022 (2015).
14. Feist, J., Galego, J. & Garcia-Vidal, F. J. Polaritonic chemistry with organic molecules. *ACS Photonics* **5**, 205–216 (2018).
15. Csehi, A., Halász, G. J., Cederbaum, L. S. & Vibók, Á. Competition between light-induced and intrinsic nonadiabatic phenomena in diatomics. *J. Phys. Chem. Lett.* **8**, 1624–1630 (2017).
16. Demekhin, P. V. & Cederbaum, L. S. Light-induced conical intersections in polyatomic molecules: general theory, strategies of exploitation, and application. *J. Chem. Phys.* **139**, 154314 (2013).
17. Hugall, J. T., Singh, A. & van Hulst, N. F. Plasmonic cavity coupling. *ACS Photonics* **5**, 43–53 (2018).
18. Zhang, Y. et al. Sub-nanometre control of the coherent interaction between a single molecule and a plasmonic nanocavity. *Nat. Commun.* **8**, 15225 (2017).
19. Kongsuwan, N. et al. Suppressed quenching and strong-coupling of Purcell-enhanced single-molecule emission in plasmonic nanocavities. *ACS Photonics* **5**, 186–191 (2018).
20. Wang, D. et al. Coherent coupling of a single molecule to a scanning Fabry-Perot microcavity. *Phys. Rev. X* **7**, 021014 (2017).
21. Kowalewski, M., Bennett, K. & Mukamel, S. Cavity femtochemistry: manipulating nonadiabatic dynamics at avoided crossings. *J. Phys. Chem. Lett.* **7**, 2050 (2016).
22. Luk, H. L., Feist, J., Toppari, J. J. & Groenhof, G. Multiscale molecular dynamics simulations of polaritonic chemistry. *J. Chem. Theory Comput.* **13**, 4324–4335 (2017).
23. Vendrell, O. Coherent dynamics in cavity femtochemistry: application of the multi-configuration time-dependent Hartree method. *Chem. Phys.* **509**, 55–65 (2018).
24. Galego, J., Garcia-Vidal, F. J. & Feist, J. Suppressing photochemical reactions with quantized light fields. *Nat. Commun.* **7**, 13841 (2016).
25. Kowalewski, M., Bennett, K. & Mukamel, S. Non-adiabatic dynamics of molecules in optical cavities. *J. Chem. Phys.* **144**, 054309 (2016).
26. Nakamura, H. *Nonadiabatic Transition: Concepts, Basic Theory and Applications* (World Scientifica, 2012, Singapore).
27. Domcke, W., Yarkony, D. & Koppel, H. *Conical Intersections: Electronic Structure, Dynamics & Spectroscopy* (World Scientific, 2004, Singapore).
28. Malhado, J. P., Bearpark, M. J. & Hynes, J. T. Non-adiabatic dynamics close to conical intersections and the surface hopping perspective. *Front. Chem.* **2**, 97 (2014).
29. Nenov, A. et al. UV-light- induced vibrational coherences: the key to understand Kasha rule violation in trans- azobenzene. *J. Phys. Chem. Lett.* **9**, 1534–1541 (2018).
30. Toniolo, A., Thompson, A. L. & Martinez, T. J. Excited state direct dynamics of benzene with reparameterized multi-reference semiempirical configuration interaction methods. *Chem. Phys.* **304**, 133–145 (2004).

31. Titov, E., Granucci, G., Gotze, J. P., Persico, M. & Saalfrank, P. Dynamics of azobenzene dimer photoisomerization: electronic and steric effects. *J. Phys. Chem. Lett.* **7**, 3591–3596 (2016).
32. Bandara, H. M. D. & Burdette, S. C. Photoisomerization in different classes of azobenzene. *Chem. Soc. Rev.* **41**, 1809 (2012).
33. Conti, I., Garavelli, M. & Orlandi, G. The different photoisomerization efficiency of azobenzene in the lowest nπ* and ππ* singlets: the role of a phantom state. *J. Am. Chem. Soc.* **130**, 5216–5230 (2008).
34. Sadovski, O., Beharry, A., Zhang, F. & Woolley, G. Spectral tuning of azobenzene photoswitches for biological applications. *Angew. Chem. Int. Ed. Engl.* **48**, 1484–1486 (2009).
35. Joshi, G. K. et al. Ultrasensitive photoreversible molecular sensors of azobenzene-functionalized plasmonic nanoantennas. *Nano Lett.* **14**, 532–540 (2014).
36. Fissi, A., Pieroni, O. & Ciardelli Photoresponsive polymers: azobenzene-containing poly(L-lysine). *Biopolymers* **26**, 1993–2007 (1987).
37. Granucci, G., Persico, M. & Toniolo, A. Direct semiclassical simulation of photochemical processes.with semiempirical wavefunctions. *J. Chem. Phys.* **114**, 10608 (2001).
38. Granucci, G. & Persico, M. Excited state dynamics with the direct trajectory surface hopping method: azobenzene and its derivatives as a case study. *Theor. Chem. Acc.* **117**, 1131–1143 (2007).
39. Bajo, J. J., Granucci, G. & Persico, M. Interplay of radiative and nonradiative transitions in surface hopping with radiation-molecule interactions. *J. Chem. Phys.* **140**, 044113 (2014).
40. Falke, S. M. et al. Coherent ultrafast charge transfer in an organic photovoltaic blend. *Science* **344**, 1001–1005 (2014).
41. Collini, E. Spectroscopic signatures of quantum-coherent energy transfer. *Chem. Soc. Rev.* **42**, 4932–4947 (2013).
42. Diau, E. W.-G. A new trans-to-cis photoisomerization mechanism of azobenzene on the S_1 (n,π*) surface. *J. Phys. Chem. A* **108**, 950–956 (2004).
43. Cusati, T. et al. Semiempirical Hamiltonian for simulation of azobenzene photochemistry. *J. Phys. Chem. A* **116**, 98–110 (2011).
44. Cantatore, V., Granucci, G., Rousseau, G., Padula, G. & Persico, M., Photoisomerization of self-assembled monolayer of azobiphenyls: Simulation to Highlight the role of packing and defects, *J. Chem. Phys. Lett.* **7**, 4027-4031 (2016)
45. Neuman, T., Esteban, R., Casanova, D., Garcia-Vidal, F. J. & Aizpurua, J. Coupling of molecular emitters and plasmonic cavities beyond the point-dipole approximation. *J. Nano Lett.* **18**, 2358–2364 (2018).
46. Barbatti, M. Nonadiabatic dynamics with trajectory surface hopping method. *Wiley Interdiscip. Rev. Comput. Mol. Sci.* **1**, 620–633 (2011).
47. Tapavicza, E., Bellchambers, G. D., Vincent, J. C. & Furche, F. Ab initio non-adiabatic molecular dynamics. *Phys. Chem. Chem. Phys.* **15**, 18336 (2013).
48. Li, X., Tully, J. C., Schlegel, H. B. & Frisch, M. J. Ab initio Ehrenfest dynamics. *J. Chem. Phys.* **123**, 084106 (2005).
49. Ragazos, I. N., Robb, M. A., Bernardi, F. & Olivucci, M. Optimization and characterization of the lowest energy point on a conical intersection using an MC-SCF Lagrangian. *Chem. Phys. Lett.* **197**, 217–223 (1992).
50. Bearpark, M. J. et al. The azulene S_1 state decays via a conical intersection: a CASSCF study with MMVB dynamics. *J. Am. Chem. Soc.* **118**, 169–175 (1996).
51. Flick, J., Appel, H., Ruggenthaler, M. & Rubio, A. Cavity Born–Oppenheimer approximation for correlated electron-nuclear-photon systems. *J. Chem. Theory Comput.* **13**, 1616–1625 (2017).
52. Worth, G. A., Hunt, P. & Robb, M. A. Nonadiabatic dynamics: a comparison of surface hopping direct dynamics with quantum wavepacket calculations. *J. Phys. Chem. A* **107**, 621–631 (2003).
53. Tully, J. C. & Preston, R. K. Molecular dynamics with electronic transitions *J. Chem. Phys.* **93**, 1061 (1990).
54. Granucci, G., Persico, M. & Zoccante, A. Surface hopping trajectory simulations with spin-orbit and dynamical couplings. *J. Chem. Phys.* **133**, 134111 (2010).
55. Bussi, G., Donadio, D. & Parrinello, M. Canonical sampling through velocity rescaling. *J. Chem. Phys.* **126**, 014101 (2007).
56. Craig, D. P. & Thirunamachandran, T. *Molecular Quantum Electrodynamics* (Academic Press, 1984, Mineola, New York).
57. Granucci, G. & Toniolo, A. Molecular gradients for semiempirical CI wavefunctions with floating occupation molecular orbitals. *Chem. Phys. Lett.* **325**, 79–85 (2001).
58. Granucci, G. & Persico, M. Gradients for configuration interaction energies with spin-orbit coupling in a semiempirical framework. *J. Comput. Chem.* **32**, 2690 2011).

Acknowledgements

J.F., E.C. and S.C. acknowledge funding from the ERC under the grant ERC-CoG-681285 TAME- Plasmons. G.G. acknowledges funding from the University of Pisa, PRA 2017 28.

Author contributions

S.C. initiated this project; J.F., G.G., M.P. and S.C. designed the investigation; J.F. and G.G. extended the specific surface hopping scheme to polaritonic states and implemented the software modifications; J.F. performed the calculations; all the authors contributed to the analysis of results and to the writing of the paper.

Additional information

Supplementary Information accompanies this paper at https://doi.org/10.1038/s41467-018-06971-y.

Competing interests: The authors declare no competing interests.

Reprints and permission information is available online at http://npg.nature.com/reprintsandpermissions/

Publisher's note: Springer Nature remains neutral with regard to jurisdictional claims in published maps and institutional affiliations.

Supplementary Movies

The Supplementary Movie 1 and 2 the non-adiabatic dynamics simulations for the azobenezene photoisomerization dynamics in the strong coupling regime. The simulations are realized under the two different conditions described in the main text, namely $E_{ph} = 1.3$ eV with $g = 0.010$ au and $E_{ph} = 2.2$ eV with $g = 0.010$ au. On the $CNNC$ coordinate, the basin on the right represents the *trans* region, while the basin on the left is the *cis* region. The states from upper left to lower right are ordered energetically from the highest to the lowest. See the main text for further info. The Supplementary Movie 3 shows the non-adiabatic dynamics for the bare molecule in weak coupling. For completeness and to ease the interpretation of the results, the Supplemental Movies are included via a QRcode in this section.

Supplementary Movie 1

Supplementary Movie 2

Supplementary Movie 3

Supplementary Movies

Supplementary Material: Manipulating azobenzene photoisomerization through strong light-molecule coupling

J. Fregoni,[†,§] G. Granucci,[‡] E. Coccia,[¶] M. Persico,[‡] and S. Corni[*,¶,§]

[†]*Dipartimento di scienze Fisiche Informatiche e Matematiche, University of Modena and Reggio Emilia*

[‡]*Dipartimento di Chimica e Chimica Industriale, Università di Pisa, I-56124 Pisa, Italy*

[¶]*Dipartimento di Scienze Chimiche, Università di Padova, I-35131 Padova, Italy*

[§]*Istituto Nanoscienze, Consiglio Nazionale delle Ricerche CNR-NANO, I-41125 Modena, Italy*

E-mail: stefano.corni@unipd.it,giovanni.granucci@unipi.it

Transition dipole moment and polaritonic energy splitting dependence on nuclear coordinates

As mentioned in the main text, the interaction between light and molecule strictly depends on the transition dipole moment component along the polarization of the electromagnetic mode, for each nuclear coordinate. Therefore, the polaritonic energy splitting dependence on the nuclear coordinates is embodied into the dependence on the transition dipole moment:

$$\hat{H}_{int}(Q) = g\hat{\boldsymbol{\mu}}_{\boldsymbol{S_0},\boldsymbol{S_1}}(\boldsymbol{Q}) \cdot \hat{\boldsymbol{\lambda}} \left(\hat{b}^\dagger + \hat{b}\right). \tag{1}$$

The transition dipole components between the ground and first excited state for the

isolated azobenzene molecule are shown in Figure S1. It is evident that the range of variation of the transition dipole moment on the geometry can cover several Debyes, depending on the alignment of the molecule. In this work, we take the field as polarized along z, i.e. the axis perpendicular to the molecular plane: as a consequence, along the avoided crossing line, the transition dipole z-component varies from zero to few Debyes. The splitting magnitude and profile also depends strictly on the field orientation with respect to the molecule. Such conditions gives origin to splittings ranging from zero to about 100 meV for a coupling constant g of 0.010 au.

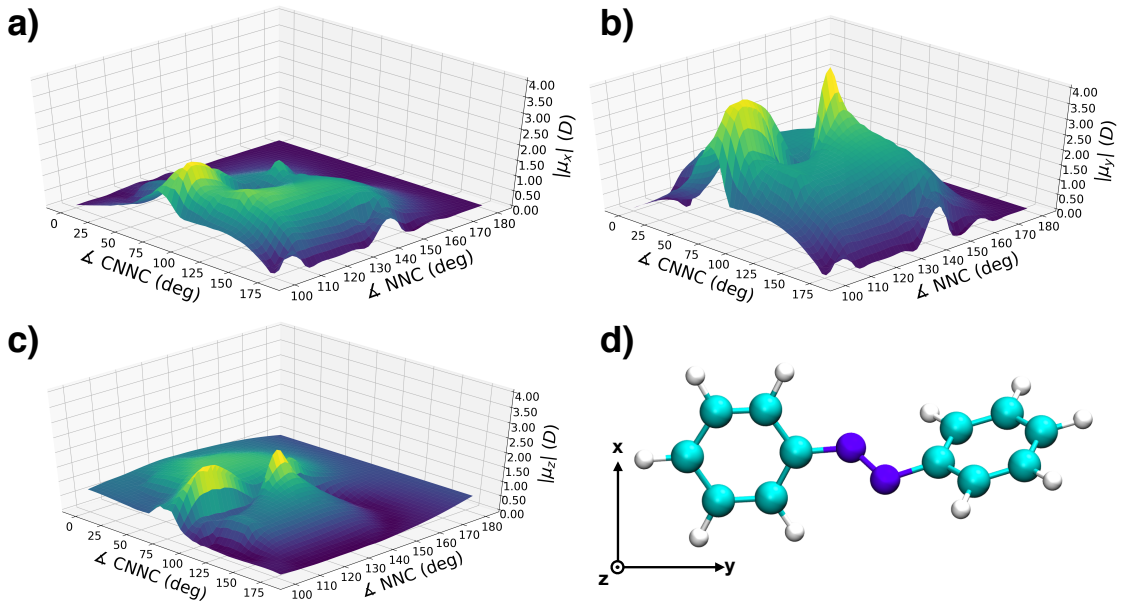

Figure S1: **Panel a),b),c)** Transition dipole moments components along the x, y and z direction respectively, as a function of the CNNC and NNC coordinates. The orientation of the trans azobenzene with respect to the x, y and z axes is shown in **Panel d)**

In Figure S2 two strong coupling avoided crossing profiles with g of 0.010 au, the field polarized along the z axis and two different photon energies are compared. In the plot, such splitting is defined as the contribution to the energy splitting between the upper and lower polariton due to the strong-coupling matrix element. The profile presented in the Panel a) corresponds to the case where the $|S_0, 1\rangle$ energy is set to E_{ph} 1.3 eV, while the Panel b) is the E_{ph} 2.2 eV case. The splitting is evaluated analytically for a two level system composed

of the states $|S_0, 1\rangle$ and $|S_1, 0\rangle$, taking into account the dependence of the dipoles on the nuclear coordinates:

$$\Delta E^{sc}_{+,-} = -\left|H_{S_1,0} - H_{S_0,1}\right| + \sqrt{\left|H_{S_0,1} - H_{S_1,0}\right|^2 + 4g^2\mu_z^2}. \tag{2}$$

As highlited in the main text, the position of the contribution of the interaction to the polaritonic splitting can be tuned by changing the photon frequencies E_{ph} (1.3 eV and 2.2 eV respectively). For both the analyzed cases the splitting goes to zero when approaching the CNNC value of 180°, signature of an intersection line between the uncoupled states with a zero interaction element. The magnitude of such contribution, instead, shows dramatic and non trivial dependence on the nuclear coordinates in both cases. As the azobenzene molecule moves out of the plane through torsion of the CNNC dihedral angle, the splitting value increases drastically, carrying a non-trivial dependence on the nuclear coordinates.

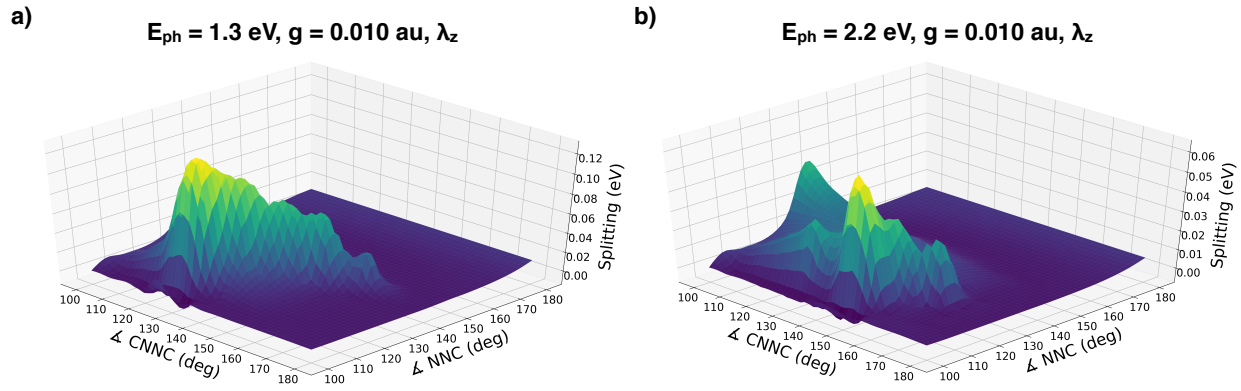

Figure S2: **Panel a)** Splitting profiles for the E_{ph} 1.3 eV **Panel b)** and 2.2 eV case.

As shown in Figure S2 the Rabi splitting approaches the zero as the CNNC angle moves towards 180 (planar molecule). The zero transition dipole moment perpendicular to the molecule together with the field polarization along the same component (used in the current work) suggests the presence of a light-induced conical intersection. In Figure S3 the polaritonic conical intersections for the 1.3 eV and the 2.2 eV cases are shown. As anticipated in the main text, the position of the polaritonic conical intersection can be tuned by changing

the photon frequency. For the 1.3 eV case, the intersection is located at 180 along the CNNC coordinate and 155.33 along the NNC (Figure S3a,b); for the 2.2 eV case, the intersection is located at 180 along the CNNC coordinate and 135 along NNC (Figure S3c,d).

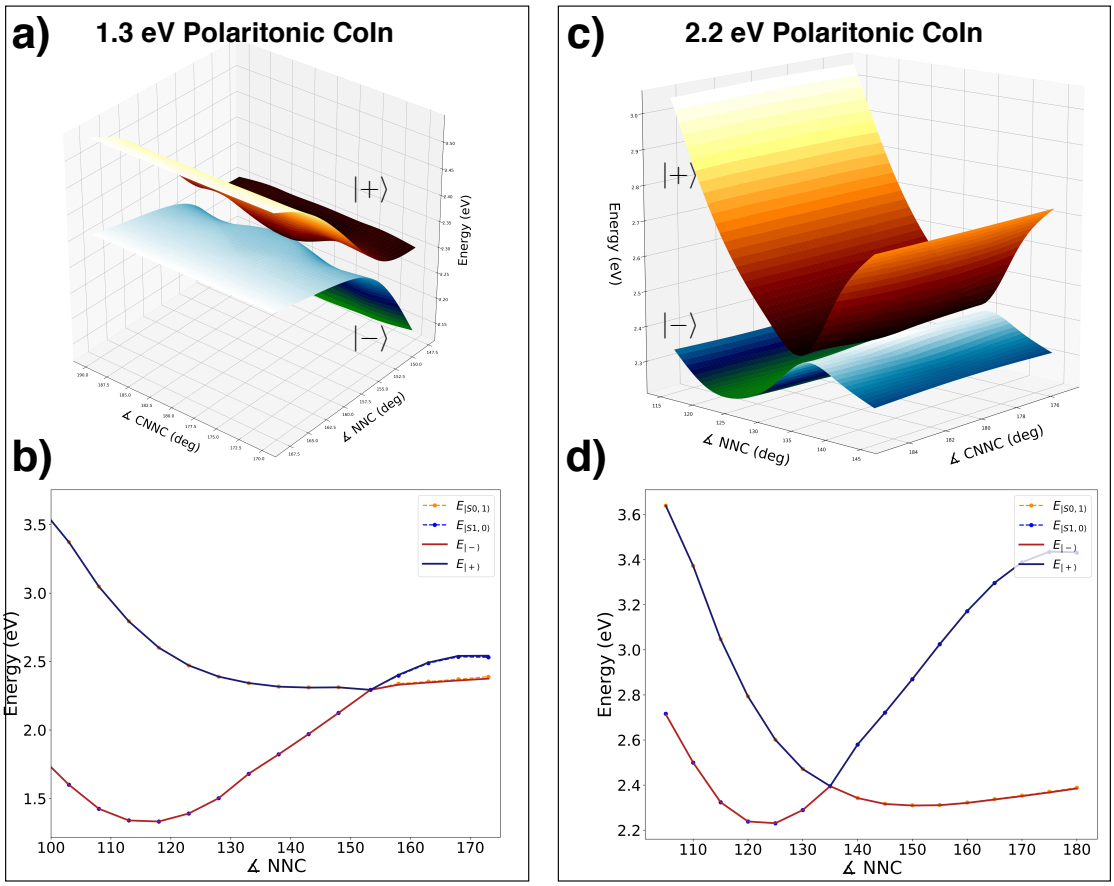

Figure S3: Polaritonic conical intersection and section of the polaritonic potential energy surfaces for **Panels a),b)** the 1.3 eV case **Panel c,d)** and 2.2 eV case.

Together with the different position of the polaritonic conical intersection, the different crossing geometry entails a substantially different shape of the polaritonic potential energy surfaces in the surroundings of the crossing seam. The effects of such difference in the two studied cases are discussed in the main text and in the next section (Figure S5a,b).

Strong coupling non-adiabatic dynamics

In this section we overview the conditions and the supplementary characterization for the two performed dynamics simulations. The sampling was performed by running 10 ps of

equilibration dynamics on the ground state of azobenzene, absent field and with a single trajectory. The initial velocities for such trajectory are distributed according to a Maxwell-Boltzmann distribution at room temperature, and the sampling dynamics is performed on the ground state with a Bussi-Parrinello stochastic thermostat, with a time constant τ of 10 fs. We sample 300 sets of positions and velocities from the equilibration dynamics. We retain the same sampling conditions for all the following dynamics in order to highlight the differences in the mechanism driven by different coupling conditions. In this way, we are able to ascribe the differences in the evolution of the wavepackets to the difference in the polaritonic potential energy surfaces. For each sampled trajectory, we compute the polaritonic states and we excite it through a Franck-Condon excitation to the upper polaritonic state. Each trajectory runs and independent dynamics for 2 ps, with a time step of 0.1 fs. We refer to Figure 4 of the main text for the discussion about the mechanism change induced by the strong coupling regime. In Figures SS4a and S4b we propose a scheme for the splitting of the wavepacket along the oscillation coordinates (Figure 4a and 4d of the main text) for the E_{ph} 1.3 eV and 2.2 eV respectively.

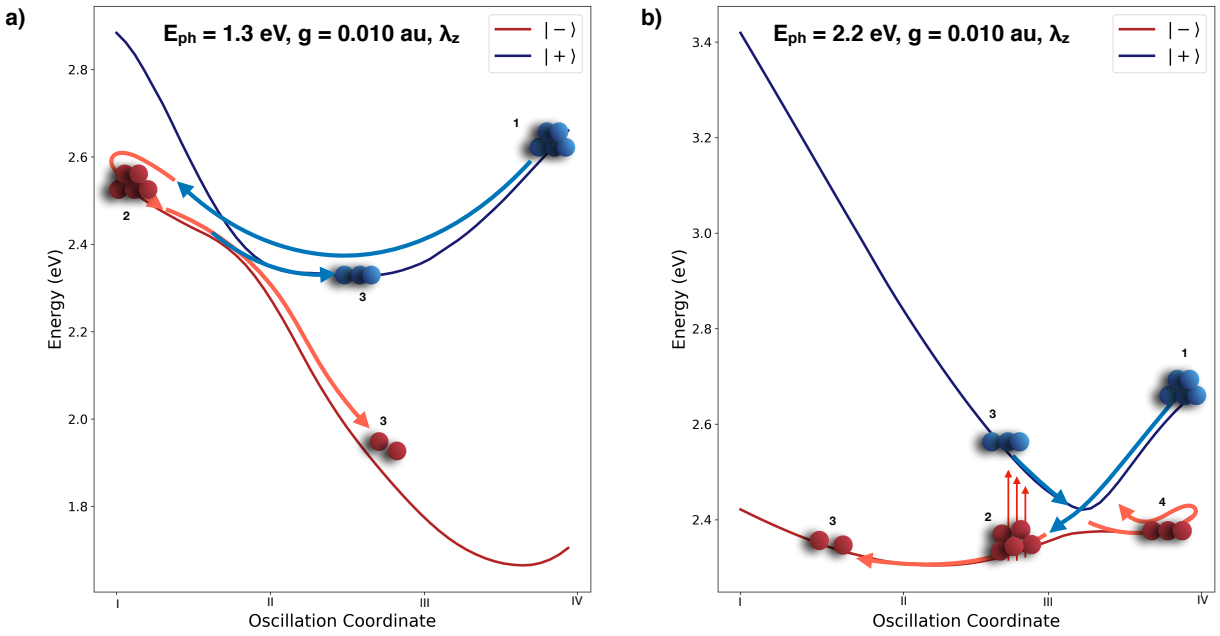

Figure S4: Scheme of the different wavepacket splitting driven by the strong coupling avoided crossing shape in the E_{ph} 1.3 eV **Panel a)** and 2.2 eV **Panel b)**, respectively.

The complete movies of the dynamics are presented as standalone files of the supplementary material. Interpreting together the hereby scheme and the proposed movies, it becomes evident how the different shaping of the avoided crossing due to different coupling conditions impacts the dynamics. In the characterization of the dynamics, we also analyzed the average oscillation of the CNNC and NNC angles, together with the oscillation of the energy difference between the polaritonic states (Figure S5 and S6). The oscillation of the angles (Figure S5) in the first 500 fs of the dynamics allowed us to extract the range of the average oscillation coordinate for the wavepacket in the two cases. The oscillation of energy in Figure S6 is a signature of the hopping between polaritonic states. In particular, the first pronounced peak implies that all the trajectories move toward the minimum of the upper polariton before splitting. As the trajectories split close to the strong-coupling avoided crossing, the oscillation in the energy difference damps progressively, following the oscillation trend of populations presented in Figure 4c and 4f (see main text).

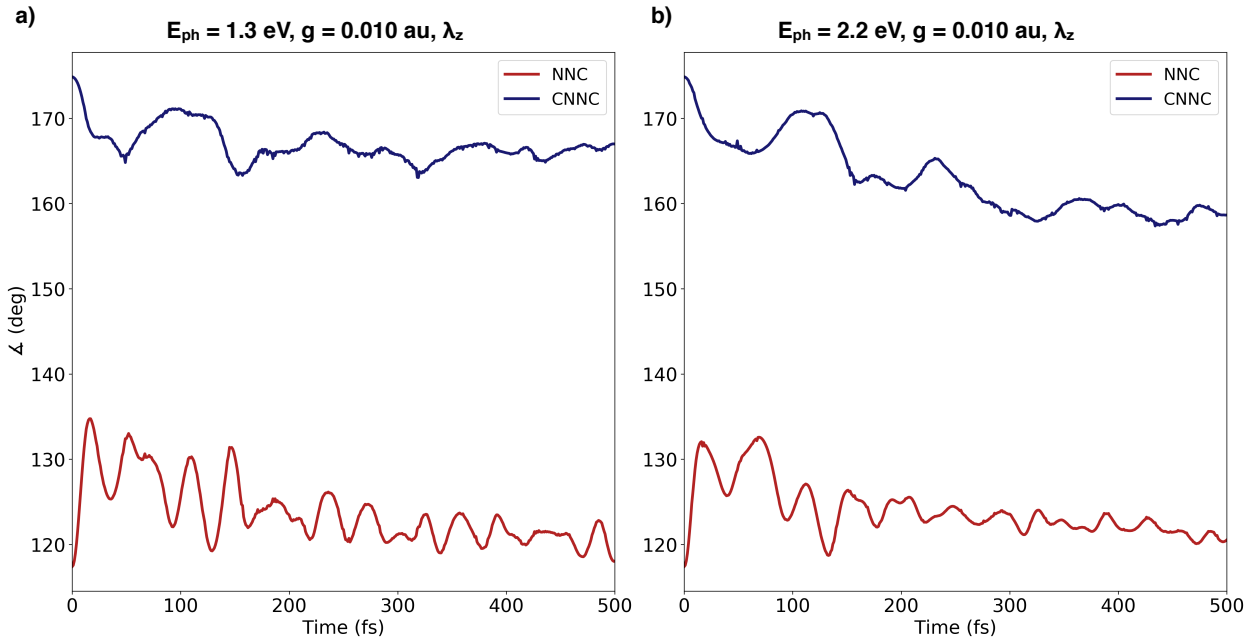

Figure S5: Oscillation of the CNNC and NNC coordinates for the E_{ph} 1.3 eV **Panel a)** and 2.2 eV **Panel b)** case, respectively.

In Figure S7 we report the quantum yields dependence on the coupling constant g and the photon frequency. Such non-monotonic dependence can be approximately split in three

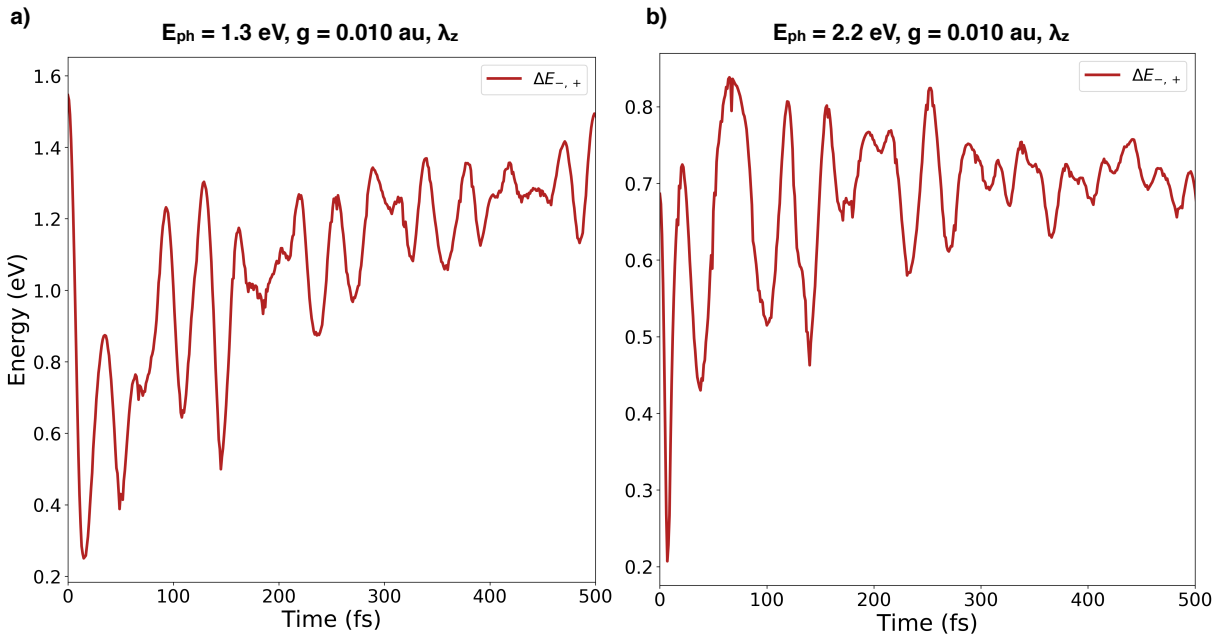

Figure S6: Oscillation of the energy difference between the $|+\rangle$ and $|-\rangle$ states for the E_{ph} 1.3 eV **Panel a)** and 2.2 eV **Panel b)** case, respectively

domains: low frequency (less than 0.8 eV), middle frequency (0.8-2.0 eV) and high frequency (higher than 2.0 eV). In the middle frequency domain the yields are very low, i.e., the photoisomerization is quenched. The origin of this behavior can be traced to the trapping in the lower polariton state, as discussed above. Remarkably, for g=0.005 au in the high frequency domain, we observe an increase of the yield, although very limited (but with statistical significance, the error being smaller than 1%). The reason for such behavior is that the PPES are modified in such a way that the system approaches the electronic conical intersection with larger velocities. As a consequence, the trajectories perform hops with a slightly higher probability towards the cis branch.

Finally, in the lower frequency domain we observe quantum yields that are recovering towards the weak-coupling value. In this case, the polaritonic avoided crossing is close to the electronic conical intersection. Accordingly, the hopping of the trajectories to the lower polaritonic state and the reaching of the conical intersection become concurrent, leading back to a mechanism similar to that in the weak coupling regime and thus to similar yields. However, such low photon frequency becomes resonant with vibrational transitions, calling

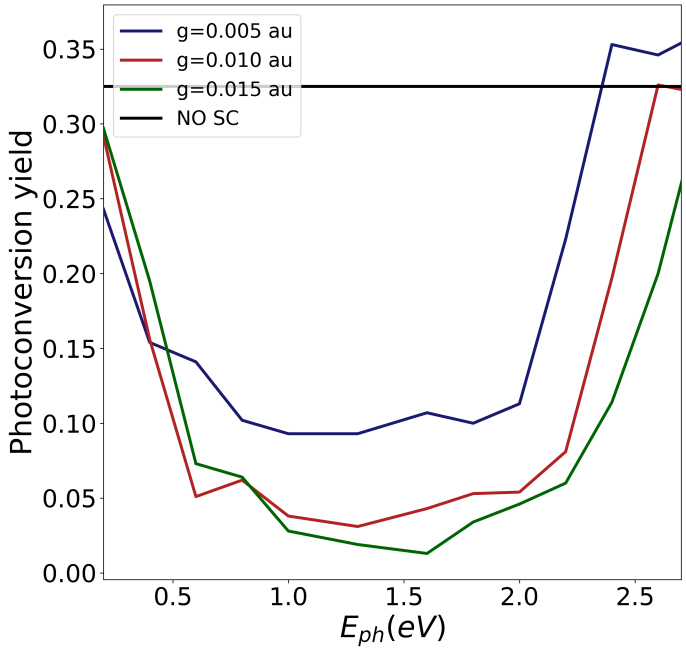

Figure S7: Dependence of the quantum yields on the photon energies and coupling constants. The quenching of the reaction is dominated by the trapping mechanism for energies between 0.8 and 2.0 eV. For different energies, the quenching-by-trapping mechanism is suppressed: at low energies, for concomitance of the strong coupling avoided crossing and electronic conical intersection; at high energies, the trapping minimum becomes less deep and the wavepacket proceeds towards the conical intersection.

for a quantum mechanical description of the nuclear motion.

Cavity Losses

The results for the inclusion of the cavity losses is already discussed in the main text for the 1.3 eV case. Here we present the effect of explicitely including the cavity lifetime for the 2.2 eV case (Figure). As for the 1.3 eV case, we take into account 4 cavity lifetimes: 10 fs, 50 fs, 100 fs (Figures a,b,c respectively) and 150 fs.

As discussed in the main text, the inclusion of the cavity lifetime impacts the decay mechanism of the system: the driving process for the de-excitation of a polaritonic system becomes the loss of coherence between the polaritonic states (Figure d). As the 2.2 eV case is characterized by a quick population drop on the lower polariton, the overall relaxation mechanism is ruled by the lower polaritonic decay. Indeed, in the 2.2 eV case the whole

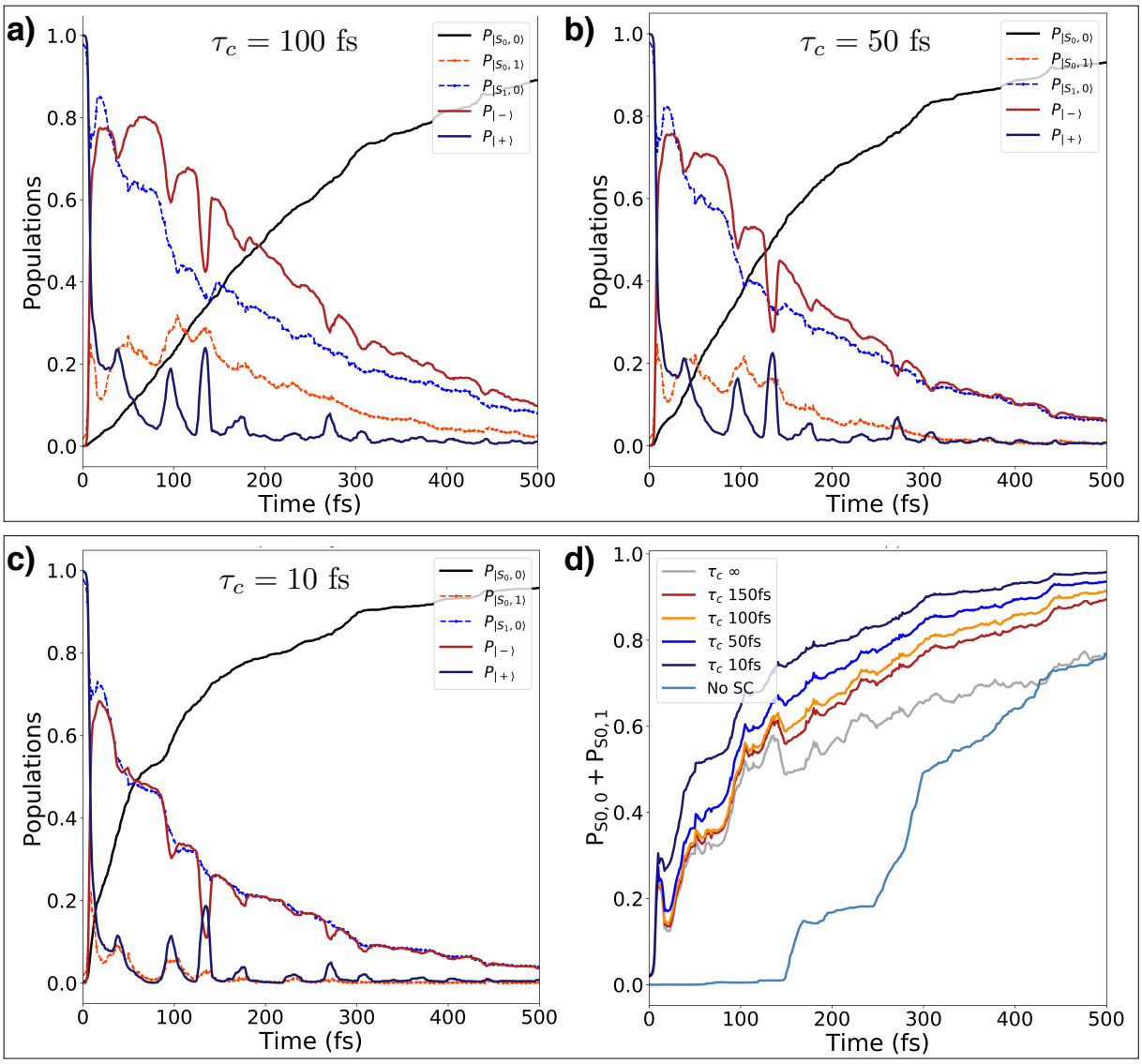

Figure S8: 2.2 eV including cavity lifetimes of 100 fs **Panel a)**, 50 fs **Panel b)**, 10 fs **Panel c)**. Ground state population retrieval for the 2.2 eV dynamics **Panel d)**.

dynamics occurs in a region where the $|S1, 0\rangle$ and $|S0, 1\rangle$ states are more mixed than in the 1.3 eV case: while in the 1.3 dynamics the evolution of the uncoupled and polaritonic states differs only at the oscillations peaks, where the wavepacket goes through the narrow crossing seam, in the 2.2 eV case (when no losses are considered) the populations of coupled and uncoupled states follow opposite trends. As shown in Figure 4f of the main text, when the lower polariton is completely populated (100 to 200 fs), the uncoupled populations are both about 0.5. The cavity loss, therefore, affects greatly the decay of both polaritonic states (Figure

c), in contrast with the 1.3 eV case, where the most affected state is the lower polariton. In particular, as the cavity loss becomes quicker, the polaritons tend to evolve as the uncoupled states earlier (Figures a,b,c) due to the loss of mixing. This behaviour becomes evident in Figure d, where the major differences between the ground state population retrieval are observed between the $\tau_c = \infty$ case and the $\tau_c = 150\ fs$ case. As addressed in the main text, we can conclude that if the wavepacket evolves in a region where the polaritonic states are mixed in nature, the decoherence between light and matter becomes the main decay channel for such system.

Gauge choice and extendend Jaynes-Cummings model

We hereby present the plots of polaritonic states obtained numerically starting from the bare electronic states as reported in the electronic structure paragraph of the Methods section. In this numerical polaritonic state calculation, we compared compare the dipolar and extended Jaynes-Cummings Hamiltonians. The dipolar Hamiltonian is obtained through the Göppert-Meyer gauge transformation starting from a minimal coupling Hamiltonian in the Coulomb gauge (C. Cohen-Tannoudj, *Photons and atoms*, Wiley Interscience, 1997). Both the hamiltonians are composed by the molecular and photonic contributions and the light-matter interaction term:

$$\hat{H} = \hat{H}_{mol} + \hat{H}_{ph} + \hat{H}_{int}. \tag{3}$$

The light-matter interaction term in the dipolar formulation is:

$$\hat{H}_{dip} = i\hat{\boldsymbol{\mu}} \cdot \hat{\boldsymbol{\lambda}} \sqrt{\omega_{ph}} A_0 \left(\hat{b} - \hat{b}^\dagger\right) + 2\left(\mu \cdot \lambda\right)^2 A_0^2, \tag{4}$$

where A_0 is the vector potential intensity, $\hat{\boldsymbol{\lambda}}$ is the polarization of the field, ω_{ph} is the frequency of the resonant mode, $\hat{b}$ and $\hat{b}^\dagger$ are the bosonic annihilation and creation operators respecitvely and $\hat{\boldsymbol{\mu}}$ is the dipolar operator. We distinguish two interaction orders in the

vector potential. The first order terms embody the interaction between states differing for one in the photon number:

$$iA_0\sqrt{\omega_{ph}}\langle n,p|\hat{\mu}\left(\hat{b}-\hat{b}^\dagger\right)|n',p\pm1\rangle = \pm iA_0\sqrt{\omega_{ph}}\sqrt{p+1}\mu_{n,n'} \tag{5}$$

where $|n,p\rangle$ is the basis of the uncoupled states (see Methods section of the main text). The first order terms consist of two kind of interactions: one mixing states with the same electronic index,

$$iA_0\sqrt{\omega_{ph}}\langle n,p|\hat{\mu}\left(\hat{b}-\hat{b}^\dagger\right)|n,p\pm1\rangle = \pm iA_0\sqrt{\omega_{ph}}\sqrt{p+1}\mu_{n,n}, \tag{6}$$

and the other depening on the transition dipole moments, which is characteristic of the strong coupling regime,

$$iA_0\sqrt{\omega_{ph}}\langle n,p|\hat{\mu}\left(\hat{b}-\hat{b}^\dagger\right)|n',p\pm1\rangle = \pm iA_0\sqrt{\omega_{ph}}\sqrt{p+1}\mu_{n',n}, \tag{7}$$

with $n \neq n'$. To compute the second order terms, we exploit a resolution of identity:

$$A_0^2\langle n,p|\hat{\mu}^2|n',p'\rangle = A_0^2\sum_i^{N_{st}}\langle n,p|\hat{\mu}|i,p'\rangle\langle i,p|\hat{\mu}|n',p'\rangle\delta_{p,p'}. \tag{8}$$

Due to the absence of any bosonic operator in the second order interaction terms, these kind of terms act only on the electronic part. Therefore, a shift of the diagonal elements of the Hamiltonian is provided by the terms:

$$\langle n,p|\hat{\mu}^2|n,p\rangle = A_0^2\sum_{i=1}^{N_{st}}\langle n,p|\hat{\mu}|i,p\rangle\langle i,p|\hat{\mu}|n,p\rangle, \tag{9}$$

together with a correction to the isolated molecule interaction between electronic states,

$$\langle n,p|\hat{\mu}^2|n',p\rangle = A_0^2\sum_{i=1}^{N_{st}}\langle n,p|\hat{\mu}|i,p\rangle\langle i,p|\hat{\mu}|n',p\rangle, \tag{10}$$

with $n \neq n'$. The extended Jaynes-Cummings model disregards the permanent dipole contributions and the second order terms and it can be recast in a dipolar-like shape:

$$\hat{H} = \hat{H}_{mol} + \hat{H}_{ph} + \hat{\boldsymbol{\mu}}_{\boldsymbol{tr}} \cdot \hat{\boldsymbol{\lambda}} \sqrt{\omega_{ph}} A_0 \left(\hat{b} + \hat{b}^{\dagger} \right) \tag{11}$$

where $\hat{\boldsymbol{\mu}}_{\boldsymbol{tr}}$ collects the transition dipole moments between the electronic states and the ratio g/ω_{ph} is $A_0/\sqrt{\omega_{ph}}$. The problem of the gauge choice in strongly coupled light-matter systems has been presented by Flick *et al.* (J. Flick, M. Ruggenthaler, H. Appel, A. Rubio, *Proc. Natl. Acad. Sci. USA*, 114(12), 3026, 2017).

In particular, they emphasized that for high g/ω_{ph} ratios (greater than 0.4 au) the full dipolar light-matter Hamiltonian must be considered. Such g/ω_{ph} ratio is peculiar of vibro-polaritonic (photon resonant with vibrational transitions) coupled systems, which are characterized by low frequencies together with high fields. Under such conditions, the second order terms are non negligible as they impact deeply the bond lengths. Nevertheless, within the conditions where the electronic transitions are resonant with a cavity mode, the involved g/ω_{ph} ratios set the system in a regime where higher order terms can be disregarded (ranging from 0.20 au to 0.12 au for the E_{ph} 1.3 eV and 2.2 eV respectively). For the sake of completeness, we numerically verified the stability of our approximation for the conditions used in this work. We computed the states involved in the non-adiabatic dynamics by taking into account two electronic states ($|n\rangle$=$|S_0\rangle$,$|S_1\rangle$) and two occupation numbers for the photon ($|p\rangle$=$|0\rangle$,$|1\rangle$). The results for the 1.3 eV and 2.2 eV cases are reported in Figure S9, where it is shown that the additional terms appearing in the dipolar formulation can be disregarded within our system conditions.

Even though negligible, the minor differences between the polaritonic states within the two models shown in Figure S9 (full lines) are amenable to the truncation of the occupation number space. When considering the truncated space, we disregard the interaction terms

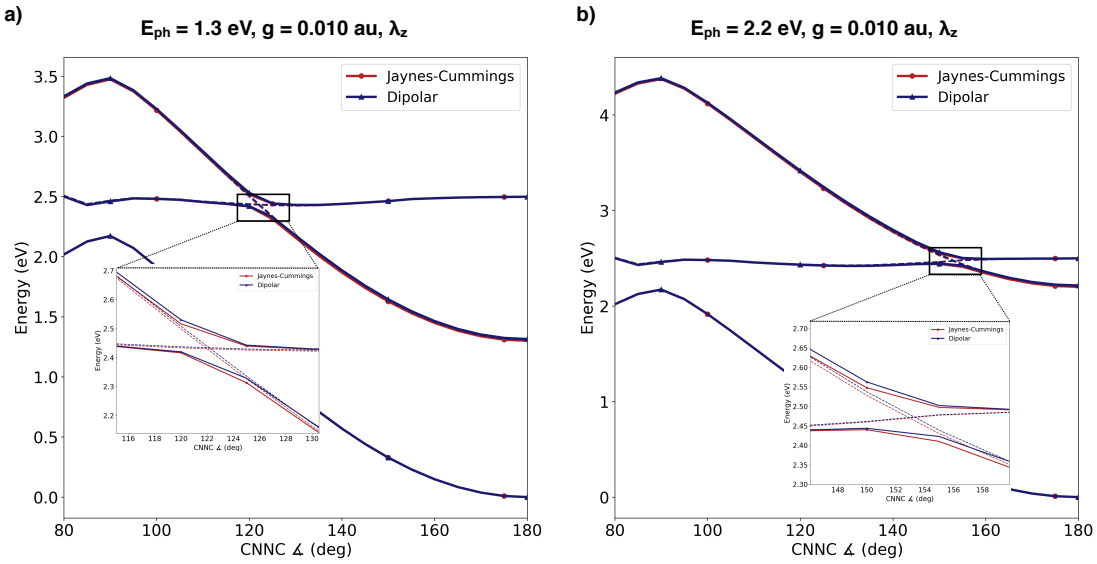

Figure S9: Numerical comparison of the light-matter interaction Hamiltonians for the E_{ph} 1.3 eV **Panel a)** and 2.2 eV **Panel b)** case respectively in the truncated space with $|0\rangle$ and $|1\rangle$ photon occupation state numbers. The coupling constant is g 0.010 au and the field is oriented along the z axis of the molecule.

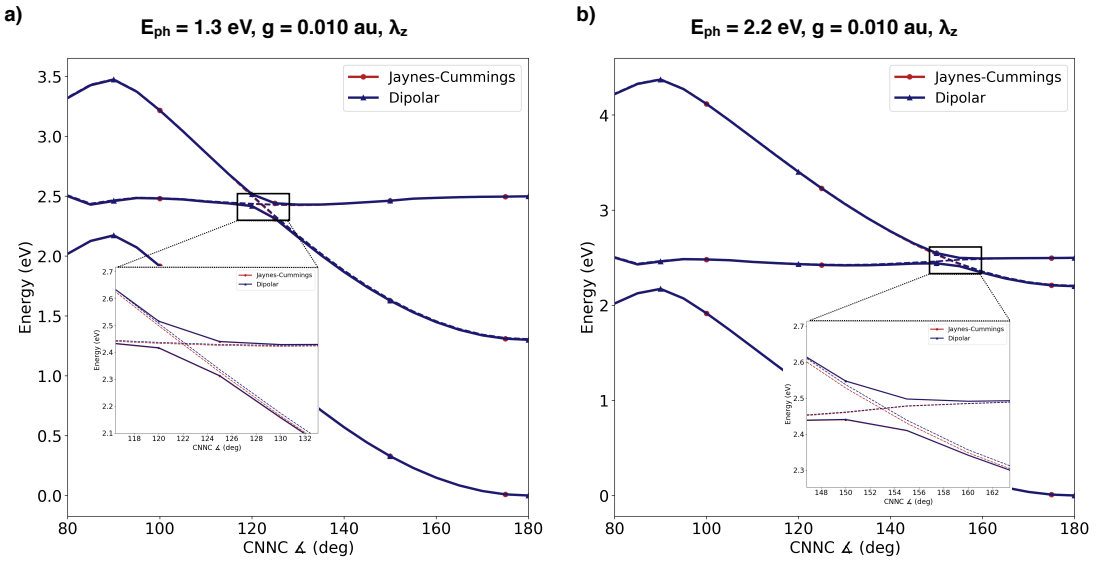

Figure S10: Numerical comparison of the light-matter interaction Hamiltonians for the E_{ph} 1.3 eV **Panel a)** and 2.2 eV **Panel b)** case respectively. In this calculation, 6 states are included: the space is spanned by the direct product of the electronic states times the occupation numbers for the photon.

of equation 6. In particular, the state $|S_0, 1\rangle$ (and $|S_1, 1\rangle$, respectively) do not interact with $|S_0, 2\rangle$ ($|S_1, 2\rangle$) in the truncated space, due to the absence of the $|2\rangle$ occupation number.

In order to reach the agreement between the two models, we include in the space one more occupation state number ($|2\rangle$) for each electronic state. As shown in Figure S10, the two models converge to the same results despite the difference in the uncoupled states (dotted line). Such difference in the uncoupled states is due to the diagonal shift coming from the second order term of the dipolar Hamiltonian (eq. 9).

On the basis of the negligible differences outlined with the numerical results presented in this section, we decided to rely on the extended Jaynes-Cummings Hamiltonian for our specific conditions. Nevertheless, it is to emphasize once more that the range of stability of this approximation must be carefully checked when treating strongly coupled systems as addressed by Flick *et. al*(J. Flick, M. Ruggenthaler, H. Appel, A. Rubio, *Proc. Natl. Acad. Sci. USA*, 114(12), 3026, 2017).

Algorithm

The following notation is used in the flowchart:

1. $|K\rangle$ and U_K are electronic states and energies (approximate eigenfunction of the electronic Hamiltonian for the free molecule). In the present case we only considered $K = S_0, S_1$. The polaritonic "diabatic" states are obtained as products $|K, n\rangle$ (n being the photon occupation number), as mentioned in the main text.

2. $\boldsymbol{\mu}_{KL} = \langle K\,|\boldsymbol{\mu}|\,L\rangle$ are the matrix elements of the molecular dipole.

3. $|A\rangle$ and E_A are the polaritonic adiabatic states (linear combinations of $|K, n\rangle$) and energies.

4. The polaritonic wavefunction is $\Psi(t) = \sum_A C_A(t)|A\rangle$

5. The state where the trajectory is running on is the "current" adiabatic state (labelled Γ).

6. $T_{\Gamma\to A}$ is the surface hopping transition probability.

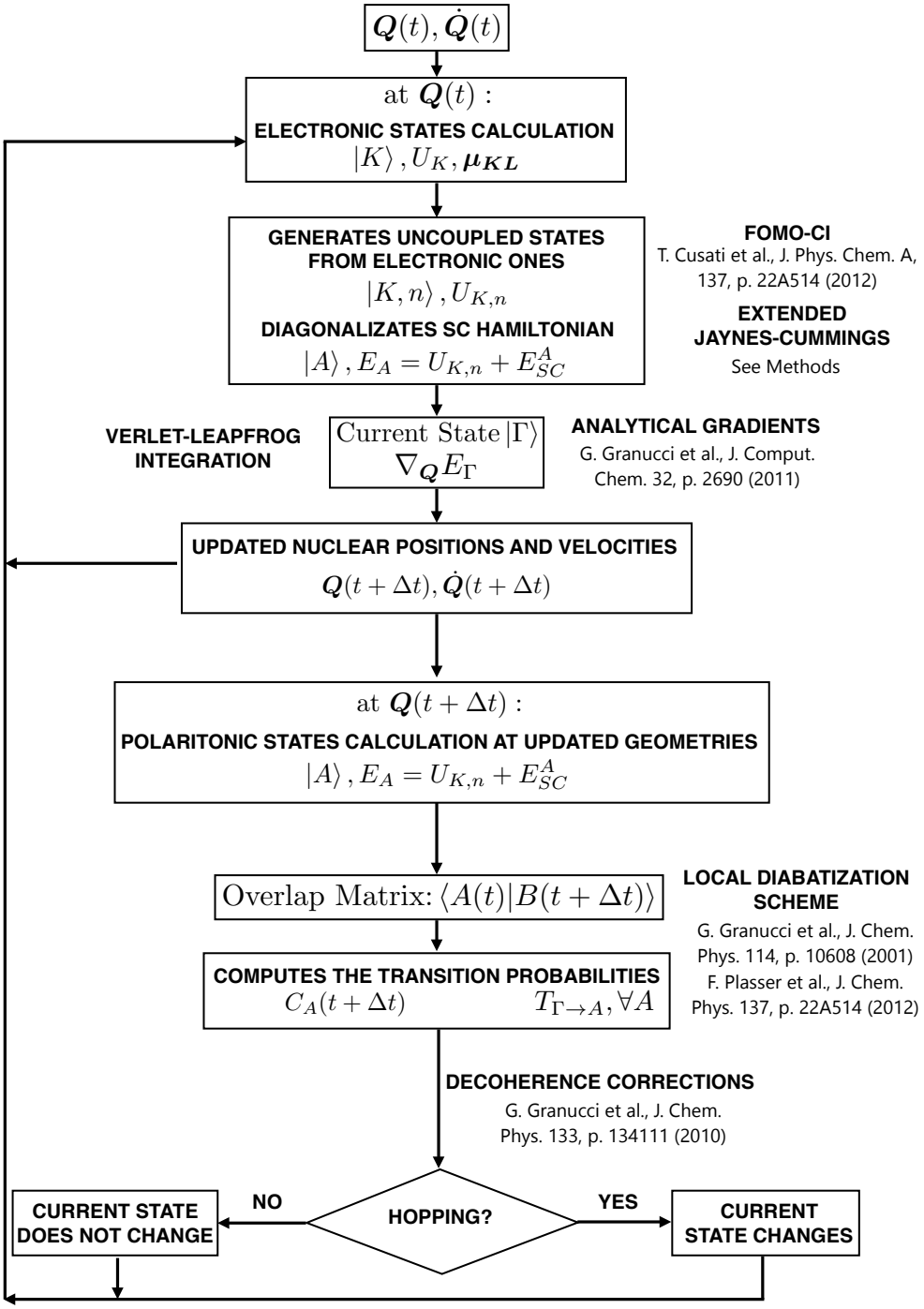

Figure S11: Flow chart for the algorithm applied to propagate each trajectory. For each sampled trajectory (see Main Text) a Franck-Condon excitation is performed to the upper polariton. At each time step the electronic and polaritonic energies and coeffiecients are computed. The gradient of the polaritonic energy is calculated to propagate the classical nuclear tajectories. The overlap between the polaritonic wavefunction at the begin and the end of the timestep is computed to evaluate the transition probability, accordingly to the local diabatization scheme on which we rely on. The decoherence correction is then applied and, if a hopping has occurred, the nuclear kinetic energy of the trajectory is readjusted to ensure total energy conservation. The propagation is then resumed. The statistical treatment of all the trajectories retrieves the branching of the wavepacket on the potential energy surfaces.

Chapter 3

This chapter is devoted to address the role of chemical and environmental complexity in polaritonic photochemistry. The dye molecule exploited in the present work is still azobenzene. With respect to the results presented in the previous Chapter, here I push the system description to a higher level of realism. The environment is simulated by mimicking the setup used to achieve single-molcule strong coupling at room temperature by Baumberg and collaborators[12] for the methylene blue molecule. In the present work, the azobenzene molecule is encapsulated by a cucurbit-7-uril molecule. The azobenzene is described at the same semiclassical level presented in previous Chapters, while the cucurbit-7-uril cage is treated at MM level. The cavity is realized by approximating the Nanoparticle on Mirror (NPoM, the experimental setup adopted by J. J. Baumberg's group) setup with layers of frozen MM gold atoms. The cavity is then filled with water molecules treated at MM level. The cavity mode is parametrized as described in Chapter 1.

In this work, I also simulate the direct and backward photoisomerization reaction of azobenzene taking into account a realistic excitation process. Here, I discuss how suitable cavity conditions can be found to enhance the photoisomerization quantum yield of the unfavoured $trans \rightarrow cis$ process, explaining the differences with the effect of strong coupling on the backward $cis \rightarrow trans$ reaction. The characterization of the mechanism leading to the enhanced quantum yield completely exploits post-processing tools I realized during the PhD activity to monitor the evolution of the wavepacket on the polaritonic potential energy surfaces. Through this means, I show how the strong coupling can quench non-reactive relaxation pathways via kinetic energy redistribution to other degrees of freedom. I comment on how such behaviour can only be observed when including all the molecular degrees of freedom. I realized supplementary movies in the same fashion of the ones presented in the previous chapter, and are hereby accessible via QRcode scan in the Supplemental Movies section. All the presented results have been originally produced during the PhD activity and

are reported in the followings as published article and supporting information. My personal contribution to this work covers all the implementations, calculations, partial devising of the analysis and the full development of the analysis tools, together with the drafting of the original paper. The article has been published in early 2020 on *Chem*, and was highlighted in a Preview.[118]

Chem

CellPress

Article

Strong Coupling with Light Enhances the Photoisomerization Quantum Yield of Azobenzene

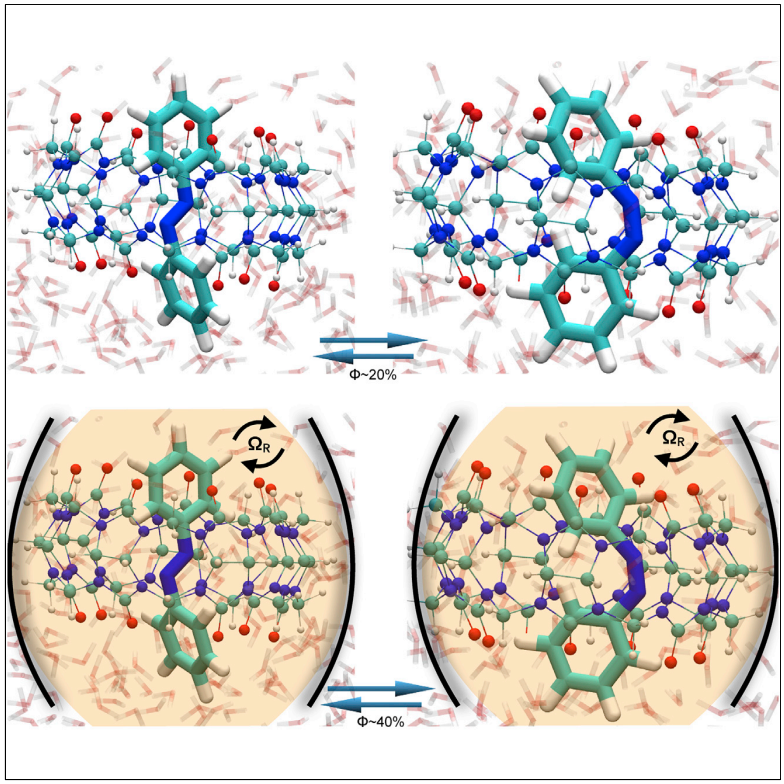

The traditional ways to control photochemical reactions range from chemical modifications to tuning the surrounding environment. Strong coupling between a molecule and light, achievable in resonant plasmonic cavities, provides an alternative toolbox to manipulate photochemistry. Here, by means of accurate quantum chemistry simulations, we show that it is possible to enhance the photoisomerization yield for azobenzene in a realistic setup with a mechanism that involves full complexity of the atomistic dynamics of the system.

Jacopo Fregoni, Giovanni Granucci, Maurizio Persico, Stefano Corni

giovanni.granucci@unipi.it (G.G.)
stefano.corni@unipd.it (S.C.)

HIGHLIGHTS

Simulation of a realistic polaritonic chemistry reaction in a realistic setup

Enhanced quantum yield predicted for azobenzene photoisomerization

Conditions to observe such enhancements are identified

Mechanism requires the high complexity of the atomistic dynamics of the system

Fregoni et al., Chem 6, 250–265
January 9, 2020
https://doi.org/10.1016/j.chempr.2019.11.001

Chem

CellPress

Article

Strong Coupling with Light Enhances the Photoisomerization Quantum Yield of Azobenzene

Jacopo Fregoni,[1,2] Giovanni Granucci,[3,*] Maurizio Persico,[3] and Stefano Corni[2,4,5,*]

SUMMARY

The strong coupling between molecules and photons in resonant cavities offers a new toolbox to manipulate photochemical reactions. Although the quenching of photochemical reactions in the strong coupling regimen has been demonstrated before, their enhancement has proven to be more elusive. Here, by means of a state-of-the-art approach, we show how the *trans*→*cis* photoisomerization quantum yield of azobenzene embedded in a realistic environment can be higher in polaritonic conditions than in the cavity-free case. We characterize the mechanism leading to such enhancement and discuss the conditions to push the photostationary state toward the unfavored reaction product. Our results provide a signature that the control of photochemical reactions through strong coupling can be extended from selective quenching to improvement of the quantum yields.

INTRODUCTION

The interaction between light and matter at the nanoscale is at the basis of a manifold of experimental applications in plasmonics,[1–4] single-molecule spectroscopies,[5,6] nanoprinting,[7] and nanocavity optics.[8–10] When light is sufficiently confined in micrometric or nanometric systems in the presence of one or more quantum emitters, its exchange of energy with the emitters becomes coherent and the system enters the strong coupling regimen.[11,12] Accordingly, the degrees of freedom of light and matter mix and the states of the system are described as hybrids between the two: the polaritons.[13,14] The first experimental realizations to pioneer the idea of controlling the chemical reactions through strong coupling of molecules with light made use of metallic cavities.[15,16] Later on, the achievement of strong coupling with plasmonic nanocavities at the single-molecule level at room temperature has been obtained with a nanoparticle on a mirror (NPoM) setup.[17,18] Such a setup has been recently improved with DNA origami for higher reproducibility.[19,20] The manifold of possibilities opened up by such experiments drove efforts to explore microcavity-based setups at low temperature, achieving longer lifetimes for the whole system.[21] Theoretical modeling followed immediately to survey the plethora of new possibilities offered by strong light-molecule coupling.[22,23] The high flexibility of the polaritonic properties has been assessed for both realized[20,24,25] and potential applications[13,26] giving rise to a new branch of chemistry[27]: the so-called polaritonic chemistry.[28]

When a resonant mode is coupled to electronic transitions, the molecules exhibit enhanced spontaneous emission at both the collective and single-molecule levels.[29–32] When the coupling is sufficiently strong, coherent energy exchange

The Bigger Picture

Strong coupling between molecules and light can be achieved in resonant cavities, giving rise to hybrid light-molecule states (polaritons). Chemistry in such states is different than the original photochemistry of the molecule. As such, polaritonic chemistry is emerging as a non-conventional approach to manipulate photochemical reactions, toward, for example, increasing reaction specificity or enhancing yields. Using accurate quantum chemistry multiscale simulations, we find that strong coupling can lead to enhanced photoisomerization yields for azobenzene in a realistic nanoplasmonic setup. Strong coupling acts on the motion of azobenzene atoms in the multi-dimensional space of internal coordinates, steering them away from unreactive pathways accessible instead in the traditional regimen. Our results show that the chemical complexity of molecules, rather than being a foe, can be turned into a friend in the strong coupling regimen, endowing polaritonic chemistry of additional potentialities.

occurs between light and photoactive molecules, potentially translating into modified photochemical properties.[15] The modifications to the potential energy surfaces (PESs) (through all the current work) driving different photophysical and photochemical behaviors are described by a basis of direct products of electronic and photonic states. Under this assumption, the states of the system are best described as hybrids between electronic and photonic.[12,14,33]

The possibility to shape the electronic states with quantum light inspired various groups to explore the role of strong light-molecule coupling in controlling photochemical processes. For collective effects, the focus has been on polariton formation in full quantum diatomic molecules[34] and several model dye molecules in a realistic environment.[35] At the single-molecule level, the non-adiabatic dynamics schemes developed allowed for the prediction of features arising on the PESs such as the creation of avoided crossings and light-induced conical intersections (CoIns).[13,36,37] Such features modify the shape of PESs, translating into a potentially different photochemical reactivity.[27,38–40] The possibility to enhance the yield of photochemical processes has been recently proven for energy transfer,[38,41] singlet fission,[42] and catalyzed reactions through vibrational strong coupling, obtained by exploiting remote catalysts.[43] For strong coupling with resonant optical frequencies, enhancement has only been suggested by calculations on model PESs[28,44] and neglecting the cavity losses and realistic non-radiative events.

As such events play a central role in the yields of photochemical reactions, the question remains if strong coupling can lead to a real enhancement of photochemical quantum yields in real molecules. Even more practically, the interest resides in the photostationary regimen and in determining whether the related concentration of products is enriched with respect to the standard reaction conditions. Here, by means of the state-of-the-art approach we devised,[45] we show that it is possible to identify conditions that lead to improved quantum yields and product-enriched photostationary states. By investigating azobenzene *trans*→*cis* photoisomerization in strong coupling, we compare to the zero-coupling case and highlight the differences between the two processes. Such a comparison allows us to propose an interpretation of the mechanism leading to the increased quantum yield for the *trans*→*cis* $\pi - \pi^*$ photoisomerization.

The model system we simulate is depicted in Figure 1 and mimics the experimental setup used by Baumberg and co-workers[17] for achieving strong coupling with a single methylene blue chromophore. The azobenzene molecules are hosted in a one-to-one arrangement by cucurbit-7-uril ring molecules, which are in turn adsorbed on a planar gold surface. In this arrangement, the azobenzene long axis is approximately perpendicular to the surface. This is relevant because the field polarization and the transition dipole for the S_0-S_1 and the S_0-S_2 transitions are all aligned in the same direction.[46] The cavity is completed by gold nanoparticles sitting on top of the cucurbituril ring and is much larger than the latter, so we simulate them as a second planar surface. Explicit water molecules fill the space between the gold layers (see Note S1).

RESULTS

Polaritons in Azobenzene

Before investigating the photochemical properties of molecules under strong coupling, we show how the coupling conditions affect the energy landscape in the

[1]Dipartimento di Scienze Fisiche, Informatiche, Matematiche, Università di Modena e Reggio Emilia, 41125 Modena, Italy

[2]Istituto di Nanoscienze, Consiglio Nazionale delle Ricerche CNR-NANO, 41125 Modena, Italy

[3]Dipartimento di Chimica e Chimica Industriale, Università di Pisa, 56124 Pisa, Italy

[4]Dipartimento di Scienze Chimiche, Università di Padova, 35131 Padova, Italy

[5]Lead Contact

*Correspondence: giovanni.granucci@unipi.it (G.G.), stefano.corni@unipd.it (S.C.)

https://doi.org/10.1016/j.chempr.2019.11.001

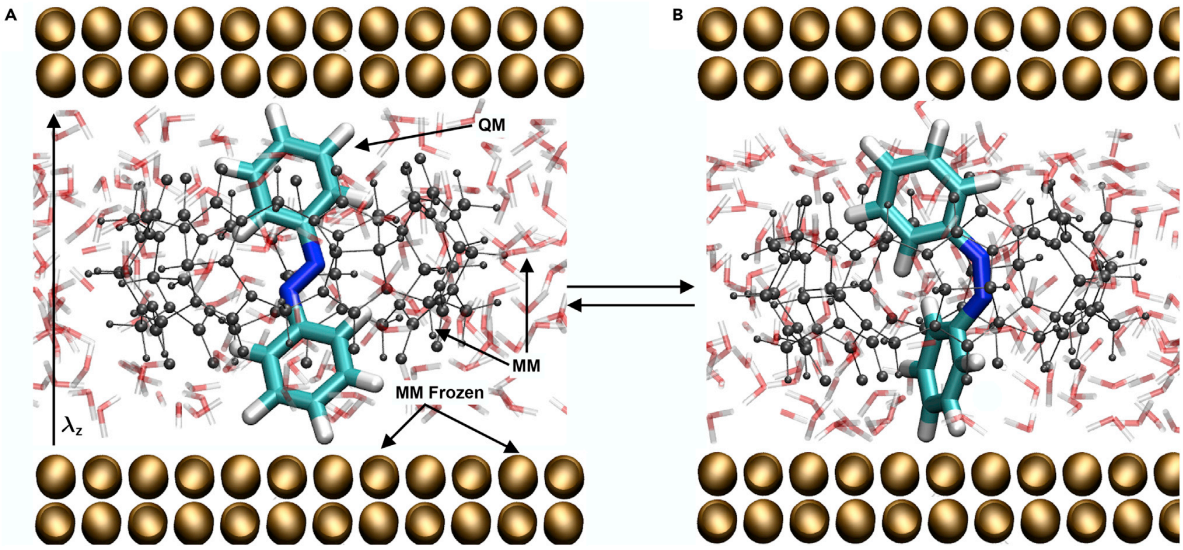

Figure 1. Simulated System

Snapshots of the simulated system mimicking a plasmonic nanocavity as the one reported by Baumberg and co-workers.[17] The molecule, here azobenzene in *trans* (A) or *cis* (B) configurations, is computed at QM level (see text and Experimental Procedures) and interacts with the MM environment by electrostatic embedding plus Lennard-Jones potentials. The environment is composed by cucurbit-7-uril (gray organic molecule cage) and gold layers (four layers on each side, frozen MM degrees of freedom), including also explicit water molecules. The cavity mode is polarized along $\boldsymbol{\lambda}_z$, and the sampling is run at room temperature.[47]

case of multiple electronic states. In this section, we aim only to provide an interpretative framework for the results of the next section, and hence the results presented in this section are computed without environment.

In Figure 2, we present two relevant cuts of the polaritonic PESs for the isolated azobenzene molecule, one along the CNNC dihedral and the other along the symmetric NNC bending (symNNC). In the former, all other degrees of freedom and also symNNC were optimized for the ground state. In the latter, the analogous constrained optimization was done for each symNNC value, except that CNNC was fixed at 165°, in order to show a clear cut of the polaritonic avoided crossing modifying the dynamics (notice that at the *trans* planar geometry the S_0,S_1 transition dipole moment vanishes). We shall exploit the PESs presented in this section to act as a qualitative and conceptual aid. By doing so, we introduce the framework to discuss the mechanism leading to the enhanced yield of the photoisomerization reaction under realistic environment.

Even in absence of environment, when a single molecule is strongly coupled with a cavity, polaritons drastically affect its PES.[12,13,45] The photochemical properties are, in turn, deeply affected by the shape of the polaritonic PESs. Aiming to thoroughly describe the molecule in the strong coupling regimen, we build the polaritonic Hamiltonian in the framework of a semiempirical wavefunction method[48]:

$$\hat{H}_{tot} = \hat{H}_{mol} + \hat{H}_{cav} + \hat{H}_{int}^{sc}. \qquad \text{(Equation 1)}$$

Here, $\hat{H}_{mol}$ is the semiempirical electronic Hamiltonian, $\hat{H}_{cav}$ is the quantized electromagnetic field Hamiltonian for an effective resonant mode set at optical

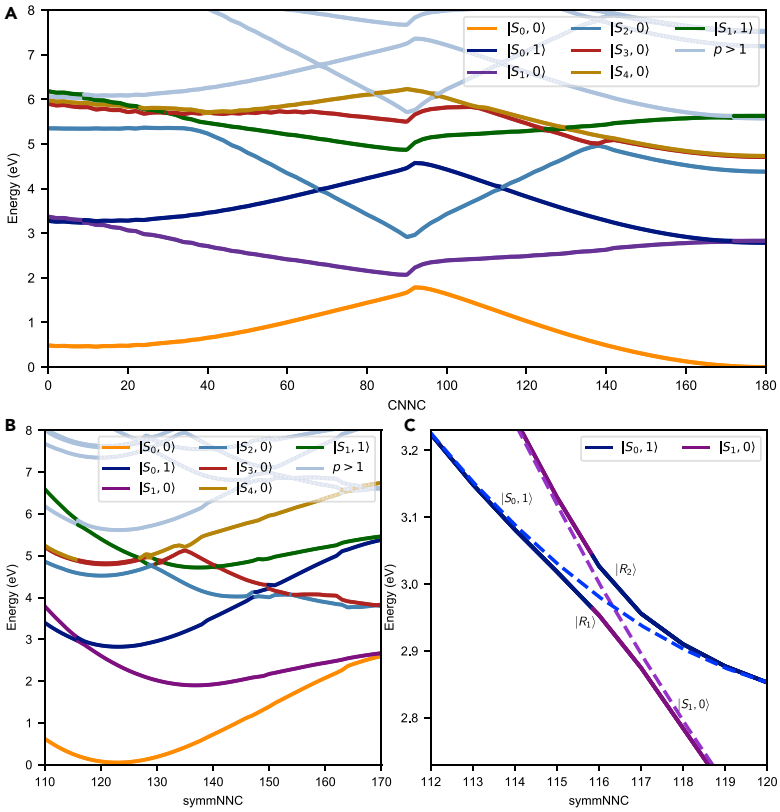

Figure 2. Polaritonic Potential Energy Curves of Azobenzene with Photon of 2.8 eV and Single-Photon Electric Field Strength E_{1ph} of 0.002 a.u

The polaritonic PESs are computed at the (A) CNNC coordinate while relaxing all the other degrees of freedom for the ground state and (B) symNNC coordinate with CNNC 165° and constrained optimization as before. Each polaritonic branch is colored depending on the uncoupled state that majorly composes the polariton at each geometry. (C) Detail of the strong coupling avoided crossing along the symNNC coordinate and between the $|S_0,1\rangle$ and $|S_1,0\rangle$ states where this feature gives rise to a different mechanism for the photoisomerization.

frequencies, and $\hat{H}_{int}^{sc}$ is the quantum interaction between light and molecule in a dipolar fashion:

$$\hat{H}_{int}^{sc} = E_{1ph}\sum_{n\neq n'}|n\rangle\boldsymbol{\lambda}\cdot\boldsymbol{\mu}(\boldsymbol{R})_{n,n'}\langle n'|(\hat{b}^{\dagger}+\hat{b}). \qquad \text{(Equation 2)}$$

E_{1ph} represents the magnitude of the single-photon electric field of the confined light mode, $\boldsymbol{\mu}_{n,n'}$ is the transition dipole moment between the electronic states, $\boldsymbol{\lambda}$ is the field polarization unit vector, and $\hat{b}^{\dagger}$ and $\hat{b}$ are the bosonic creation and annihilation operators. The nuclear motion is treated classically, using the surface-hopping approach[45] (see Experimental Procedures). By relying on a semiempirical wavefunction method, we provide a detailed description of the electronic structure at low computational cost. Such electronic structure method exploits a solid parameterization[49] of the semiempirical electronic Hamiltonian and has been previously validated against experimental data in a number of applications.[50–53]

To gain more insight on the features of the polaritonic PESs, we refer to the basis of uncoupled products of light and matter wavefunctions, given by the diagonalization

of $\widehat{H}_{mol} + \widehat{H}_{cav}$, labeled as $|n,p\rangle$. Here, n (e.g., S_0,S_1) is the electronic state index and p is the photon occupation number, either 0 or 1 in the present work. We consider a cavity photon of frequency 2.8 eV. Therefore, states with $p \geq 2$ lay at least 5.6 eV higher in energy than the ground state, i.e., more than 1 eV above our excitation window, which reaches up to 4.5 eV. Because of such a high energy difference, they cannot be populated during the dynamics, and therefore they are disregarded in our simulations of the photoisomerization dynamics (see Note S2). To clearly distinguish the uncoupled states in strong coupling and the electronic states in the zero-coupling frameworks, we refer to the set of uncoupled states $\{|n,p\rangle\}$ with the ket notation, e.g., $|S_0,1\rangle$ or $|S_1,0\rangle$, whereas the zero-coupling electronic states $\{n\}$ are named by the state label only, e.g., S_0, S_1. The polaritonic eigenstates of $\widehat{H}_{tot}$, labeled as $|R_k\rangle$, are expressed in the $|n,p\rangle$ basis:

$$\left|R_k\right\rangle = \sum_{n,p} D^k_{n,p} \left|n,p\right\rangle. \qquad \text{(Equation 3)}$$

The coefficients $D^k_{n,p}$ of the uncoupled states in the wavefunction provide a simple interpretation for the system under strong coupling. The states with $p = 0$ represent no free photon in the cavity, the states with $p = 1$ represent one free photon in the cavity, and so on. In turn, the time-dependent polaritonic wavefunction can be expressed in either the polaritonic or the uncoupled basis set:

$$\left|\Psi(t)\right\rangle = \sum_k C_k(t) \left|R_k\right\rangle = \sum_k C_k(t) \sum_{n,p} D^k_{n,p} \left|n,p\right\rangle. \qquad \text{(Equation 4)}$$

By the inclusion of the light-molecule interaction, a polaritonic avoided crossing or CoIn is originated where the uncoupled states would cross. In Figure 2, we show such crossings along two reactive coordinates: the torsion of the CNNC dihedral and the symNNC. Here, the states labeled as $p>1$ are included in the PESs' calculations, yet they are not included in the dynamics presented in the next section.

The Rabi splitting between the polaritonic states is proportional to the transition dipole moment between the electronic states at the correspondent crossing geometry for the uncoupled states through Equation 2. The magnitude of such splitting represents the coherent energy exchange rate between light and molecule in a confined system. In Figure 2C, we focus on the polaritonic avoided crossings laying in the *trans* region (CNNC 165°). We anticipate that such crossings deeply impact the photoisomerization mechanism of azobenzene, leading to enhanced *trans*→*cis* photoisomerization quantum yield.

Photochemistry on Polaritonic States: Tuning the Photostationary Equilibrium

In photoreversible processes, the ratio between the quantum yields of the direct and backward process determines the product yield Q at the photostationary state,[54] as shown in Equation 5

$$Q = \frac{[c]_\infty}{[c]_\infty + [t]_\infty} = \frac{J_{t\to c}}{J_{c\to t} + J_{t\to c}} = \frac{\varepsilon_t \Phi_{t\to c}}{\varepsilon_c \Phi_{c\to t} + \varepsilon_t \Phi_{t\to c}} \qquad \text{(Equation 5)}$$

where t and c refer to the *trans* and *cis* isomers, respectively, J is the reaction rate, ε is the molar extinction coefficient integrated over the excitation wavelength window, and Φ is the quantum yield. The quantities $[c]_\infty$ and $[t]_\infty$ are the asymptotic concentrations of the *cis* and *trans* isomers, respectively, which in this framework correspond to the *cis* and *trans* populations at the end of the dynamics. The ratio between the molar extinction coefficients depends on the excitation wavelength, and we shall assume $\varepsilon_t/\varepsilon_c = 7.9$ as determined by their integral average over the present

excitation interval from the experimental data of azobenzene in methanol.[54] Such a ratio impacts the position of the photostationary state, allowing it to shift selectively toward the *cis* and *trans* isomer depending on the irradiation wavelength. Nevertheless, the tunability is limited by the quantum yields of the individual processes, according to Equation 5. Aiming to manipulate the photostationary state position in azobenzene photoisomerization, we focus on improving the quantum yield of the unfavored process, namely the *trans*→*cis* photoisomerization.

To perform the polaritonic photoisomerization simulations, we exploit an on-the-fly surface-hopping approach[45,55–57] and take into account all the nuclear degrees of freedom of azobenzene. Within this framework, the nuclear wavepacket moving on the polaritonic PESs is mimicked by a swarm of independent classical nuclear trajectories (see Experimental Procedures).

To build the polaritonic states, we sought a field frequency to maximize the quantum yields for the $\pi - \pi^*$ *trans*→*cis* photoisomerization. We set the cavity resonant frequency to 2.80 eV, which allows modification of the crucial region of the first excited state at CNNC close to 180° (detailed in Figure 2C) and the surrounding geometries, i.e., the region of the PESs where the geometry of the molecule starts to partially twist but it is essentially *trans*. The coupling strength E_{1ph} is 0.002 au, corresponding to a splitting of ~100 meV with a transition dipole of ~1 a.u. for the present case, consistent with the observed 80–100 meV in the experiment by Baumberg and co-workers.[17] We sample the ground state distribution at thermostated[47] room temperature. For each sampled configuration, we mimic the excitation by near-UV light with a central wavelength of 313 nm (3.96 eV) and a full bandwidth of 1 eV. The excitation window is chosen to include the absorption spectral features corresponding to the first $\pi \rightarrow \pi^*$ transitions of *trans*- and *cis*-azobenzene, though a narrower excitation bandwidth centered at the same frequency yields the same results (see Note S1 and Figure 3). Upon absorption, the trajectories are vertically excited from the ground state to the polaritonic states. The excitation procedure is described in the Experimental Procedures section.[58] The polaritonic states initially populated are $|R_3\rangle$, $|R_4\rangle$, and $|R_5\rangle$ that correspond essentially to $|S_2, 0\rangle$, $|S_3, 0\rangle$, and $|S_4, 0\rangle$ in the Franck-Condon region, respectively. Their populations at time t = 0 are 0.76, 0.21, and 0.03, respectively. In the zero-coupling case, the initial populations of the corresponding S_2, S_3 are 0.78 and 0.22, whereas S_4 is empty.

The polaritonic non-adiabatic dynamics simulations results are reported in Figure 3 (see Videos S1 and S2 for the dynamics with strong and zero coupling along the reactive coordinates). The capability of strong coupling to affect photochemistry is strikingly evident in Figure 3A, where we compare the population of *trans* and *cis* isomers for the *trans*→*cis* photoisomerization process obtained by zero and strong coupling. Such populations are evaluated at each time step by counting the number of trajectories with a CNNC dihedral greater (*trans*) and smaller (*cis*) than 90°. The populations are then normalized to the total number of trajectories.

Remarkably, the *cis* formation is significantly more efficient for the strong coupling. This is one of the main results of the present work, as the enhancement of a realistic reaction via electronic strong coupling has not been reported so far. As a first step to analyze the mechanism driving such an increased yield of product, in Figure 3B, we plot the fraction of reactive trajectories (reaching CNNC<90°) for each starting state separately. Each of such individual processes in strong coupling (orange lines) is indeed more efficient than the corresponding one in zero coupling (purple lines). The strong coupling processes are on average slower than the zero-coupling case,

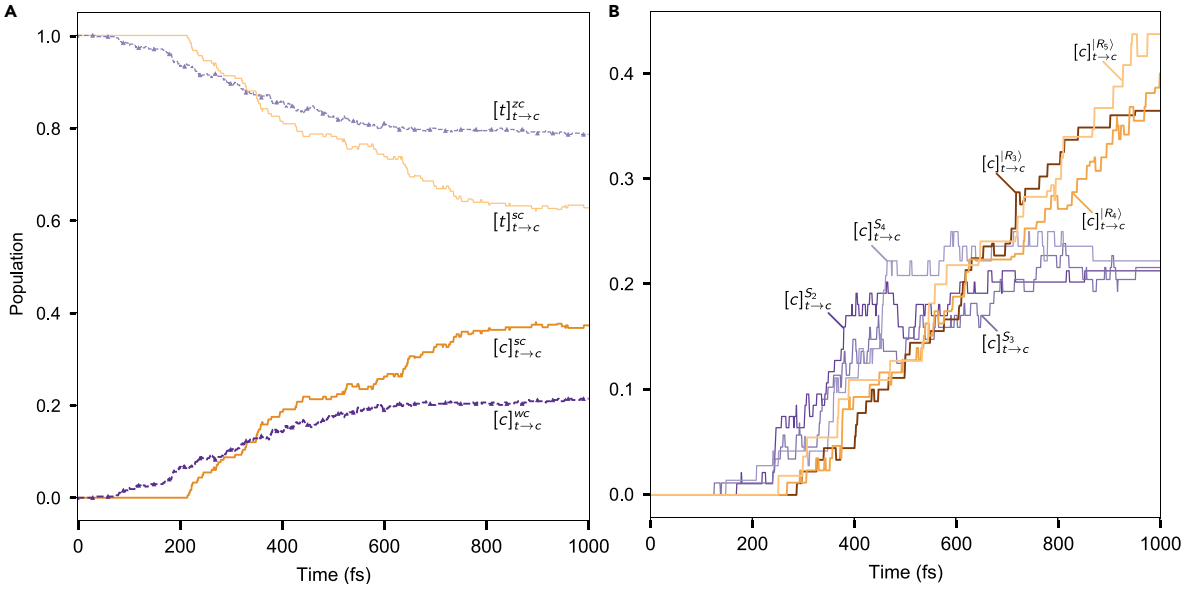

Figure 3. Product-Enriched *Trans*→*Cis* Photoisomerization of Azobenzene under Strong Coupling

(A) Populations of azobenzene *trans* (light) and *cis* (dark) isomers in the zero-coupling (purple) and strong-coupling (orange) cases for the *trans*→*cis* $\pi-\pi^*$ photoisomerization, computed with a photon energy E_{ph} of 2.8 eV and a coupling strength E_{1ph} equal to 0.002 au.

(B) Comparison between the *cis* formation for processes starting on different electronic or polaritonic states in zero coupling (purple-blue) and strong coupling (orange-red). The individual processes are investigated by running ~100 trajectories. For each pair of initial states in zero coupling and strong coupling, the same sampling is used, i.e., $|R_3\rangle$ with S_2, $|R_4\rangle$ with S_3, and $|R_5\rangle$ with S_4.

i.e., the torsion around the N=N double bond is delayed, together with the decay to the ground state (Figures 4A and 4B). Although paradoxically contrasting with the higher yields observed with respect to the zero-coupling case, the slower dynamics offers a first hint to explain the change in the mechanism brought about by the strong coupling regimen, as detailed later in this work (see Video S3 for an example of the dynamics along a reactive trajectory).

The factor capable of both slowing the kinetics and increasing the quantum yields in polaritonic processes is the existence of the $|S_0,1\rangle$ state and its coupling with $|S_1,0\rangle$. Aiming to characterize the nature of the polaritonic states involved in the dynamics and to obtain a more meaningful comparison with the zero-coupling case, it is convenient to investigate the processes on the uncoupled state basis. To this aim, Figure 4A compares the uncoupled states' populations (full lines) with those of the corresponding states in the zero coupling simulation (dashed lines, circle markers). Here, the population of the $|S_2,0\rangle$, $|S_3,0\rangle$, and $|S_4,0\rangle$ manifold is represented as P_{sum} to highlight the relevant processes. The first striking difference is that the S_1 state in the zero-coupling case is populated quicker than in the strong-coupling case. In addition, a longer permanence of the trajectories on the $|S_1,0\rangle$ state is observed in strong coupling, mainly because part of the population oscillates between $|S_1,0\rangle$ and $|S_0,1\rangle$ (see Table S1). Consequently, $|S_1,0\rangle$ (strong coupling) can be found still populated at times where S_1 (zero coupling) is already decayed (see Figure 4A). The role of the $|S_0,1\rangle$ state in delaying the depletion of $|S_1,0\rangle$ is to act as a supplementary reservoir for the $|S_1,0\rangle$ population during the first 400 fs. In fact, nonradiative electronic state decays from $|S_0,1\rangle$ are blocked given that the molecule is in its ground state.

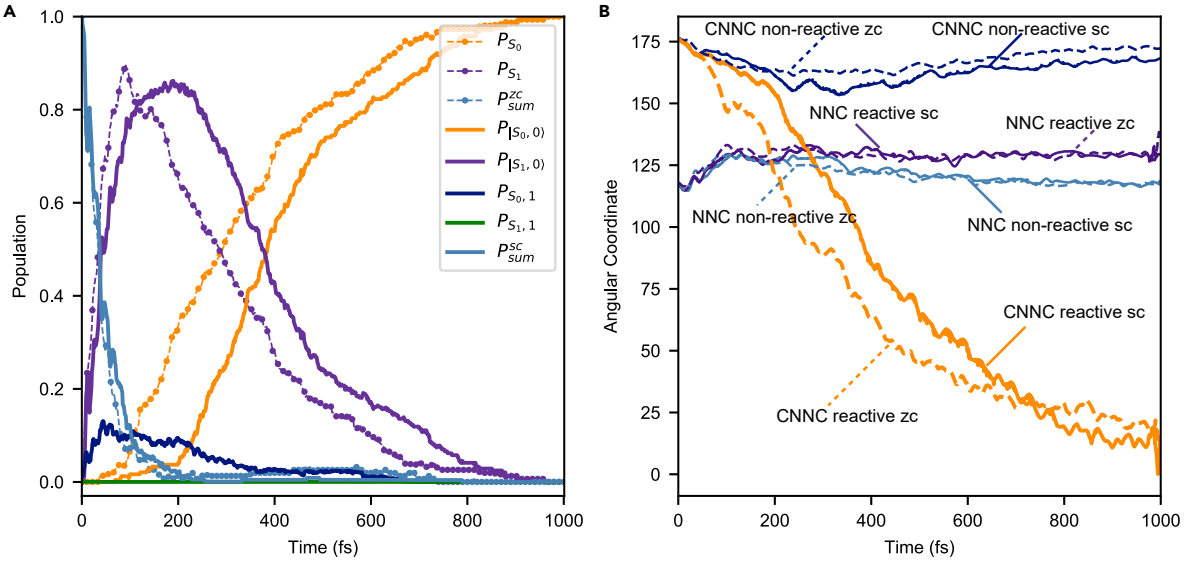

Figure 4. Population and Geometrical Relaxation Dynamics Upon Photoisomerization

(A) Population evolution on the uncoupled states in strong coupling (full lines), directly compared with the zero-coupling population evolution involving the same states (dashed lines with markers). The strong-coupling population evolution is slowed by the presence of $|S_0, 1\rangle$ (blue full line), which is transiently populated during the dynamics.

(B) CNNC and NNC angles averaged over the reactive and non-reactive trajectories in zero coupling (dashed lines) and strong coupling (full lines), computed as a function of time. See Note S4 for the corresponding *cis*→*trans* plot.

The shape of the $|R_1\rangle$ and $|R_2\rangle$ PESs (see Figure 2) in the transoid region explains why the torsion is initially delayed in the strong-coupling case. Most of the hops that populate these two states go from $|R_3\rangle$ to $|R_2\rangle$ (i.e., essentially $|S_2, 0\rangle \rightarrow |S_1, 0\rangle$). Subsequently, more transitions back and forth between $|R_1\rangle$ and $|R_2\rangle$ occur because of the avoided crossing involving $|S_1, 0\rangle$ and $|S_0, 1\rangle$ (see Table S1). The upper surface, belonging to $|R_2\rangle$, is less favorable than that of $|R_1\rangle$ to the torsional and the symNNC motions (see Figure 2A), i.e., to the decrease of the CNNC dihedral and to the increase of both NNC angles. By partially populating $|R_2\rangle$, the progress along the reaction coordinate CNNC and the symNNC vibrational excitation are both hindered.

The association of slower torsional motion and slower $|S_1, 0\rangle$ decay with higher $\Phi_{t\rightarrow c}$ quantum yield, which characterizes the strong coupling with respect to the zero-coupling case, is not so intuitive. Still, this effect is reminiscent of the same joint trends observed in simulations of the *trans*→*cis* photoisomerization in solvents of increasing viscosity, in agreement with experimental quantum yields and fluorescence lifetimes for the field-free case.[50] A similar hindrance of the motion along the reaction coordinate, caused by strong coupling, was highlighted by Galego et al.[40] by full quantum simulations but unavoidably led to suppression of the photoisomerization because the one-dimensional model cannot account for the competition between radiationless electronic transitions and geometry relaxation. Using a different one-dimensional model, Herrera and Spano showed how strong coupling can instead increase the electron transfer rate in disordered molecular ensembles.[38]

The reason why a slower progress along the reaction coordinate leads to a higher quantum yield for the realistic model we are using here can be found in the shape of the S_1, S_0 crossing seam. Note that, after leaving the surroundings of the

Franck-Condon region by twisting the N=N bond and/or increasing the symNNC angles, $|R_1\rangle$ becomes almost pure $|S_1,0\rangle$. In the new region, its energy gets closer to that of $|R_0\rangle$: a crossing seam between the two PESs exists. Even more, the crossing seam is practically unaltered with respect to the zero-coupling case (see Note S4 of the present work and Figure 1 in Cusati et al.[50]). The energy minimum of such a seam (optimized CoIn) is found at a twisted geometry (CNNC = 95°), the seam is also accessible and coincides with the global minimum in S_1, therefore, it is accessible even in the absence of vibrational excitation. However, the crossing seam can also be approached at larger CNNC values by opening the symNNC bond angles, as indicated by our semiempirical PESs and confirmed by accurate *ab initio* calculations.[59,60] At planar transoid geometries the seam is slightly higher in energy than the Franck-Condon point and much higher than the S_1 minimum, so a strong excitation of the symNNC mode is needed to reach it. Recent work based on time-resolved spectroscopy has demonstrated the importance of the symNNC vibration, especially in the case of the $S_0 \rightarrow S_2$ excitation.[60]

In zero coupling, the symNNC bending mode is excited once the S_1 state is populated by internal conversion from S_2, explainable by comparing the equilibrium values of the NNC angles in S_1 and in S_0/S_2 (132° versus 118° and 110° at planar geometries). This excitation results in the opening of the symNNC angle and, in turn, promotes the internal conversion of S_1 to the ground state by making the seam accessible at transoid regions, resulting in a rather low *trans*→*cis* photoisomerization quantum yield. On the contrary, in strong coupling, the hindering of the twisting and bending motions discussed above decreases the extent of symNNC excitation. In fact, with more time spent at transoid geometries, symNNC is also quenched by vibrational energy transfer to other internal modes and the medium. As such, the detrimental effect of the symNNC on the *trans*→*cis* photoisomerization quantum yield is partially suppressed. The essential role played by (at least) one additional vibrational mode other than the reaction coordinate shows the limitations of one-dimensional models, which might capture some essential features of the dynamics[40] but fail to faithfully describe molecules of useful complexity. Such limitation becomes critical in strong coupling as the PESs and the wavepacket motion are altered by the coupling along all modes. The present case gives a clear example of the need to resort to multi-dimensional models: the trajectories are steered away from the highly excited symNNC bending (zero coupling) toward the less excited symNNC bending (strong coupling). The alternative pathway due to strong coupling along a secondary coordinate is mainly reflected in the motion along the main isomerization coordinate, resulting in a higher yield pathway not predictable through the one-dimensional models.

The behavior hereby described is well highlighted in Figure 5, where we compare the distribution of the geometrical coordinates at the moment of the S_1-S_0 ($|R_1\rangle - |R_0\rangle$) hoppings in zero coupling (strong coupling), depicted for the non-reactive and reactive trajectories in the upper and lower panels, respectively. Additional data, including the hopping times, are also provided in Table S1. The reactive trajectories are shown to hop at CNNC closer to 90°, whereas the non-reactive ones count many hops at large values of both CNNC and symNNC. Moreover, a significantly wider distribution of symNNC is observed for the zero-coupling case (purple), a signature that the symNNC is more excited in zero coupling than in strong coupling. Large symNNC (symNNC >150°) in zero coupling is accompanied by many hops at CNNC >130°, confirming that the excitation of the symmetric NNC vibration promotes the internal conversion at transoid geometries. The narrower interval of symNNC for the strong-coupling case, instead, causes the trajectories to

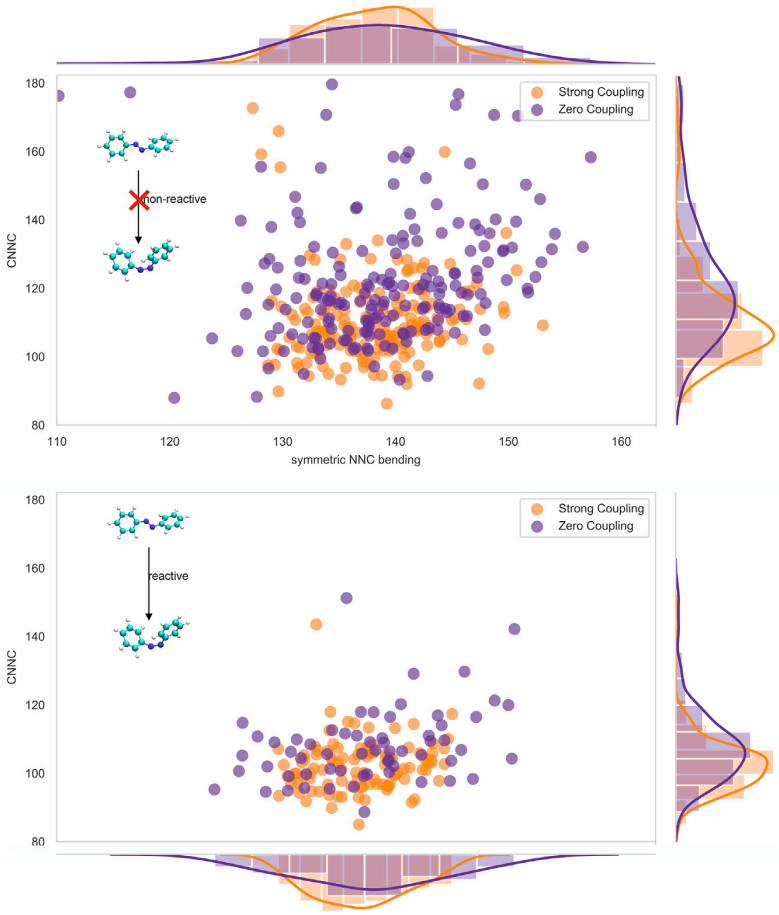

Figure 5. Non-reactive and Reactive Photoisomerization Dynamics for Strong Coupling and Zero Field upon $S_1 - S_0$ Hopping

Non-reactive (upper) and reactive (lower) distributions of the reactive coordinates (symNNC and CNNC), computed upon the $S_1 - S_0$ hops for the zero-field case (purple) and $|R_1\rangle - |R_0\rangle$ for the strong-coupling case (orange). The distributions, in particular the non-reactive one, show that high excitation of symNNC causes hops at less twisted CNNC values, resulting in a lower photoisomerization yield in zero coupling with respect to strong coupling.

hop (on the average) at more twisted geometries, accompanied by a higher probability of successful photoconversion to the *cis* isomer.

Until now, we have shown that the coherent exchange of energy between light and matter impacts both the kinetics of the dynamics and the mechanism, resulting in a non-trivial trend in the quantum yields. To verify the consequence of this result on the photostationary ratio of *cis and trans* populations, the *cis*→*trans* photoreaction at the same excitation frequency must be simulated as well. We found that such a process in strong coupling shows the same yield with respect to the zero-coupling case, $\Phi_{c\to t} = 58\%$ and $\Phi_{c\to t} = 61\%$, respectively. This is consequent to the more favorable slope of the PESs in the *cis* side, which also makes the *cis*→*trans* photoisomerization quantum yield insensitive to environmental hindrances.[50,51,53] Going from the *cis* to the *trans* isomer, such steep PESs make the effect of the $|S_0, 1\rangle$ state

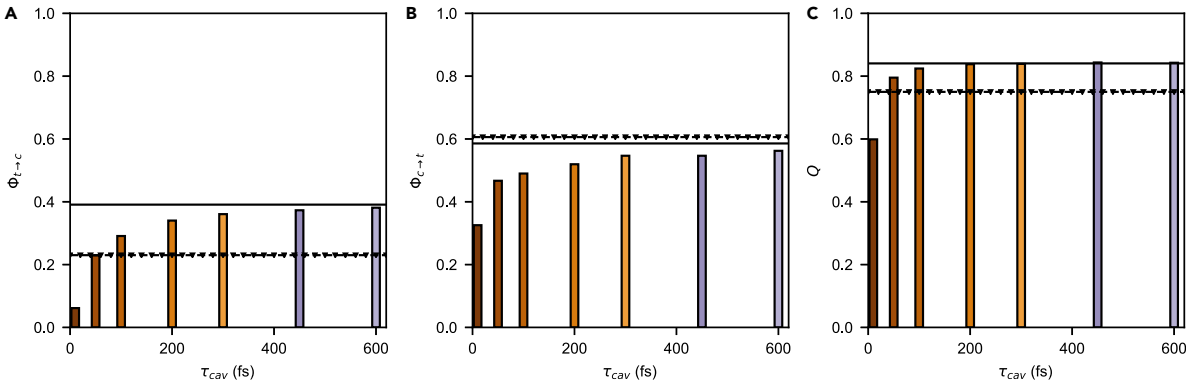

Figure 6. Effect of Cavity Losses on the Photostationary State

Quantum yields comparison for the (A) *trans*→*cis* and (B) *cis*→*trans* isomerization in strong coupling as a function of the cavity photon lifetime. The black dotted line is the zero-coupling limit, whereas the full line is the lossless cavity limit. The transient role of $|S_0, 1\rangle$ is reflected by lower quantum yields for very lossy cavities with respect to the zero-coupling case. (C) The product yield at the photostationary state computed by taking into account the forward and backward reaction. The molar extinction coefficients are obtained by their integral average over the present excitation interval, starting from the experimental data reported by Vetrakova and collaborators.[54] The product yield Q at the photostationary state is shifted toward the strong coupling limit for τ_{cav} greater than 50 fs.

in the dynamics almost irrelevant, resulting in the *cis*→*trans* photoisomerization occurring on much shorter timescales (150 fs, see Note S4) than in the *trans*→*cis* photoisomerization. Therefore, the substantial rise of the yields in the *trans*→*cis* process is sufficient to push the photostationary state toward the *cis* isomer.

When the system is in its free-photon state $|n, 1\rangle$, a loss of the photon can occur (e.g., by leakage from the cavity or absorbed by the cavity walls). As a consequence, the coherent exchange between light and matter is disrupted and the molecule collapses from a mixture of $|n', 0\rangle$ and $|n, 1\rangle$ states to $|n, 0\rangle$ only (see Experimental Procedures).

To test how robust the results seen above are with respect to photonic losses in the resonant cavity, we simulate the *trans*→*cis* and *cis*→*trans* photoisomerization processes in the presence of a finite cavity lifetime τ_{cav} and compare the so-obtained quantum yields to the zero-coupling case (see Figure 6). The photostationary state yield of *cis* product exceeds the zero-coupling one for $\tau_{cav} \geq 50$ fs (Figure 6A). Remarkably, this time is much shorter than the typical photoisomerization timescale, whereas intuitively one would expect that cavity lifetimes comparable to the photoisomerization time are needed to observe enhanced reactions. The photoisomerization timescales are longer than the permanence time of the trajectories on $|S_0, 1\rangle$, which is the only $|n, 1\rangle$ state with a non-negligible population at any time. Although the decay to the ground state and photoisomerization take around 800 fs to be completed, the average permanence time in $|S_0, 1\rangle$ can be estimated to about 35 fs from its time-dependent population. We see then why a photonic loss timescale much shorter than the timescale of the whole photochemical process is compatible with the observation of strong coupling effects. Below τ_{cav} = 100 fs, however, the *trans*→*cis* conversion yield is quite sensitive to cavity lifetime. On the other hand, the *cis*→*trans* process is less affected because of the more favorable slope of the PESs and faster photoisomerization dynamics (see Figure 2 and Note S4).

DISCUSSION

By building the polaritonic states of azobenzene, we have shown how the molecular complexity can be taken into account for a single molecule strongly coupled to a resonator. The inclusion of a detailed treatment for the molecule and its environment allowed us to investigate the shape of single-molecule polaritons when a manifold of excited states are involved in the strong coupling.

We have shown that strong coupling deeply affects the dynamical processes taking place on polaritonic PESs. In particular, we have found a remarkable increase in the quantum yield of the $\pi - \pi^*$ *trans*→*cis* photoisomerization due to subtle changes in the mechanism: the shape of the polaritonic PESs and the time spent in the one-photon states bring about a lower degree of excitation of the symNNC vibration, which is the main cause of early decay from the S_1 state in zero-coupling conditions. As a result, under strong coupling more molecules reach a torsion of the N=N bond closer to *cis* before relaxing to the ground state and thus photoisomerize with a higher probability. By taking into account the backward reaction (*cis*→*trans*), such an effect results in an increase of the photostationary concentration of the *cis* isomer.

Through the simulation of a realistic system, i.e., by including the effects of environment and cavity losses, we could estimate a minimum cavity lifetime of 50 fs to observe a shift of the photostationary equilibrium toward higher *trans*→*cis* photoconversions. Although currently the lifetimes of typical plasmonic nanocavities do not exceed the 10 fs, new experiments are actively devising prototypical setups to achieve high reproducibility[17,19,20] and longer lifetimes for these systems[21,61] at the single-molecule level. The quickly growing interest in polaritonic applications bodes well for polaritonic devices to be exploited in real-life polaritonic chemistry.

Our results show promising possibilities in this field. Among them, the enhancement of the quantum yields and photostationary concentrations in experimentally achievable systems opens up a pathway toward a real control of photochemical reactions (i.e., quenching and enhancement). Concerning the role of polaritons in the photochemistry of single molecules, we think that the physics of polariton-mediated reactivity is far from being thoroughly investigated. Among the yet-to-be-explored possibilities, we mention multistate and bielectronic polaritonic processes, such as photoreactions mediated by excitation transfer.

EXPERIMENTAL PROCEDURES

Strong Coupling Hamiltonian

The Hamiltonian describing the system is given in Equation 1. Aiming to include all the degrees of freedom of azobenzene, we exploit a semiempirical Austin model 1 (AM1) Hamiltonian reparametrized for the first few electronic excited states of azobenzene.[49] In addition, it includes the molecular interaction with the environment (see next section). The basis on which we build the polaritonic states is the set of electronic-adiabatic singlets $\{n\}$, from S_0 to S_4. The cavity Hamiltonian of the quantized electromagnetic field is:

$$\hat{H}_{cav} = \hbar\omega_{cav}\left(\hat{b}^{\dagger}\hat{b} + \frac{1}{2}\right) \qquad \text{(Equation 6)}$$

where ω_{cav} is the resonator frequency and $\hat{b}^{\dagger}$ and $\hat{b}$ are the bosonic creation and annihilation operators. As reported in the main text, the eigenvectors of the non-interacting Hamiltonian $\hat{H}_{mol} + \hat{H}_{cav}$ constitute the uncoupled state basis $\{|n, p\rangle\}$. To obtain the polaritonic states (Equation 4) and energies, we selected a subset

of states $|n,p\rangle$ of interest, in which we performed a confidence interval (CI) calculation including the dipolar light-molecule interaction at QM level (Equation 2), working in the coulomb gauge and long wavelength approximation. The stability of the dipolar approximation has been proven to break up when reaching high couplings.[62–65] To prove the robustness of such approximation in the current case, test calculations have been performed as in the previous work[45] (see Note S3).

Inclusion of the Environment

The environment is included at quantum mechanics/molecular mechanics (QM/MM) level interfaced with the electronic semiempirical Hamiltonian. The molecular Hamiltonian for the system is partitioned as[66]:

$$\hat{H}_{mol} = \hat{H}_{QM} + \hat{H}_{QM/MM} + \hat{H}_{MM}. \qquad \text{(Equation 7)}$$

The QM part is composed by the azobenzene molecule and the MM part is composed by the cucurbit-7-uril molecule (150 atoms), 710 water molecules, and eight frozen layers of gold encapsulating the system (418 atoms each, only van der Waals interactions). The force field used to evaluate the MM part is all-atom optimized potentials for liquid simulations (OPLS-AA) contained in the TINKER code.[67] The QM/MM interactions are modeled by electrostatic embedding plus Lennard-Jones atom-atom potentials[53,68,69] (see Note S1).

Surface Hopping on Polaritonic States

After building the molecule embedded in the environment and optimizing the geometry at MM level, the equilibrium trajectory is run on the ground state by QM/MM dynamics. At the end of such dynamics, a few hundred of the initial conditions (nuclear phase space point and polaritonic or electronic state) are extracted by evaluating the transition probability from the ground state to the S_2,S_3, and S_4 electronic states (zero coupling) or $|R_3\rangle, |R_4\rangle, |R_5\rangle$ polaritonic states (strong coupling). Both the zero coupling and strong coupling states are excited within the same energy window, i.e., centered at 3.96 eV (from 3.46 to 4.46 eV). More details can be found in Note S1.

The non-adiabatic molecular dynamics is performed by exploiting the direct trajectory surface-hopping approach.[55] A few hundred classical nuclear trajectories (230 to 270) are computed on the fly on the polaritonic PESs independently. The hopping probability between the states is a modified version of Tully's fewest switches.[70] The modifications added take into account the strong coupling contributions[45] and the decoherence corrections needed to properly describe the decoupling of wavepackets traveling on different states.[56]

As usual in surface hopping, the population of a polaritonic state $|R_m\rangle$ is represented by the fraction of trajectories evolving on $|R_m\rangle$ (called the "current" state) at the given time. Consistently, the population of unmixed states $|n,p\rangle$, shown in Figure 4A, are obtained by averaging $|D^m_{n,p}|^2$ over the full swarm of trajectories, where $|R_m\rangle$ is again the current state.

Cavity Losses

The decay probability to account for cavity losses is evaluated through a stochastic approach. In particular, it is taken to be proportional to the square of the coefficients of the uncoupled states $|n,p\rangle$, with $p>0$ ($p=1$ in the present work), composing the time-dependent polaritonic wavefunction (see Equation 4):

$$P_{loss} = \sum_{n,p\geq 1}^{n_{st}} \frac{1}{\tau_{cav}} \Delta t \left| \sum_m C_m D^m_{n,p} \right|^2 = \sum_{n,p\geq 1}^{n_{st}} P_{|n,p\rangle}. \qquad \text{(Equation 8)}$$

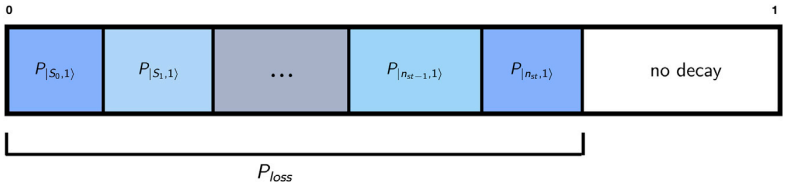

Figure 7. Algorithm to Include the Photon Loss Probability
Interval subdivision to evaluate from which state the photon is lost.

Here, τ_{cav} denotes the cavity lifetime while Δt is the integration time step. The decay probabilities referred to each state are indicated as $P_{|n,1\rangle}$, and n_{st} denotes the total number of electronic states included in the calculation. A uniform random number is generated between 0 and 1 and compared with the above interval. A check if the random number falls in any subinterval up to $P_{|n_{st},1\rangle}$ is performed (see Figure 7). If that is the case, the photon is lost from $|n',1\rangle$. The decay operator $\widehat{D}_{n'}$ is then applied to the polaritonic wavefunction:

$$\widehat{D}_{n'}|\Psi\rangle = |n',0\rangle\langle n',1|\Psi\rangle. \qquad \text{(Equation 9)}$$

The arrival state $|F\rangle$ is determined by taking the adiabatic state, which has the largest overlap $\langle n',0|F\rangle$ with the electronic state $|n',0\rangle$. The dynamics is then resumed by taking $|F\rangle$ as the new current state. We, hereby, point out that, for our current work, the decay always occurs from the $|S_0,1\rangle$ state, as it is the only state with $p>0$ with a non-negligible population during the dynamics. Even more, the arrival state is always $|R_0\rangle$, as it is almost purely $|S_0,0\rangle$ at all the relevant geometries (see Note S2). More generally, the wavefunction after the jump should be written as an electronic wavepacket, maintaining the possible electronic coherence present within the $p>0$ manifold.

DATA AND CODE AVAILABILITY

The calculations were based on a locally modified version of MOPAC2002 and TINKER and are available from G.G. and M.P. upon reasonable request. The analysis and the Supplemental Videos are based on *ad-hoc* tools which are available from J.F. upon request.

SUPPLEMENTAL INFORMATION

Supplemental Information can be found online at https://doi.org/10.1016/j.chempr.2019.11.001.

ACKNOWLEDGMENTS

J.F. and S.C. acknowledge funding from the ERC under the grant ERC-CoG-681285 TAME- Plasmons. G.G. and M.P. acknowledge funding from the University of Pisa, PRA 2017 28 and PRA 2018 36.

AUTHOR CONTRIBUTIONS

S.C. initiated this project; J.F., G.G., M.P., and S.C. designed the investigation; J.F. performed the calculations; all the authors contributed to the analysis of results and writing of the paper.

DECLARATION OF INTERESTS

The authors declare no competing interests.

Received: July 16, 2019
Revised: September 27, 2019
Accepted: October 31, 2019
Published: November 21, 2019

REFERENCES AND NOTES

1. Fang, Y., and Sun, M. (2015). Nanoplasmonic waveguides: towards applications in integrated nanophotonic circuits. Light: Sci. Appl. *4*, e294.

2. Dahlin, A.B., Wittenberg, N.J., Höök, F., and Oh, S.H. (2013). Promises and challenges of nanoplasmonic devices for refractometric biosensing. Nanophotonics *2*, 83–101.

3. Stockman, M.I. (2008). Ultrafast nanoplasmonics under coherent control. New J. Phys. *10*, 025031.

4. Savage, K.J., Hawkeye, M.M., Esteban, R., Borisov, A.G., Aizpurua, J., and Baumberg, J.J. (2012). Revealing the quantum regime in tunnelling plasmonics. Nature *491*, 574–577.

5. Stockman, M.I., Kling, M.F., Kleineberg, U., and Krausz, F. (2007). Attosecond nanoplasmonic-field microscope. Nat. Photonics *1*, 539–544.

6. Punj, D., Mivelle, M., Moparthi, S.B., van Zanten, T.S., Rigneault, H., van Hulst, N.F., García-Parajó, M.F., and Wenger, J. (2013). A plasmonic 'antenna-in-box' platform for enhanced single-molecule analysis at micromolar concentrations. Nat. Nanotechnol. *8*, 512–516.

7. Barner-Kowollik, C., Bastmeyer, M., Blasco, E., Delaittre, G., Müller, P., Richter, B., and Wegener, M. (2017). 3D Laser micro- and nanoprinting: challenges for chemistry. Angew. Chem. Int. Ed. Engl. *56*, 15828–15845.

8. Taminiau, T.H., Stefani, F.D., Segerink, F.B., and van Hulst, N.F. (2008). Optical antennas direct single-molecule emission. Nat. Photonics *2*, 234–237.

9. Taminiau, T.H., Stefani, F.D., and van Hulst, N.F. (2011). Optical nanorod antennas modeled as cavities for dipolar emitters: evolution of sub- and super-radiant modes. Nano Lett. *11*, 1020–1024.

10. Hugall, J.T., Singh, A., and van Hulst, N.F. (2018). Plasmonic cavity coupling. ACS Photonics *5*, 43–53.

11. Jaynes, E.T., and Cummings, F.W. (1963). Comparison of quantum and semiclassical radiation theories with application to the beam maser. Proc. IEEE *51*, 89–109.

12. Flick, J., Ruggenthaler, M., Appel, H., and Rubio, A. (2017). Atoms and molecules in cavities, from weak to strong coupling in quantum-electrodynamics (qed) chemistry. Proc. Natl. Acad. Sci. USA *114*, 3026–3034.

13. Galego, J., Garcia-Vidal, F.J., and Feist, J. (2015). Cavity-induced modifications of molecular structure in the strong-coupling regime. Phys. Rev. X *5*.

14. Neuman, T., Esteban, R., Casanova, D., García-Vidal, F.J., and Aizpurua, J. (2018). Coupling of molecular emitters and plasmonic cavities beyond the point-dipole approximation. Nano Lett. *18*, 2358–2364.

15. Schwartz, T., Hutchison, J.A., Genet, C., and Ebbesen, T.W. (2011). Reversible switching of ultrastrong light-molecule coupling. Phys. Rev. Lett. *106*, 196405.

16. Hutchison, J.A., Schwartz, T., Genet, C., Devaux, E., and Ebbesen, T.W. (2012). Modifying chemical landscapes by coupling to vacuum fields. Angew. Chem. Int. Ed. Engl. *51*, 1592–1596.

17. Chikkaraddy, R., de Nijs, B., Benz, F., Barrow, S.J., Scherman, O.A., Rosta, E., Demetriadou, A., Fox, P., Hess, O., and Baumberg, J.J. (2016). Single-molecule strong coupling at room temperature in plasmonic nanocavities. Nature *535*, 127–130.

18. Kongsuwan, N., Demetriadou, A., Chikkaraddy, R., Benz, F., Turek, V.A., Keyser, U.F., Baumberg, J.J., and Hess, O. (2018). Suppressed quenching and strong-coupling of Purcell-enhanced single-molecule emission in plasmonic nanocavities. ACS Photonics *5*, 186–191.

19. Chikkaraddy, R., Turek, V.A., Kongsuwan, N., Benz, F., Carnegie, C., van de Goor, T., de Nijs, B., Demetriadou, A., Hess, O., Keyser, U.F., and Baumberg, J.J. (2018). Mapping nanoscale hotspots with single-molecule emitters assembled into plasmonic nanocavities using DNA origami. Nano Lett. *18*, 405–411.

20. Ojambati, O.S., Chikkaraddy, R., Deacon, W.D., Horton, M., Kos, D., Turek, V.A., Keyser, U.F., and Baumberg, J.J. (2019). Quantum electrodynamics at room temperature coupling a single vibrating molecule with a plasmonic nanocavity. Nat. Commun. *10*, 1049.

21. Wang, D., Kelkar, H., Martin-Cano, D., Utikal, T., Götzinger, S., and Sandoghdar, V. (2017). Coherent coupling of a single molecule to a scanning Fabry-Perot microcavity. Phys. Rev. X *7*, 1–8.

22. Flick, J., Rivera, N., and Narang, P. (2018). Strong light-matter coupling in quantum chemistry and quantum photonics. Nanophotonics *7*, 1479–1501.

23. Ribeiro, R.F., Martínez-Martínez, L.A., Du, M., Campos-Gonzalez-Angulo, J., and Yuen-Zhou, J. (2018). Polariton chemistry: controlling molecular dynamics with optical cavities. Chem. Sci. *9*, 6325–6339.

24. Hutchison, J.A., Liscio, A., Schwartz, T., Canaguier-Durand, A., Genet, C., Palermo, V., Samorì, P., and Ebbesen, T.W. (2013). Tuning the work-function via strong coupling. Adv. Mater *25*, 2481–2485.

25. Fontcuberta i Morral, A., and Stellacci, F. (2012). Light-matter interactions: ultrastrong routes to new chemistry. Nat. Mater *11*, 272–273.

26. Zhang, Y., Meng, Q.S., Zhang, L., Luo, Y., Yu, Y.J., Yang, B., Zhang, Y., Esteban, R., Aizpurua, J., Luo, Y., et al. (2017). Sub-nanometre control of the coherent interaction between a single molecule and a plasmonic nanocavity. Nat. Commun. *8*, 15225.

27. Bennett, K., Kowalewski, M., and Mukamel, S. (2016). Novel photochemistry of molecular polaritons in optical cavities. Faraday Discuss *194*, 259–282.

28. Feist, J., Galego, J., and Garcia-Vidal, F.J. (2018). Polaritonic chemistry with organic molecules. ACS Photonics *5*, 205–216.

29. Strauf, S. (2010). Lasing under strong coupling. Nat. Phys. *6*, 244–245.

30. Sawant, R., and Rangwala, S.A. (2017). Lasing by driven atoms-cavity system in collective strong coupling regime. Sci. Rep. *7*, 11432.

31. Du, W., Zhang, S., Shi, J., Chen, J., Wu, Z., Mi, Y., Liu, Z., Li, Y., Sui, X., Wang, R., et al. (2018). Strong exciton–photon coupling and lasing behavior in all-inorganic CsPbBr3 micro/nanowire Fabry-Pérot cavity. ACS Photonics *5*, 2051–2059.

32. Gies, C., Florian, M., Gartner, P., and Jahnke, F. (2011). The single quantum dot-laser: lasing and strong coupling in the high-excitation regime. Opt. Express *19*, 14370–14388.

33. Garziano, L., Ridolfo, A., De Liberato, S., and Savasta, S. (2017). Cavity qed in the ultrastrong coupling regime: photon bunching from the emission of individual dressed qubits. ACS Photonics *4*, 2345–2351.

34. Vendrell, O. (2018). Coherent dynamics in cavity femtochemistry: application of the multi-configuration time-dependent Hartree method. Chem. Phys. *509*, 55–65.

35. Luk, H.L., Feist, J., Toppari, J.J., and Groenhof, G. (2017). Multiscale molecular dynamics simulations of polaritonic chemistry. J. Chem. Theor. Comput. *13*, 4324–4335.

36. Halász, G.J., Vibók, Á., and Cederbaum, L.S. (2015). Direct signature of light-induced conical intersections in diatomics. J. Phys. Chem. Lett. *6*, 348–354.

37. Szidarovszky, T., Halász, G.J., Császár, A.G., Cederbaum, L.S., and Vibók, Á. (2018). Conical

intersections induced by quantum light: field-dressed spectra from the weak to the ultrastrong coupling regimes. J. Phys. Chem. Lett. *9*, 6215–6223.

38. Herrera, F., and Spano, F.C. (2016). Cavity-controlled chemistry in molecular ensembles. Phys. Rev. Lett. *116*, 238301.

39. Kowalewski, M., Bennett, K., and Mukamel, S. (2016). Non-adiabatic dynamics of molecules in optical cavities. J. Chem. Phys. *144*, 054309.

40. Galego, J., Garcia-Vidal, F.J., and Feist, J. (2016). Suppressing photochemical reactions with quantized light fields. Nat. Commun. *7*, 13841.

41. Sáez-Blázquez, R., Feist, J., Fernández-Domínguez, A.I., and García-Vidal, F.J. (2018). Organic polaritons enable local vibrations to drive long-range energy transfer. Phys. Rev. B *97*, 241407.

42. Martínez-Martínez, L.A., Du, M., F Ribeiro, R.F., Kéna-Cohen, S., and Yuen-Zhou, J. (2018). Polariton-assisted singlet fission in acene aggregates. J. Phys. Chem. Lett. *9*, 1951–1957.

43. Du, M., Ribeiro, R.F., and Yuen-Zhou, J. (2019). Remote control of chemistry in optical cavities. Chem *5*, 1167–1181.

44. Galego, J., Garcia-Vidal, F.J., and Feist, J. (2017). Many-molecule reaction triggered by a single photon in polaritonic chemistry. Phys. Rev. Lett. *119*, 136001.

45. Fregoni, J., Granucci, G., Coccia, E., Persico, M., and Corni, S. (2018). Manipulating azobenzene photoisomerization through strong light–molecule coupling. Nat. Commun. *9*, 4688.

46. Cusati, T., Granucci, G., Persico, M., and Spighi, G. (2008). Oscillator strength and polarization of the forbidden n–>pi* band of trans-azobenzene: a computational study. J. Chem. Phys. *128*, 194312.

47. Bussi, G., Donadio, D., and Parrinello, M. (2007). Canonical sampling through velocity rescaling. J. Chem. Phys. *126*, 014101.

48. Granucci, G., and Toniolo, A. (2000). Molecular gradients for semiempirical CI wavefunctions with floating occupation molecular orbitals. Chem. Phys. Lett. *325*, 79–85.

49. Cusati, T., Granucci, G., Martínez-Núñez, E., Martini, F., Persico, M., and Vázquez, S. (2012). Semiempirical hamiltonian for simulation of azobenzene photochemistry. J. Phys. Chem. A *116*, 98–110.

50. Cusati, T., Granucci, G., and Persico, M. (2011). Photodynamics and time-resolved fluorescence of azobenzene in solution: a mixed quantum-classical simulation. J. Am. Chem. Soc. *133*, 5109–5123.

51. Cantatore, V., Granucci, G., and Persico, M. (2014). .Simulation of the $\pi \rightarrow \pi^*$ photodynamics of azobenzene: decoherence and solvent effects. Comp. Theor. Chem. *1040–1041*, 126–135.

52. Favero, L., Granucci, G., and Persico, M. (2016). Surface hopping investigation of benzophenone excited state dynamics. Phys. Chem. Chem. Phys. *18*, 10499–10506.

53. Benassi, E., Granucci, G., Persico, M., and Corni, S. (2015). Can azobenzene photoisomerize when chemisorbed on a gold surface? An analysis of steric effects based on nonadiabatic dynamics simulations. J. Phys. Chem. C *119*, 5962–5974.

54. Vetráková, Ľ., Ladányi, V., Al Anshori, J., Dvořák, P., Wirz, J., and Heger, D. (2017). The absorption spectrum of cis-azobenzene. Photochem. Photobiol. Sci. *16*, 1749–1756.

55. Granucci, G., Persico, M., and Toniolo, A. (2001). Direct semiclassical simulation of photochemical processes with semiempirical wave functions. J. Chem. Phys. *114*, 10608–10615.

56. Granucci, G., Persico, M., and Zoccante, A. (2010). Including quantum decoherence in surface hopping. J. Chem. Phys. *133*, 134111.

57. Bajo, J.J., Granucci, G., and Persico, M. (2014). Interplay of radiative and nonradiative transitions in surface hopping with radiation-molecule interactions. J. Chem. Phys. *140*, 044113.

58. Persico, M., and Granucci, G. (2014). An overview of nonadiabatic dynamics simulations methods, with focus on the direct approach versus the fitting of potential energy surfaces. Theor. Chem. Acc *133*, 1526.

59. Casellas, J., Bearpark, M.J., and Reguero, M. (2016). Excited-state decay in the photoisomerisation of azobenzene: a new balance between mechanisms. ChemPhysChem *17*, 3068–3079.

60. Nenov, A., Borrego-Varillas, R., Oriana, A., Ganzer, L., Segatta, F., Conti, I., Segarra-Marti, J., Omachi, J., Dapor, M., Taioli, S., et al. (2018). UV-light-induced vibrational coherences: the key to understand kasha rule violation in trans-azobenzene. J. Phys. Chem. Lett. *9*, 1534–1541.

61. Rattenbacher, D., Shkarin, A., Renger, J., Utikal, T., Götzinger, S., and Sandoghdar, V. (2019). Coherent coupling of single molecules to on-chip ring resonators. New J. Phys. *21*, 062002.

62. De Bernardis, D., Jaako, T., and Rabl, P. (2018). Cavity quantum electrodynamics in the nonperturbative regime. Phys. Rev. A *97*, 1–18.

63. De Bernardis, D., Pilar, P., Jaako, T., De Liberato, S., and Rabl, P. (2018). Breakdown of gauge invariance in ultrastrong-coupling cavity qed. Phys. Rev. A *98*, 1–15.

64. Stokes, A., and Nazir, A. (2019). Gauge ambiguities imply Jaynes-Cummings physics remains valid in ultrastrong coupling qed. Nat. Commun *10*, 499.

65. Di Stefano, O., Settineri, A., Macrì, V., Garziano, L., Stassi, R., Savasta, S., and Nori, F. (2019). Resolution of gauge ambiguities in ultrastrong-coupling cavity quantum electrodynamics. Nat. Phys. *15*, 803–808.

66. Warshel, A., and Levitt, M. (1976). Theoretical studies of enzymic reactions: dielectric, electrostatic and steric stabilization of the carbonium ion in the reaction of lysozyme. J. Mol. Biol. *103*, 227–249.

67. Ponder, J.W., and Richards, F.M. (1987). An efficient newton-like method for molecular mechanics energy minimization of large molecules. J. Comput. Chem. *8*, 1016–1024.

68. Toniolo, A., Ciminelli, C., Granucci, G., Laino, T., and Persico, M. (2004). QM/MM connection atoms for the multistate treatment of organic and biological molecules. Theor. Chem. Acc *111*, 270–279.

69. Ciminelli, C., Granucci, G., and Persico, M. (2005). Are azobenzenophanes rotation-restricted? J. Chem. Phys. *123*, 174317.

70. Tully, J.C. (1990). Molecular Dynamics with electronic transitions. J. Chem. Phys. *93*, 1061–1071.

Supplemental Movies

The Supplemental Movie 1 and 2 show an animated version of the non-adiabatic dynamics simulations for the strong coupling regime (polaritonic, Supplemental Movie 1) and zero coupling regime (electronic, Supplemental Movie 2) for the trans-cis photoisomerization of azobenzene. On the $CNNC$ coordinate, the basin on the right represents the trans region, while the basin on the left is the cis region. The states from upper left to lower right are ordered energetically from the highest to the lowest. The light blue trajectories are the ones which will not isomerize, while the orange ones depict the reactive trajectories. The Supplemental Movie 1 involves 6 states, while the Supplemental Movie 2 involves 4 states. The polaritonic PES are shown within the same energy window of the S_0, S_1, S_2, S_3 states for the weak coupling case. Supplemental Movie 3 shows a rendered example of a reactive trajectory. For completeness and to ease the interpretation of the results, the Supplemental Movies are included via a QRcode in this section.

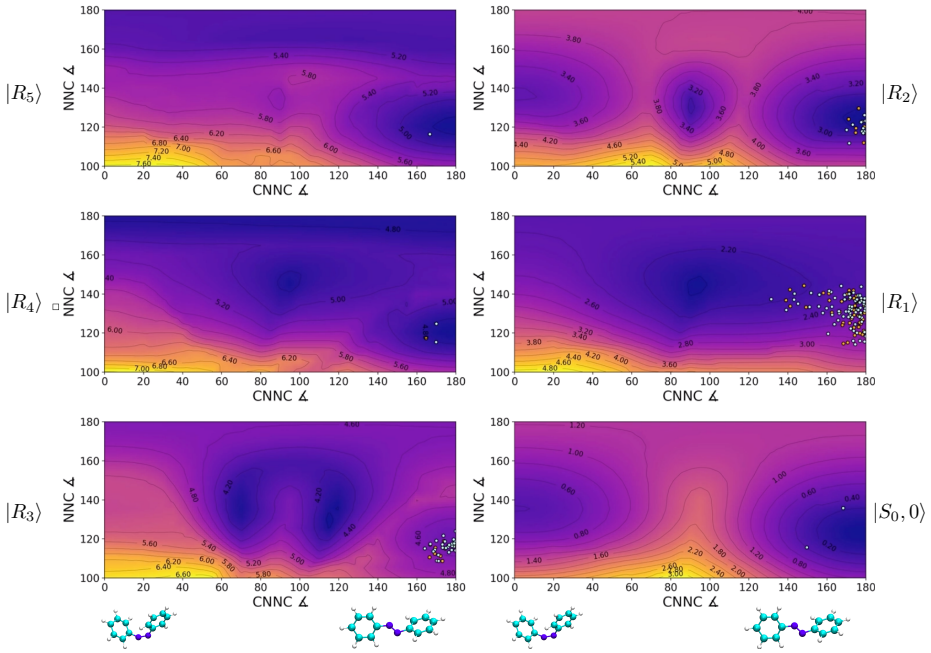

Snapshots of Supplemental Movie 1 showing the non-adiabatic dynamics on polaritonic states. The polaritonic states are labeled in this Figure as $|R_n\rangle$

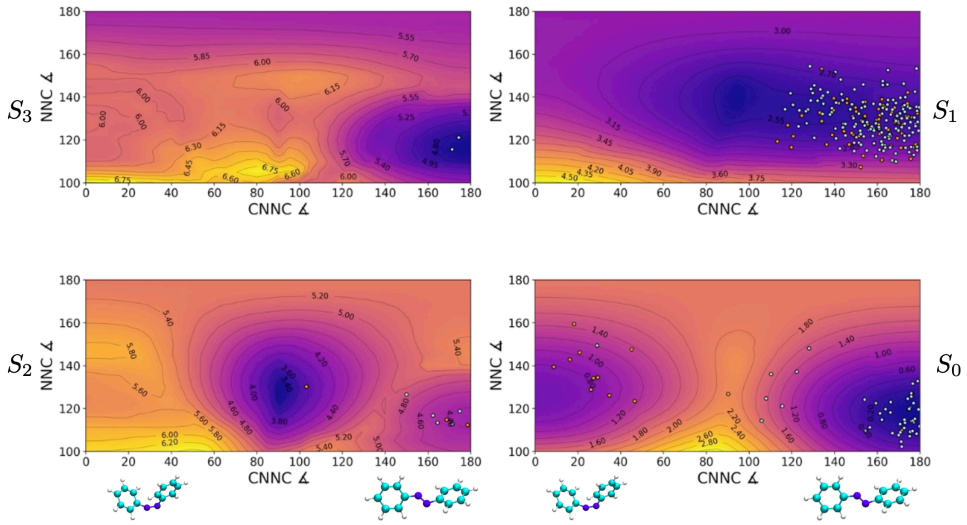

Snapshots of Supplemental Movie 2 showing the non-adiabatic dynamics on purely electronic states. The electronic states are labeled in this Figure as S_n after the notation used in the main text.

Supplemental Movie 1

Supplemental Movie 2

Supplemental Movie 3

Supplemental Movies

Supplemental Information: Strong coupling of molecule with light enhances the photoisomerization quantum yield of azobenzene

J. Fregoni *et al.*

E-mail:

Supplemental Data Items

Table S1: **Related to Figure 5 of the main text.** Complete data of the hops between adiabatic states in the strong coupling regime and in the zero coupling one. Averages and standard deviations for the following quantities at the time of hops: energy difference between initial and final state, CNNC dihedral, time elapsed from the excitation.

strong coupling						
initial state	final state	number of hops	ΔE (eV)	CNNC (degrees)	symNNC (degrees)	time (fs)
$\|R_5\rangle$	$\|R_4\rangle$	35	0.0972±0.0643	175.52±3.37	116.24±2.63	24.43±41.93
$\|R_5\rangle$	$\|R_3\rangle$	7	0.2018±0.0510	175.09±3.72	119.70±1.98	14.57±15.55
$\|R_4\rangle$	$\|R_5\rangle$	11	-0.1702±0.1002	175.26±2.58	115.64±1.41	41.09±36.44
$\|R_4\rangle$	$\|R_3\rangle$	155	0.1545±0.0757	174.87±3.98	116.00±3.01	31.72±47.26
$\|R_3\rangle$	$\|R_5\rangle$	1	-0.2488±0.0000	179.97±0.00	111.92±0.00	74.00±0.00
$\|R_3\rangle$	$\|R_4\rangle$	34	-0.2078±0.0732	175.33±4.18	115.87±3.16	60.91±76.93
$\|R_3\rangle$	$\|R_2\rangle$	419	0.1181±0.0801	173.18±4.40	112.93±3.03	64.65±56.57
$\|R_3\rangle$	$\|R_1\rangle$	6	0.2877±0.0406	168.48±5.73	112.24±3.16	58.50±38.65
$\|R_2\rangle$	$\|R_3\rangle$	194	-0.1331±0.0738	173.78±4.22	117.94±2.70	66.15±55.66
$\|R_2\rangle$	$\|R_1\rangle$	529	0.0881±0.0591	172.22±5.26	117.94±3.45	186.52±173.06
$\|R_1\rangle$	$\|R_2\rangle$	270	-0.0883±0.0621	172.65±5.17	118.30±3.43	270.94±170.59
$\|R_1\rangle$	$\|R_0\rangle$	285	0.1207±0.0802	104.61±7.91	133.73±7.22	446.40±188.13
$\|R_0\rangle$	$\|R_1\rangle$	21	-0.1606±0.0886	103.38±8.92	136.54±7.40	412.48±208.55
zero coupling						
initial state	final state	number of hops	ΔE (eV)	CNNC (degrees)	symNNC (degrees)	time (fs)
$\|S_4\rangle$	$\|S_3\rangle$	116	0.1557±0.0750	164.42±29.47	115.84± 5.50	90.77±205.69
$\|S_4\rangle$	$\|S_2\rangle$	6	0.2362±0.0406	170.41±5.59	111.28± 2.20	141.17±282.43
$\|S_3\rangle$	$\|S_4\rangle$	62	-0.1665±0.0703	161.79±34.66	116.88± 4.97	112.23±235.44
$\|S_3\rangle$	$\|S_2\rangle$	291	0.1686±0.0812	168.93±15.97	114.99± 5.29	71.11±147.11
$\|S_3\rangle$	$\|S_1\rangle$	7	0.2401±0.0653	173.26±4.28	108.82± 1.28	59.86±90.4
$\|S_2\rangle$	$\|S_4\rangle$	1	-0.2710±0.0000	19.95±0.00	113.24± 3.17	977.00±0.00
$\|S_2\rangle$	$\|S_3\rangle$	138	-0.1804±0.0818	168.40±19.08	115.30± 5.13	91.79±170.83
$\|S_2\rangle$	$\|S_1\rangle$	315	0.1582±0.0832	169.73±13.17	112.83± 5.10	72.10±108.81
$\|S_1\rangle$	$\|S_2\rangle$	79	-0.1506±0.0812	168.56±19.7	113.88± 5.39	71.03±93.39
$\|S_1\rangle$	$\|S_0\rangle$	264	0.1320±0.0789	107.07±11.23	138.85±10.24	353.06±199.07
$\|S_0\rangle$	$\|S_1\rangle$	25	-0.1573±0.0944	102.90±10.36	140.10± 7.32	395.32±212.66

Supplemental Experimental Procedures

Supplemental Note 1: Setup of the system for the dynamics simulation

In this section, we provide further detail to the system setup. The core of the system is composed by azobenzene, treated at QM level. The MM molecules are divided in three classes: cucurbit-7-uril molecule (126 atoms, Figure S1a) gold layers (3342 atoms) and water molecules (2700 atoms). The cucurbit-7-uril molecule encages the azobenzene and is placed between 8 squared gold layers (4 on top, 4 on bottom). The 900 water molecules fill the space within the layers (Figure S1b).

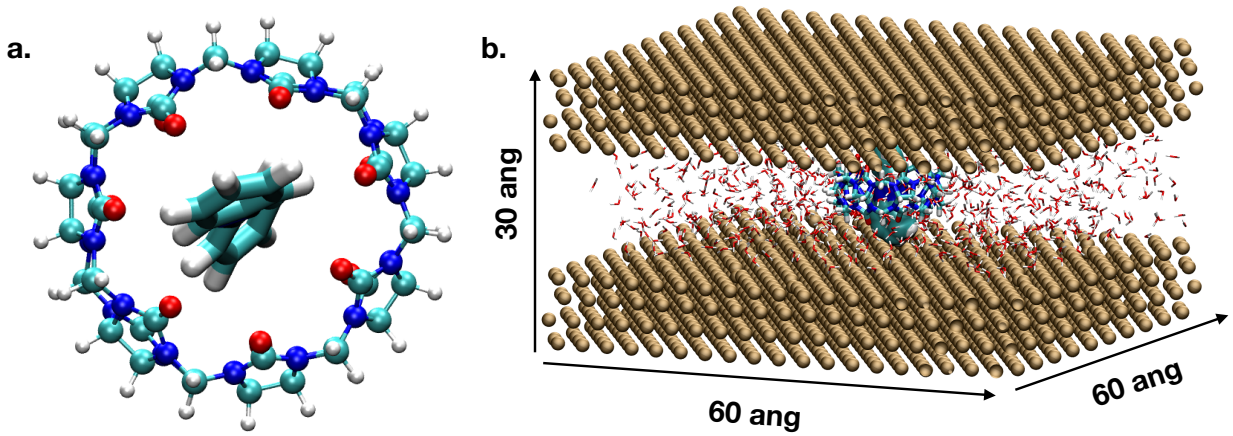

Figure S1: **Simulated system**— **a)** Cucurbit-7-uril encapsulating azobenzene. **b)** The encapsulated subsystem is then placed within a 60 by 60 by 30 angstrom box. The cavity is simulated by placing four gold layers in the top and four in bottom positions. The cavity is then filled with water molecules. The field polarization of the cavity mode is directed along the 30 angstrom dimension.

A preliminary minimization of the structure is performed with the TINKER[1] code. Then, a full MM equilibration trajectory is run at 300K for 100 ps. The final geometry is taken as a starting point for a QM/MM equilibration (with locally modified MOPAC2002 interfaced with TINKER) in presence of the Bussi-Parrinello thermostat[2] at 300K for 50 ps. The forcefield used for the system is OPLS-AA. The charges of the nitrogens of cucurbit-7-uril

have been locally rescaled to match the neutrality of the cyclic molecule. Water are represented by the TIP3P potential and, since TIP3P does not provide a Lennard-Jones potential for the hydrogen atoms belonging to water molecules, it is necessary to define specific van der Waals interaction parameters between the hydrogens belonging to water and the solute atoms.[3,4] The gold layers are kept fixed and they interact with the other parts of the system by Lennard-Jones potentials, specifically defined for gold atoms.[5]

Two thousands configurations are extracted from the last 20 ps of the QM/MM equilibration trajectory outcome of such dynamics. This procedure mostly populates the S_2-S_3 excited states (or the polaritonic equivalents $|R_3\rangle$, $|R_4\rangle$), proportionally to their squared transition dipoles. The excitation process is simulated by mimicking the absorption of radiation (centered at 313 nm with an energy width of 1 eV) through the procedure outlined in reference.[6] The excitation energy window $3.46 < \Delta E_{exc} < 4.46$ eV was imposed to include the absorption spectrum features corresponding to the first $\pi \rightarrow \pi^*$ transitions of trans and cis azobenzene. The absorption spectra of cis and trans, compared with the excitation window, are shown in Figure S2. It is apparent for both trans and cis that the actual energy bandwidth of the excitation is less than 1 eV (~ 0.5 eV), due to the features of the absorption spectra.

Supplemental Note 2: Discussion on the approximations

Truncation of the CI-space As described in the main text, we work in the single excitation space with a single photon mode and maximum photon occupation number equal to 1. Figure 2 in the main text suggests that, for the excitation window used in this work, states with $p \geq 2$ are too high in energy to be relevant in the excitation process. To prove that this is the case during the dynamics, the energy difference between the current state (i.e. the state where the given trajectory is running on) and either $|S_1, 1\rangle$ or $|S_0, 2\rangle$ are reported in Figure S3. Indeed, they are found to be always larger than 1 eV and we stress that we

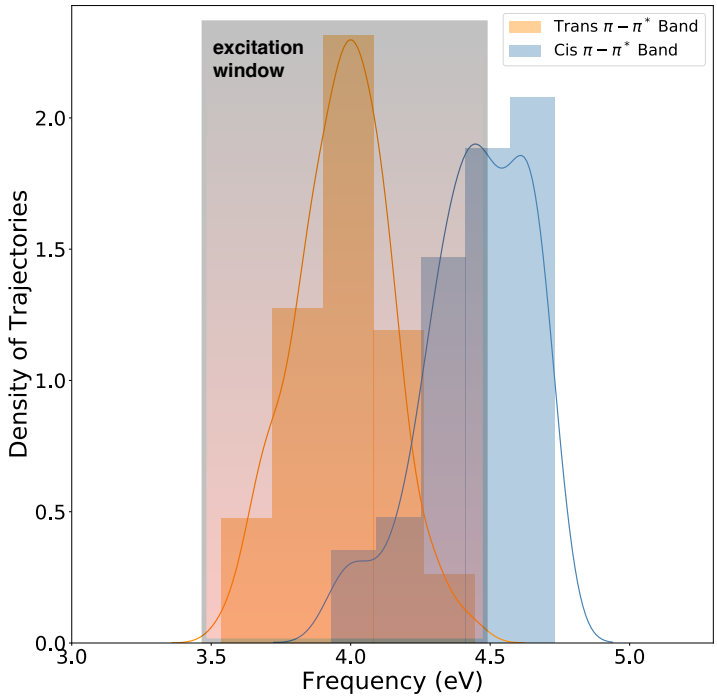

Figure S2: **Excitation windows of trans and cis azobenzene**— Comparison between the $\pi - \pi^*$ excitation bands of trans- (orange) and cis- (blue) azobenzene, with respect to the excitation window between 3.46 eV and 4.46 eV. The absorption spectra are obtained by the ground state sampled configuration, excited in a wider excitation window (3 to 5 eV).

compute such difference along all the degrees of freedom, therefore there are no orthogonal coordinates where the states might be close enough in energy to allow hoppings going upwards.

Even though states with $p \geq 2$ are never populated during the dynamics, they might affect the shape of the PESs due to the counter rotating terms. To check this is not the case for our conditions, in Figure S3 we report the energy values for the active polaritonic states computed at relevant geometries. At trans-equilibrium, cis-equilibrium and conical intersection geometries, we compute the polaritonic energies by progressively expanding the CI space. The expansion is accomplished by adding uncoupled states with p=1, p=2 and p=3 respectively. The excellent agreement between $p = 1$ and $p \geq 1$ shows that is safe to truncate the CI space at $p = 1$ for the conditions reported in the present work.

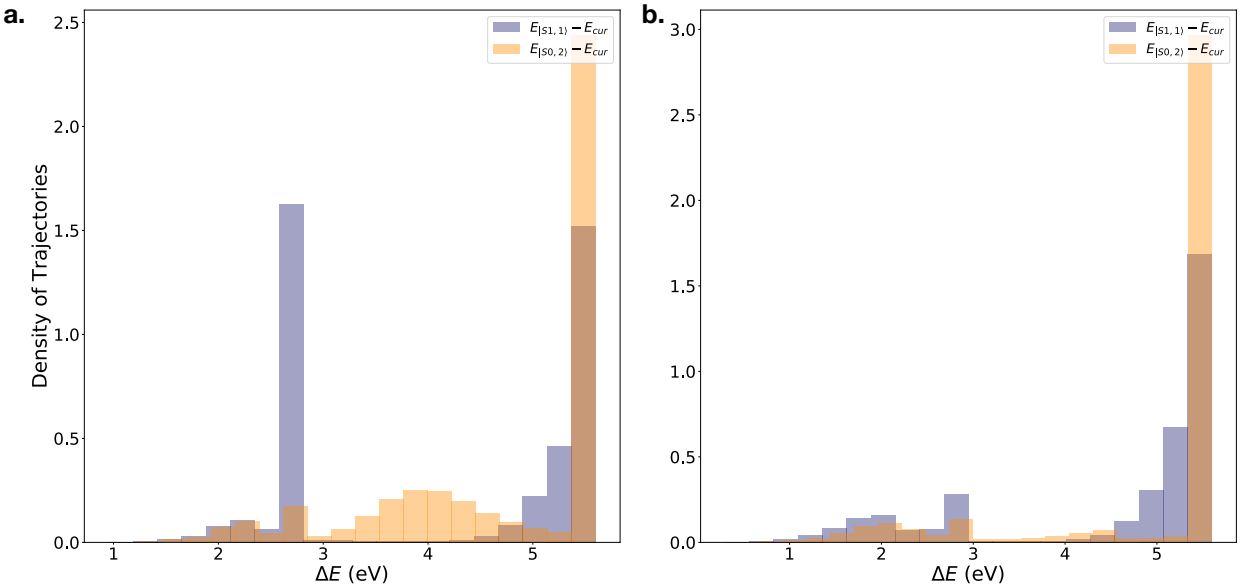

c.

		State energy (eV)		
		p=1	**p=2**	**p=3**
Trans	R_0	0.00000000	-0.00000210	-0.00000210
	R_1	2.79173674	2.78710291	2.78709670
	R_2	2.83251761	2.83251739	2.83251739
	R_3	4.38252676	4.38249059	4.38249054
	R_4	4.70864277	4.70860263	4.70860244
Cis	R_0	0.46292653	0.46292650	0.46292650
	R_1	3.26253558	3.26229946	3.26229944
	R_2	3.31486489	3.31486445	3.31486445
	R_3	5.33960984	5.33960965	5.33960965
	R_4	5.84783202	5.84782930	5.84782930
Coln	R_0	1.77822973	1.77822957	1.77822957
	R_1	2.30730298	2.30730276	2.30730276
	R_2	3.10931025	3.10930954	3.10930954
	R_3	4.57621758	4.57495182	4.57495133
	R_4	5.10911925	5.10770660	5.10770597

Figure S3: **Distribution of the energy differences between the current state and $|S_1, 1\rangle, |S_0, 2\rangle$ states** —Panels **a)** and **b)** refer respectively to simulations starting from trans or cis. Peaks at 5.6 eV correspond to trajectories running on the ground state. **c)** Energy values for relevant geometries computed by truncating the photon space at p=1, p=2 and p=3 respectively.

Decay algorithm When treating the cavity losses, we resort to the algorithm described in the methods section. The presented algortihm takes the polaritonic wavefunction at each

time step, expands it on the uncoupled state basis and evaluates the probability that the photon is dissipated by any $|n', 1\rangle$ state. The choice of such state relies on a Monte Carlo approach, by comparing for each trajectory at each time step a uniform random number with respect to a probability of transition. Strictly speaking, the photon loss has the effect to disrupt only the photonic part. This is realized by projecting the wavefunction over the $p = 1$ subspace from which the photon is lost. The associated decay operator $\hat{D}_2$ acts as:

$$\hat{D}_2|\Psi\rangle = \left[\mathbf{I_{el}} \otimes \hat{b}\right]|\Psi\rangle = \sum_{R,n'} C_R D^R_{n',1}|n', 0\rangle, \tag{1}$$

where $\mathbf{I_{el}}$ is the identity over the electronic subspace and $\hat{b}$ is the bosonic annihilation operator. The electronic coherence is preserved.

In the current case, our algorithm presented in the main text represents a good approximation of the whole algorithm. As shown in the previous subsection and in Figure 3a of the main text, the $|S_1, 1\rangle$ state is hardly populated during the whole dynamics. As a consequence, the photon must necessarily be lost from the $|S_0, 1\rangle$ state, which collapses on the ground state ($|S_0, 0\rangle$), and so the operator $\hat{D}_2$ in eq. 1 is practically identical to $|S_0, 0\rangle\langle S_0, 1|$.

Even when the arrival state is univocally determined as $|S_0, 0\rangle$, there is a specificity of the surface hopping to take into account. In this framework, it is the fact that the propagation of the nuclei must be on a polaritonic state. To fulfilll this requirement, the first step is to expand the final electronic state $|S_0, 0\rangle$ on the polaritonic basis:

$$|S_0, 0\rangle = \sum_R D_R^{S_0,0}|R\rangle. \tag{2}$$

In our implemented version, we choose to resume the dynamics from the polaritonic state $|F\rangle$, which has the maximum overlap $\langle S_0, 0|F\rangle\}$ with $|n'0\rangle$.

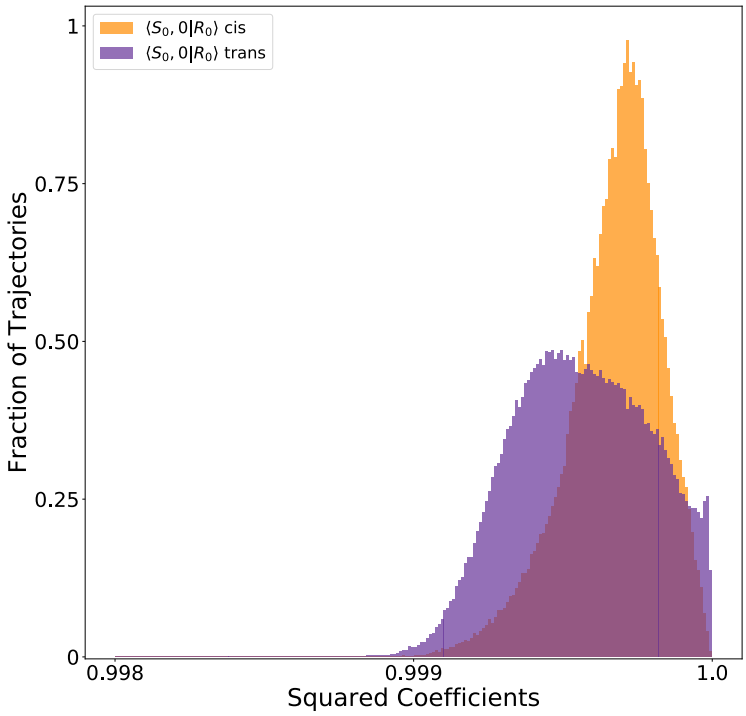

Figure S4: **Composition of the $|S_0, 0\rangle$ state over the polaritonic basis** —$|S_0, 0\rangle$ state composition on the polaritonic basis for the **a)**cis-trans and **b)** trans-cis dynamics, at each step of the dynamics. The orange distribution shows that $|S_0, 0\rangle$ coincides with $|R_0\rangle$, while the expansion coefficients of $|S_0, 0\rangle$ on $|R_1\rangle$ is 2-3 orders of magnitude lower.

A more rigorous possibility would be to the state $|F\rangle$ randomly with a probability proportional to $|D_R|^2$, that can be implemented as a Monte Carlo algorithm. In the present case the two approaches coincide within our conditions. We show in Figure S4 the composition of the $|S_0, 0\rangle$ state on the polaritonic basis over all the dynamics. It appears that $|S_0, 0\rangle$ coincides always with $|R_0\rangle$. Hence, in case of photon loss, the photon is only lost from $|S_0, 1\rangle$ and the only possible arrival state is $|R_0\rangle$.

The data shown in Figure 6 of the main text are complemented here by a trajectory-averaged photon-loss statistics of the performed dynamics (Figure S5). The photon statistics reveals that the $p = 1$ states are never populated more than 20%. As a consequence of the mixing, the average life of the photon within the cavity is extended beyond the nominal cavity lifetime. For low τ_{cav}, we also note that the photon population (and therefore the

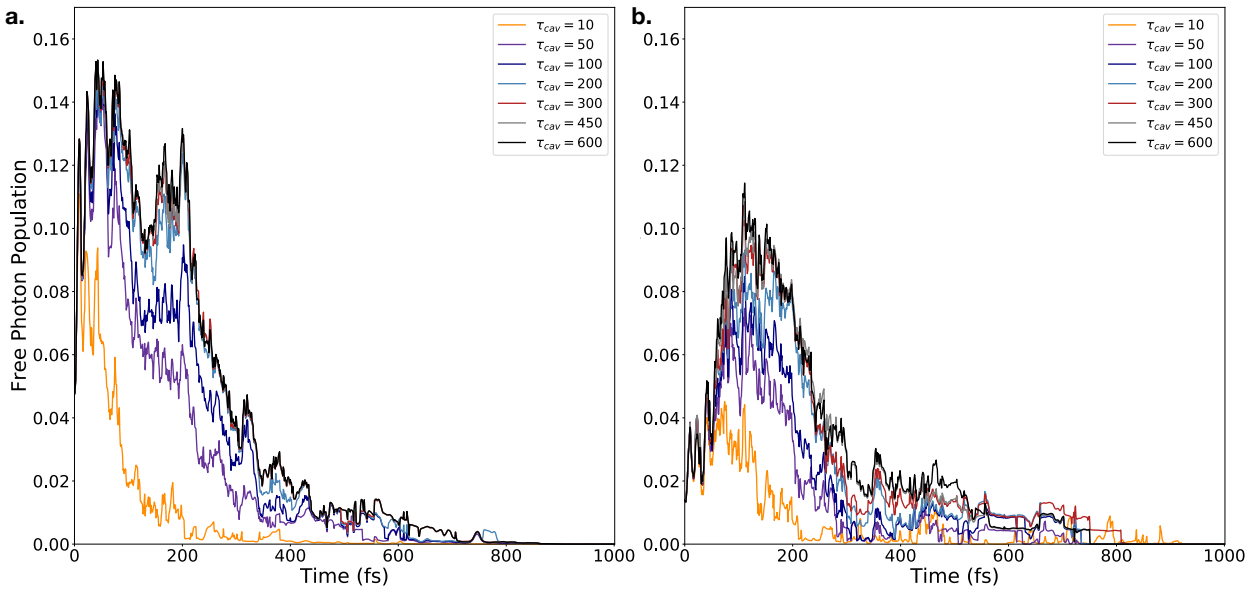

Figure S5: **Photon population within the cavity during the dynamics for different cavity lifetimes—a)** Trans-cis and **b)** cis-trans photoisomerizations. Coherently with the quenched yields reported in Figure 6 of the main text, for $\tau_{cav} = 10$ fs the photon loss occurs on a timescale much shorter than the photoisomerization. A behaviour approaching the lossless case is obtained for $\tau_{cav} = 200$ fs for each individual process, despite the fact that the enhanced of the photostationary equilibrium can be observed starting from 50 fs.

probability of the photon exiting the cavity) is non-monotonic, depending on the molecular dynamics.

Supplemental Note 3: Stability of dipolar approximation in the Coulomb gauge

Through all our work, we resort to a dipolar interaction between the photonic degree of freedom and the molecule, in the Coulomb gauge and long-wavelength approximation. As recently debated,[7–10] the dipolar choice is rather controversial in materials at the ultrastrong coupling regime (USC). When moving to strong coupling between light and molecules, Rubio and collaborators[11] have proven that large enough couplings ($g/\omega_c \geq 0.1$) can break down the Jaynes-Cummings approximation. To prove the robustness of our results within the present work, we numerically compare the Jaynes-Cummings plus counter rotating terms

(JC+CRT) to a full dipolar Hamiltonian (eqs. 3, 4).

$$\hat{H}_{JC+CRT} = \hat{H}_{mol} + \hat{H}_{cav} + E_{1ph} \sum_{n \neq n'} |n\rangle \boldsymbol{\lambda} \cdot \hat{\boldsymbol{\mu}}_{n,n'} \langle n'| \left(\hat{b}^\dagger + \hat{b}\right) \tag{3}$$

$$\hat{H}_{full} = \hat{H}_{mol} + \hat{H}_{cav} + \boldsymbol{\lambda} \cdot \hat{\boldsymbol{\mu}} E_{1ph} \left(\hat{b}^\dagger + \hat{b}\right) + 2(\hat{\mu} \cdot \lambda)^2 (\frac{E_{1ph}}{\sqrt{\omega_p}})^2 \tag{4}$$

The JC+CRT approximation is the one applied in our work, while the full dipolar Hamiltonian has been obtained by the Power-Zienau-Wolley gauge transformation of the minimal coupling Hamiltonian.[12] We stress that our aim is not to solve the controversy about of the gauge transformation but to test the reliability of our findings.

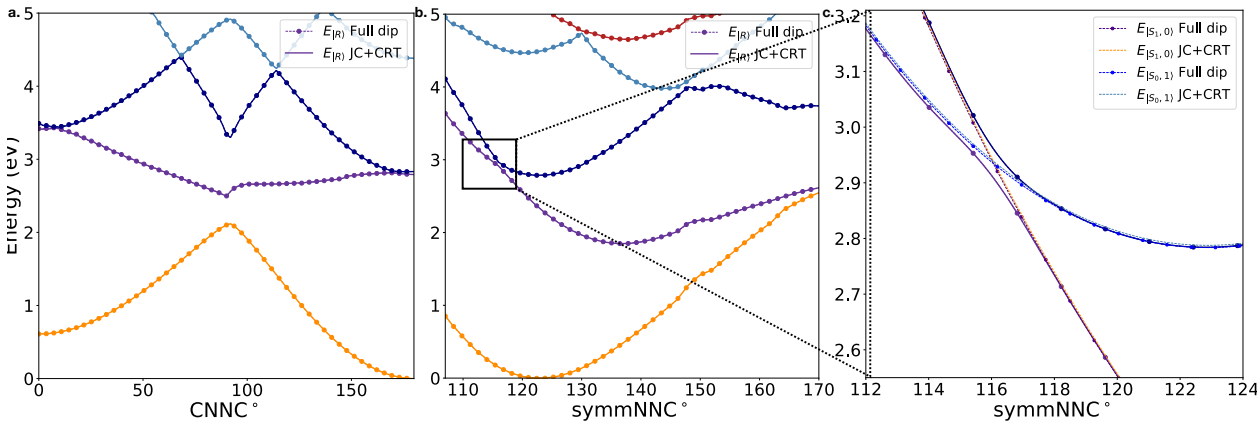

Figure S6: **Comparison between JC+CRT and full dipolar Hamiltonians in strong coupling**— Through all the panels, the circular marker indicate the full dipolar calculation and the full lines are the JC+CRT calculation, showing excellent agreement at both uncoupled and polaritonic conditions

As a test case, we investigate the first few polaritonic states which are directly involved in the findings reported in the main text. We repropose the calculation of the energy curves in the same conditions reported in the main text, *i.e.* an electric field E_{1ph} of 0.002 au and ω_p of 2.80 eV. The cuves are computed along CNNC by relaxing all the other degrees of freedom S6a and along symmNNC by constraining CNNC at 165°. Figure S6 compares the JC+CRT(full lines) approach vs the full dipolar approach (circular markers) showing

excellent agreement between the two models for the system treated in this work.

As reported in refs.,[7,8] a relevant deviation between the two models is expected to appear for values of $g/\omega_p \geq 0.1$ au. In those works, g represents the coupling, *i.e.* includes the magnitude of the transition dipole moment. In a realistic treatment, the explicit dependence of the transition dipole moment on the nuclear coordinate may alter the quality of the approximation in different regions of the conformational space. However, in consideration of the very small differencies found in the PES for the current work, it is safe to assume that within the coupling conditions chosen in this work the JC+CRT is a good approximation to the full dipolar treatment.

Supplemental Note 4: Analysis of nonadiabatic transitions.

Here we provide supplementary data for the analysis of the photoisomerization mechanism.

Figure S7 shows the minimum potential energy curve for the S_1 state, as a function of the CNNC dihedral, along with the energies of S_0 and S_2 at the same geometries. It can be noted that the potential energy between trans and twisted conformations in S_1 is very flat, while on the cis side it is much steeper. Besides the individual state energies, we also show the S_0/S_1 crossing seam, *i.e.* the energy of the two states with the constraint of degeneracy. The crossing seam coincides with the minimum energy pathway (MEP) in S_1 when CNNC is in the range 85°-105°. By approaching the trans conformation, the crossing seam is found at progressively higher energies with respect to the MEP and can be reached by opening both NNC bond angles. This is the reason why the degree of excitation of the symmetric bending mode is important for the lifetime of S_1 and the trans→cis photoisomerization quantum yield.

Figure S8 shows the state populations and averaged internal coordinates for the cis→trans photoisomerization and is analogous to Figure 4 of the main text. The two figures highlight how faster is the dynamics by excitation of the cis isomer, in comparison with excitation of the trans one. This is due to the larger slope of the PES on the cis side (see Figure S7) and determines the lower sensitivity of the cis→trans quantum yield to the environment, to the strong coupling conditions, and to the cavity losses.

In Table S1 we provide information concerning the nonadiabatic events (hops) between states: their number, as well as the average and standard deviation of internal coordinates and times at which the hops occur. These data complement those of Figure 5 in the main text. They show how fast are the radiationless transitions between pairs of states and the degree of reversibility of such processes (lower state→upper state versus upper→lower). Of particular interest is the large number of $|R_1\rangle \rightarrow |R_2\rangle$ hops in the strong coupling case, about

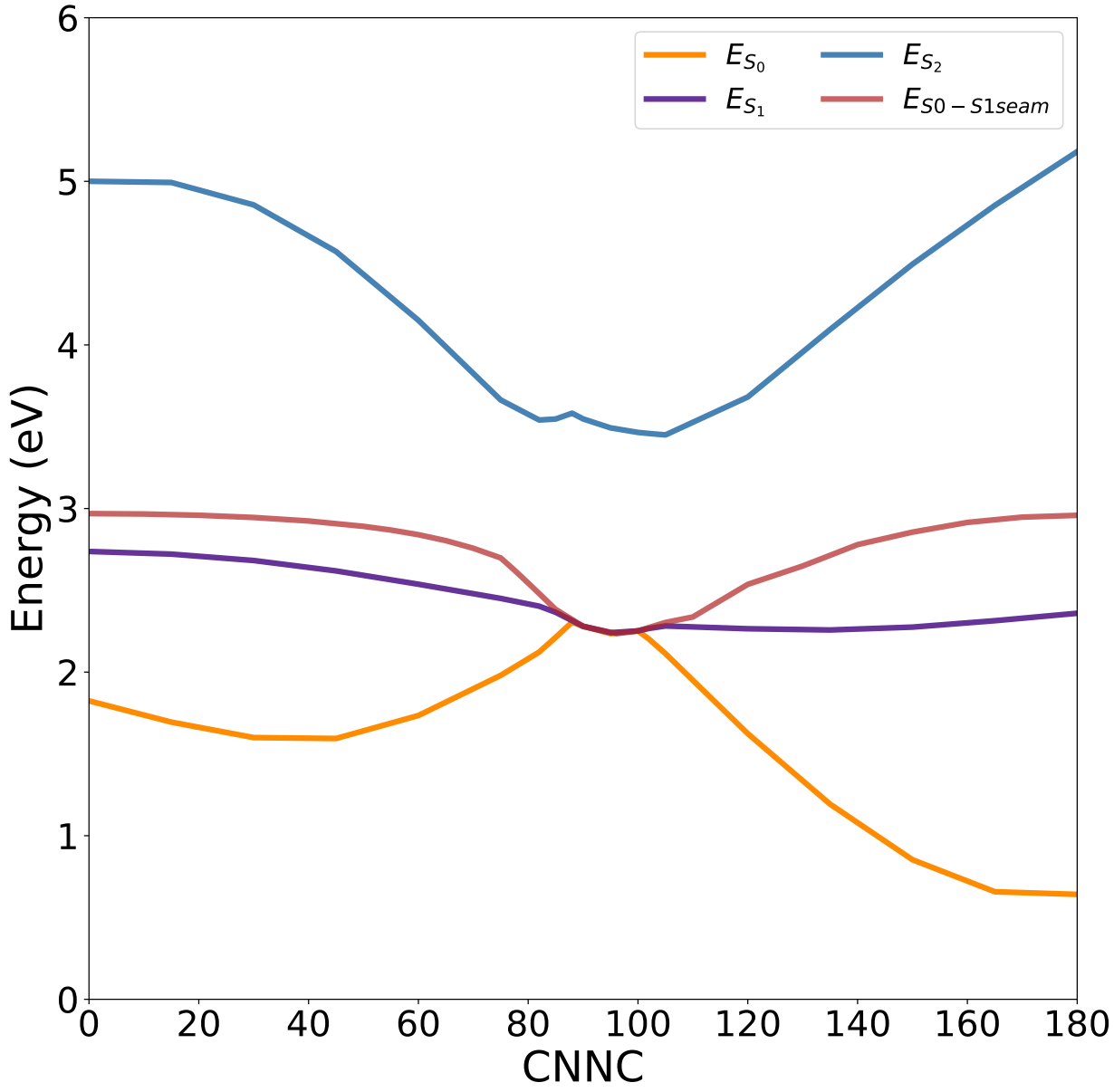

Figure S7: S_0, S_1 **and** S_2 **PESs** The PESs are computed along the CNNC coordinate by relaxing all the other degrees of freedom with respect to S_1. The colorscheme matches the one reported in the main text. The red line shows the S_0-S_1 crossing seam, *i.e.* the energy of two states minimized with the constraint of degeneracy.

half of the $|R_2\rangle \rightarrow |R_1\rangle$ ones (see discussion of the trans→cis photoisomerization in the main text).

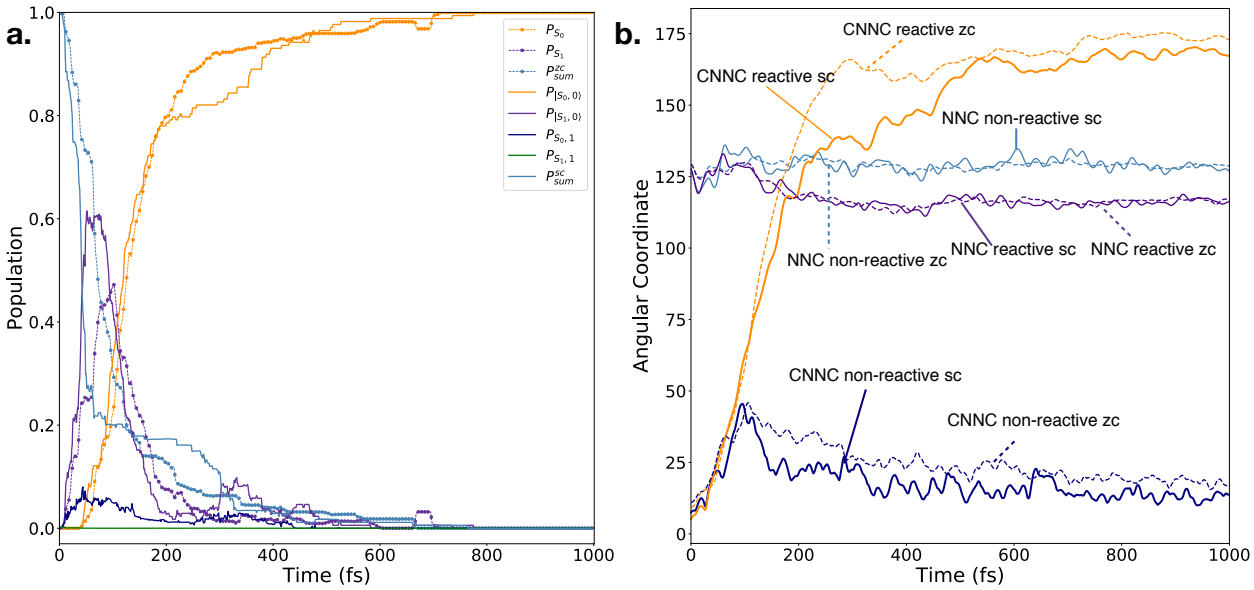

Figure S8: **a)** Population evolution and **b)** dynamics of the reactive coordinates in the cis-trans dynamics, in the same fashion of Figure 4 of the main text. With respect to the trans-cis case, the dynamics occur on much quicker timescales. Indeed, at 200 fs the photoisomerization reaction has almost completely occurred (vs 600 fs for the trans-cis case)

Supplemental References

(1) Ponder, J. W. TINKER-Software tool for molecular dynamics. *J. Comput. Chem.* **1987**, *8*, 1016–1024.

(2) Bussi, G.; Donadio, D.; Parrinello, M. Canonical sampling through velocity rescaling. *J. Chem. Phys* **2007**, *126*, 014101.

(3) Toniolo, A.; Granucci, G.; Martínez, T. J. Conical Intersections in Solution: A QM/MM Study Using Floating Occupation Semiempirical Configuration Interaction Wave Functions. *J. Phys. Chem. A* **2003**, *107*, 3822–3830.

(4) Aguilera-Porta, N.; Corral, I.; Munoz-Muriedas, J.; Granucci, G. Excited state dynamics of some nonsteroidal anti-inflammatory drugs: A surface-hopping investigation. *Comput. Theor. Chem.* **2019**, *1152*, 20 – 27.

(5) Benassi, E.; Granucci, G.; Persico, M.; Corni, S. Can Azobenzene Photoisomerize When Chemisorbed on a Gold Surface? An Analysis of Steric Effects Based on Nonadiabatic Dynamics Simulations. *J. Chem. Phys. C* **2015**, *119*, 5962–5974.

(6) Persico, M.; Granucci, G. An overview of nonadiabatic dynamics simulations methods, with focus on the direct approach versus the fitting of potential energy surfaces. *Theor. Chem. Acc.* **2014**, *133*, 1526.

(7) De Bernardis, D.; Jaako, T.; Rabl, P. Cavity quantum electrodynamics in the nonperturbative regime. *Phys. Rev. A* **2018**, *97*, 043820.

(8) De Bernardis, D.; Pilar, P.; Jaako, T.; De Liberato, S.; Rabl, P. Breakdown of gauge invariance in ultrastrong-coupling cavity QED. *Phys. Rev. A* **2018**, *98*, 053819.

(9) Di Stefano, O.; Settineri, A.; Macrì, V.; Garziano, L.; Stassi, R.; Savasta, S.; Nori, F. Resolution of gauge ambiguities in ultrastrong-coupling cavity quantum electrodynamics. *Nat. Phys.* **2019**,

(10) Stokes, A.; Nazir, A. Gauge ambiguities imply Jaynes-Cummings physics remains valid in ultrastrong coupling QED. *Nat. Commun.* **2019**, *10*, 499.

(11) Flick, J.; Ruggenthaler, M.; Appel, H.; Rubio, A. Atoms and molecules in cavities, from weak to strong coupling in quantum-electrodynamics (QED) chemistry. *Proc. Natl. Acad. Sci. USA* **2017**, *114*, 3026.

(12) Cohen-Tannoudji, C.; Dupont-Roc, J.; Grynberg, G. *Photons and Atoms*; Wiley-VCH Verlag GmbH, 2007; pp I–XIX.

Chapter 4

Until now, it was shown and discussed how the inclusion of chemical complexity in polaritonic systems may impact the outcome of a reaction and lead to new reactive pathways. So far, we have based our description on a high level of molecular accuracy coupled with a single quantized mode of a model electromagnetic field. As we aim at achieving a satisfactory description for all the subcomponents of the nanoparticle-molecule-environment system, we now focus on improving the description of the field to account for the geometrical features of the nanoparticle. A realistic description of the nanoparticle is not only relevant for polaritonic photochemistry applications, as it is also pivotal in spectroscopic techniques down to the submolecular level.[5–9,119–122] In particular, plasmonic hotspots are widely exploited to enhance the molecular Raman response. Most of the setups rely on the inhomogeneities of the plasmonic field to achieve a coupling strong enough to observe enhanced signals.[7,123–125] The access to nanoparticle-molecule interaction at the sub-molecular scale has been demonstrated also for strongly confined optical modes,[13,48] spurring the expectation to exploit strong coupling to modify chemistry on even portion of the molecules. Having to account for the local behaviour of both the plasmonic field in nanostructures and molecular transition density, it becomes mandatory to devise a method being able to support both the degrees of complexity. While full quantum methods can be pushed to simulate only a small portion of a nanoparticle system, the direct quantization of the plasmonic field from classical modes allows to account for the spatial features of plasmonic field and molecular complexity.[31,126]

While a satisfactory description of the molecule has already been exploited through all the present work, this Chapter is devoted to treat the quantum coupling between a realistic nanoparticle and a quantum molecule. Here, I make use of a particular eigenmode decomposition of BEM methods (IEF-BEM diagonal[25,26,127,128]) to compute the plasmonic mode of two nanoparticle setups and quantize them. I derive some of the quantities presented in Chapter 1 and build hybrid plasmon-molecule states. Through these means, the quantum

coupling between plasmons and molecules is obtained. After validating the method for a spherical nanoparticle and a dipolar molecule against analytical results,[16] I make use of such method to discuss the effect of the plasmonic field inhomogeneities on the coupling with the azobenzene molecule. This Chapter is then concluded with a brief perspective on the applicability of this approach to the Surface Hopping machinery presented and exploited in the previous Chapters.

All the presented results have been originally produced during the PhD activity and are part of my original contribution to this work. They are reported in the followings as a draft of a manuscript. Based on an original sketched derivation by S. Corni, I worked out the details of the theory and I implemented it in the group's code TDPlas. I implemented the interface with MOPAC2002 to compute and investigate the quantum coupled polaritonic potential energy surfaces. Finally I collaborated with the group by Prof. H. Koch's (SNS Pisa) to interface this approach with their Coupled Clusters code, eT. I have personally implemented and developed the tools to produce the validation tests and the figures presented in the followings and drafted the original text.

Quantum coupling between classical nanoparticles and quantum molecules

J. Fregoni[†,‡,¶] and S. Corni[*,¶,‡]

†*Dipartimento di Scienze Fisiche, Informatiche e Matematiche, University Modena and Reggio Emilia, I-41125 Modena, Italy*

‡*Istitute of Nanosciences, Consiglio Nazionale delle Ricerche CNR-Nano, I-41125 Modena, Italy*

¶*Dipartimento di Scienze Chimiche, University of Padova, I-35131 Padova, Italy*

E-mail: stefano.corni@unipd.it

Abstract

The near-field enhancement in plasmonic nanoparticles drives exotic phenomena on molecules which see their photophysical and photochemical properties strongly modified. The field enhancement is modulated through different shapes, materials and arrangements of the nanoparticles. As a result, powerful spectroscopic techniques with sub-molecular resolution have been devised in recent years. As a second outcome, the interest is rapidly shifting towards investigating the capabilities of such setups to modify chemical and photochemical properties at the sub-molecular level, namely by confining molecules and electromagnetic field via nanocavities and nanotips setups. Simulating these systems requires a high-level of accuracy from both the nanoparticle and the molecular ends. Here we present a method suitable to describe the quantum coupling between nanoparticles and molecules from the weak to the strong coupling regime. This method is grounded on an intuitive-yet-realistic representation of the

quantized plasmonic modes and allows to retrieve high-resolution results without disregarding the molecular description.

1. Introduction

As light shines on metal nanoparticles, collective excitations of the surface charges are triggered on the nanoparticle surface. Such excitations go by the name of plasmons.[1] In most cases, the electromagnetic field in the close proximity of the metal nanoparticles is strongly enhanced by the plasmon resonance. The region where the field-enhancement occurs can be arranged by exploiting nanoparticles of different shapes or geometrical disposition. A prominent display of setups which exploits the properties of such enhanced near-field are nanocavities, where the enhanced field is confined in nanometric volumes.[2–4] When a molecule is placed in the close proximity of nanoparticles surfaces, it experiences the enhancement electromagnetic field. Consequently, its optical and chemical properties are strongly affected. This effect is of paramount importance: on one hand, the enhanced optical response of the molecule to the plasmonic field is exploited in advanced spectroscopic techniques, such as Surface Enhanced Raman Scattering,[5,6] Tip Enhanced Raman Scattering[7,8] or Plasmon Enhanced Fluorescence Spectroscopy.[9] The molecular response in such cases is so enhanced that the signal can be detected down to the single molecule or even sub-molecular level.[10,11] On the other hand, the nanoparticles-molecule coupling is known to affect the chemical properties of molecules,[12–14] potentially resulting in modified chemical/photochemical reactivity[15–19] and relaxation dynamics,[20–23] along with other coherent processes.[24–27]

As most of the mentioned applications strongly rely on the quantum nature of the plasmon-molecule coupling in the near field, the level of description of molecules, nanoparticles and their coupling strongly affects the predictive power of said methods. In general, two main paradigms are adopted by the methods treating coupled nanoparticle-molecule sys-

tems.[17,18,28,29] According to the first, the field is treated as a single, parametric mode to focus on the molecular modified properties.[24,26,30] Otherwise, the description can privilege the field properties by disregarding the chemical complexity, taking the risk of flattening the rich nanoparticle-molecule phenomenology. Even more practically, when the coupling affects the molecule on a sub-molecular level (namely, a portion of the molecule),[10,31] a sub-molecular resolution in both the nanoparticle and the molecular description is no longer an optional. This translates in devising methods able to describe both the geometrical features of the molecular charge density and the geometrical features of the electromagnetic field originated by a nanoparticle of arbitrary shape, with just few works being able to describe the quantum system beyond a dipolar approximation for the molecule.[10,32]

Here, we present an approach to compute the quantum light-molecule coupling which accounts for the geometrical features of the nanoparticles setups without disregarding the molecular complexity. We exploit the quantization of the plasmonic modes computed from a classical nanoparticle of an arbitrary shape based on a diagonal-BEM version of the IEF-PCM technique.[33,34] We interface the so-obtained quantum plasmonic modes to interface with high-level quantum chemical descriptions of the molecule (FOMO-CI[35,36] and EOM-CCSD[37–39]). However, we stress that the method presented here can be interfaced to any quantum chemical level of description.

Firstly, the implemented theory has been compared with the case of a spherical nanoparticle. In this simple test, we compute the transition potential acting on the nanoparticle by a realistic molecule and compare it to the point-dipole description. The presented test also allows to directly compare with the analytic results for the quantum coupling between nanoparticles and point-dipolar molecules provided by A. Delga *et al.*[40] Finally, we exploit the presented theory to show the interaction between a nanotip realized after ref.[10] and the azobenzene molecule. Through these means, we show and discuss the importance of describing the geometrical features of the system beyond the dipolar approximation through a brief

perspective on the further development. In particular, we anticipate that it does not lack any capability to achieve an unprecedented level of realism in the description of interacting nanoparticle-molecule dynamical processes.

2. Quantization of the modes in a plasmonic BEM nanoparticle

2.1. IEF-BEM diagonal formulation

The first subsystem to treat is the nanoparticle. Being unable to fully treat the system at quantum level due to its dimensions, we approach the NP problem by an electromagnetic perspective. This translates into computing classically the plasmon modes. The more refined approximations to the electromagnetic problem in nanoparticles are safely able to reproduce the plasmonic features at a good level of realism. Among such features, the inhomogeneity of the electric field driven by the irregular shape of the nanoparticles is particularly relevant, as such irregularities are known to strongly influence the molecular properties.

To classically compute the nanoparticle surface properties means to classically solve the Maxwell Equation's for a continuous dielectric (nanoparticle) under an external perturbation. Put differently, simulating the plasmons of a nanoparticle calls for the computation of the nanoparticle linear response to the external perturbation. In the quasi-static limit, *i.e.* λ greater of the nanoparticle, the external perturbation is associated to an electrostatic potential $\boldsymbol{V}(\omega)$ acting on the nanoparticle surface. Such potential induces polarisation charges that, in turn, generate an additional electrostatic potential. A commonly adopted solution to the electrostatic problem is to resort to discretisation techniques (Figures 1a and 1b) such as Boundary Element Method (BEM) in the quasi-static limit.[41,42]

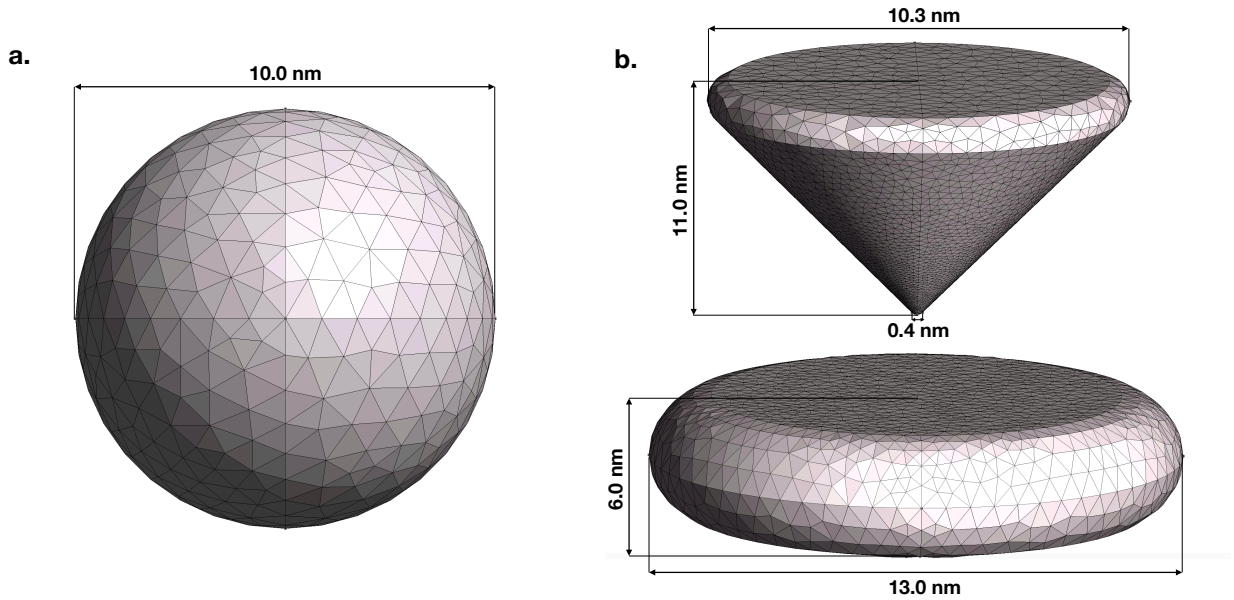

Figure 1: **Nanoparticles surfaces discretised with BEM— a)** Surface discretization of a 10 nm spherical nanoparticle, which will be used in the tests of the presented method. **b)** Discretisation of a nanotip setup. The dimensions are reproduced after ref.[10]

A particularly convenient formulation of BEM in such regards is based on the Integral Equation Formalism (IEF-BEM). Within such formulation, a set of charges (Apparent Surface Charges, ASC) sitting on the representative points of the nanoparticle discretised surface is used to represent the electrostatic potential which solves the Poisson equations. Such charges represent the linear dielectric response of the nanoparticle to the external perturbation at different ω. The IEF-BEM equation defining the apparent surface charges ($\boldsymbol{q}$) is

$$\boldsymbol{q}(\omega) = \boldsymbol{Q}^{IEF}(\omega)\boldsymbol{V}(\omega) \tag{1}$$

where $\boldsymbol{Q}^{IEF}(\omega)$ is the frequency-dependent response matrix to the external perturbation $\boldsymbol{V}(\omega)$. The $\boldsymbol{Q}^{IEF}(\omega)$ matrix is computed following the standard IEF formalism as:[34]

$$\boldsymbol{Q}^{IEF}(\omega) = -\boldsymbol{S}^{-1}\left(2\pi\frac{\varepsilon(\omega)+1}{\varepsilon(\omega)-1}\boldsymbol{I} + \boldsymbol{DA}\right)^{-1}(2\pi\boldsymbol{I} + \boldsymbol{DA})\,. \tag{2}$$

Here, $\varepsilon(\omega)$ is the dielectric function of the medium, $\boldsymbol{A}$ is a diagonal matrix containing the

area of the tesserae, while $\boldsymbol{S}$ and $\boldsymbol{D}$ are the Calderon's projectors, respectively storing information on the electrostatic potentials and the electric field between charges sitting on different tesserae:

$$S_{ij} = \frac{1}{|\boldsymbol{s_i} - \boldsymbol{s_j}|} \qquad D_{ij} = \frac{(\boldsymbol{s_i} - \boldsymbol{s_j}) \cdot \boldsymbol{n_j}}{|\boldsymbol{s_i} - \boldsymbol{s_j}|^3}, \tag{3}$$

with $\boldsymbol{s_i}$, $\boldsymbol{s_j}$ the coordinates of the $i-$th and $j-$th tessera and $\boldsymbol{n_j}$ the unit vector directed along the normal of the $j-$th tessera. Examining the response function in eq. 2, the frequency dependence is embodied in the choice of the dielectric function $\varepsilon(\omega)$. Following the procedure outlined in previous works,[33,34] it is possible to reformulate the problem in a diagonal form:

$$\boldsymbol{Q}^{IEF}(\omega) = -\boldsymbol{S}^{-\frac{1}{2}}\boldsymbol{T}\left(2\pi\frac{\varepsilon(\omega)+1}{\varepsilon(\omega)-1}\boldsymbol{I} + \boldsymbol{\Lambda}\right)^{-1}(2\pi\boldsymbol{I} + \boldsymbol{\Lambda})\,\boldsymbol{T}^{\dagger}\boldsymbol{S}^{-\frac{1}{2}}, \tag{4}$$

Here, the diagonal matrix $\boldsymbol{\Lambda}$ and the matrix $\boldsymbol{T}^{\dagger}$ collect the eigenvalues and eigenvectors of $\boldsymbol{S}^{-\frac{1}{2}}\boldsymbol{D}\boldsymbol{A}\boldsymbol{S}^{-\frac{1}{2}}$, which is (formally) symmetric. A compact form to indicate the diagonalized version of $\boldsymbol{Q}^{IEF}(\omega)$ is to collect all the central terms of eq. 4 into a single diagonal matrix $\boldsymbol{K}(\omega)$:

$$\boldsymbol{Q}^{IEF}(\omega) = -\boldsymbol{S}^{-\frac{1}{2}}\boldsymbol{T}\boldsymbol{K}(\omega)\boldsymbol{T}^{\dagger}\boldsymbol{S}^{-\frac{1}{2}}, \tag{5}$$

$$K_p(\omega) = \frac{2\pi + \Lambda_p}{2\pi\frac{\varepsilon(\omega)+1}{\varepsilon(\omega)-1} + \Lambda_p}. \tag{6}$$

K_p and Λ_p are respectively the diagonal elements of the $\boldsymbol{K}(\omega)$ and $\boldsymbol{\Lambda}$ matrices.

2.2. Quantization of the plasmonic modes

To quantize the plasmonic modes, we assume the metal nanoparticle as a continuous dielectric of an arbitrary shape, characterized by a Drude-Lorentz dielectric function $\varepsilon(\omega)$:

$$\varepsilon(\omega) = 1 + \frac{A}{\omega_0^2 - \omega^2 - i\gamma\omega}, \tag{7}$$

Plugging eq. 7 into eq.6:

$$K_p(\omega) = \frac{\left(1 + \frac{\Lambda_p}{2}\right)\frac{A}{2}}{\omega_0^2 - \omega^2 - i\gamma\omega + \left(1 + \frac{\Lambda_p}{2}\right)\frac{A}{2}}. \tag{8}$$

Renaming $\omega_0^2 + \left(1 + \frac{\Lambda_p}{2}\right)\frac{A}{2}$ as ω_p^2 and working out the denominator, we get:

$$K_p(\omega) = \frac{\omega_p^2 - \omega_0^2}{\omega_p} \frac{\omega_p}{\left(\omega_p - \omega - i\frac{\gamma}{2}\right)\left(\omega_p + \omega + i\frac{\gamma}{2}\right)} \tag{9}$$

$$= \frac{\omega_p^2 - \omega_0^2}{2\omega_p} \left(\frac{1}{\left(\omega_p + \omega + i\frac{\gamma}{2}\right)} + \frac{1}{\left(\omega_p - \omega - i\frac{\gamma}{2}\right)} \right). \tag{10}$$

We now recognize the typical structure of response function denominator coming from Linear Response Theory[43] where ω_p are the excitation frequencies of the plasmonic system. We can retrieve the full form of the response function $\boldsymbol{Q}^{IEF}(\omega)$ from eq. 5

$$\boldsymbol{Q}_{kj}(\omega) = \sum_p \left(\boldsymbol{S}^{-\frac{1}{2}}\boldsymbol{T}\right)_{k,p} \sqrt{\frac{\omega_p^2 - \omega_0^2}{2\omega_p}} \left(\frac{1}{\omega_p + \omega + i\frac{\gamma}{2}} + \frac{1}{\omega_p - \omega - i\frac{\gamma}{2}} \right) \sqrt{\frac{\omega_p^2 - \omega_0^2}{2\omega_p}} \left(\boldsymbol{T}^\dagger \boldsymbol{S}^{-\frac{1}{2}}\right)_{p,j}. \tag{11}$$

Each matrix element of $\boldsymbol{Q}^{IEF}(\omega)$ is evaluated on a couple of tesserae representative points, namely k, j. $\boldsymbol{Q}^{IEF}(\omega)$ is the response function providing quantization charges $\boldsymbol{q}$ induced by an external potential V. Our goal now is to identify the quantities characterising the nanoparticle quantized excited states (ie, plasmons) relevant to devise the coupling with the molecule. To this end, we identify the plasmonic matrix elements between ground (no plasmons) and the excited states of the nanoparticle. We compare eq. 11 to the structure of a general response function $\boldsymbol{R}(\omega)$ induced by the operator $\hat{q}$.[44] We conveniently write $\boldsymbol{R}(\omega)$ matrix elements in its spectral representation for the dynamical linear response case:[45,46]

$$R_{kj}(\omega) = -\sum_p \left(\frac{\langle 0|\hat{q}_k|p\rangle\langle p|\hat{q}_j|0\rangle}{\omega_p + \omega + i\gamma} + \frac{\langle p|\hat{q}_k|0\rangle\langle 0|\hat{q}_j|p\rangle}{\omega_p - \omega - i\gamma} \right), \tag{12}$$

By comparison of the first term of eq. 11 and eq. 12, we verify that ω_p represents the

excitation frequencies of the plasmonic system, while we can identify $\langle 0|\hat{q}_j|p\rangle$ with:

$$\langle 0|\hat{q}_j|p\rangle = -\left(\boldsymbol{S}^{-\frac{1}{2}}\boldsymbol{T}\right)_{p,j}\sqrt{\frac{\omega_p^2-\omega_0^2}{2\omega_p}}. \tag{13}$$

Here we will label the right hand side as q_p, j from now on, as that term represents the sitting on the j-th tessera, associated to the mode p. Such charges play the same role as the transition densities for molecules. Indeed, they correspond to the plasmonic matrix elements $\langle 0|\hat{q}_j|p\rangle$. Put differently, the ensemble of the $q_{p,j}$ set of charges for a given value of p represents the normal mode of the plasmonic system at frequency ω_p. The first normal modes of a spherical plasmonic system and a nanotip on a support are shown in Figure 2.

In the following section, we use this formulation to compute and validate the quantum coupling element between two material systems, namely a molecule and a plasmonic mode p, represented by its charges $\boldsymbol{q_p}$. While in the present work we focus on the quantum coupling between the two material systems (molecule and nanoparticle), the IEF-BEM diagonal formalism is general. Consequently, the response function of the nanoparticle and the related quantized description can take into account other effects as the driving of an external field.

2.3. Nanoparticle-Molecule Hamiltonian

In this section, we focus on computing the coupling element between a molecule and the plasmons of a spherical nanoparticle. The quantized plasmon-molecule Hamiltonian is:

$$\hat{H} = \hat{H}_{mol} + \hat{H}_p + \hat{H}_{int} \tag{14}$$

where we make no assumptions on the form of the molecular Hamiltonian, provided it is a suitable method to compute excited states. To quantize the plasmons in the dielectric

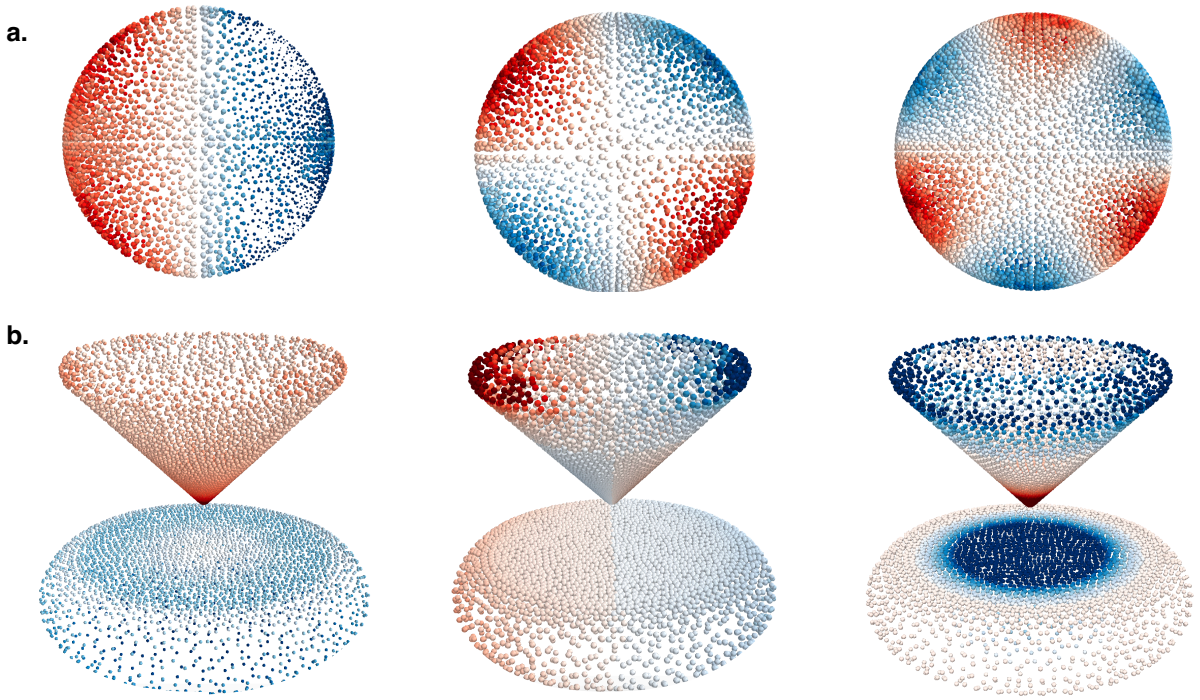

Figure 2: **Examples of plasmonic modes computed at IEF-BEM diagonal—a)** Plasmonic modes for a 10 nm sphere. The p index does not take into account the $2l+1$ degeneracy for the modes of the sphere. From left to right example of dipolar, quadrupolar and octupolar mode. Here, the dipolar modes are $p=2$ t;o $p=4$, the quadrupolar modes are $p=5$ to $p=9$ and so on. **b)** Normal modes for a nanotip on a support. The system is the one described in ref.[10] The dimensions of the system are about 10 by 10 nm (see Figure 1b). The $p=2$ and p=7 modes are suitable for TERS applications,[7,8,11] as the charge density is concentrated on the tip.

nanoparticle[47,48] we work in the assumption described in the previous section, namely that the dielectric responds linearly to an external perturbation and that such response is instantaneous.[49] Under such assumptions, the plasmonic Hamiltonian is written as the Hamiltonian of a quantized electromagnetic field:

$$\hat{H}_p = \sum_p \omega_p \left(\hat{b}_p^\dagger \hat{b}_p \right) \tag{15}$$

where ω_p is the p mode frequency computed at IEF-BEM diagonal level with a Drude-Lorentz dielectric and $\hat{b}_p^\dagger$, $\hat{b}_p$ are the bosonic creation and annihilation operators for the same mode.

The interaction term $\hat{H}_{int}$ is taken in the quasi-static limit as:[44]

$$\hat{H}_{int} = \sum_p \left(\hat{b}_p^\dagger + \hat{b}_p\right) \sum_j q_{p,j} \hat{V}_j, \tag{16}$$

where $\hat{V}_j$ is the potential induced by the molecule on the nanoparticle, evaluated at each tessera representative point j. Compared to the usual dipolar formulation of the quantized light-matter interaction (reported few equations below in eq. 19), this interaction presents two major advantages: on one side, we compute explicitly the nanoparticle modes as apparent surface charges $q_{p,j}$ allowing to obtain realistic quantities for the electromagnetic field without recurring to arbitrary parameters. The quantization allows to take into account the inhomogeneities of the electromagnetic field due to different nanoparticle shapes and setups. On the other side, this interaction is fully general and can easily be interfaced to advanced electronic structure calculations. The only requirement is to compute the potential V_j from the output electronic density of the quantum chemistry calculation.

Based on eq.16, we define for each mode the plasmon mode-molecule coupling operator $\hat{g}_p$ as

$$\hat{g}_p = \sum_j q_{p,j} \hat{V}_j, \tag{17}$$

hence reducing the interaction Hamiltonian to:

$$\hat{H}_{int} = \sum_p \hat{g}_p \left(\hat{b}_p^\dagger + \hat{b}_p\right). \tag{18}$$

A common approximation to the interaction Hamiltonian is to consider the molecule as a dipole within the cavity, allowing to retrieve a Tavis-Cummings-like[50,51] interaction for the nanoparticle and the molecule.[13,30,52,53] We report the approximated interaction as it will be

used only for test purposes:

$$\hat{H}_{int}^{dip} = \sum_{p} E_{1ph,p} \boldsymbol{\lambda_p} \cdot \hat{\boldsymbol{\mu}} \left(\hat{b}_p^\dagger + \hat{b}_p \right). \tag{19}$$

$$\hat{g}_p^{dip} = E_{1ph,p} \boldsymbol{\lambda_p} \cdot \hat{\boldsymbol{\mu}} \tag{20}$$

where $\hat{g}_p^{dip}$ is the dipole truncated analogous of $\hat{g}_p$ (eq. 17) when the molecule is considered as a point dipole. $E_{1ph,p}$ is the single-plasmon electric field amplitude associated to the plasmon mode p, while the polarization of the field associated to mode is $\boldsymbol{\lambda_p}$.

As a test, we will compare the coupling between a spherical nanoparticle and a molecule obtained in three different ways of increasing realism, as sketched in Figure 3:

- Coupling between analytical spherical plasmonic modes and a point-dipole molecule (Figure 3a). This approach was proposed by Delga *et al.*[40]
- Coupling between the plasmonic modes computed at IEF-BEM diagonal level and a point dipole (Figure 3b). This is done to directly compare with the analytical results.
- Coupling between the plasmonic modes computed at IEF-BEM diagonal level and a realistic molecule, computed at EOM-CCSD level (Figure 3c). This is the central feature of this work.

As a test molecule, we take HF due to its simple structure and longitudinal dipolar $S_0 \rightarrow S_1$ transition. Such dipolar behaviour of said transition allows us to compare the coupling computed with the realistic molecule (Figure 3c) to the other cases where the molecule is a point-dipole (Figures 3a and 3b).

Aiming at describing the interaction between plasmon and molecule, we firstly define the states of the non-interacting system. The eigenstates of the non-interacting system are obtained by diagonalization of the non-interacting Hamiltonian $\hat{H}_{mol} + \hat{H}_p$. We shall label

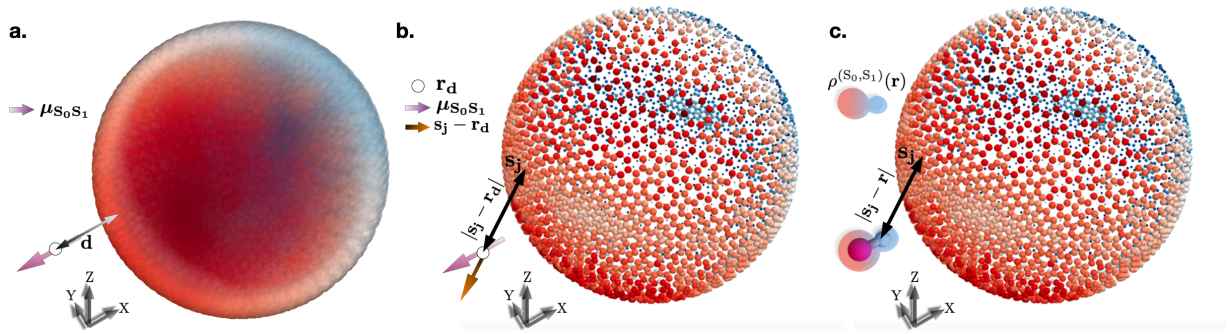

Figure 3: **Dipolar plasmonic mode of a spherical nanoparticle (diameter=10 nm) interacting with a molecule—a)** The molecule is represented as a point dipole distant $\boldsymbol{d}$ from the nanoparticle surface, while the nanoparticle is taken as a continuous Drude-Lorentz metal. The computed coupling is analytical, following ref.[40] **b)-c)** The plasmonic modes are computed at IEF-BEM diagonal level. In Panel **b)**, the molecule is represented as a point dipole corresponding to the $S_0 \rightarrow S_1$ transition dipole moment of the HF molecule. The transition dipole moment $\mu_{S_0S_1} = 1.695$ Debyes is computed at EOM-CCSD level. The EOM-CCSD calculations have been realized by Tor S. Haugland (SNS) using the eT code[54] with a cc-PVTZ basis set. In Panel **c)** The molecule is represented with its $\rho^{(S_0,S_1)}(\boldsymbol{r})$ electronic transition density computed at CCSD level. The plasmon-molecule interactions are accounted via eqs. 19 and 16 for panels **b** and **c**, respectively.

such states as uncoupled states. Such states are expressed as a product states between the molecular electronic states manifold, $\{n\}$, and the Hilbert space of the plasmonic modes:

$$|n, p_1, p_2, ..., p_{N_{mod}}\rangle = |n\rangle \otimes |p_1\rangle \otimes ... \otimes |p_{N_{mod}}\rangle, \tag{21}$$

where n is the electronic state index, p_k denotes the occupation number of the k-th plasmonic mode and N_{mod} is the total number of plasmonic modes. To compute the coupling between the $S_0 \rightarrow S_1$ transition and the nanoparticle, we momentarily focus on a single plasmonic mode of the nanoparticle, $\boldsymbol{q}_p$. The uncoupled states for this reduced system are written as $|n, p\rangle$: n is either the ground state S_0 or the first excited state S_1 of the molecule, while p is the occupation number of the plasmonic mode we are focusing on (either 0 or 1 in this example). Moving to the plasmon-molecule interaction, the interaction elements are evaluated for the three cases presented above and in Figure 3. For the analytical modes and

the point dipole molecule (Figure 3a):

$$g_p^{an,dip} = E_{1ph,p} \left\langle S_0, 1 \left| \hat{g}_p^{dip} b_p^\dagger \right| S_1, 0 \right\rangle = E_{1ph,p} \boldsymbol{\lambda_p} \cdot \boldsymbol{\mu_{S_0,S_1}} \tag{22}$$

where $\boldsymbol{\mu_{S_0,S_1}}$ is the transition point-dipole associated to the $S_0 \rightarrow S_1$ transition in the HF molecule. For the BEM nanoparticle and the point-dipole molecule (Figure 3b):

$$g_p^{bem,dip} = \left\langle S_0, 1 \left| \sum_j q_{p,j} \frac{(\boldsymbol{s_j} - \boldsymbol{r_d}) \cdot \boldsymbol{\mu_{S_0,S_1}}}{|\boldsymbol{s_j} - \boldsymbol{r_d}|^3} b_p^\dagger \right| S_1, 0 \right\rangle = E_{q_p} \boldsymbol{\lambda_{q_p}} \cdot \boldsymbol{\mu_{S_0,S_1}} \tag{23}$$

Here, the plasmonic electric field interacting with the dipole, $E_{q_p}\boldsymbol{\lambda_{q_p}}$, is the electric field associated to the apparent surface charges of the plasmonic mode under investigation $\boldsymbol{q_p}$:

$$E_{q_p} \boldsymbol{\lambda_{q_p}} = \sum_j q_{p,j} \frac{(\boldsymbol{s_j} - \boldsymbol{r_d})}{|\boldsymbol{s_j} - \boldsymbol{r_d}|^3} \tag{24}$$

where $\boldsymbol{s_j} - \boldsymbol{r_d}$ is the distance between the tessera representative point $\boldsymbol{s_j}$ and the position of the point dipole $\boldsymbol{r_d}$. Computing the interaction element between the nanoparticle and a realistic molecule requires to get rid of the point dipole approximation. Put differently, one needs to take into account the spatial features of the transition density (Figure 3c). The interaction element between the BEM mode $\boldsymbol{q_p}$ and a realistic molecule beyond the dipolar approximation then reads:

$$g_p^{bem,full} = \left\langle S_0, 1 \left| \hat{g}_p \hat{b}^\dagger \right| S_1, 0 \right\rangle = \sum_j q_{p,j} V_j^{(S_0,S_1)} \tag{25}$$

where $V_j^{(S_0,S_1)}$ is the potential originated by the $S_0 \rightarrow S_1$ transition on the j-th tessera. The problem is then reduced to find an expression for such potential. To this purpose, it is convenient to describe the local behaviour of the molecule in terms of the one-particle electronic density. The potential acting on the j-th tessera is then the potential associated to the one-particle electron density operator $\hat{\rho}(\boldsymbol{r})$, expanded on the basis of the molecular

orbitals $\phi_r(\boldsymbol{r})$, $\phi_s(\boldsymbol{r})$:

$$\hat{V}_j = \int_{Vol} d^3\boldsymbol{r} \frac{\hat{\rho}(\boldsymbol{r})}{|\boldsymbol{s_j} - \boldsymbol{r}|} = \sum_{rs} \int_{Vol} d^3\boldsymbol{r} \frac{\rho_{rs}(\boldsymbol{r}) \hat{a}_r^\dagger \hat{a}_s}{|\boldsymbol{s_j} - \boldsymbol{r}|} = \sum_{rs} V_j^{rs} \hat{a}_r^\dagger \hat{a}_s. \tag{26}$$

Consequently, the molecule-nanoparticle coupling operator $\hat{g}_p$ can be obtained as:

$$\hat{g}_p = \sum_{rs} g_p^{rs} \hat{a}_r^\dagger \hat{a}_s = \sum_{rs} q_{p,j} V_j^{rs} \hat{a}_r^\dagger \hat{a}_s. \tag{27}$$

The coupling element between the $S_0 \rightarrow S_1$ transition is then evaluated as:

$$g_p^{bem,full} = \left\langle S_0, 1 \left| \sum_{rs} g_p^{rs} \hat{a}_r^\dagger \hat{a}_s \hat{b}^\dagger \right| S_1, 0 \right\rangle = \sum_{rs} \rho_{rs}^{(S_0,S_1)} g_p^{rs}, \tag{28}$$

where we made use of the transition density matrix $\rho_{rs}^{(S_0,S_1)}(\boldsymbol{r})$ to retrieve a similar formalism to the one proposed by Aizpurua and collaborators.[10,32]

The molecule nanoparticle coupling in the classical plasmon framework was described beyond the point approximation before,[55] here we extend it to the quantized plasmon case.

3.1. Comparison to analytical results

As a test case, we take into account a spherical geometry for the nanoparticle. Indeed, the spherical geometry of the nanoparticle causes the plasmonic mode to be degenerate, depending on their angular momentum. By following the notation of A. Delga *et al.*,[40] we consider as l the angular momentum of the quantized nanoparticle, with the plasmonic modes $2l + 1$ degenerate. We compute the analytical coupling values g_l^{an} by grouping the degenerate plasmonic modes by angular momentum. From the derivation presented in ref.,[40] we recast the analytical coupling presented in eq. 29 into:

$$\left(g_l^{an,dip}\right)^2 = \frac{\sqrt{l}(l+1)^2 \mu_{S_0,S_1}^2}{2} \sqrt{\frac{A}{2l+1}} \frac{r_s^{(2l+1)}}{d^{(2l+4)}}; \tag{29}$$

where l is the angular momentum associated to the nanoparticle plasmonic modes manifold (three dipolar modes, five quadrupolar modes and so on) and A is the Drude-Lorentz parameter determining ω_p (eq. 7). Here r_s and d are respectively the radius of the sphere and the distance of the point dipole from the nanoparticle surface.

To directly compare to the analytical ($g_l^{an,dip}$) value, we need to compute the interaction with the same modes, hence taking into account the degeneracy of the sphere. To this aim, we group the squared values of $g_p^{bem,dip}$ and $g_p^{bem,full}$ by angular momentum, respectively obtaining $(g_l^{bem,dip})^2$ and $(g_l^{full,dip})^2$. In Figure 5a, we compare the values of $(g_l)^2$ for the three models. As plasmonic modes, we take the $l = 1$ (dipolar modes) and $l = 2$ (quadrupolar modes).

A good agreement between analytical model and the BEM variants is shown for both the interaction elements with $\ell = 1$ and $\ell = 2$ up to $\sim$3 $\mathring{A}$ distance, comparable to the molecule-nanoparticle distance in plasmonic nanocavities and TERS setups.[10,56,57] For real molecules, shorter distances would not be realistic anyway. The same behaviour is shown for both the variants of the coupling computed with the BEM plasmonic modes. The choice of a dipole-like molecule as HF ensures that no major effects due to the shape of the transition density arise. Indeed, no difference is displayed when moving from point-dipole molecule ($g^{bem,dip}$) to the full molecular description ($g^{bem,full}$). The difference from the analytical model is then due to the numerical accuracy of the BEM calculation, in turn related the surface density of the tesserae. The effect becomes evident in Figure 5b, where we show the molecule-nanoparticle interaction for $\ell = 1$ obtained by varying the density of tesserae (and hence of apparent surface charges). An increase in the quality of the description is obtained by increasing the number of tesserae from two thousands to seven thousands. A further improvement is observed by inhomogeneously distributing the seven thousand tesserae on the spherical surface, thickening the mesh close to the molecule. In such last case, the agreement

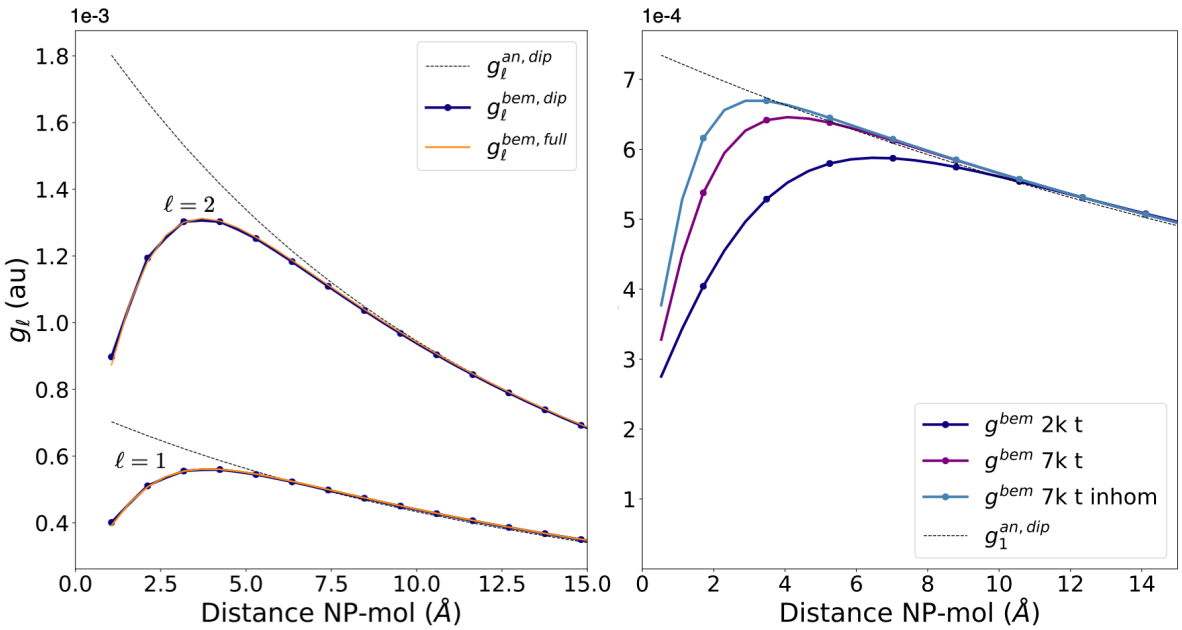

Figure 4: **Interaction between a molecule and the $\ell = 1$ (dipolar), $\ell = 2$ (quadrupolar) plasmonic modes of a nanosphere (diameter=10 nm)**— **a** Comparison between the analytical value reported in (dashed black line) with the $g_\ell^{bem,dip}$ and $g_\ell^{full,dip}$. **b** Interaction element for the $\ell = 1$ for the same case. The number of tesserae is increased from two thousands (labelled as 2k t, blue line) to seven thousands (labelled as 7k t, purple line). An even closer agreement between the analytical model and the BEM-based model is obtained by keeping seven thousands tesserae and making the mesh denser close to the molecule(labelled as 7k t inhom, light blue line).

between the analytical model and the BEM-based one holds down to ~ 2.5 $\mathring{A}$, which is even smaller than the typical non-bond distances of $3.5\mathring{A}$. The great accuracy achieved for a very dipolar-like molecule such as HF ensures a reliable interaction in the near-field.

3.2. Quantum coupling between a nanotip and azobenzene

As a last case, we take the plasmonic mode of the nanotip shown in Figure 2b (left panel) and let it interact with two mostly dark transitions of the azobenzene molecule: $S_0 \rightarrow S_1$ and $S_0 \rightarrow S_3$. Despite the low coupling magnitude expected due to the dark transitions, the choice of dark transitions allows to highlight the limits of neglecting the full structure of the molecule. To this aim, we take two different molecular representations: point-dipole and

realistic. For both cases, the molecular properties are computed via the FOMO-CI semiempirical method[35,36] we already exploited in previous works as a basis for photochemistry in the strong coupling regime.[19,30] The reason of the choice is the high-level of the description of the azobenzene coming from the *ad-hoc* parameterization.[58]

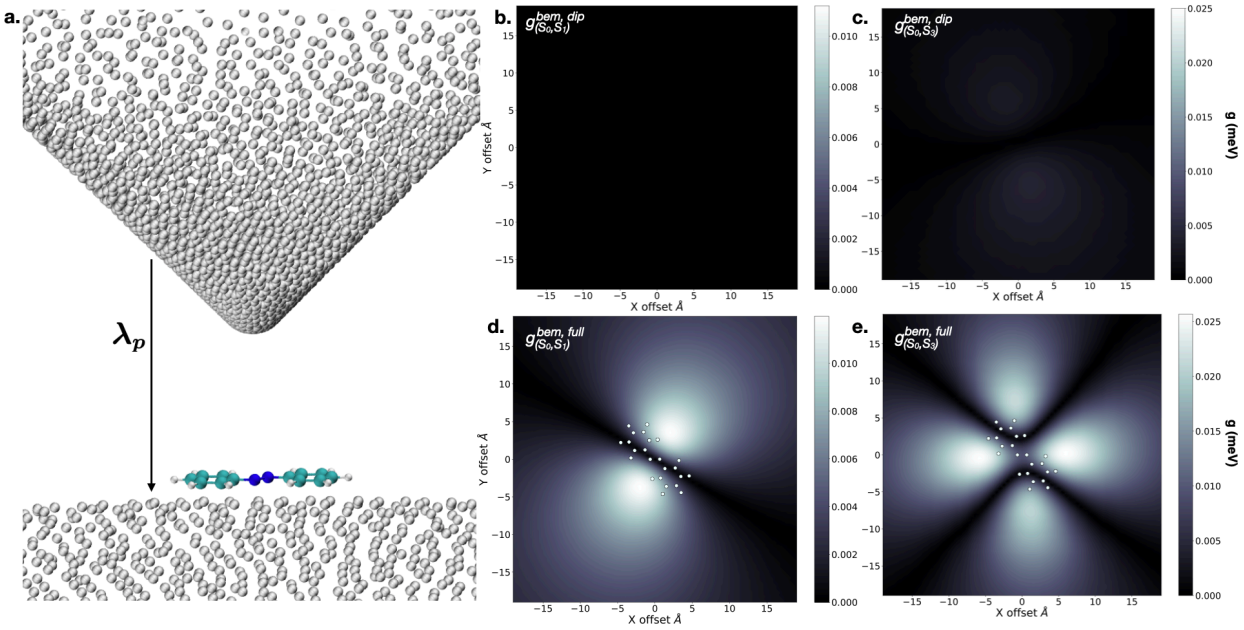

Figure 5: **Quantum Interaction between two dark transitions of azobenzene and a nanotip- a)** Sketch of the setup with the *trans*-azobenzene in a C_{2h} configuration and lies on the plane perpendicular to the rotational axis of the tip. **b)**, **c)** Maps of the interaction between the plasmonic mode shown in Figure 2b (left) and the $S_0 \rightarrow S_1$ and $S_0 \rightarrow S_3$ molecular transitions, respectively. Here the molecule is represented as a point-dipole. The maps are obtained by displacing the tip with respect to the molecule. The maps in panels **d)** and **e)** are the maps for the same transitions when the full electronic transition density is taken into account.

The azobenzene molecule is taken in its *trans*-planar equilibrium configuration and it lies on the plane perpendicular to the rotational axis of the tip (Figure 5a). Instead, the polarization ($\boldsymbol{\lambda_p}$) of the electric field associated to the plasmonic mode is perpendicular to the plane containing the molecule (Figure 5a) and oriented along the rotational axis of the tip. The point-dipole representation is obtained by taking the transition dipole moments obtained through the FOMO-CI calculation and by locating the point-dipole vector at the

center of mass of the molecule. For the full representation, we take the whole transition density of the molecule expanded on the Molecular Orbitals (MO) basis. The nanoparticle-molecule interaction elements for the two representations are then respectively computed via eqs. 23 and 28. Namely, we label them as $g^{bem,dip}_{(S_0,S_1)}$ $\left(g^{bem,dip}_{(S_0,S_3)}\right)$ and $g^{bem,full}_{S_0,S_1}$ $\left(g^{bem,full}_{S_0,S_3}\right)$ as they refer to the $S_0 \rightarrow S_1$ ($S_0 \rightarrow S_3$) molecular transition. At the molecular geometry in exam, azobenzene displays a totally dark $S_0 \rightarrow S_1$ optical transition due to symmetry. At the same geometry, the $S_0 \rightarrow S_3$ transition is almost vanishing, even if it conserves a very small ($\sim$0.02 Debye) $S_0 \rightarrow S_3$ transition dipole moment component in the plane containing the molecule.

In Figures 5b and 5c, we show the interaction computed with the point-dipole representation, respectively for the $S_0 \rightarrow S_1$ and $S_0 \rightarrow S_3$ transitions. The interaction maps are obtained by displacing the tip with respect to the molecule and exploring its surroundings. As the $S_0 \rightarrow S_1$ is completely dark, no interaction between the nanoparticle and the point-dipolar molecule arises at any geometry (Figure 5b). Instead, a very weak dipolar-like interaction is observed for the $S_0 \rightarrow S_3$ transition.

The maps reported in Figures 5d and 5e represent the same interaction when taking the full transition density of the molecule. In particular, the map in Figure 5d is referred to the $S_0 \rightarrow S_1$ transition, while Figure 5e is referred to $S_0 \rightarrow S_3$. Rather straightforwardly, major differences are present when comparing the interactions in the two representation for the two transition cases. While the $S_0 \rightarrow S_1$ in the dipolar representation does not interact at all with the nanoparticle, a weak dipolar-like interaction arises when taking the transition density of the molecule. Even more interesting is the case of the $S_0 \rightarrow S_3$ transition: the interaction in the realistic representation is quadrupolar, whereas the point-dipole case is flattened to a dipolar transition. Both of such differences are indeed due to the spatial features of the transition density of the molecule, since the nanoparticle treatment is the same in both cases.

To qualitatively understand the shape of the interaction maps, we sketch the approximated electronic transition densities associated to $S_0 \rightarrow S_1$ and $S_0 \rightarrow S_3$ respectively in Figure 6a and Figure 6b.

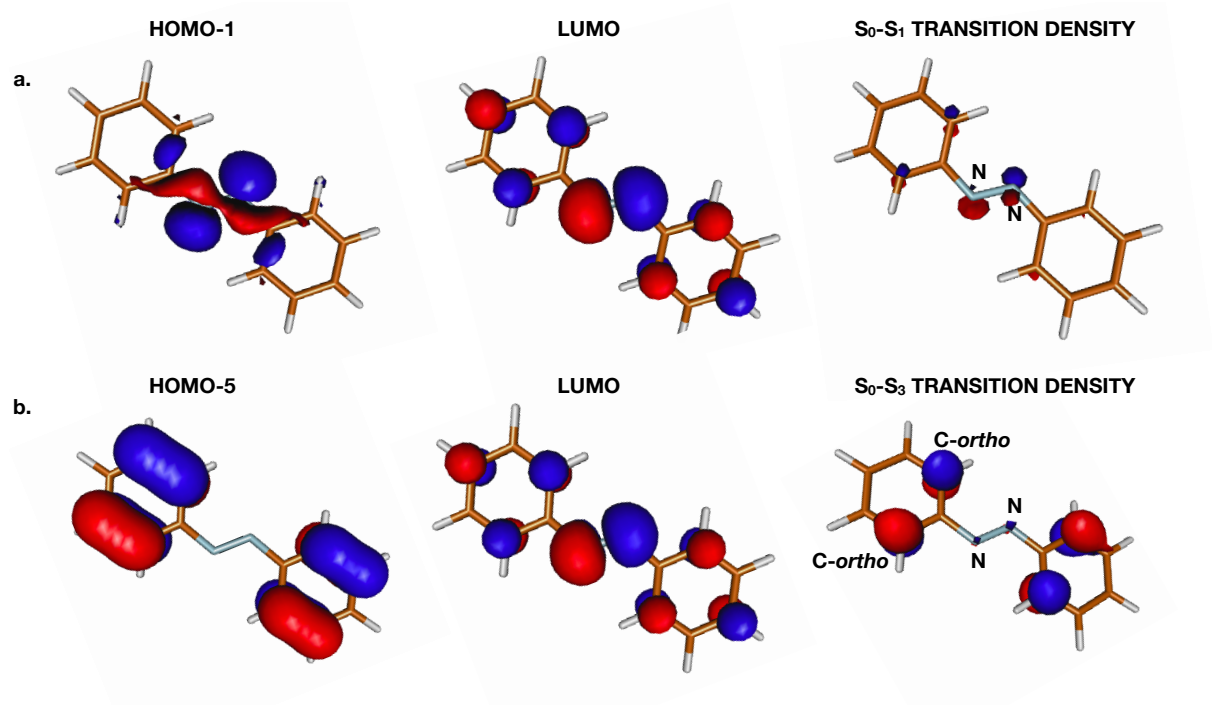

Figure 6: **Sketch of the $S_0 \rightarrow S_1$ and $S_0 \rightarrow S_3$ transition densities-a)** The $S_0 \rightarrow S_1$ transition density is well approximated as a product of the $HOMO-1$ and $LUMO$ orbitals and it is mostly dipolar along the direction perpendicular to the N=N bond. **b)** The $S_0 \rightarrow S_3$ transition density is mostly quadrupolar. This density is approximated by the product of the $HOMO-5$ and $LUMO$ orbitals which govern the transition. The poles of the quadrupole sit on the C atoms in *ortho* position with respect to the N atoms.

Although computed at a multiconfigurational wavefunction level, the $S_0 \rightarrow S_1$ and $S_0 \rightarrow S_3$ transitions are respectively governed by the $HOMO-1 \rightarrow LUMO$ and the $HOMO-5 \rightarrow LUMO$ excitations. As a consequence, the product of the molecular orbitals involved in each transition is a good approximation to the full transition density, which is instead exploited in the calculation of the interaction. Figure 6 shows the $HOMO-1 \rightarrow LUMO$ orbitals and product, associated to $S_0 \rightarrow S_1$. Indeed, the shape of the approximated $S_0 \rightarrow S_1$ is dipolar and it is oriented in-plane and perpendicular to the N=N double bond of azobenzene. Directly comparing to the map in Figure 5d with this

density, we then see why displacing the tip with respect to the molecular center would yield a dipolar interaction for the $S_0 \rightarrow S_1$ transition. The same considerations can be applied to the $S_0 \rightarrow S_3$ transition density: indeed, the product between the $HOMO - 5$ and $LUMO$ orbitals governing the transition yields a quadrupolar shape to the approximated transition density, with the poles of the quadrupole sitting on the C atoms in *ortho* position with respect to the N=N double bond. The same quadrupolar-like shape is well reproduced by the interaction maps in Figure 5e. Even more, a careful analysis of the interaction map reveals a region of minor interaction on located on the N=N double bond, corresponding to the barely-visible component of $S_0 \rightarrow S_3$ transition density on the same bond.

This simple example allows us to comment on two features of the method: firstly, our formulation of the interaction clearly accounts for the spatial features of the molecular transition density. Secondly, the IEF-BEM diagonal correctly accounts for the different charge density associated to different modes down to the atomic level. Indeed, if any of the aspects was absent, we would not be able to reproduce the correct shape of the transition density. Our results prove that the proposed method is an advantageous tool to compute nanoparticle-molecule interaction which requires few computational effort to treat the nanoparticle-molecule interaction with sub-molecular resolution.

4. Conclusions

In this work we have introduced a new methodology to treat the quantum coupling between nanoparticle setups of arbitrary shape and realistic molecules. We have adapted a diagonal formulation coming from the polarizable continuum model community[55,59] to directly obtain quantized plasmonic modes. Here, we represent the plasmonic mode as individual sets of independent charges sitting on the nanoparticle surface, which allows us to treat inhomogeneities of the electromagnetic field due to the shape and setups of the nanoparticles. By

exploiting such intuitive representation of the plasmonic modes as set of charges, we reformulated the quantum interaction between molecules and plasmonic modes with a more general formalism. The strength of this reformulation is to rewrite the interaction terms on the basis of the molecular orbitals. Two major advantages arise from this approach: the principal is to account for local changing in the molecular electronic density due to the presence of a nanoparticle of arbitrary shape, achieving a sub-molecular resolution in the quantum coupling. The second is that it can be easily interfaced with high-accuracy quantum chemistry methods.

As a test case, we compared the results of our formulation to the analytical results for a spherical nanoparticle and a point-dipole molecule, reaching great agreement for distances even smaller of the normal non-bonding distance (~ 3.5 $\mathring{A}$). To prove the necessity of moving beyond the dipolar formulation, we took the interaction of a nanotip and two dark transitions of the azobenzene molecule. Here, we observed a major difference between the dipolar interaction and our model. In particular, the dipolar approximation fails in describing the coupling in both cases, where our presented model reproduces well the features of the transition density.

This approach, motivated by the encouraging results, has the simplicity and flexibility to be interfaced with more complex simulation frameworks. Indeed, it has the potential to bring the simulation of nanoparticle-molecule systems to an even higher level of realism. It does not lack a high capability of supporting experiments trying to both investigate and manipulate the chemical properties at the sub-molecular level. Such experiments range from the reproduction of typical TERS setups[7,8,10,11] to molecules in nanocavities.[3,4,31,56]

References

(1) Tame, M.; Mcenery, K. R.; Ozdemir, S.; Lee, J.; Maier, S.; Kim, M. Quantum plasmonics. *Nat. Phys.* **2013**, *9*, 329–340.

(2) Hugall, J. T.; Singh, A.; van Hulst, N. F. Plasmonic Cavity Coupling. *ACS Photonics* **2018**, *5*, 43–53.

(3) Benz, F.; Schmidt, M. K.; Dreismann, A.; Chikkaraddy, R.; Zhang, Y.; Demetriadou, A.; Carnegie, C.; Ohadi, H.; de Nijs, B.; Esteban, R.; Aizpurua, J.; Baumberg, J. J. Single-molecule optomechanics in "picocavities". *Science* **2016**, *354*, 726–729.

(4) Carnegie, C.; Griffiths, J.; de Nijs, B.; Readman, C.; Chikkaraddy, R.; Deacon, W. M.; Zhang, Y.; Szabó, I.; Rosta, E.; Aizpurua, J.; Baumberg, J. J. Room-Temperature Optical Picocavities below 1 nm3 Accessing Single-Atom Geometries. *J. Phys. Chem. Lett.* **2018**, *9*, 7146–7151.

(5) Campion, A.; Kambhampati, P. Surface-enhanced Raman scattering. *Chem. Soc. Rev.* **1998**, *27*, 241–250.

(6) Otto, A.; Mrozek, I.; Grabhorn, H.; Akemann, W. Surface-enhanced Raman scattering. *J. Phys. Condens. Matter* **1992**, *4*, 1143–1212.

(7) Zrimsek, A. B.; Chiang, N.; Mattei, M.; Zaleski, S.; McAnally, M. O.; Chapman, C. T.; Henry, A.-I.; Schatz, G. C.; Van Duyne, R. P. Single-Molecule Chemistry with Surface- and Tip-Enhanced Raman Spectroscopy. *Chem. Rev.* **2017**, *117*, 7583–7613.

(8) Verma, P. Tip-Enhanced Raman Spectroscopy: Technique and Recent Advances. *Chem. Rev.* **2017**, *117*, 6447–6466.

(9) Li, J.-F.; Li, C.-Y.; Aroca, R. F. Plasmon-enhanced fluorescence spectroscopy. *Chem. Soc. Rev.* **2017**, *46*, 3962–3979.

(10) Doppagne, B.; Neuman, T.; Soria-Martinez, R.; López, L. E. P.; Bulou, H.; Romeo, M.; Berciaud, S.; Scheurer, F.; Aizpurua, J.; Schull, G. Single-molecule tautomerization tracking through space- and time-resolved fluorescence spectroscopy. *Nat. Nanotechnol.* **2020**, *15*, 207–211.

(11) Chen, X.; Liu, P.; Hu, Z.; Jensen, L. High-resolution tip-enhanced Raman scattering probes sub-molecular density changes. *Nat. Commun.* **2019**, *10*, 2567.

(12) Hutchison, J. A.; Schwartz, T.; Genet, C.; Devaux, E.; Ebbesen, T. W. Modifying Chemical Landscapes by Coupling to Vacuum Fields. *Angew. Chem. Int. Ed.* **2012**, *51*, 1592.

(13) Galego, J.; Garcia-Vidal, F. J.; Feist, J. Cavity-Induced Modifications of Molecular Structure in the Strong-Coupling Regime. *Phys. Rev. X* **2015**, *5*, 041022.

(14) Climent, C.; Galego, J.; Garcia-Vidal, F. J.; Feist, J. Plasmonic Nanocavities Enable Self-Induced Electrostatic Catalysis. *Angew. Chem. Int. Ed.* **2019**, *58*, 8698–8702.

(15) Thomas, A.; George, J.; Shalabney, A.; Dryzhakov, M.; Varma, S. J.; Moran, J.; Chervy, T.; Zhong, X.; Devaux, E.; Genet, C.; Hutchison, J. A.; Ebbesen, T. W. Ground-State Chemical Reactivity under Vibrational Coupling to the Vacuum Electromagnetic Field. *Angew. Chem. Int. Ed.* **2016**, *55*, 11462–11466.

(16) Schwartz, T.; Hutchison, J. A.; Genet, C.; Ebbesen, T. W. Reversible Switching of Ultrastrong Light-Molecule Coupling. *Phys. Rev. Lett.* **2011**, *106*, 196405.

(17) Ribeiro, R. F.; Martínez-Martínez, L. A.; Du, M.; Campos-Gonzalez-Angulo, J.; Yuen-

Zhou, J. Polariton chemistry: controlling molecular dynamics with optical cavities. *Chem. Sci.* **2018**, *9*, 6325–6339.
(18) Yuen-Zhou, J.; Menon, V. M. Polariton chemistry: Thinking inside the (photon) box. *Proc. Natl. Acad. Sci. USA* **2019**, *116*, 5214–5216.
(19) Fregoni, J.; Granucci, G.; Persico, M.; Corni, S. Strong Coupling with Light Enhances the Photoisomerization Quantum Yield of Azobenzene. *Chem* **2019**,
(20) Dunkelberger, A. D.; Spann, B. T.; Fears, K. P.; Simpkins, B. S.; Owrutsky, J. C. Modified relaxation dynamics and coherent energy exchange in coupled vibration-cavity polaritons. *Nat. Commun.* **2016**, *7*, 13504.
(21) Gu, B.; Mukamel, S. Manipulating nonadiabatic conical intersection dynamics by optical cavities. *Chem. Sci.* **2020**, *11*, 1290–1298.
(22) Groenhof, G.; Climent, C.; Feist, J.; Morozov, D.; Toppari, J. J. Tracking Polariton Relaxation with Multiscale Molecular Dynamics Simulations. *J. Phys. Chem. Lett.* **2019**, *10*, 5476–5483.
(23) Groenhof, G.; Climent, C.; Feist, J.; Morozov, D.; Toppari, J. J. Tracking Polariton Relaxation with Multiscale Molecular Dynamics Simulations. *J. Phys. Chem. Lett.* **2019**, *10*, 5476–5483.
(24) Luk, H. L.; Feist, J.; Toppari, J. J.; Groenhof, G. Multiscale Molecular Dynamics Simulations of Polaritonic Chemistry. *J. Chem. Theor. Comput.* **2017**, *13*, 4324–4335.
(25) Coccia, E.; Corni, S. Role of coherence in the plasmonic control of molecular absorption. *J. Chem. Phys.* **2019**, *151*, 044703.
(26) Vendrell, O. Coherent dynamics in cavity femtochemistry: Application of the multiconfiguration time-dependent Hartree method. *Chem. Phys.* **2018**, *509*, 55 – 65.
(27) Zhang, P.; Protsenko, I.; Sandoghdar, V.; Chen, X.-W. A Single-Emitter Gain Medium for Bright Coherent Radiation from a Plasmonic Nanoresonator. *ACS Photonics* **2017**, *4*, 2738–2744.
(28) Hertzog, M.; Wang, M.; Mony, J.; Börjesson, K. Strong lightmatter interactions: a new direction within chemistry. *Chem. Soc. Rev.* **2019**, *48*, 937–961.
(29) Herrera, F.; Owrutsky, J. Molecular polaritons for controlling chemistry with quantum optics. *J. Chem. Phys.* **2020**, *152*, 100902.
(30) Fregoni, J.; Granucci, G.; Coccia, E.; Persico, M.; Corni, S. Manipulating azobenzene photoisomerization through strong light–molecule coupling. *Nat. Commun.* **2018**, *9*, 4688.
(31) Ojambati, O. S.; Chikkaraddy, R.; Deacon, W. D.; Horton, M.; Kos, D.; Turek, V. A.; Keyser, U. F.; Baumberg, J. J. Quantum electrodynamics at room temperature coupling a single vibrating molecule with a plasmonic nanocavity. *Nat. Commun.* **2019**, *10*, 1049.
(32) Neuman, T.; Esteban, R.; Casanova, D.; García-Vidal, F. J.; Aizpurua, J. Coupling of Molecular Emitters and Plasmonic Cavities beyond the Point-Dipole Approximation. *Nano Lett.* **2018**, *18*, 2358–2364.
(33) Corni, S.; Pipolo, S.; Cammi, R. Equation of Motion for the Solvent Polarization Apparent Charges in the Polarizable Continuum Model: Application to Real-Time TDDFT. *J. Phys. Chem. A* **2015**, *119*, 5405–5416.
(34) Pipolo, S.; Corni, S. Real-Time Description of the Electronic Dynamics for a Molecule Close to a Plasmonic Nanoparticle. *J. Phys. Chem. C* **2016**, *120*, 28774–28781.
(35) Granucci, G.; Persico, M.; Toniolo, A. Direct semiclassical simulation of photochemical

processes with semiempirical wave functions. *J. Chem. Phys.* **2001**, *114*, 10608–10615.
(36) Granucci, G.; Toniolo, A. Molecular gradients for semiempirical CI wavefunctions with floating occupation molecular orbitals. *Chem. Phys. Lett.* **2000**, *325*, 79–85.
(37) Koch, H.; Jorgensen, P. Coupled cluster response functions. *J. Chem. Phys.* **1990**, *93*, 3333–3344.
(38) Koch, H.; Kobayashi, R.; Sanchez de Mers, A.; Jorgensen, P. Calculation of sizeintensive transition moments from the coupled cluster singles and doubles linear response function. *J. Chem. Phys.* **1994**, *100*, 4393–4400.
(39) Caricato, M. Exploring Potential Energy Surfaces of Electronic Excited States in Solution with the EOM-CCSD-PCM Method. *J. Chem. Theor. Comput.* **2012**, *8*, 5081–5091.
(40) Delga, A.; Feist, J.; Bravo-Abad, J.; Garcia-Vidal, F. J. Quantum Emitters Near a Metal Nanoparticle: Strong Coupling and Quenching. *Phys. Rev. Lett.* **2014**, *112*, 253601.
(41) Hohenester, U.; Trügler, A. MNPBEM A Matlab toolbox for the simulation of plasmonic nanoparticles. *Comput. Phys. Commun.* **2012**, *183*, 370 – 381.
(42) Waxenegger, J.; Trügler, A.; Hohenester, U. Plasmonics simulations with the MNPBEM toolbox: Consideration of substrates and layer structures. *Comput. Phys. Commun.* **2015**, *193*, 138 – 150.
(43) Boyd, R. W. *Nonlinear Optics, Third Edition*, 3rd ed.; Academic Press, Inc.: USA, 2008; pp 135–171.
(44) Guido, C.; Rosa, M.; Cammi, R.; Corni, S. An open quantum system theory for polarizable continuum models. *J. Chem. Phys.* **2020**, *152*.
(45) Parr, R. G. Density Functional Theory of Atoms and Molecules. Horizons of Quantum Chemistry. Dordrecht, 1980; pp 210–213.
(46) Kristensen, K.; Kauczor, J.; Thorvaldsen, A. J.; Jorgensen, P.; Kjaergaard, T.; Rizzo, A. Damped response theory description of two-photon absorption. *J. Chem. Phys.* **2011**, *134*, 214104.
(47) Huttner, B.; Barnett, S. M. Quantization of the electromagnetic field in dielectrics. *Phys. Rev. A* **1992**, *46*, 4306–4322.
(48) Dung, H. T.; Knöll, L.; Welsch, D.-G. Three-dimensional quantization of the electromagnetic field in dispersive and absorbing inhomogeneous dielectrics. *Phys. Rev. A* **1998**, *57*, 3931–3942.
(49) Alpeggiani, F.; Andreani, L. C. Quantum Theory of Surface Plasmon Polaritons: Planar and Spherical Geometries. *Plasmonics* **2014**, *9*, 965–978.
(50) Tavis, M.; Cummings, F. W. Exact Solution for an N-Molecule—Radiation-Field Hamiltonian. *Phys. Rev.* **1968**, *170*, 379–384.
(51) Garraway, B. M. The Dicke model in quantum optics: Dicke model revisited. *Philos. Trans. R. Soc. A* **2011**, *369*, 1137–1155.
(52) Kowalewski, M.; Bennett, K.; Mukamel, S. Non-adiabatic dynamics of molecules in optical cavities. *J. Chem. Phys.* **2016**, *144*, 054309.
(53) Herrera, F.; Spano, F. C. Absorption and photoluminescence in organic cavity QED. *Phys. Rev. A* **2017**, *95*, 053867.
(54) Folkestad, S. D. et al. eT 1.0: an open source electronic structure program with emphasis on coupled cluster and multilevel methods. 2020.

(55) Corni, S.; Tomasi, J. Enhanced response properties of a chromophore physisorbed on a metal particle. *J. Chem. Phys.* **2001**, *114*, 3739–3751.
(56) Chikkaraddy, R.; de Nijs, B.; Benz, F.; Barrow, S. J.; Scherman, O. A.; Rosta, E.; Demetriadou, A.; Fox, P.; Hess, O.; Baumberg, J. J. Single-molecule strong coupling at room temperature in plasmonic nanocavities. *Nature* **2016**, *535*, 127.
(57) Hugall, J. T.; Singh, A.; van Hulst, N. F. Plasmonic Cavity Coupling. *ACS Photonics* **2018**, *5*, 43–53.
(58) Cusati, T.; Granucci, G.; Martínez-Núñez, E.; Martini, F.; Persico, M.; Vázquez, S. Semiempirical Hamiltonian for Simulation of Azobenzene Photochemistry. *J. Phys. Chem. A* **2012**, *116*, 98.
(59) Tomasi, J.; Mennucci, B.; Cammi, R. Quantum Mechanical Continuum Solvation Models. *Chem. Rev.* **2005**, *105*, 2999–3094.

Future developments

Further developments of the method are currently being addressed on three fronts:

- The interface between the approach for quantum coupling treated in this Chapter and the polaritonic photochemistry machinery presented in Chapter 1 is currently being devised. Currently, the interface I realized only achieves single-point calculations on the system, as shown in the interaction maps in Figure 5. The further development is to derive and implement the analytical gradients approach for polaritonic photochemistry with a IEF-BEM nanoparticle. The implementation is in collaboration with Giovanni Granucci and Maurizio Persico at the University of Pisa.

- To overcome the limitations due to a Drude-Lorentz dielectric constant for the choice of the metal, a fitting approach with a generalized dielectric constant has been implemented by Giulia Dall'Osto and Gabriel Gil (Unipd) for the BEM computation of the interaction between a classical nanoparticle and a quantum molecule. We plan to extend it to the quantum coupling in the near future.

- To achieve a more general and higher level of accuracy in the molecular description, we are currently interfacing this interaction scheme with the EOM-CCSD method in collaboration with Tor Haugland and Prof. Henrik Koch in Scuola Normale Superiore (Pisa). The results of the interaction maps for the free-base porphyrin molecule are currently in production. The aim of this part of the project is to develop a tool to investigate changes in the electronic structure and even ground state properties of molecules in strong coupling. While the high accuracy of the EOM-CCSD approach ensures the quality in the molecular description, the extension of the BEM approach to generic dielectric constants ensures to simulate nanoparticles in experimental conditions. Consequently, the interface of BEM with EOM-CCSD is expected to provide a benchmark for realistic coupling conditions without assuming parameters.

Summary and Conclusions

This thesis is devoted to the development of a method able to tackle the photochemical complexity in polaritonic photochemistry simulations. To this aim, different layers of complexity have been taken into account.

Firstly, the computation of the polaritonic states and energies are computed by adapting a quick-yet-accurate multiconfigurational wavefunction method relying on a semiempirical electronic Hamiltonian and floating occupation numbers for the SCF calculation. To simulate polaritonic photochemistry, the Direct Trajectory Surface Hopping method has been extended to tackle both the intrinsic transition probability and overcoherence biases of the more traditional Fewest-Switches Surface-Hopping.

My original contribution in this field dealt with the theoretical development and implementation in scientific codes to extend such methods, together with devising and developing the interpretative tools to recover the chemical intuition in polaritonic systems. Such tools have proven to be a valid aid for investigating the changes in photochemical reaction mechanisms induced by strong light-molecule coupling. Even more, the devised method has proven useful to include and interpret all the photochemical and environmental complexity in the simulated reaction. Initially, we approached the problem by deriving the relevant quantities such as polaritonic eigenstates and eigenvalues, trying to map the diabatic/adiabatic behaviour to the polaritonic case and recover a chemical picture. In this process, we adapted the non-adiabtic dynamics technique to the polaritonic case by deriving the analytical gradients for the polaritonic energy. In the beginning we took into account only few molecular states and a singly-occupied photonic mode. That was sufficient to glimpse at the modified dynamics. Motivated by the chemically-friendly method, we then moved to include various features of the photochemical and environmental complexities: multiple states in the simulations, mimicking of the excitation process, environment and losses.

We have shown that, with different cavity parameters, a photoisomerization reaction can be selectively quenched or enhanced. Also, we have exploited the direct correspondence of electronic states and polaritonic states in the uncoupled representation and several *ad-hoc* tools of analysis to give an intuitive chemical explanation of the mechanism leading to both the quenching and the enhancement. While the quenching occurs because the modified shape of the PESs leads to a trap of the wavepacket, the mechanism leading to the enhancement is more involved. An intuitive explanation is that strong coupling intrinsically quenches some reaction channels in a polaritonic photochemical reaction. In such regards, we made use of the quenching effect to deactivate a fast relaxation channel of the *trans-cis* photoisomerization reaction, which would normally lead to an inefficient photoisomerization. By the deactivation of this relaxation channel, we are able to achieve a remarkably higher quantum yield for the same process.

Aiming to describe the system even more realistically, and taking into account the state-of-the-art direction in experiments, we decided to move on two fronts. On one hand, we refined the method by including the mode with a higher occupation number and exploited a quatum optics Monte Carlo approach to account for cavity losses. On the second front, we aim at investigating how strong coupling can can be locally achieved at the sub-molecular level. To this aim, we devised a method to quantize the plasmonic modes coming from classical electrodynamics calculation. This approach is based on previous works in the field of the solvent-molecule interaction, as well as on state-of-the-art works in the molecular polaritonics community. The tests and results obtained so far are already enough to investigate optical properties of molecules in cavities. However, the aim is to interface this hybrid classical electrodynamics-quantum chemistry method to the Surface Hopping machinery to also investigate dynamical processes. As a perspective on the nanoparticle-molecule interaction, we aim at explicitly treating the interaction of few quantized plasmonic modes with

the molecule. The other modes can be then described as an effective dissipative mode, as depicted by Delga *et al.*

Finally, during my last year of PhD I could also explore the non-adiabatic dynamics on few molecular modes by resorting to a full quantum approach. The work was mostly conducted during a visit in collaboration with Dr. Simone Felicetti and Dr. Johannes Feist at IFIMAC (Universidad Autonoma de Madrid). The visit helped me consolidating the knowledge on strong light-molecule coupling models and Quantum Optics approaches interfaced with grid methods to propagate a fully quantum wavefunction. The results are not reported in the present work, although a first publication is expected for the near to medium future.

The approach introduced here investigates the photochemical properties of polaritonic systems at an unprecedented level of realism. With respect to the up-to-date state of the art, the methodology developed led to discover a novel reactivity pathway resulting in enhanced photoisomerization quantum yields, which was hidden in the chemical complexity. Even more, the high level of description allowed to dig into the reaction mechanism and, consequently, to understand how to turn the chemical complexity from a foe to a friend. This was realized by also including environmental effects of a realistic experimental setup. In conclusion, the method presented in this thesis carries the promise to both guide and support challenging experiments in the emerging-yet-propitious field of polaritonic chemistry, together with providing a powerful tool of analysis to disentangle the richness of polaritonic phenomenology.

Bibliography

(1) Partington, J. R. History of Chemistry. In *A History of Chemistry by J. R. Partington*; St Martin's Press Inc,, Ed.; Macmillan Publishers Limited, 1964.
(2) Dirac, P. *The Principles of Quantum Mechanics*; Comparative Pathobiology - Studies in the Postmodern Theory of Education; Clarendon Press, 1981.
(3) Hecht, J. *Applied optics* **2010**, *49*, F99–122.
(4) Yu, H.; Peng, Y.; Yang, Y.; Li, Z.-Y. *npj Comput. Mater.* **2019**, *5*, 45.
(5) Li, J.-F.; Li, C.-Y.; Aroca, R. F. *Chem. Soc. Rev.* **2017**, *46*, 3962–3979.
(6) Campion, A.; Kambhampati, P. *Chem. Soc. Rev.* **1998**, *27*, 241–250.
(7) Etchegoin, P. G.; Le Ru, E. C. *Phys. Chem. Chem. Phys.* **2008**, *10*, 6079–6089.
(8) Zrimsek, A. B.; Chiang, N.; Mattei, M.; Zaleski, S.; McAnally, M. O.; Chapman, C. T.; Henry, A.-I.; Schatz, G. C.; Van Duyne, R. P. *Chem. Rev.* **2017**, *117*, 7583–7613.
(9) Verma, P. *Chem. Rev.* **2017**, *117*, 6447–6466.
(10) Hutchison, J. A.; Schwartz, T.; Genet, C.; Devaux, E.; Ebbesen, T. W. *Angew. Chem. Int. Ed.* **2012**, *51*, 1592.
(11) Schwartz, T.; Hutchison, J. A.; Genet, C.; Ebbesen, T. W. *Phys. Rev. Lett.* **2011**, *106*, 196405.
(12) Chikkaraddy, R.; de Nijs, B.; Benz, F.; Barrow, S. J.; Scherman, O. A.; Rosta, E.; Demetriadou, A.; Fox, P.; Hess, O.; Baumberg, J. J. *Nature* **2016**, *535*, 127.
(13) Ojambati, O. S.; Chikkaraddy, R.; Deacon, W. D.; Horton, M.; Kos, D.; Turek, V. A.; Keyser, U. F.; Baumberg, J. J. *Nat. Commun.* **2019**, *10*, 1049.
(14) Fregoni, J.; Granucci, G.; Coccia, E.; Persico, M.; Corni, S. *Nat. Commun.* **2018**, *9*, 4688.
(15) Fregoni, J.; Granucci, G.; Persico, M.; Corni, S. *Chem* **2019**,
(16) Delga, A.; Feist, J.; Bravo-Abad, J.; Garcia-Vidal, F. J. *Phys. Rev. Lett.* **2014**, *112*, 253601.
(17) Feist, J.; Galego, J.; Garcia-Vidal, F. J. *ACS Photonics* **2018**, *5*, 205.
(18) Luk, H. L.; Feist, J.; Toppari, J. J.; Groenhof, G. *J. Chem. Theory Comput.* **2017**, *13*, 4324–4335.
(19) Groenhof, G.; Climent, C.; Feist, J.; Morozov, D.; Toppari, J. J. *The J. Chem. Phys. Lett.* **2019**, *10*, 5476–5483.
(20) Jaynes, E. T.; Cummings, F. W. *Proc. IEEE* **1963**, *51*, 89.
(21) Rabi, I. I. *Phys. Rev.* **1936**, *49*, 324–328.
(22) Dicke, R. H. *Phys. Rev.* **1954**, *93*, 99–110.
(23) Tavis, M.; Cummings, F. W. *Phys. Rev.* **1968**, *170*, 379–384.
(24) Hohenester, U.; Trgler, A. *Comput. Phys. Commun.* **2012**, *183*, 370 – 381.
(25) Corni, S.; Pipolo, S.; Cammi, R. *J. Phys. Chem. A* **2015**, *119*, 5405–5416.
(26) Pipolo, S.; Corni, S. *J. Phys. Chem. C* **2016**, *120*, 28774–28781.
(27) Rokaj, V.; Welakuh, D. M.; Ruggenthaler, M.; Rubio, A. *J. Phys. B: Atomic, Molecular and Optical Physics* **2018**, *51*, 034005.
(28) Flick, J.; Ruggenthaler, M.; Appel, H.; Rubio, A. *Proc. Natl. Acad. Sci. USA* **2017**, *114*, 3026.
(29) De Bernardis, D.; Jaako, T.; Rabl, P. *Phys. Rev. A* **2018**, *97*, 043820.
(30) De Bernardis, D.; Pilar, P.; Jaako, T.; De Liberato, S.; Rabl, P. *Phys. Rev. A* **2018**,

98, 053819.
(31) Neuman, T.; Esteban, R.; Casanova, D.; García-Vidal, F. J.; Aizpurua, J. *Nano Lett.* **2018**, *18*, 2358–2364.
(32) Aguilar-Galindo, F.; Díaz-Tendero, S.; Borisov, A. G. *J. Phys. Chem. C* **2019**, *123*, 4446–4456.
(33) Bennett, K.; Kowalewski, M.; Mukamel, S. *Faraday Discuss.* **2016**, *194*, 259.
(34) Kowalewski, M.; Bennett, K.; Mukamel, S. *J. Chem. Phys.* **2016**, *144*, 054309.
(35) Herrera, F.; Spano, F. C. *Phys. Rev. Lett.* **2016**, *116*, 238301.
(36) Ribeiro, R. F.; Martínez-Martínez, L. A.; Du, M.; Campos-Gonzalez-Angulo, J.; Yuen-Zhou, J. *Chem. Sci.* **2018**, *9*, 6325–6339.
(37) Yuen-Zhou, J.; Menon, V. M. *Proc. Natl. Acad. Sci. USA* **2019**, *116*, 5214–5216.
(38) Zhong, X.; Chervy, T.; Zhang, L.; Thomas, A.; George, J.; Genet, C.; Hutchison, J. A.; Ebbesen, T. W. *Angew. Chem.* **2017**, *129*, 9162–9166.
(39) Schachenmayer, J.; Genes, C.; Tignone, E.; Pupillo, G. *Phys. Rev. Lett.* **2015**, *114*, 196403.
(40) Sáez-Blázquez, R.; Feist, J.; Fernández-Domínguez, A. I.; García-Vidal, F. J. *Phys. Rev. B* **2018**, *97*, 241407.
(41) Martínez-Martínez, L. A.; Du, M.; Ribeiro, R. F.; Kéna-Cohen, S.; Yuen-Zhou, J. *The J. Chem. Phys. Lett.* **2018**, *9*, 1951–195u.
(42) Du, M.; Ribeiro, R. F.; Yuen-Zhou, J. *Chem* **2019**, *5*, 1167–1181.
(43) Galego, J.; Garcia-Vidal, F. J.; Feist, J. *Phys. Rev. X* **2015**, *5*, 041022.
(44) Rossi, T. P.; Shegai, T.; Erhart, P.; Antosiewicz, T. J. *Nat. Commun.* **2019**, *10*, 3336.
(45) Groenhof, G.; Climent, C.; Feist, J.; Morozov, D.; Toppari, J. J. *The J. Chem. Phys. Lett.* **2019**, *10*, 5476–5483.
(46) Ulusoy, I. S.; Gomez, J. A.; Vendrell, O. *J. Phys. Chem. A* **2019**, *123*, 8832–8844.
(47) Sanvitto, D.; Kéna-Cohen, S. *Nat. Materials* **2016**, *15*, 1061–1073.
(48) Benz, F.; Schmidt, M. K.; Dreismann, A.; Chikkaraddy, R.; Zhang, Y.; Demetriadou, A.; Carnegie, C.; Ohadi, H.; de Nijs, B.; Esteban, R.; Aizpurua, J.; Baumberg, J. J. *Science* **2016**, *354*, 726–729.
(49) Carnegie, C.; Griffiths, J.; de Nijs, B.; Readman, C.; Chikkaraddy, R.; Deacon, W. M.; Zhang, Y.; Szabó, I.; Rosta, E.; Aizpurua, J.; Baumberg, J. J. *The J. Chem. Phys. Lett.* **2018**, *9*, 7146–7151.
(50) Zasedatelev, A. V.; Baranikov, A. V.; Urbonas, D.; Scafirimuto, F.; Scherf, U.; Stöferle, T.; Mahrt, R. F.; Lagoudakis, P. G. *Nat. Photonics* **2019**, *13*, 378–383.
(51) Kéna-Cohen, S.; Forrest, S. R. *Nat. Photonics* **2010**, *4*, 371–375.
(52) Jayaprakash, R.; Georgiou, K.; Coulthard, H.; Askitopoulos, A.; Rajendran, S. K.; Coles, D. M.; Musser, A. J.; Clark, J.; Samuel, I. D. W.; Turnbull, G. A.; Lagoudakis, P. G.; Lidzey, D. G. *Light Sci. Appl.* **2019**, *8*, 81.
(53) Hill, N. S.; Coote, M. L. In *Chapter Seven - A comparison of methods for theoretical photochemistry: Applications, successes and challenges*; Dixon, D. A., Ed.; Annu. Rep. Computat. Chem.; Elsevier, 2019; Vol. 15; pp 203 – 285.
(54) Garavelli, M. *Theor. Chem. Acc.* **2006**, *116*, 87–105.
(55) Persico, M.; Granucci, G. *Theor. Chem. Acc.* **2014**, *133*, 1526.
(56) Abedi, A.; Maitra, N. T.; Gross, E. K. U. *Phys. Rev. Lett.* **2010**, *105*, 123002.
(57) Requist, R.; Gross, E. K. U. *Phys. Rev. Lett.* **2016**, *117*, 193001.

(58) Worth, G. A.; Meyer, H.-D.; Köppel, H.; Cederbaum, L. S.; Burghardt, I. *Int. Rev. Phys. Chem.* **2008**, *27*, 569–606.
(59) Richings, G.; Polyak, I.; Spinlove, K.; Worth, G.; Burghardt, I.; Lasorne, B. *Int. Rev. Phys. Chem. 34*, 269–308.
(60) Ben-Nun, M.; Quenneville, J.; Martínez, T. J. *J. Phys. Chem. A* **2000**, *104*, 5161–5175.
(61) Tapavicza, E.; Tavernelli, I.; Rothlisberger, U. *Phys. Rev. Lett.* **2007**, *98*, 023001.
(62) Toniolo, A.; Granucci, G.; Martínez, T. J. *J. Phys. Chem. A* **2003**, *107*, 3822–3830.
(63) Ciminelli, C.; Granucci, G.; Persico, M. *Chem. Eur.* **2004**, *10*, 2327–2341.
(64) Barbatti, M. *WIREs Comput. Mol. Sci.* **2011**, *1*, 620–633.
(65) Agostini, F.; Tavernelli, I.; Ciccotti, G. *Eur. Phys. J. Phys.* **2018**, *91*, 139.
(66) Granucci, G.; Persico, M.; Zoccante, A. *J. Chem. Phys.* **2010**, *133*, 134111.
(67) Cantatore, V.; Granucci, G.; Persico, M. *Comput. Theor. Chem.* **2014**, *1040-1041*, 126–135.
(68) Jain, A.; Alguire, E.; Subotnik, J. E. *J. Chem. Theory Comput.* **2016**, *12*, 5256–5268.
(69) Jaeger, H. M.; Fischer, S.; Prezhdo, O. V. *J. Chem. Phys.* **2012**, *137*, 22A545.
(70) Levine, B. G.; Coe, J. D.; Virshup, A. M.; Martnez, T. J. *Chem. Phys.* **2008**, *347*, 3 – 16, Ultrafast Photoinduced Processes in Polyatomic Molecules.
(71) Shimojo, F.; Ohmura, S.; Mou, W.; Kalia, R. K.; Nakano, A.; Vashishta, P. *Comput. Phys. Commun.* **2013**, *184*, 1 – 8.
(72) Gossel, G. H.; Lacombe, L.; Maitra, N. T. *J. Chem. Phys.* **2019**, *150*, 154112
(73) Mignolet, B.; Curchod, B. F. E. *J. Phys. Chem. A* **2019**, *123*, 3582–3591.
(74) Barbatti, M.; Lan, Z.; Crespo-Otero, R.; Szymczak, J. J.; Lischka, H.; Thiel, W. *J. Chem. Phys.* **2012**, *137*, 22A503.
(75) Granucci, G.; Persico, M. *J. Chem. Phys.* **2007**, *126*, 134114.
(76) Polli, D.; Altoè, P.; Weingart, O.; Spillane, K. M.; Manzoni, C.; Brida, D.; Tomasello, G.; Orlandi, G.; Kukura, P.; Mathies, R. A.; Garavelli, M.; Cerullo, G. *Nature* **2010**, *467*, 440–443.
(77) Armstrong, G. *Nat. Chem.* **2010**,
(78) Matsika, S.; Krause, P. *Annu. Rev. Phys. Chem.* **2011**, *62*, 621–643.
(79) Polivka, T.; Sundstrom, V. *Chem. Phys. Lett.* **2009**, *477*, 1 – 11.
(80) Hashimoto, H.; Uragami, C.; Yukihira, N.; Gardiner, A. T.; Cogdell, R. J. *J. R. Soc. Interface* **2018**, *15*, 20180026.
(81) Feng, J.; Tseng, C.-W.; Chen, T.; Leng, X.; Yin, H.; Cheng, Y.-C.; Rohlfing, M.; Ma, Y. *Nat. Commun.* **2017**, *8*, 71.
(82) Dreuw, A.; Head-Gordon, M. *J. Am. Chem. Soc.* **2004**, *126*, 4007–4016.
(83) Ufimtsev, I. S.; Martínez, T. J. *J. Chem. Theory Comput.* **2008**, *4*, 222–231.
(84) Parrish, R. M.; Hohenstein, E. G.; McMahon, P. L.; Martínez, T. J. *Phys. Rev. Lett.* **2019**, *122*, 230401.
(85) Liu, F.; Sanchez, D. M.; Kulik, H. J.; Martnez, T. J. *Int. J. Quantum Chem.* **2019**, *119*, e25760.
(86) Conti, I.; Alto, P.; Stenta, M.; Garavelli, M.; Orlandi, G. *Phys. Chem. Chem. Phys.* **2010**, *12*, 5016–5023.
(87) Segatta, F.; Cupellini, L.; Garavelli, M.; Mennucci, B. *Chem. Rev.* **2019**, *119*, 9361–9380.

(88) Keal, T. W.; Koslowski, A.; Thiel, W. *Theor. Chem. Acc.* **2007**, *118*, 837–844.
(89) Cusati, T.; Granucci, G.; Martínez-Núñez, E.; Martini, F.; Persico, M.; Vázquez, S. *J. Phys. Chem. A* **2012**, *116*, 98.
(90) Alexandrova, A. N.; Tully, J. C.; Granucci, G. *J. Phys. Chem. B* **2010**, *114*, 12116–12128.
(91) Toniolo, A.; Thompson, A. L.; Martnez, T. J. *Chem. Phys.* **2004**, *304*, 133 – 145.
(92) Granucci, G.; Persico, M.; Toniolo, A. *J. Chem. Phys.* **2001**, *114*, 10608–10615.
(93) Granucci, G.; Persico, M. *Theor. Chem. Acc.* **2007**, *117*, 1131–1143.
(94) Granucci, G.; Toniolo, A. *Chem. Phys. Lett.* **2000**, *325*, 79–85.
(95) Granucci, G.; Persico, M. *J. Comput. Chem.* **2011**, *32*, 2690.
(96) Stewart, J. J. P. *Fujitsu Limited* **2000**, Tokyo.
(97) Mennucci, B.; Corni, S. *Nat. Rev. Chem.* **2019**, *3*, 315–330.
(98) Tomasi, J.; Mennucci, B.; Cammi, R. *Chem. Rev.* **2005**, *105*, 2999–3094.
(99) Cancs, E.; Mennucci, B.; Tomasi, J. *J. Chem. Phys.* **1997**, *107*, 3032–3041.
(100) Tomasi, J.; Mennucci, B.; Cancs, E. *J. Mol. Struct.* **1999**, *464*, 211 – 226.
(101) Eilmes, A. *Theor. Chem. Acc.* **2014**, *133*, 1538.
(102) Cerón-Carrasco, J.; Jacquemin, D.; Laurence, C.; Planchat, A.; Reichardt, C.; Sraïdi, K. *J. Phys. Chem. B* **2014**, *118*, 4605–4614.
(103) Chibani, S.; Budzàk, S.; Medved, M.; Mennucci, B.; Jacquemin, D. *Phys. Chem. Chem. Phys.* **2014**, *16*, 26024–26029.
(104) Caricato, M.; Mennucci, B.; Tomasi, J. *Mol. Phys.* **2006**, *104*, 875–887.
(105) Coccia, E.; Troiani, F.; Corni, S. *J. Chem. Phys.* **2018**, *148*, 204112.
(106) Coccia, E.; Corni, S. *J. Chem. Phys.* **2019**, *151*, 044703.
(107) Vukovic, S.; Corni, S.; Mennucci, B. *J. Phys. Chem. C* **2009**, *113*, 121–133.
(108) Corni, S.; Tomasi, J. Studying SERS from Metal Nanoparticles and Nanoparticles Aggregates with Continuum Models. In *Surface-Enhanced Raman Scattering: Physics and Applications*; Kneipp, K., Moskovits, M., Kneipp, H., Eds.; Springer Berlin Heidelberg: Berlin, Heidelberg, 2006; pp 105–123.
(109) Morton, S. M.; Jensen, L. *J. Chem. Phys.* **2011**, *135*, 134103.
(110) Rosa, M.; Gil, G.; Corni, S.; Cammi, R. *J. Chem. Phys.* **2019**, *151*, 194109.
(111) Loco, D.; Lagardre, L.; Cisneros, G. A.; Scalmani, G.; Frisch, M.; Lipparini, F.; Mennucci, B.; Piquemal, J.-P. *Chem. Sci.* **2019**, *10*, 7200–7211.
(112) Loco, D.; Jurinovich, S.; Cupellini, L.; Menger, M. F. S. J.; Mennucci, B. *Photochem. Photobiol. Sci.* **2018**, *17*, 552–560.
(113) Alto, P.; Stenta, M.; Garavelli, M. *AIP Conf. Proc.* **2007**, *963*, 689–692.
(114) Dokukina, I.; Nenov, A.; Garavelli, M.; Marian, C. M.; Weingart, O. *ChemPhotoChem* **2019**, *3*, 107–116.
(115) Ponder, J. W.; Richards, F. M. *J. of Comput. Chem.* **1987**, *8*, 1016–1024.
(116) Dalibard, J.; Castin, Y.; Mølmer, K. *Phys. Rev. Lett.* **1992**, *68*, 580–583.
(117) Plenio, M. B.; Knight, P. L. *Rev. Mod. Phys.* **1998**, *70*, 101–144.
(118) Herrera, F. *Chem* **2020**, *6*, 7 – 9.
(119) Liu, H.; Zhang, L.; Lang, X.; Yamaguchi, Y.; Iwasaki, H.; Inouye, Y.; Xue, Q.; Chen, M. *Sci. Rep.* **2011**, *1*, 112.
(120) Garoli, D.; Yamazaki, H.; Maccaferri, N.; Wanunu, M. *Nano Lett.* **2019**, *19*, 7553–7562.

(121) Liu, H.; Zhang, L.; Lang, X.; Yamaguchi, Y.; Iwasaki, H.; Inouye, Y.; Xue, Q.; Chen, M. *Sci. Rep.* **2011**, *1*, 112.
(122) Verma, P.; Ichimura, T.; Yano, T.-a.; Inouye, Y.; Kawata, S. *Proc. SPIE* **2008**, *6793*.
(123) Tame, M. S.; McEnery, K. R.; Özdemir, Ş. K.; Lee, J.; Maier, S. A.; Kim, M. S. *Nat. Phys.* **2013**, *9*, 329–340.
(124) Sur, U. K. Surface-Enhanced Raman Scattering. In *Raman Spectroscopy and Applications*; Maaz, K., Ed.; IntechOpen: Rijeka, 2017; Chapter 14.
(125) Stranahan, S. M.; Willets, K. A. *Nano Lett.* **2010**, *10*, 3777–3784.
(126) Doppagne, B.; Neuman, T.; Soria-Martinez, R.; López, L. E. P.; Bulou, H.; Romeo, M.; Berciaud, S.; Scheurer, F.; Aizpurua, J.; Schull, G. *Nat. Nanotechnol.* **2020**, *15*, 207–211.
(127) Hohenester, U.; Trgler, A. *Comput. Phys. Commun.* **2012**, *183*, 370 – 381.
(128) Waxenegger, J.; Trgler, A.; Hohenester, U. *Comput. Phys. Commun.* **2015**, *193*, 138 – 150.